Dissertation

submitted to the
Combined Faculties for the Natural Sciences and for Mathematics
of the Ruperto-Carola University of Heidelberg, Germany
for the degree of
Doctor of Natural Sciences

Put forward by
Philipp Albert
born in Ulm
Oral examination: 27.05.2015

Modeling Cell Dynamics on Micropatterned Substrates with a Cellular Potts Model

Referees: Prof. Dr. Ulrich Schwarz
Prof. Dr. Heinz Horner

Modeling Cell Dynamics on Micropatterned Substrates with a Cellular Potts Model

Tools from materials science are increasingly used to decrease the variability that often limits the quantitative analysis of cell experiments. Most prominently, micropatterned substrates can be used to normalize cell shape and internal organization. For long-term experiments, however, cells must be able to divide and migrate. This creates the need to design networks of micropatterns that ensure normalization to be maintained even in a dynamic context. The design of such networks requires an efficient model predicting the degree of normalization for dividing and migrating cells. Here we extend earlier formulations of the two-dimensional cellular Potts model with the aim to achieve good agreement with existing cell experiments on cell shape and forces on micropatterns. We show that our model correctly predicts cell spreading, division and migration on micropatterns, both for single cells and cell communities. The inverse problem of network optimization is then addressed with genetic algorithms.

Modellierung von Zelldynamik auf mikrostrukturierten Substraten mit einem zellulären Potts-Modell

Methoden aus der Materialwissenschaft werden zunehmend eingesetzt, um die Variabilität in der quantitativen Analyse von Zellexperimenten zu verringern. Von größter Bedeutung sind dabei mikrostrukturierte Substrate, welche benutzt werden können, um Zellform und deren inneren Aufbau zu normieren. Für Langzeitstudien müssen die Zellen allerdings in der Lage sein, sich zu teilen und zu migrieren. Folglich müssen mikrostrukturierte Netzwerke entworfen werden, welche die Erhaltung der Zellnormierung auch in einem dynamischen Kontext gewährleisten. Um diese Netzwerke entwerfen zu können, wird ein effizientes Modell benötigt, welches den Grad der Normierung von sich teilenden und migrierenden Zellen vorhersagt. Hierfür erweitern wir das bereits etablierte zweidimensionale zelluläre Potts-Modell. Ziel ist dabei, eine gute Übereinstimmung mit bestehenden Experimenten zu Zellform und -kraft auf mikrostrukturierten Substraten zu erzielen. Wir zeigen, dass unser Modell Zellausbreitung, -teilung und -migration auf mikrostrukturierten Substraten korrekt vorhersagt, sowohl für einzelne Zellen als auch für Zellgruppen. Für das inverse Problem der Netzwerkoptimierung führen wir dann einen genetischen Algorithmus ein.

Contents

1 Introduction

1.1. The Shape of Cells

Over the last two decades, physical features like cell shape and forces have emerged as determinants of cell fate that are equally important as are biochemical and genetic factors. It has been shown that cells do not need only nutrition and growth factors to survive and grow, but also a certain level of spatial extension and force generation [4–7].

Most cells in animal or plant tissue grow in an environment where neighboring cells provide defined boundary conditions resulting in a very regular cell shape [8]. To study animal cells in detail, however, they are usually grown in cell culture on a two-dimensional substrate. The lower dimensionality in cell culture compared to tissue makes them easier to image and many experiments would not be possible without the simplification a two dimensional environment brings. As in physics, reducing degrees of freedom and studying systems under controlled conditions is an integral part of biology.

Unlike inanimate objects, however, cells react to changes in their environment. Figure 1.1a shows cells grown in cell culture. Without the confinement and boundary conditions imposed by neighbouring cells in three-dimensional tissue the cells display a large variety of sizes and shapes although all cells belong to the same cell type. The cells shown in Figure 1.1a are stained with fluorophores which can be modified to bind to specific components of the cell. In the image shown, green fluorescent dye binds to actin, which forms the mechanical backbone of the cell, blue dye to DNA marking the nucleus and red dye to mitochondria generating the energy needed by the cell to live. The green actin is present throughout the whole cell and also marks its outline. Each nucleus indicated by the blue dots belongs to a single cell and without any further information, it is almost impossible to identify boundaries between cell or to even determine their size. Experiments with structure related readouts, such as the

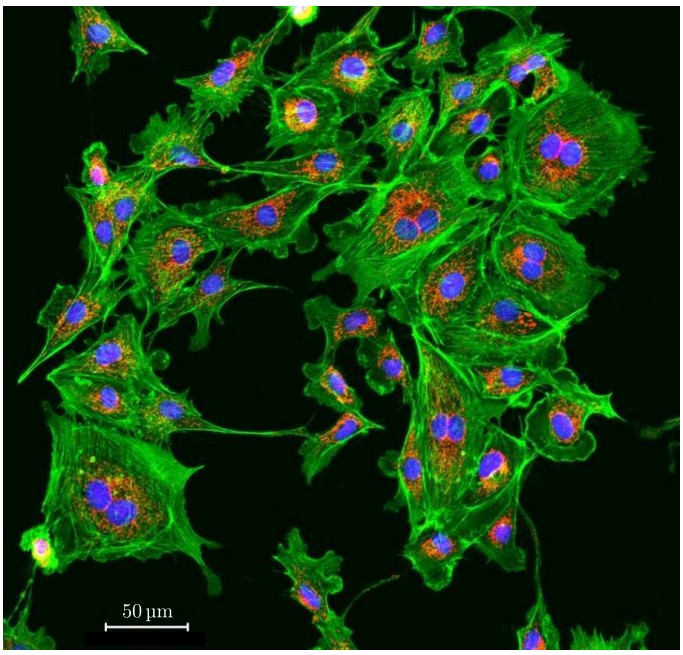

(a)

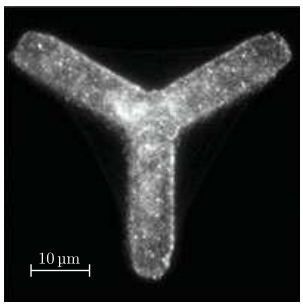

(b)

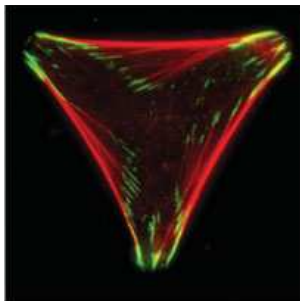

(c)

Figure 1.1. (a) Epithelial cells grown in cell culture stained for actin (green), nucleus (blue) and mitochondria (red) [9]. Without constrains the cell shape is very irregular and cells adhere to each other. (b) [Y] shaped micropattern. The extracellular matrix made of fibronectin (white) is printed on a nonadhesive background of polyethylene glycol [10]. Cells can only adhere to the extracellular matrix. (c) A single cell on [Y] shaped pattern stained for actin (red) and vinculin (green) which is involved in cell adhesion [10]. The cell has a very regular shape determined by the micropattern.

organization of actin or distribution of cell organelles, are hard to quantify due to the inherent variability of cell shape in cell culture. The initial simplification by studying cells extracted from the complex tissue environment turns out to be a drawback when it comes to shape and structure related readouts.

However, there exists a method from material science to restore a defined geometry in cell culture. Most cell types need a surface, called the extracellular matrix (ECM), they can adhere to in order to stay alive. The ECM is a mixture of different proteins and without it present on the substrate in sufficient quantities cells die [4]. Thus, by controlling the ECM, boundary conditions can be imposed on cells again in cell culture.

Photolithography well established for semiconductors allows to manufacture surfaces with specific ECM geometries. Either by printing ECM proteins from a stamp produced by lithography [11] or by using lithography directly to modify the surface the ECM binds to [12]. A even more direct method without a photomask is the use of high energy lasers to modify the surface [13].

Figure 1.1b shows a substrate with micrometer sized features printed on. Such micropatterns provide a defined geometry of ECM proteins to cells which can only

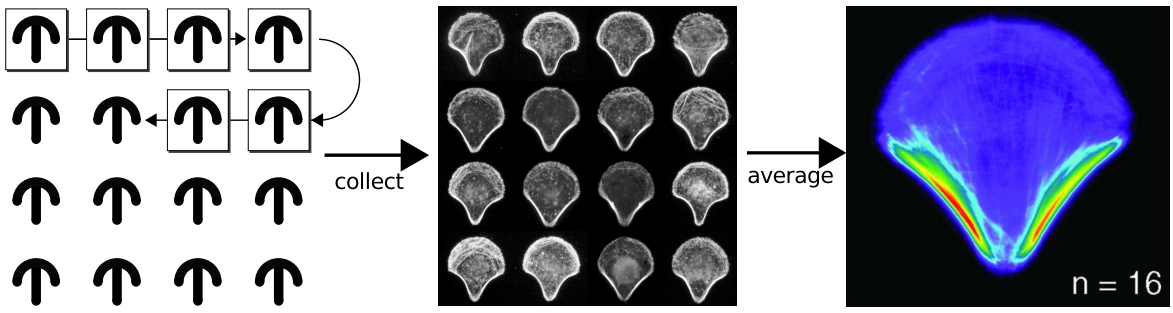

Figure 1.2. Cell normalization. Cells are grown on an array of micropatterns. Images of the cells are collected and averaged. The cells are stained for actin and the averaged cell displays prominent actin features at concave segments of the cell boundary. 16 cells where averaged. Figure Adapted from [14] with the cell images in part (b) obtained by the collaboration with Dr. Starkuviene.

adhere to the printed pattern. As shown in Figure 1.1c a cell growing on such a [Y] shaped pattern has a defined shape. This time, actin is stained in red and vinculin, a protein involved in the adhesion of the cell to the substrate, in green. Adhesion occurs only on the ECM but the cell spans also non-adhesive regions resulting in the almost triangular shape.

Seeding many cells on micropatterns as depicted in Figure 1.2 results in an array of regular shaped cells. Superposition of many such cells averages variations inherent to biological experiments and result in the normalized cell shown in Figure 1.2c. Bright red areas indicate regions with increased actin density which strongly localizes to convex parts of cells. Micropatterns allow to quantify differences in actin distribution and other cellular proteins [14]. Moreover, they allow to relate form and function of cells systematically [15].

The possibility to shape cells, control boundary conditions and repeatability offers many more possibilities [8, 16] which will be review in greater detail below. But this first requires an understanding of cell mechanics [17].

1.2. The Contractile Cell

Cells are not static objects. They actively explore their environment and constantly change their internal organization and adhesion to the substrate [18]. The key structural element for most mammalian cell is the protein actin. In its monomeric form, it is a globular polar protein with a size of 6 nm [19]. It can polymerize into double stranded polar filaments of several µm length [19]. Addition of new subunits happens preferentially at the so called barbed end and depolymerization at the pointed end [20] as depicted in Figure 1.3b. The polymerization is driven by hydrolysis of adenosine triphosphate (ATP) providing an energy of 80 pN nm which is much larger than the thermal energy of $k_bT = 4.1\,\mathrm{pN\,nm}$ at 300 K available in cells [21, see Appendix

B therein]. Special proteins associated with the barbed or pointed ends regulate the polymerization allowing control of the filament length [22].

Filaments are not restricted to a linear geometry. Branching is mediated through a protein complex called Arp2/3. It allows new filaments to grow out from existing ones with a defined angle of 70° [20] also depicted in Figure 1.3b. Together with crosslinkers connecting single filaments, branching allows actin to assembly into networks. Another mode of higher order organization are bundles of parallel actin filaments which are stabilized by crosslinker proteins like α-actinin.

All of the above actin structures are present in cells and are commonly referred to as the actin cytoskeleton (ACS) . Figure 1.3a shows a cell on a two dimensional substrate. The interface between the cell and the surrounding medium is formed by a lipid double layer called the cell membrane [23]. Underneath the cell membrane and connected to it lies the actin cortex, a network of crosslinked actin filaments stabilizing the membrane [24]. The cortex in Figure 1.3a is only shown at the outline of the two dimensional cell, but it actually spans across the whole membrane removed in the image to show the interior of the cell. Bundles of parallel actin filaments are formed at several locations. Stress fibers [25] span across the whole cell and end in focal adhesions (purple dots), large protein complexes responsible for cell adhesion discussed below. Filopodia are actin filled protrusions exploring the surrounding. They originate from the lamellipodium, an actin rich region with a branched and crosslinked network of filaments.

The cell shown in Figure 1.3a is moving in the direction of the lamellipodium which requires the asymmetric distributions of the different actin structures. At the front, the so called leading edge, actin polymerizes and the elongating filaments push against the membrane moving it forward [20, 27, 28]. At the back, the cell cortex is strongly contracted by myosin II, a molecular motor introduced below, to drag the rear of the cell along. The branched network in the lamellipodium generates a uniform pushing force and a broad propagating cell front is formed. In contrast, the crosslinked parallel filaments pushing in filopodia generate spike like protrusions. A few microns behind the leading edge, in the lamella, the branched network disappears and stress fibers are formed [29] which involves non-muscle myosin II, another key player in cell mechanics.

Myosin II is a molecular machine converting chemical energy stored in ATP into motion. It consists of a head domain responsible for the ATP conversion and a long tail which allows assembly of many myosin proteins into larger structures. Myosin II is present in large quantities in muscles where it generates the force for contraction [23]. It moves along actin filaments into the direction of barbed ends. Single myosin motors can generate forces of several pN [19] and work in groups to increase cooperativity and force output. In non-muscle cells 14-20 myosin molecules assemble into bipolar filaments with head domains pointing in opposite directions [30]. Because the minifilaments are bipolar, the myosin heads at opposite ends can pull actin filaments with the right polarity toward each other as depicted in Figure 1.3c.

Myosin contraction starts a few microns behind the lamellipodium. The force induced by it partly breaks filaments in the previously grown network down and helps to disassemble it [20]. The remodeling of the network by myosin also helps in the assem-

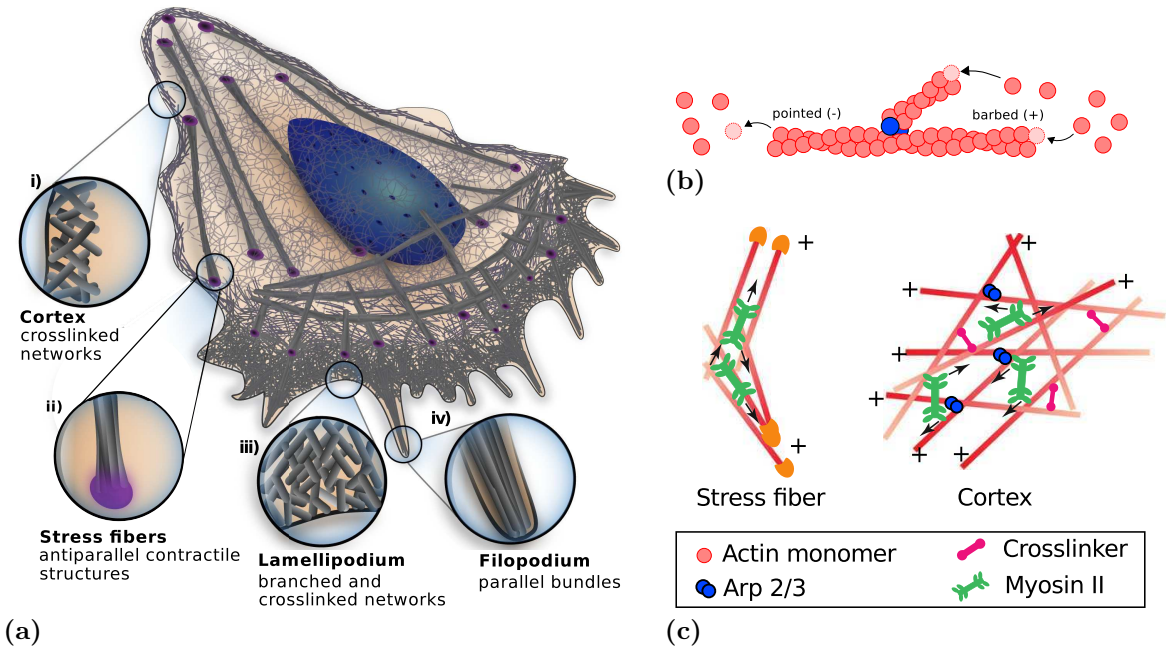

Figure 1.3. (a) Migrating cell with different types of actin structures (gray) forming the actin cytoskeleton (ACS). The nucleus is shown in blue and focal adhesions connecting the cell to the substrate in purple. Adapted from [20]. (b) Polymerizing actin filament. Actin monomers (circles) assemble into polar helical filaments. Polymerization preferentially happens at the barbed end and depolymerization at the pointed. Branching is enabled through the Arp2/3 protein complex (blue) which binds to existing filaments and provides a nucleation site for a new filament. Branched filaments grow out with an angle of 70° from existing filaments. (c) Actin structures contracted by bipolar myosin II minifilaments (green). Myosin moves towards the barbed (+) end of actin. Assembled into bipolar filaments it generates contractile forces in actin with antiparallel organization in stress fibers and random organization in the cortex. Adapted from [26].

bly of stress fibers [29]. The antiparallel actin filament organization of the fibers allows them to be strongly contracted by the bipolar filaments. Myosin is also present in the actin cortex where it controls cell shape. In migrating cells its activity is increased in the rear to contract it and drag it along [27].

Contractile fibers or polymerizing networks could not generate forces without being anchored to the substrate. Without anchorage, the fibers would just slide past each other without any resistance. Anchorage occurs via large protein complexes called focal adhesions [31]. Focal adhesions link actin filaments through the membrane to the ECM and can only form and grow if they experience pulling forces through their actin connection [18]. They start to form as focal complexes in the lamella a few microns behind the lamellipodium [18, 20, 26] (compare Figure 1.3a). Forces generated at the leading edge by polymerization are transmitted to the substrate by them [27]. In a similar fashion stress fibers are anchored. The forces generated by myosin in them

are used by the cell to deform and probe the ECM. In this way, cells can translate environmental properties such as the rigidity of the matrix into signals in a process called mechanotransduction [32, 33]. The complex array of molecules focal adhesions are made of is thought to be involved in the transfer of mechanical responses into chemical signals [33]. Models for myosin II suggest that the motors also react to changes in of the ECM rigidity supporting the sensing by focal adhesions [1, 2]. The sensing of the environment is important e.g. in tissue to get information about when to grow or migrate. In turn, it plays an important role in disease. The most prominent example is the invasion of healthy tissue by cancer cells which are assumed to have lost the ability to sense other cells [20].

The migrating cell in figure 1.3a can now be fully understood. Actin polymerizing at the leading edge pushes the membrane forward and is anchored to the substrate by focal adhesions. A few microns behind the leading edge, myosin contraction starts, the actin network is remodeled and depolymerizes partly. Elongation at the front and depolymerization at the back form a treadmill like structure [34] moving the cell front forward. Focal adhesions are disassembled at the rear of the cell where also increased myosin activity in the cortex helps to retract the moving cell. Lamellipodia do not only exist in migrating cells. They are also formed during cell spreading and are used to explore the environment.

1.3. Micropatterns Control Cell Shape and Behavior

The insights micropatterns reveal about cell mechanics is already demonstrated by the averaged cell in Figure 1.2. It shows that actin strongly localizes to concave sections of the cell contour which is now easy to understand. The contractile actin cortex beneath the membrane tries to pull the contour inwards while the stress fibers forming in the cell periphery resist the contraction and pull the contour outwards allowing the cell to spread over a wider area. The circular shape of cells at regions without ECM was investigated in more detail on dot patterns as show in Figure 1.4a [15]. The free spanning arcs are indeed circular as shown in the bottom of the Figure indicating a type of Laplace law involved. It was further observed, that the arc radius depends on the distance between dots, which gives further insights in the forces acting along arcs [15].

Besides the mechanical aspects pattern where used in a pioneering study which showed that cell survival depends not only on the amount of ECM ligand offered to the cell but also also on the spatial extensions of it [4]. The internal organization of cells was also investigated in great detail with micropatterns, including the distribution of stress fibers [10, 37], the influence of cell geometry on cell division [38–41] or how shape and drugs influence the machinery responsible for intracellular transport [42].

Micropatterns are not limited to define shape, they also provide defined geometries for cell migration. Initial studies where performed on cells on isolated island to investigate the impact of shape on lamellipodium formation [43] and the preferred migration direction after removal of the pattern constraint [44]. Arrangement of triangles as

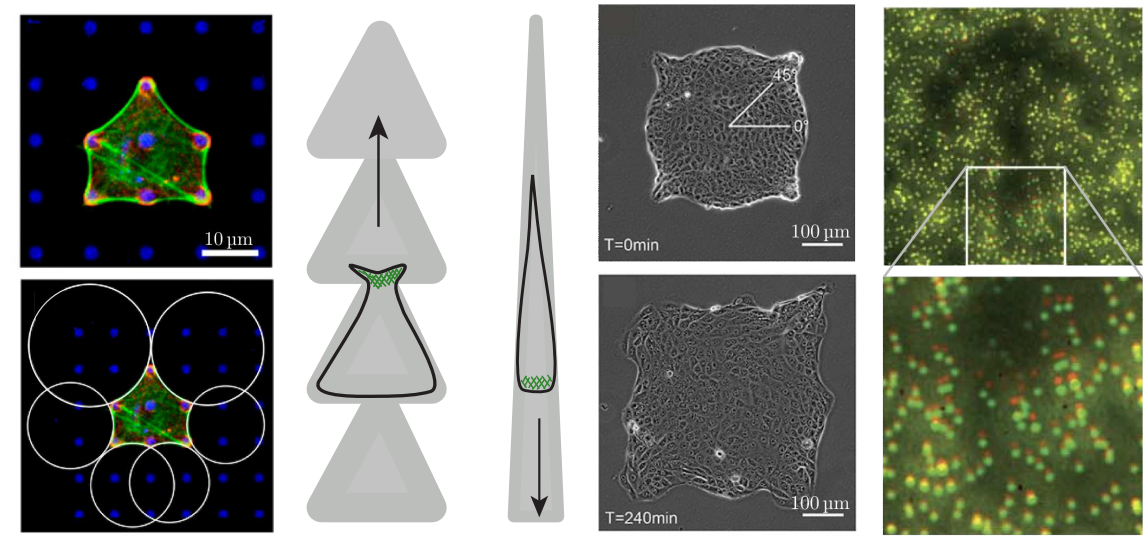

Figure 1.4. (a) Cell on dot pattern (blue) stained for actin (green). Prominent stress fibers are visible at the edge of the cell. The same cell is shown in the bottom image with circles fitted to the arcs spanning between dots [15]. (b) Cell migration biased by pattern geometry. The green mesh indicates the branched actin network in the lamellipodium and the migration direction is indicated by arrows. Variation of the triangular shape can reverse migration direction. Adapted from [16]. (c) Phase contrast image of epithelial cells confined to a circular shape by a stencil (top). After stencil removal leader cells guiding the migration preferentially form at the tips of spikes (bottom) [35]. (d) Principle of traction force microscopy. Fluorescent beads are embedded into an elastic substrate. The magnification of the substrate at the bottom shows beads before (red) and after (green) cell detachment. The displacement of the beads is used to reconstruct forces. This experiment combined micropatterns with elastic substrates, the shape of the [crossbow] pattern can be seen in the top image. Adapted from [36].

depicted in Figure 1.4b were shown to bias cell migration into one direction [45, 46], gaps between patterns have an influence on the bias [45, 47] and variations of the triangle shape can reverse migration direction [16].

Multicellular systems have also been investigated in great detail. Cell pairs placed on circular and square shaped patterns display a rotational motion [48] which persists if the cell number is increased but eventually breaks down into several swirls for very large numbers of cells [49]. The rotational motion can be completely stopped by variations of the pattern geometry [50], e.g. by putting cell pairs on [H] shaped patterns. The collective migration of many cells is important for wound healing and comb shaped patterns have demonstrated the ability of cell sheets to bridge wide nonadhesive areas [51]. Cues for the migration direction can arise from the curvature of the cell front as shown in Figure 1.4c [35].

Cellular sensing of micropattern geometry is closely related to stiffness sensing of the ECM, as both depend on cellular forces being developed in the ACS. Those forces are transmitted to the ECM via focal adhesions [18]. In order to measure cellular forces on flat elastic substrates, different variants of traction force microscopy have been developed [52–54]. They work by placing fluorescent beads into an elastic substrate as shown in Figure 1.4d. A cell adhering to the substrate contracts and deforms it. From the displacement of the beads in the substrate the force generated by the cell can be reconstructed. This approach is now increasingly combined with micropatterning of cell shape, for example by using microcontact printing [55] or deep UV-illumination of polyacrylamide substrates [36, 56] or lift-off techniques on silicone rubber substrates [57].

1.4. Modeling Cell Shape and Forces

Micropatterning of cell shape is naturally complemented by quantitative image processing and modeling. Several types of mathematical models have been developed to predict cell shape on micropatterns [17, 58]. The simplest type is a contour model. Motivated by circular arc features of cells adhering to homogeneous substrates, it has been suggested early that Laplace-type models arise from the competition of tension in the periphery (geometrically a line tension) and tension in the cell body (geometrically a surface tension) [59, 60]. In the following, we will call this approach the simple tension model (STM). A quantitative analysis of cell shape on dot patterns (compare Figure 1.4a) has shown that in the presence of strong contour reinforcement by peripheral actin bundles, the simple tension model has to be modified by elastic elements, leading to the tension-elasticity model (TEM) [15]. Both STM and TEM not only describe cell shape, but also cell forces [61]. Recently it has been shown that the TEM emerges as a good approximation to a bulk model for contractile cells if the the bulk arcs do not accumulate compression energy [62, 63].

The natural starting point for a bulk model of cell shape is continuum mechanics, which can be implemented with the Finite Element Method (FEM). To represent contractility in such a framework, one can use isotropic thermoelasticity, which represents contractility by a negative pressure in the elastic equations, as it can be induced in passive materials by lowering temperature. This approach is commonly used for model contraction in cell monolayers [64–66]. Recently also the shape and forces of cells on micropatterns have been predicted with such an isotropic thermoelastic model [67]. In order to represent the anisotropic effect of stress fibers, the isotropic thermoelastic approach has been extended by an orientation-dependent order parameter field for contractility [68, 69]. The strength of a stress fiber is determined by a positive feedback mechanism regarding how much force can be built up in a given direction, favoring directions of large effective stiffness. Cell shapes and forces then can be predicted if the attachment sites are known, for example for micropatterns [62, 70] and pillar arrays [71].

FEM-based models for cell shape usually assume linear elastic or hyperelastic mate-

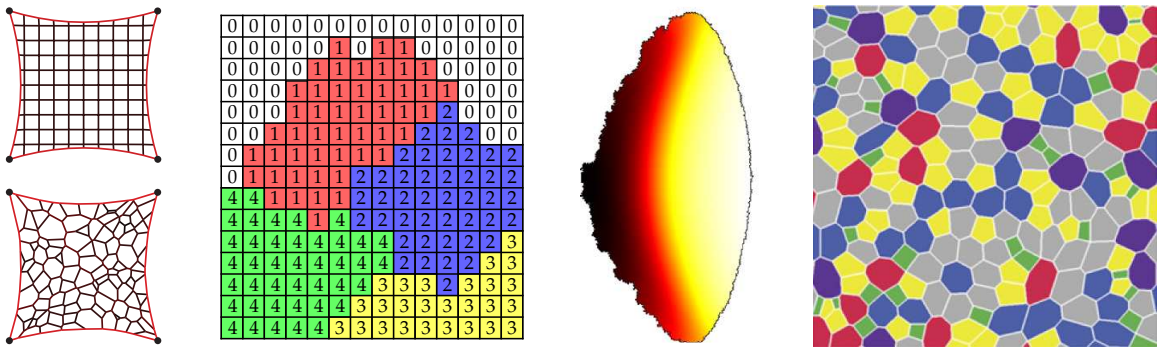

(a) (b) (c) (d)

Figure 1.5. Cell representations in different two-dimensional models. (a) Cable network model representation with regular and irregular networks. The cells are pinned at the four corners and the network edges are contractile. Both network topologies result in similar cell contours. Adapted from [63]. (b) Two dimensional lattice based cell representation in a cellular Potts model (CPM). All lattice sites with the same spin orientation (indicated by a number and color) belong to one cell. The medium surrounding cells is labeled with 0. (c) Keratocyte crawling to the right described by a CPM. Migration is driven by a reaction diffusion system of the small G-proteins solved in the domain defined by the cell. Small G-proteins interact with actin and myosin. The color encodes Arp2/3 concentration which is at maximum at the leading edge [72]. (d) Vertex model representation of tissue. Each face surrounded by edges represents a cell. The edges usually meet in three fold vertices. The color of the cells encodes the number of neighbors [73].

rial laws for the mechanical properties of cells. Indeed often this is a good assumption, for example on the large scale of tissues or for single cells with conserved volume. However, for cells adhering to a substrate, the projected area is not a conserved quantity and volume can be exchanged with the third dimension. In this case, the mechanical response is mainly determined by the actin cytoskeleton, which behaves like an elastic solid under extension, but does not resist compression because actin filaments under compression can buckle, depolymerize and slide. When modeling cells on an intermediate length scale, this fundamental asymmetry between tension and compression can be represented by cable networks [74, 75]. If actomyosin contractility is not represented by a reduced resting length, but rather by a constant pull between neighboring nodes, one arrives at the model of actively contracting cable networks [15, 63] shown in Figure 1.5a. Because contractile tension dominates in the bulk and passive elastic tension in the periphery, the corresponding computer simulations are described well by the analytical predictions of the TEM, both for actively contracting cable networks [63] and thermoelastic continuum models [62].

All of the above models are relatively static in nature and assume that the general features of cell shape (in particular pinning points to the substrate) are already known. Here we aim to develop a model that predicts the dynamics of cell shape and traction

forces on micropatterned substrates without any a priori assumptions regarding the final shape. Two types of models seem to qualify in particular for this purpose. Phase fields models (also known as level set methods) have recently been used to predict cell shape in the context of cell migration, because they are particularly suited to represent propagating contours [76–80]. In order to represent contractility, however, cellular Potts models (CPM) seem to be more appropriate. CPMs are lattice-based and represent a cell by a collection of spins (compare Figure 1.5b), thus allowing for arbitrary cell shapes. By defining an energy functional on the spin configuration and exploiting the slow time scale for cell spreading, one can use Metropolis dynamics to propagate the system. CPMs are commonly used to model tissues, as reviewed in [81]. One prominent application is the study of cell sorting by the differential adhesion hypothesis [82, 83]. Besides applications to tissue, CPM have also been used in systems consisting of only a few cells [84]. Recently, however, a CPM has been applied also to predict the shape of single cells on micropatterned substrates [85]. Moreover single keratocyte movement has been modeled with a CPM by coupling the Metropolis dynamics to a model for actin polymerization [72, 86] with a typical cell shown in Figure 1.5c.

Like for the Ising model, the shapes predicted by the CPM are dominated by interfacial tension. This generates a close relation not only to contour models, but also to vertex models, which however are not lattice-based but rather define energy functionals for cell shapes with straight contours as shown in Figure 1.5d. They have been used e.g., to explore the role of mechanical interactions for growth of the *Drosophila* wing imaginal disk [87] or to investigate the influence of cell elasticity, cell-cell interaction and cell proliferation on cell sheet packing geometry [73, 88]. However, vertex models cannot be used to model single cells on micropatterns because they cannot account for arbitrary shapes.

Phase field, CPM and vertex models have in common that they describe the cell by an energy functional but they differ in how they represent cells and minimize the functional. CPM with their lattice based description and phase field models can account for arbitrary shapes. CPM use Metropolis dynamics to propagate the cell and phase field models overdamped dynamics. Vertex models are limited to straight contours and often use conjugated gradient methods to minimize the energy functional.

1.5. Aim and Outline of This Work

This theoretical work was motivated by the experimental need for micropatterns that are suitable for long time cell experiments. For example, the combination of micropatterns with RNA interference experiments. RNA interference is a tool to selectively knock down genes [89–91] without the need of genome modifications. The normalization micropatterns provide should make the identification of relevant RNAs easier [42], but the method requires cells to stay on the patterns for several days. During such a long time cells start to divide which ceases the normalization effect of the patterns. After all, the patterns were designed to provide shape normalization for one cell as

depicted in Figure 1.6a. To maintain cell normalization even after several cell divisions networks of patterns as shown in Figure 1.6b are required.

The cell normalization of a network shown in the Figure 1.6b is an idealization and experiments show that the arrangement of [Y] in an hexagonal lattice does not normalize cells. One cannot know if the cells divide in the right orientation such that one daughter cell is able to move on to the next pattern. Similarly, it is not known if two cell sitting on the same island are stable or start to migrate or even if a single cell already migrates to the next pattern. Trying out many different network layouts would take too much time and resources. Therefore, models are needed to predict the normalization effect a given layout has on cells.

The aim of this work is to develop a model which correctly predicts the behavior of cells on micropatterned substrates and to use this model to optimize the pattern layout with respect to cell normalization. Due to the complex nature of cells a computational model is the only choice. To optimize the pattern layouts a mechanism generating layouts is needed. The computer generated layouts are then evaluated by the model which requires it to be fast enough to allow evaluation of many possible candidates.

We choose a cellular Potts model (CPM) to describe cells because of its ability to describe single and multicellular systems dynamically and its computational simplicity. The model needs to fulfill certain requirements. Firstly, it needs to be mechanically coherent predicting the correct cell shapes and scaling behaviors found by the tension-elasticity model on the one hand and correct forces generated by the cell on the other. In addition, it needs to predict the placement of daughter cells after cell division, cell-cell interaction and cell migrations on arbitrary patterns correctly.

Following these requirements, the first chapter introduces the CPM and its Hamiltonian. Each term of the Hamiltonian is motivated on a single cell basis. We show that our approach can predict cell spreading dynamics, shapes and traction forces correctly. The second chapter introduces cell division and cell-cell interactions to the model. We show that a mapping of the pattern geometry to an ellipse is enough to predict the location of daughter cells correctly. The second part of this chapter discusses cell-cell adhesion and its implementation in detail. The third chapter extends the model by cell migration. Forces generated by actomyosin activity can be integrated in the CPM framework naturally and combined with an mechanism setting the cell polarity the stability of cell pairs on micropatterns can be predicted correctly.

The second part of this work addresses the optimization of the pattern layout with a genetic algorithm. The previously developed model is used to evaluate the normalization capabilities of layouts generated by the genetic algorithm. First, methods to generate arbitrary patterns are introduced and the genetic algorithm is tested with tasks where solutions are known. It is then applied to the optimization of micropattern networks.

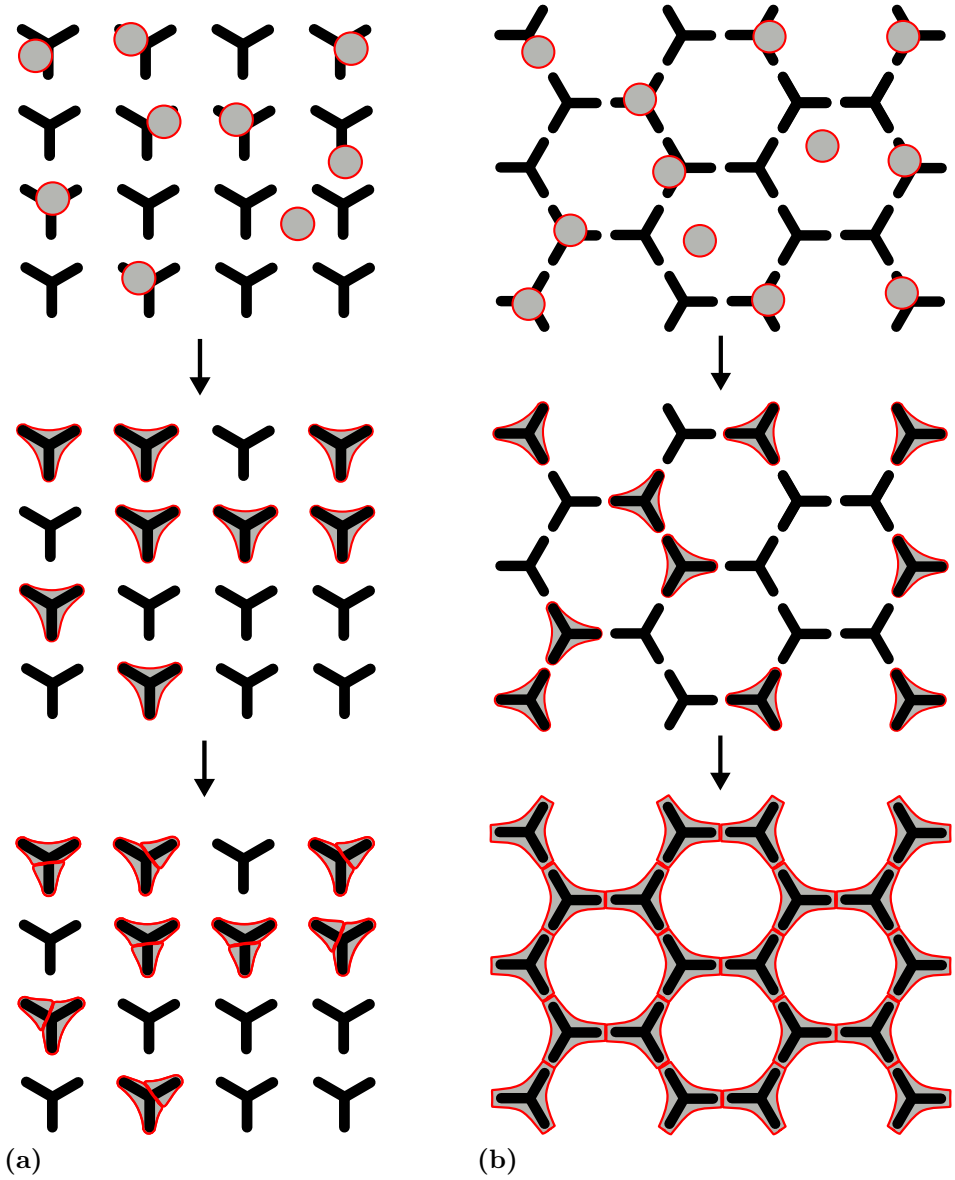

Figure 1.6. (a) Arrangement of isolated micropatterns. Spherical cells initially suspended in a medium make contact with the substrate and attach to adhesive micropatterns (top). Cells without contact to patterns die and cells with contact spread over the pattern. The micropatterns normalize the cell shape (middle). Cells start to divide and with neighboring patterns to far away two cells are stuck on one island (bottom). The normalization ceases, the cell pair might start to rotate or oscillate, and the cells might be in an unfavorable condition because they have to little area to spread. (b) Arrangement of micropatterns into a network. Cell make contact and adhere (top). Their shape gets normalized (middle). After cell division the daughter cells have neighboring patterns to explore and migrate there (bottom). The cells adhere to each other but stay normalized even after cell division.

2 The Cellular Potts Model

2.1. Introduction

The cellular Potts model (CPM) has been mainly used for multicellular systems with little exceptions [72, 85, 86]. On micropatterns cells are often isolated or the cell density is low which requires modifications of the Hamiltonian defining the cell model in several regards. In this chapter, we use insights from the tension-elasticity model (TEM) to derive a Hamiltonian for single cells on micropatterned substrates. The energy functional is based on the different kinds of tensions acting in the cell. The tensions are balanced by the adhesive substrate and can be interpreted as traction forces acting on it. Thus, the model derived in this way not only predicts cell shapes but also allows the extraction of traction forces for any adhesive geometry in a very efficient manner in good agreement with experimental results.

In the first part the classical CPM model and its origin from systems driven by interfacial tension is introduced. In a Potts model, the configuration space is often explored by Metropolis dynamics. The same dynamics is used for cells, although cells are nonequilibrium systems which needs justification. The second and main part of this chapter focuses on motivating the CPM Hamiltonian on a single cell basis. This part is based on the manuscript about cell dynamics and traction forces [3].

2.2. The Classical Cellular Potts Model

The cellular Potts model was developed to study cell sorting as proposed by the differential adhesion hypothesis [82, 83]. It originates from the Potts model [92] which is a generalized Ising model with more than two spin components. The spins usually reside on a regularly spaced two dimensional lattice and their interaction is described by an Hamiltonian. In the Potts model spin orientations are confined to a two-dimensional

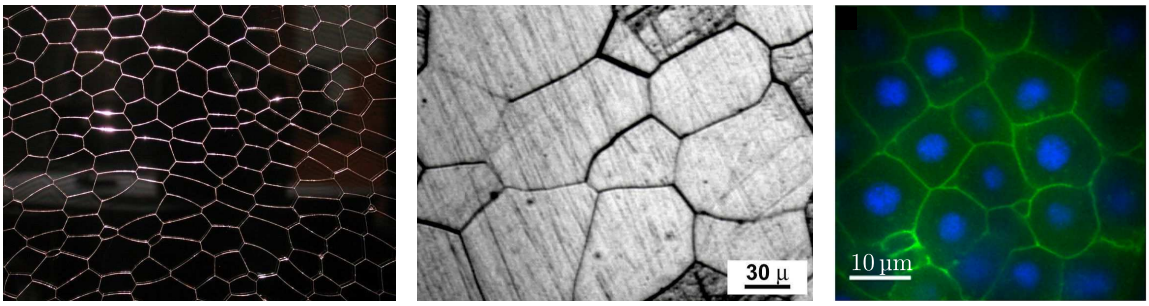

(a) **(b)** **(c)**

Figure 2.1. Systems with domains shaped by interfacial tension (a) Soap froth between glass plates [94]. (b) Polycrystalline metal grains etched to highlight grain boundaries [95]. (c) Zebrafish cell aggregate. Cell boundaries are green and the nuclei blue [96] .

plane and take orientations [92]

$$\Theta = \frac{2\pi n}{q}, \qquad n = 0, 1, \ldots, q-1, \tag{2.1}$$

where q denotes the number of possible spin orientations. One of the simplest interactions between neighboring spins is set by their relative orientation. The corresponding Hamiltonian is equal to

$$H_{\text{Potts}} = J \sum_{\langle \mathbf{i},\mathbf{j} \rangle} \cos(\Theta_{\mathbf{i}} - \Theta_{\mathbf{j}}), \tag{2.2}$$

where $\langle \mathbf{i}, \mathbf{j} \rangle$ denotes summation over all sites and their neighbors located at $\mathbf{i}$ and $\mathbf{j}$ on the two dimensional lattice. $\Theta_{\mathbf{i}}$ and $\Theta_{\mathbf{j}}$ are the corresponding orientations of the spins at those locations and J is their interaction strength. For $q = 2$ the Ising model is recovered.

The configuration space is usually explored with Metropolis dynamics. The energy $\Delta H = H_{\text{final}} - H_{\text{intial}}$ associated with a spin reorientation is calculated and the spin change is accepted with the probability

$$P(\Delta H) = \begin{cases} 1 & \text{if } \Delta H < 0, \\ e^{-\Delta H / k_b T} & \text{if } \Delta H \geq 0, \end{cases} \tag{2.3}$$

where T is the temperature of the system. For large values of T almost all configuration changes are accepted and no domains with similar spin orientations form. For T approaching zero the spin system may reach the ground state [93].

In a degenerated version the energy depends only on whether a neighboring spin has a different orientation but not on its value:

$$H_{\text{Grain}} = J \sum_{\langle \mathbf{i},\mathbf{j} \rangle} 1 - \delta(\Theta_{\mathbf{i}}, \Theta_{\mathbf{j}}), \tag{2.4}$$

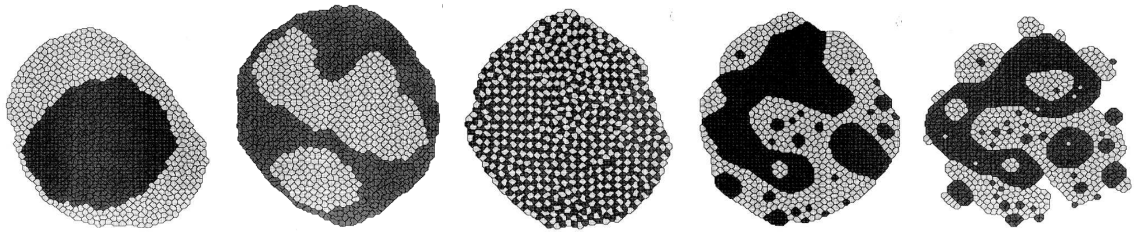

(a) complete **(b)** inverted **(c)** checkerboard **(d)** partial **(e)** dispersal

Figure 2.2. Outcomes of cell sorting for two cell types labeled dark and light. Adapted from [83]. The analogy of cells to molecules of liquids is often used. Cell types with low cell-cell interaction energies $J(\Theta_\mathbf{i}, \Theta_\mathbf{j})$ are viewed analogous to a liquid with a high surface tension. The relative strength of the cell-cell and cell-medium interaction energies sets the degree of cell sorting. (a) Interactions between dark-dark cells have the lowest interaction energy leading to complete engulfment. Cell medium interactions are the same for both types. (b) Engulfment is inverted by increasing the interaction energy between light cells and the medium. (c) If energy between light-dark interfaces is the smallest and cell-medium are equal cells are completely mixed. (d) Similar interaction energies between cells lead to partial sorting. (e) Similar interaction energies between cells and the medium lead to dispersal.

where $\delta(\Theta_\mathbf{i}, \Theta_\mathbf{j}) = 0$ if the spins at $\mathbf{i}$ and $\mathbf{j}$ have different orientations and 1 if they have the same. Systems driven by interfacial tension are well described by this Hamiltonian. Examples range from soap froth to grain growth [97] which closely resemble cells in tissue, a system also driven by interfacial tension [98] (compare Figure 2.1). All of these systems are three dimensional but the small extension of the third dimension is usually neglected. Domains formed in these systems are described by regions of same spin orientation (compare Figure 1.5b) and interface energies by spin-spin interactions.

The simple description of foam and grain growth by a Hamiltonian and their similarity to cells in tissue motivated the development of the CPM [81]. However, besides their similarity in shape, cells differ in a few aspects from soap and grains which requires modifications of the Hamiltonian. E.g. size variations of cells in tissue are small and cells stay cohesive which is achieved by a low enough simulation temperature. The low temperature ensures that domains of equal spin orientation seldom break up into separated domains. In the classical CPM the Hamiltonian is given by [82, 83]

$$H_{\text{cCPM}} = \sum_{\langle \mathbf{i},\mathbf{j} \rangle} [1 - \delta(\Theta_\mathbf{i}, \Theta_\mathbf{j})] J(\Theta_\mathbf{i}, \Theta_\mathbf{j}) + \kappa \sum_{\text{cell } i} [a_i - A_i]^2. \tag{2.5}$$

Each cell is now represented by a domain with the same spin orientation. To implement different cell types, an implementation needs to keep track what spin orientation is associated with a specific type. The interaction energies $J(\Theta_\mathbf{i}, \Theta_\mathbf{j})$ are usually different between different cell types. The last term constrains the cell area a_i of cell i to a target area A_i by a Lagrange multiplier κ and is motivated by a roughly constant cell area observed in tissue. The medium surrounding the cells is treated as a cell without

area constraint. The area of a cell is measured by counting all spins with the same orientation.

The variable interface energy $J(\Theta_\mathbf{i}, \Theta_\mathbf{j})$ drives cell sorting [82, 83] with examples shown in Figure 2.2 for two species represented by dark and light cells. The analogy of cells an molecules in a liquid is often used where the interface energies are viewed as inter-molecular forces. The interface energies $J(\Theta_\mathbf{i}, \Theta_\mathbf{j})$ set the adhesion strength between cells. For all $J(\Theta_\mathbf{i}, \Theta_\mathbf{j})>0$ a low value of $J(\Theta_\mathbf{i}, \Theta_\mathbf{j})$ means strong adhesion. E.g. if the energy between dark-dark cell interfaces is the lowest, those cells can be seen as a liquid with high surface tension and are completely engulfed by the light cells. This requires the cell-medium interaction energy to be the largest and similar for both cell types, otherwise cells disperse or the engulfment is inverted. Depending on the relative strength of the interaction energies the various states of cell sorting shown in Figure 2.2 are obtained.

2.2.1. Metropolis Dynamics in Nonequilibrium Systems

Cells are a nonequilibrium system. They constantly consume ATP, migrate and dissipate energy into their surrounding. Nevertheless, they are described by the Metropolis algorithm which is formulated for equilibrium systems. This works because of a separation of time scales. Forces on the membrane at any point equilibrate within milliseconds [99], a time scale where cell migration and large reorganizations of the actin cytoskeleton (ACS) are not important. Thus, the membrane can always be considered in equilibrium. The energy consuming processes on a long time scale such as cell migration can be viewed as a tilt of the energy landscape driving spin reorientation at one side of a cell.

Another important aspect to justify the use of Metropolis dynamics are membrane fluctuations. The size of fluctuations observed in cells is too large to be of thermal origin. They arise from the activity of actin and myosin beneath the membrane. Cells actively explore their surrounding by forming membrane protrusion. Actin polymerizes in localized areas protruding the membrane which is then contracted by myosin again giving rise to a fluctuation like movement of the membrane. It is generally assumed that the actomyosin activity, which is an nonequilibrium process, is equivalent to an effective temperature [81, 100, 101]. Therefore, the application of Metropolis dynamics is justified. Due to the non-thermal origin of the fluctuations the temperature T used in the Metropolis dynamics (2.3) does not correspond to the actual temperature of the biological cells.

Remodeling of the cytoskeleton is a dissipative process due to the formation and breakage of bonds. Modifications of the Metropolis dynamics accounting for dissipation have been suggested [102] where the probability for a spin flip becomes

$$P(\Delta H) = \begin{cases} 1 & \text{if } \Delta H < -Y, \\ e^{-\frac{\Delta H + Y}{k_b T}} & \text{if } \Delta H \geq Y. \end{cases} \tag{2.6}$$

The parameter Y represents a dissipative cost for deforming the cell boundary and can

be interpreted as a force acting on it [81, p. 110]. Throughout this work the Metropolis algorithm as defined in equation (2.3) will be used. Dissipative effects are unimportant for the model introduced in this chapter because cells are stationary. In Chapter 4 which extend the CPM by cell migration dissipation is assumed to be included in the migratory machinery introduced there.

2.3. Motivating the Hamiltonian on a Single Cell Basis

2.3.1. Cell shape Model

Single cells on flat micropatterned substrates are effectively two-dimensional and often form invaginated circular arcs along free edges [15] as shown in Figure 1.4a. The circular shape can be understood in context of a Laplace law, where a surface tension σ, which draws the contour inwards, is balanced by a line tension λ, which wants to draw the contour straight [59, 60] as illustrated in Figure 2.3a. The surface tension results from the combined action of the plasma membrane wrapping the whole cell body and the actin cortex underlying it [98]. In particular, the actin cortex is contracted by myosin II minifilaments. The line tension reflects the fact that plasma membrane and actin cortex are folded back onto themselves at the cell periphery and thus lead to a geometrically different contribution than in the bulk. Moreover it reflects the fact that actin filament bundles tend to accumulate in these folded parts at the cell edge. The appearance of circular arcs is not restricted to cells on dot pattern, but also occurs on concave parts of the micropatterned island [10, 14], as depicted for the [crossbow] shape in Figure 2.3c. Here the surface tension σ pulls the contour inwards, while the line tension λ pulls the contour outwards. This is different at the convex parts, where both surface tension and line tension pull inwards. This pull is balanced by the adhesion sites along the cell contour. Because the cell periphery is less reinforced by actin bundles along the convex parts, the line tension there is expected to be weaker.

The simplest model for the situation depicted in Figure 2.3c is the simple tension model (STM), which assume both line tension λ_s and surface tension σ to be constant. Then a Laplace law results that predicts circular arcs with a constant radius $R_s = \lambda_s/\sigma$ to occur along free parts of the contour. In experiments a correlation of the arc radius R and the spanning distance d between two adhesive islands was observed which can be understood in terms of the tension elasticity model (TEM) [15]. In this model, the reinforced actin edge fibers forming at the free spanning edges contribute with an elastic line tension $\lambda_e = EA(L - L_0)/L_0$, where the one-dimensional elastic modulus EA for the rigidity of the contour and L and L_0 are the contour length and rest length, respectively (see Figure 2.3c). Pinned parts of the contour are not reinforced and we assume only the simple tension λ_s acting there. For the free arcs one then has the overall line tension $\lambda = \lambda_s + \lambda_e$. Like the STM, the TEM also leads to a Laplace law. Combining this with the elastic line tension and the geometrical relation between arc

radius R and spanning distance d, one finds a self-consistent equation for $R(d)$:

$$R = l_f \left(\frac{2R}{L_0} \arcsin\left(\frac{d}{2R}\right) - 1 \right) + \frac{\lambda_s}{\sigma}, \tag{2.7}$$

where $l_f = EA/\sigma$ is a length scale defined by the relative weight of the one-dimensional elastic modulus and the surface tension. Therefore circular arcs also arise in the TEM, but with a radius R that increases with spanning distance d and with contour reinforcement l_f [15].

Like these contour models, the cellular Potts model (CPM) also centers around the concept of geometrical tension, but allows for much more variable geometries. Our CPM implementation uses a two-dimensional square lattice where the cell is represented by occupied lattice sites, compare Figure 2.3b. The adhesive pattern is realized by marking the corresponding lattice sites as adhesive. Typically a pattern is made from 200 x 200 spins and the cell is represented by 30.000 spins. The length l of the total cell interface is calculated with a modified marching square algorithm. Because cell spreading is a relatively slow process (typical time scale 10 min), one can assume that the system is close to mechanical equilibrium and the Metropolis algorithm can be used to propagate cell shape. During each step a lattice site at the periphery of the cell is selected at random and inverted. Then, an appropriate Hamiltonian H is used to calculate the energy difference $\Delta H = H_{invert} - H_{current}$. The inversion is accepted with the probability defined in equation (2.3). The effective temperature T governs the contour fluctuation amplitude (typical value 0.2 in dimensionless units). Only lattice sites at the periphery of the cells are chosen for update attempts because cells do not form spontaneous holes in the bulk or nucleate new material far away from the bulk. For a cell with n lattice sites in its periphery a Monte Carlo sweep (MCS) defined as n inversion attempts. A more detailed description of the implementation can be found in the Appendix, section A.1.3.

The core of the CPM is defined by the cell Hamiltonian which we choose to be

$$H = \sigma A + \lambda_s l + \sum_{\text{arc } i} \frac{EA}{2L_{0,i}} (L_i - L_{0,i})^2 - \frac{E_0}{A_{\text{ref}} + A_{\text{ad}}} A_{\text{ad}}. \tag{2.8}$$

The first term accounts for the surface tension which scales with the cell area A as conjugated quantity. The second term is the contribution of the simple line tension which scales with the cell perimeter l. The third term is the sum over the contribution from each actin edge fiber and a circle is fit [103] to the corresponding part of the contour to calculate L_i. All of the previously mentioned tensions contract a convex shaped cell and are balanced by the adhesive geometry accounted for by the fourth term. Cells form adhesive contacts with the substrate and the bond energy of each contact lowers the total energy. The number of adhesion molecules in a cell is finite and the energy gain by covering more adhesive area therefore saturates with the covered area A_{ad}. This choice ensures a linear growth during initial spreading which later slows down and plateaus as observed for many different cell types [104, 105]. Strength

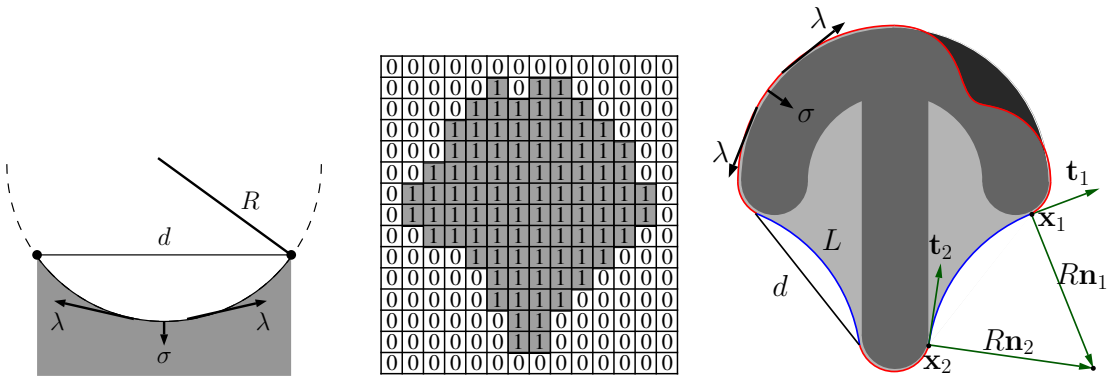

(a) **(b)** **(c)**

Figure 2.3. (a) Contour spanning between pinned points of distance d. The surface tension σ and line tension λ result in circular contour of radius R (b) of a cell in the cellular Potts model (CPM). Occupied lattice sites are indicated by the index 1, empty sites by 0. With a sufficiently large number of spins, the resulting shapes are smooth and can be compared to other models or experiments. (c) Schematic representation of a cell (light gray) not fully spread on a [crossbow]-shaped micropattern (dark gray). Both the line tension λ and the surface tension σ act on the contour. Free spanning arcs form at concave parts of the pattern. They are characterized by the spanning distance d and arc contour length L. In the tension-elasticity model (TEM), the line tension λ of the arcs is augmented by an elastic part. For the arc on the right side, the anchoring points of the contour are indicated by $\mathbf{x}_1$ and $\mathbf{x}_2$ with tangents $\mathbf{t_1}$ and $\mathbf{t_2}$. The normals $\mathbf{n}_1$ and $\mathbf{n}_2$ point to the center of the circular arc with radius R.

and saturation of the adhesive energy are controlled by E_0 and A_{ref}.

Cells in tissue are often described by CPM or vertex models with an energy functional including an elastic (harmonic) constraint on the cell area [73, 82–85, 87]. In contrast to tissue, single cells on a substrate are essentially two-dimensional and can increase their projected surface area by taking material from the third-dimension or by making use of the excess area stored in the plasma membrane or close-by vesicles. We therefore do not use an elastic area constraint in our energy functional. The implications of an elastic area constraint on the spreading dynamics and on the dependence of arc radius on spanning distance are discussed in the Appendix, section A.1.1. There it is also shown that the fourth term in equation (2.8) can alternatively be interpreted as a saturation effect in membrane tension (section A.1.2).

2.3.2. Parameter Estimation

The surface tension has been estimated before as $\sigma \approx 2\,\text{nN}\,\mu\text{m}^{-1}$ from pillar deflections for endothelial cells [61] and as $\sigma \approx 0.7\,\text{nN}\,\mu\text{m}^{-1}$ from analysis of the traction forces of epithelial cell sheets [66]. The simple line tension should be of the order of $\lambda_s \approx 10\,\text{nN}$, which is the typical force acting on focal adhesion connected to the actin cytoskeleton [106]. The rest length L_0 of the elastic arc is assumed to be equal to the spanning

distance d. The ratio $l_f = EA/\sigma$ of elastic rigidity and surface tension describes the degree of arc reinforcement and is taken to be constant for computational simplicity, although in practice it might vary dynamically during cell spreading. It has been estimated for BRL cells on hard substrates with purely elastic arcs and a rest length of $L_0 = 1.01d$ as $l_f = 1300\,\mu\text{m}$ [15]. In our case, this value has to be reduced for several reasons: here we consider soft substrates, we have both simple and elastic tension, and we assume $L_0 = d$. For typical arcs with $R = 15\,\mu\text{m}$ and $d = 12\,\mu\text{m}$, the same arc tension as in the purely elastic case is reached for $l_f \approx 340\mu\text{m}$ ($\sigma = 0.7\,\text{nN}\,\mu\text{m}^{-1}, \lambda_s = 10\,\text{nN}$). For a typical bundle radius of 100 nm, this would correspond to a Young modulus in the MPa-range, as found experimentally [107].

The two remaining parameters E_0 and A_{ref} can be estimated from the adhesive energy density and the average cell size on homogeneous substrates. For weakly spread cells the adhesive energy gain in equation (2.8) becomes $W = E_0/A_{\text{ref}}$ as the number of adhesive contacts is not yet saturated . This adhesive energy density reflects the amount of adhesion receptors available to the cell and has been estimated before as $W = 20\,\text{nN}\,\mu\text{m}^{-1}$ [108]. Epithelial MCF10A cell on 3kP gels reach a spread area of $A_0 \approx 1700\,\mu\text{m}^2$ with an approximately round shape [109]. In order to relate these values to our model, we note that there are no edge bundles on a homogeneous substrate and the spread area A and adhesive area A_{ad} in equation (2.8) are equal. The energy functional equation (2.8) depends then only on A and its minimum determines the final cell size. From this we calculate

$$E_0 = W A_{\text{ref}}, \tag{2.9}$$

$$A_{\text{ref}} = A_0 \frac{\sigma\sqrt{A_0} + \lambda_s\sqrt{\pi} + \sqrt{\sigma W A_0 + \lambda_s W \sqrt{A_0 \pi}}}{(W-\sigma)\sqrt{A_0} - \lambda_s\sqrt{\pi}}. \tag{2.10}$$

From these formula, we obtain typical values for the adhesion parameters as $E_0 = 10^4\text{nN}\,\mu\text{m}$ and $A_{\text{ref}} = 530\ \mu\text{m}^2$ ($\sigma = 0.7\,\text{nN}\,\mu\text{m}^{-1}, \lambda_s = 10\,\text{nN}$). In experiments, these values can be varied for example by using micropatterns with different ligand density or with mixtures of functional and denatured proteins.

2.3.3. Traction Forces

Contractile forces generated in cells are balanced by the adhesive substrate. Both the surface tension σ and the simple line tension λ_s pull normally to the contour, but the latter force depends on the curvature of the contour. For a given part of the contour with length $\mathrm{d}l$ the force is [61]

$$\mathrm{d}\mathbf{F} = -(\sigma + \lambda_s\kappa)\mathbf{n}\,\mathrm{d}l, \tag{2.11}$$

where κ is the curvature and $\mathbf{n}$ the normal vector of unit length pointing outwards of the contour. Free spanning arcs are anchored at their endpoints and exert a force tangential to the contour [61]

$$\mathbf{F}_{arc} = \lambda_e \mathbf{t}, \tag{2.12}$$

where $\mathbf{t}$ is the tangent at the endpoints. Note that the edge bundles only exert a tangential force at their endpoints if their line tension $\lambda_s + \lambda_e$ is different from the value λ_s of the rest of the contour.

By calculating the curvature and normal (as explained in the Appendix, section A.1.3) for each lattice site along the contour for cell shapes predicted with our CPM, equation (2.11) gives the traction force acting on the adhesive part of the pattern beneath the contour. From circles fitted to the free spanning arcs the tangent at the anchoring points, arc length and spanning distance are estimated which are used in equation (2.12) to calculate the force acting on the anchoring points (represented by a single lattice site in the simulations). Together with the force generated by the adhesive part this gives the total traction force resulting from our shape model.

In order to compare to experimental results, several issues have to be taken into account. First our model predicts spatially strongly localized forces, while in practice they are typically distributed over a stripe of focal adhesions along the cell contour [14]. We therefore distribute our simulated forces on a stripe of 2µm width beneath the membrane using a disk shaped kernel. Second our model shows stochastic fluctuations in the cell contour which are expected to be averaged out in experiments. We therefore average it over 5×10^5 Monte Carlo sweeps to account for the fluctuating contour due to the finite simulation temperature. Third traction forces are typically reconstructed in experiments by an inverse procedure that filters out displacement noise. To obtain traction data which is comparable to experimental results, we use the finite element method (FEM) as implemented in the deal.II library to calculate the displacement from our CPM. In our FEM calculations the forces generated by the cell are applied to the surface of a 250µm $\times$ 250µm wide and 100µm deep linear elastic material with a displacement free boundary at the bottom stress free boundaries at the sides. The hexahedral mesh is locally refined beneath the cell. We then apply the Fourier-transform traction cytometry method (FTTC) [53, 54] to obtain a traction pattern which can be compared directly with experimental results. A complete cycle of simulated forces, calculated displacements fields and reconstructed forces can be found in the Appendix, Figure A.4.

Momentum Conservation and Force Magnitude

We now show that for our model the sum of all traction forces vanishes as required by momentum conservation. For a contour $\mathbf{x}(l) = (x(l), y(l))$ parameterized by contour length l, the tangent is normalized and we can use equation (2.11) to write the sum of the traction forces resulting from the part of the contour extending from $\mathbf{x}_1 = \mathbf{x}(l_1)$ to $\mathbf{x}_2 = \mathbf{x}(l_2)$ as

$$\begin{aligned} -\int_{l_1}^{l_2} (\sigma + \lambda_s \kappa)\mathbf{n}\,\mathrm{d}l &= -\int_{l_1}^{l_2} \left(\sigma \frac{\mathrm{d}}{\mathrm{d}l}\begin{pmatrix} y \\ -x \end{pmatrix} - \lambda_s \frac{\mathrm{d}\mathbf{t}}{\mathrm{d}l}\right) \mathrm{d}l \\ &= -\sigma M\Big(\mathbf{x}_2 - \mathbf{x}_1\Big) + \lambda_s(\mathbf{t_2} - \mathbf{t_1}). \end{aligned} \tag{2.13}$$

The minus in the second term comes from the normal pointing outwards. M is the matrix for a 90° counterclockwise rotation and $\mathbf{t_1}$ and $\mathbf{t_2}$ are the tangents at the endpoints of the contour as illustrated in Figure 2.3c. For cells without arcs the start and end points of the integral are the same and thus it vanishes as required by momentum conservation.

For cells with a single arc, we can apply this calculation only to the complementary part of the contour. Moreover we now have to account for the elastic line tension in the arc according to equation (2.12). Because the arc is circular, the contour endpoints and circle normals are related by $\mathbf{x}_2 - \mathbf{x}_1 = -R(\mathbf{n}_2 - \mathbf{n}_1)$. With equation (2.13) and equation (2.12), the total force becomes

$$\int_{l_1}^{l_2} \mathrm{d}\mathbf{F} + \mathbf{F}_{\mathrm{arc}} = \sigma R M(\mathbf{n}_2 - \mathbf{n}_1) + (\lambda_s + \lambda_e)(\mathbf{t_2} - \mathbf{t_1}). \tag{2.14}$$

Rewriting the arc radius in terms of tension, $R = (\lambda_e + \lambda_s)/\sigma$, and rotating the normals with the matrix M shows that the net force vanishes. This also ensures momentum conservation in the STM as this simply corresponds to setting the elastic tension λ_e to zero. For cells with more than one arc, the same result follows by recursion.

We finally comment on the magnitude of the total traction force. For cells on a homogeneous substrate this is simply

$$\int |(\sigma + \lambda_s \kappa)\mathbf{n}| \mathrm{d}l = \sigma l + 2\pi\lambda_s. \tag{2.15}$$

Thus the total traction force scales linearly with cell perimeter l as previously described for cell colonies [66]. Both shape and size of the cell change the perimeter l and therefore influence the total force through the surface tension σ. Larger cells or cells which deviate from a round shape exert a higher total force on the substrate than round cells with the same area, as it was found experimentally for rectangular micropatterns [55].

2.4. Results

2.4.1. Equilibrium Shapes and Cell Spreading

We first discuss the steady state shape of cells on micropatterns. In Figure 2.4 we compare experimental and simulated shapes for HeLa-cells plated on three fibronectin-coated patterns commonly used for cell normalization, namely the [crossbow], [Y] and [H] patterns. The pattern width is equal to 30 µm and the CPM simulation uses a lattice constant of 0.15 µm/pixel. One sees that our model predicts very well the typical sequence of convex and concave parts along the cell contour. Moreover the arc reinforcement modeled by the TEM is clearly visible in all three actin images. Note that here the same parameter set ($\lambda_s = 10\,\mathrm{nN}$, $\sigma = 0.7\,\mathrm{nN\,\mu m^{-1}}$, $l_f = 340\,\mu\mathrm{m}$, $A_0 = 1200\,\mu\mathrm{m}^2$, $E_0 = 7800\,\mathrm{nN\,\mu m}$ and $A_{\mathrm{ref}} = 390\,\mu\mathrm{m}^2$) is used for all three cases

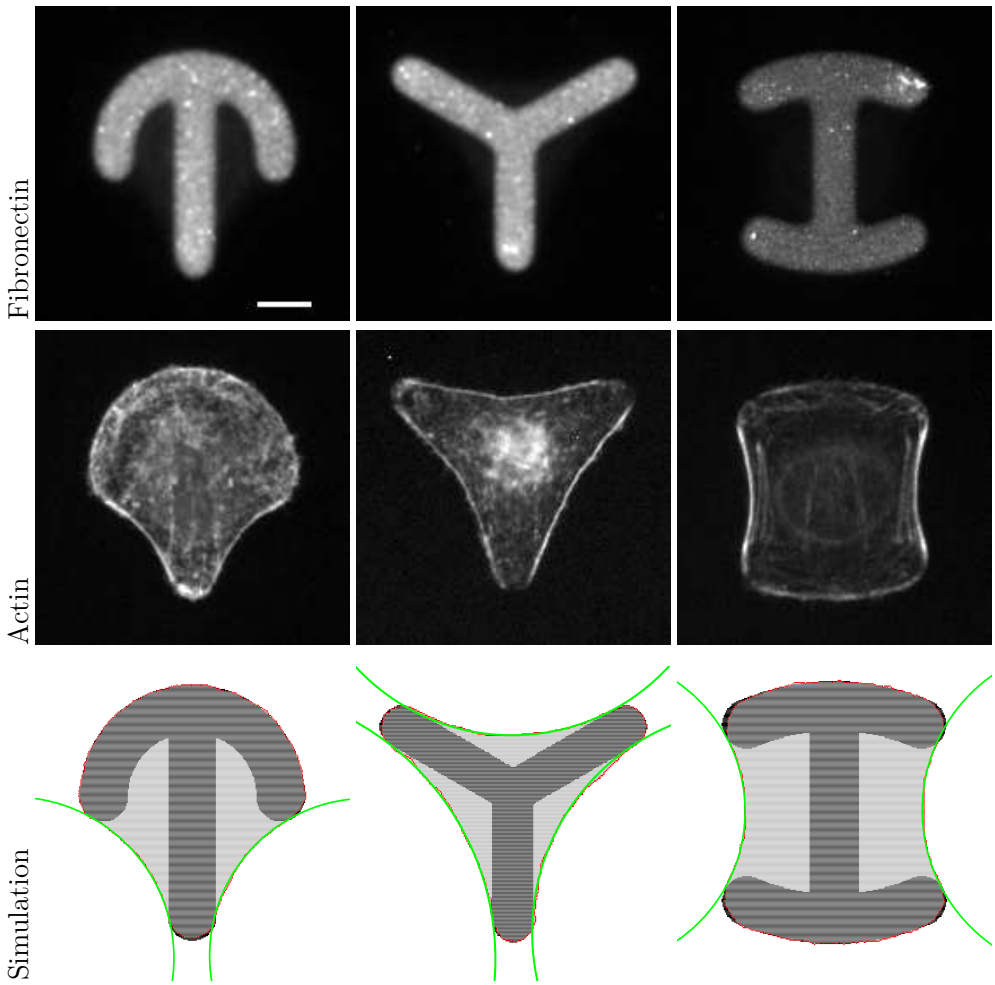

Figure 2.4. The top row shows experimental images for [crossbow], [Y] and [H] patterns coated with fibronectin. Scale bar represents 10 µm. The middle row shows HeLa-cells stained for actin on those patterns. The bottom row hows shape predictions by the CPM with circles fitted to the free spanning arcs. Experimental images kindly provided by Gintarė Garbenčiūtė and Vytaute Starkuviene-Erfle.

because they have been realized on the same chip with the same cell type and the same culture conditions.

The steady state shapes shown in Figure 2.4 results from a dynamical spreading process which cannot be easily described by standard models for cell shape. We now show that the CPM also describes this process very well. In our simulations, we start with a small spreading area of about 10 µm in diameter at an arbitrary location on the pattern and then let the cell spread. Here we choose the [V] shaped pattern which has been studied before experimentally [10]. For the RPE1 cells used in this study, the steady state arcs have an unusual small curvature, indicating that these cells have a weak bulk contractility or very strong arc reinforcement. For both STM and TEM, we first fix the model parameters such that this final steady state shape is

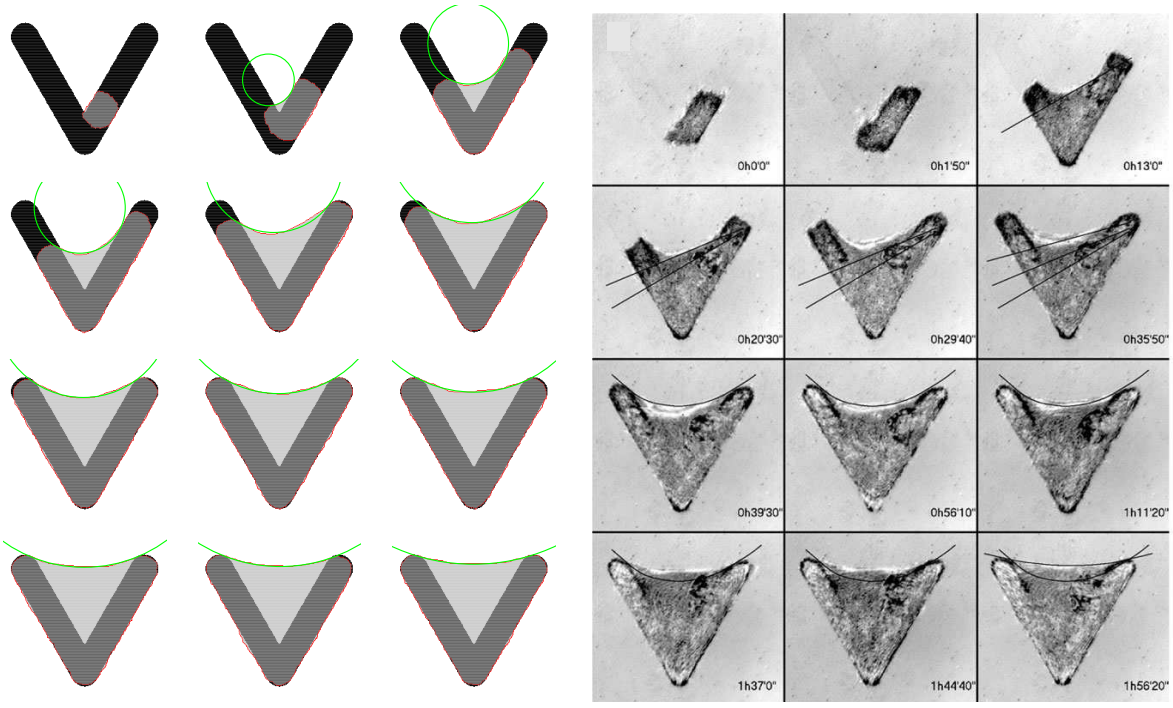

(a) (b)

Figure 2.5. Cell shapes predicted by the CPM with surface tension $\sigma = 0.6\text{nN}\,\mu\text{m}^{-1}$, simple tension $\lambda_s = 10\text{nN}$, arc rigidity $EA = 2000\text{nN}$, adhesive energy density $W = 60\text{nN}\,\mu\text{m}^{-1}$ and cell target area of $A_0 = 1700\mu\text{m}^2$. (a) Cell spreading on [V] shaped pattern. The arms have an length of 46µm and the final spanning distance and radius are $d \approx 33\mu\text{m}$ and $R \approx 61\mu\text{m}$. A circle is fitted to the edge bundle. (b) Phase contrast images of cell spreading on [V] with tangents and circles fitted to the contour. Adapted from [10].

achieved. We use a relatively small surface tension of $\sigma = 0.6\,\text{nN}\,\mu\text{m}^{-1}$. In the STM this surface tension requires a simple line tension of $\lambda_s = 36.6\,\text{nN}$ to reach the final arc radius of 61µm. Then adhesive energies of $W = 60\,\text{nN}\,\mu\text{m}^{-1}$ are required to allow spreading, which is several times larger than previous estimates [108]. For the TEM the simple line tension can be reduced to $\lambda_s = 10\text{nN}$ because the final arc radius is also determined by the elastic contribution to the line tension. The required elastic tension of $EA = 2000\,\text{nN}$ to match the final arc radius is similar to values reported previously for stiff substrates [15]. In this case, an adhesive energy of $W = 10\,\text{nN}\,\mu\text{m}^{-1}$ is sufficient to allow spreading.

With these parameters in place, we now can simulate the spreading dynamics as shown in Figure 2.5a. When the cells bridges the non-adhesive gap of the [V] shaped pattern, an actin edge bundle is formed as indicated by a circle. After a main spreading phase, during which the cell covers the complete adhesive area of the pattern, the free spanning edge continues to move outwards, thereby increasing the spanning distance and the radius of the edge bundle. The same two-step process is seen in experiments

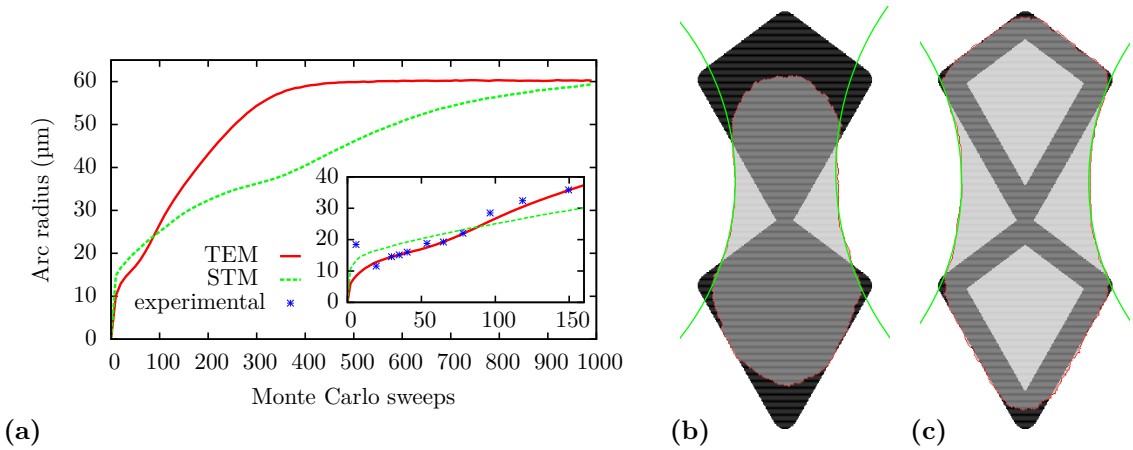

Figure 2.6. Continuation of Figure 2.5 (a) Radius of the circle fitted to the edge as function of Monte Carlo sweeps for cells described by the STM and TEM. The radius is averaged over 10^4 cells all starting to spread at the same position as in the previous figure. Here, each Monte Carlo sweeps consists of 2×10^4 attempts to invert one of the boundary lattice sites. For the simulation of the STM cells a simple line tension of $\lambda_s = 36.6$nN was used resulting in the same final radius as for the TEM cells. The inset shows the initial spread phase and data taken from [10]. (b) Final cell shape on adhesive pattern which cannot be fully covered by the cell. Pattern has a with of 40µm and height of 96µm. (c) same as the previous figure but with a hollow adhesive geometry.

[10] (compare Figure 2.5b). The STM and TEM models differ strongly in the timescale of spreading. Figure 2.6a shows the radius of the circles fitted to the edge bundles averaged over 10^4 cells spreading on a [V] shaped pattern. Cells described by the TEM spread faster than cells described by the STM. The reason lies in the increased simple line tension of the STM needed to reach the same final radius as the TEM. The inset of Figure 2.6a compares the curves for the initial spreading phase with experimental data [10]. TEM-cells cover the whole adhesive area of the pattern after 80 Monte Carlo sweeps while STM take up to 300 Monte Carlo sweeps. During these periods the curves of the two models are qualitatively similar. However, only the TEM-data can be fit well to the experimentally measured data. This implies an important role of arc reinforcement for the spreading process and sets the time scale to 30 min for the 80 MC sweeps. One can understand the TEM as a mechanism which allows the cell to pull its contour outwards above non adhesive parts of the substrate without sacrificing any spreading potential above adhesive parts. Spreading within the STM on the [V] shaped pattern with moderate choices for the simple tension and adhesive energy would only be possible with an reduced surface tension.

In contrast to elastic continuum models, the CPM also finds equilibrium shapes on adhesive islands which are too large to be fully covered by the cell. This is demonstrated in Figure 2.6b. Here, a trade off between the adhesive energy gain which favors a large cell, the line tension which favors a small round cells and circular arcs which

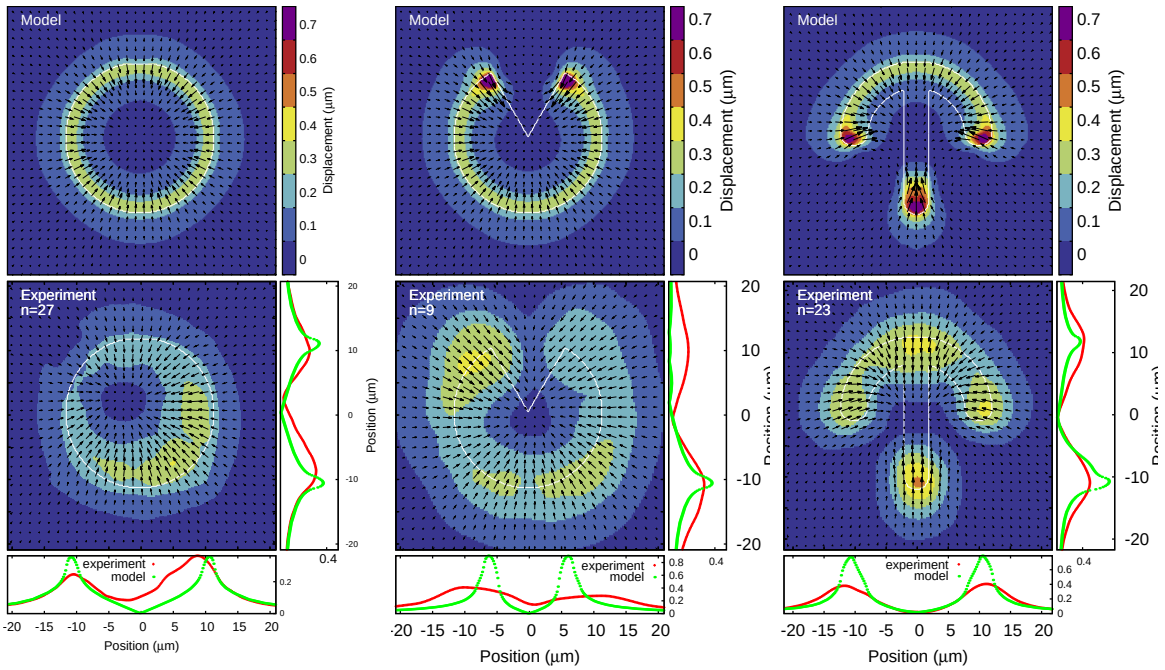

Figure 2.7. Calculated displacements (upper panel) and experimental displacements (lower panel) for MCF10A-cells on fibronectin patterns on a polyacrylamide substrate with a Young modulus of 5kPa [36]. The smaller side panels are vertical and horizontal one dimensional slices of the displacement data. The slices always go through the center of the pattern except for the [pacman] shape where the horizontal slice goes through the tips. The number of averaged cells is indicated by n for each pattern. Experimental data kindly provided by Martial Balland.

should be as flat as possible to minimize the energy has to be found. The result is a cell shape without sharp kinks and arcs ending as parallel as possible to the pattern contour with a large radius. In Figure 2.6c the same adhesive shape as in Figure 2.6b is used but with hollow diamond shapes. Now, the cell is able to cover the whole island because the reduction in adhesive surface leads to a less saturated adhesive energy gain in equation (2.8). In addition arcs form inside the diamonds while the cell is spreading giving the cell an overall concave shape with reduced area as opposed to the partly convex cell on the filled diamond pattern in Figure 2.6b.

2.4.2. Prediction of elastic substrate displacements

Although our final aim is to predict traction force patterns for different micropatterns, we start our discussion of traction patterns with displacement fields, because these are the immediate outcome of experiments. Therefore we use the FEM to calculate from our simulated forces displacement fields for an elastic substrate. We then compare to experimental data and fit our three main model parameters, namely surface tension σ, simple line tension λ_s and elastic line tension EA. In Figure 2.7 we show our

results (upper panel) and compare them to experimental data (lower panel) [36]. The parameters E_0 and A_{ref} responsible for the adhesive energy gain are found to be unimportant for the fit quality. Due to the small number of cells on the [pacman] pattern we exclude it from the fit.

Both the [pacman] and circular [disc] show the localization of displacements at the cell contour as predicted by our model. For the circular [disc], which only has continuously adhesive edges, the displacements are directed radially inward everywhere. This changes for the [pacman] where displacements both in the simulation and the experiment deviate from the radial symmetry at the tips of the wedge. The displacements there point inward because of the actin edge bundle forming across the wedge. Cells described by the STM would have displacements pointing slightly away from the wedge because of the curvature of the cell contour there. The fit of our model parameters is dominated by the larger adhesive parts of the contour for those patterns. The STM and TEM predict similar magnitudes which makes it difficult to distinguish between the two. Displacements for the [crossbow] are dominated more strongly by the two actin edge bundles and are largest at the extremities of the pattern due to the high curvature and bundles originating there. The experimental displacements in both arms of the [crossbow] are directed more upwards than expected from the model. This might indicate the effect of internal actin fibers connecting from the tips to the top of the micropattern. On the other hand, displacements of the circular pattern and circular part of the [crossbow] pattern are very similar in magnitude and direction, indicating that polarized internal fibers only play a minor role in this case.

To quantify the quality of the fit we use the norm $L_2 = \sum(u_{exp,i} - u_{sim,i})^2 / \sum u_{exp,i}^2$, that is the squared and normalized distance between the experimental and simulated displacement fields. For the STM the fit yields a simple line tension of $\lambda_s = 5.53\text{nN}$, surface tension of $\sigma = 0.56\,\text{nN}\,\mu\text{m}^{-1}$ and a L_2-value of 0.16. For the TEM the fit yields $\lambda_s = 2.30\,\text{nN}$, $\sigma = 0.83\,\text{nN}\,\mu\text{m}^{-1}$, $EA = 40\,\text{nN}$ and a L_2-value of 0.15. The TEM fits the data better, but the difference is small, since both the [disc] and [crossbow] are dominated by large convex parts where actin edge bundles are unimportant.

The TEM decreases the simple line tension while increasing the surface tension. As discussed above for spreading on the [V] shaped pattern, the TEM allows the cell to pull its contour outwards above non-adhesive parts of the substrate with a reduced simple tension. The increased surface tension in the TEM compensates for the reduced simple tension, but the contribution of the surface tension is curvature independent. Thus, the TEM allows smaller forces in regions of high curvature while keeping forces in small curvature regions the same as in the STM.

The overall agreement of our model with the experimental displacements demonstrated in Figure 2.7 is quite good. However, the experimental displacements decay slower than the simulated ones. This can have several reasons. First, the 2µm wide stripe beneath the membrane where we apply forces to the substrate might be too narrow and the size of the adhesions might vary with force [106, 110]. The agreement with the experimental data can be improved by increasing the stripe width to 4µm, but this does not appear to be reasonable given the actual size of the adhesions and the feature size of the micropattern. It is therefore more likely that the disagreement

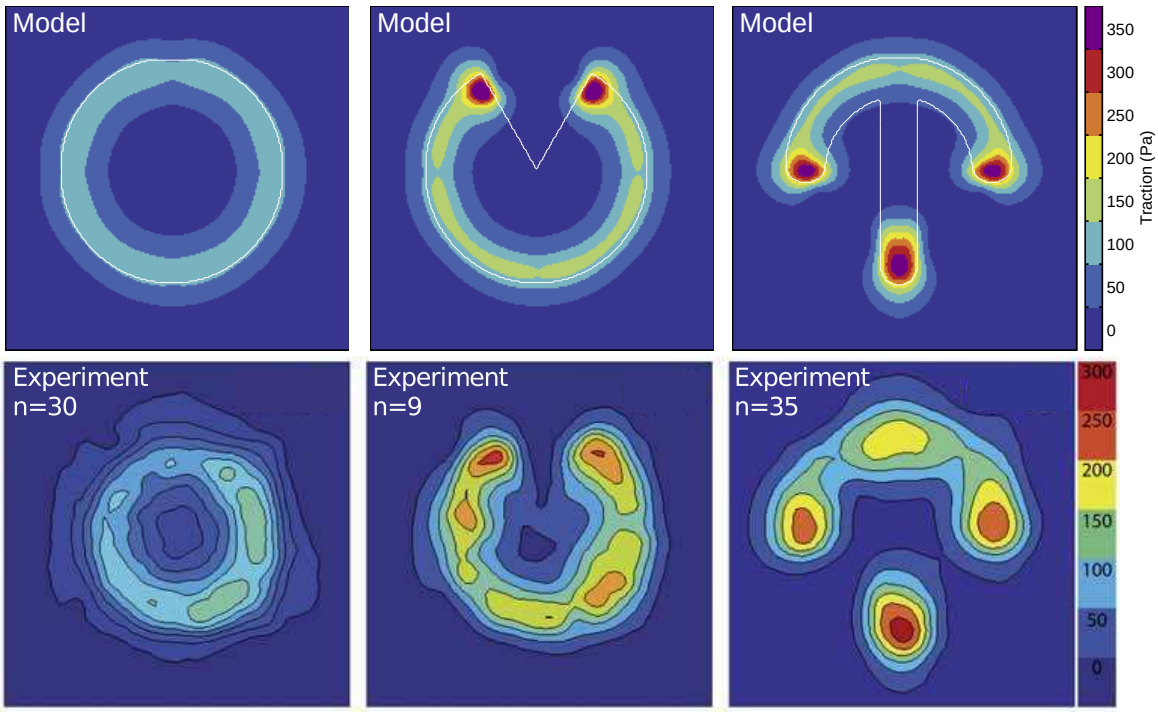

Figure 2.8. The top row shows reconstructed traction forces for the TEM with the best fit parameters ($\lambda_s = 2.30\text{nN}$, $\sigma = 0.83\text{nN}\,\mu\text{m}^{-1}$, $EA = 40\text{nN}$) and the bottom row traction forces reconstructed from experimental data for MCF10A-cells on fibronectin patterns on a polyacrylamide substrate. Experimental data reproduced from [36] with permission of The Royal Society of Chemistry.

arises from the limited resolution of the bead tracking and from the registration and averaging procedures, which both blur the displacement fields. Variations in the pattern shapes from manufacturing or by deformation from the cells also widen the force spots and make pattern registration more difficult. Because these experimental limitations might be improved in the future, for our theoretical predictions here we keep the 2µm scale for the adhesion width.

2.4.3. Prediction of traction forces

Given the displacement data discussed above, one now can reconstruct traction forces which resemble the ones obtained from experimental data. For this purpose, we use FTTC with regularization [53, 54]. In the top row of Figure 2.8 we show the traction force reconstructed from the simulations shown in Figure 2.7. A comparison with the experimental data shown in the bottom row [36] shows that our procedure predicts most of the experimental features. The only exception seems to be the additional localization of experimental traction forces in the upper part of the [crossbow] pattern, which might be due to the occasional presence of internal stress fibers along the long side of this pattern.

The influence of cell shape on force generation is best seen by gradually changing

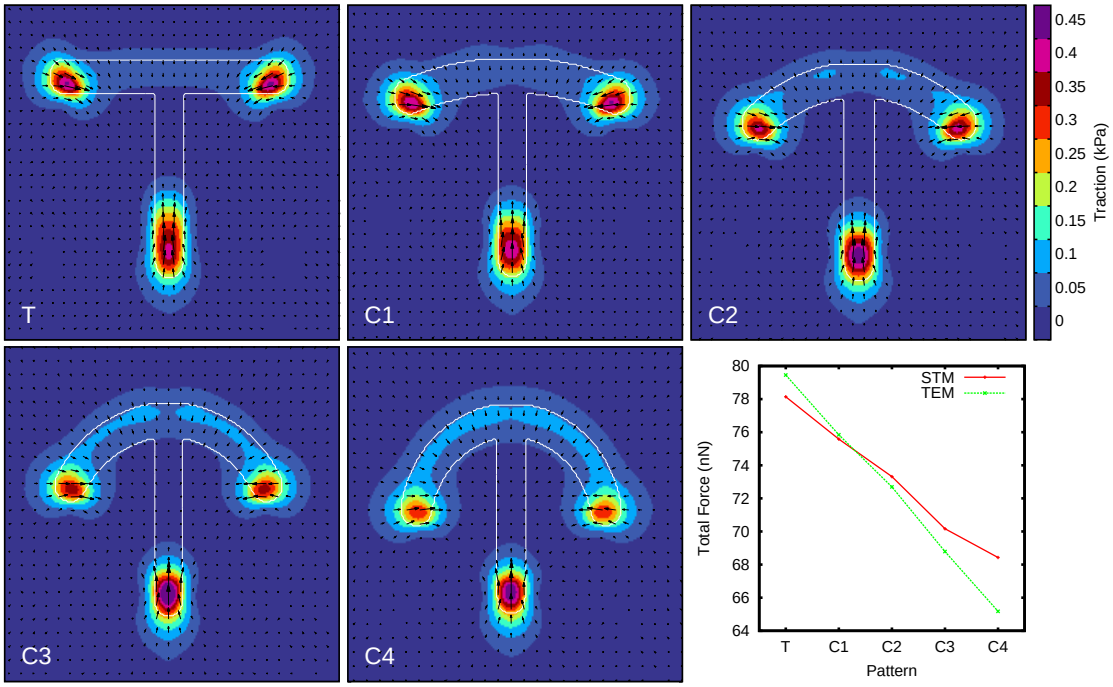

Figure 2.9. Reconstructed traction force for [T]-shaped pattern changing the curvature of the top bar into a [crossbow] shaped pattern. Cells are modeled with the TEM with $\sigma = 0.65\text{nN}\,\mu\text{m}^{-1}, l_f = 184\mu\text{m}, \lambda_s = 2.7\text{nN}$. The final panel shows the total force for the different curvatures both for TEM and STM cells with $\sigma = 0.5\,\text{nN}\,\mu\text{m}^{-1}, \lambda_s = 6.5\,\text{nN}$. The pattern widths are T = 32 µm, C1 = 30.8 µm, C2 = 29.34 µm, C3 = 27.49 µm, C4 = 25 µm and ensure the same cell area on all patterns.

the adhesive geometry. Both curvature and spanning distance of the free arcs are varied in Figure 2.9 as the [T]-shaped pattern is transformed into a [crossbow] for cells described by the TEM. For all shapes the forces are localized to the extremities of the patterns but increasing the curvature relocalizes them from the end points to the adhesive edge of the contour and at the same time the force direction in the prominent force spots changes from being aligned with the edge bundles to a more radial orientation. Both observations, the force increase in the adhesive contour and orientation change, have been observed for RPE1 cells [111]. The increase of forces with higher curvature at the adhesive contour is a consequence of the simple line tension acting in the contour (compare equation (2.11)). The prominent force spots in the extremities are due to the larger curvature and the edge bundles being anchored there. Changing the curvature of the top bar also decreases the spanning distance and therefore the force in the bundles from 7.75 nN in the [T]-shaped pattern to 4.33 nN in the final [crossbow] which explains the decrease of forces in the prominent spots and also the directional change since arc forces become less important. The force spot at the bottom of the T-shaped pattern is less localized compared to the final [crossbow] because the edge bundles do not always attach to the outermost part of this pattern.

The STM yields similar results for the total force but forces are always pointing

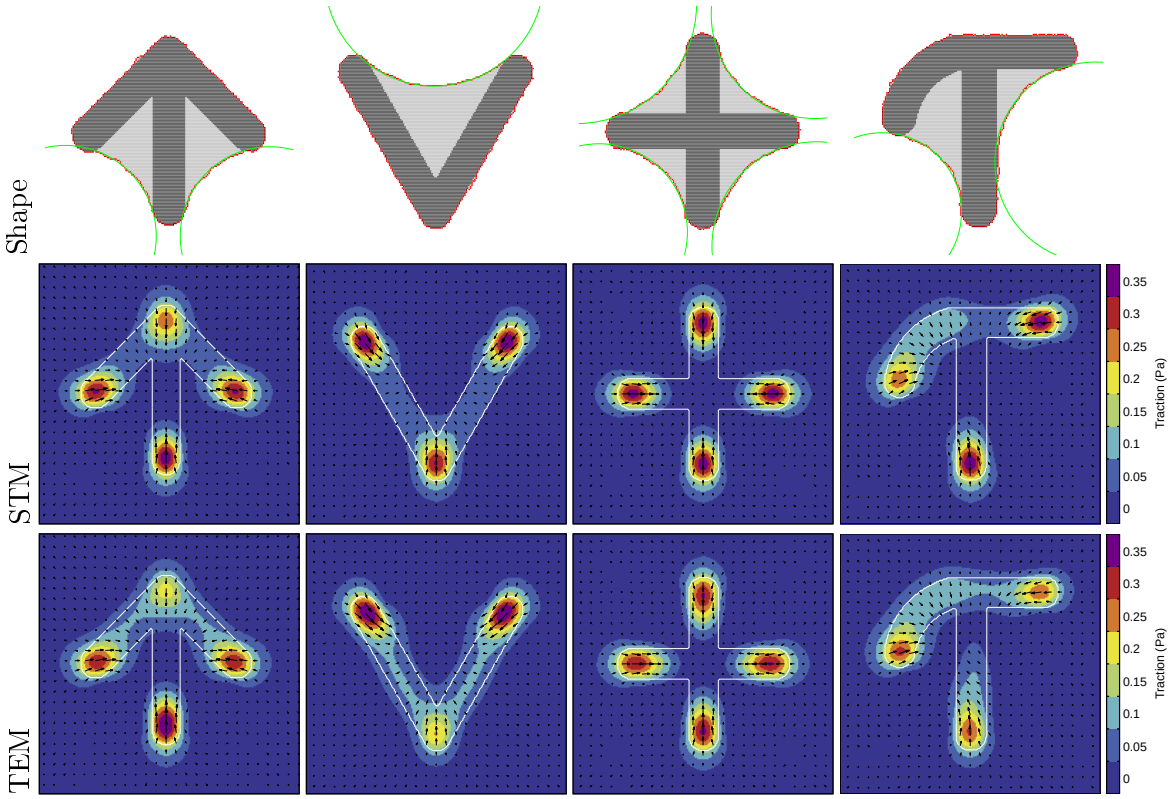

Figure 2.10. Predicted shapes and traction forces for further adhesive geometries, both for STM and TEM. All patterns have a width of 25 µm. The parameters are taken from the best fit to the displacement data from Fig. 2.7. STM with $\sigma = 0.56\,\mathrm{nN\,\mu m^{-1}}$, $EA = 0$, $\lambda_s = 5.53\,\mathrm{nN}$. TEM with $\sigma = 0.83\,\mathrm{nN\,\mu m^{-1}}$, $EA = 40\,\mathrm{nN}$, $\lambda_s = 2.3\,\mathrm{nN}$.

radially inward. The decrease of the total force in the STM is a consequence of the more round shape of the cells on the [crossbow] pattern as stated by equation (2.15) (the pattern dimensions are chosen to ensure the same cell area on all patterns but their perimeter decreases linear). For cells described by the TEM the total force is also influenced by the decreased bundle tension which is reflected by the steeper slope in the last panel of Figure 2.9 which shows the total force as function of curvature. In Figure 2.10 we show a gallery of additional shape and traction predictions for micropatterns for which no traction force fields have been reported yet in the experimental literature. Because these simulations are computationally very cheap, the CPM-approach is a very helpful exploratory tool to quickly assess the effect of a newly designed micropattern.

2.5. Conclusion

In summary, the CPM is a versatile tool to robustly predict cell shapes and forces on any micropattern of interest. The underlying reason is that it actually models the dynamic process of shape determination. Therefore it also makes predictions on

spreading dynamics and does not require any *a priori* knowledge of the final shape. As shown above, all of our predictions agree quite well with published experimental data.

In order to adapt the CPM for the prediction of shapes and forces of single cells on two-dimensional micropatterns, we have made several modifications to the original formulation of the CPM model for cell shape in tissue. Despite its large success in understanding cell sorting and cell shapes in tissue [81], the CPM has been used before only a few times to describe single cells [85, 86]. To further advance this approach, we have added two essential elements to the conventional CPM-formulation. Motivated by the TEM, we have added an elastic line tension to describe the effect of contour reinforcement of edge bundles. Moreover we have added an adhesion term to the energy functional that does not constrain cell area, but acts like a reservoir for additional area that can be used if sufficient ligand is present. The good agreement of our model with experimental data demonstrated here confirms that our energy functional describes the main features of this system. One of the biggest advantages of our approach is that it is computationally cheap (typical run-time is below seconds), thus making it an ideal exploratory tool to quickly establish typical cell behavior on micropatterns without any a priori knowledge of the final shape.

Our model revealed that the TEM model allows for faster cell spreading within a reasonable parameter range and that elastic arcs act to relieve tension from adhesive parts of the contour while maintaining the same cell shape. The TEM makes spreading above non-adhesive parts easier and at the same time allows the cell to generate traction forces more by bulk than contour tension. Our CPM assumes that spreading is limited mainly by the availability of adhesion receptors, thus leading to saturation in adhesive area. This approach neglects other potential limitations of spreading, most notable the effect of increased membrane tension [112]. As shown in the Appendix, section A.1.2, to first order the energy functional of equation (2.8) does not make a fundamental distinction between these two limitations for spreading. However, appropriately designed micropatterns might in fact be an appealing way to investigate these important questions in the future, both in experiments and in the framework of the CPM.

The combination of the CPM with a contour model allowed us to interpret the energy terms in the CPM energy functional as tensions and provides an easy way to predict traction forces. The contour model also connects our three model parameters, namely simple line tension, elastic line tension and surface tension, to the cell geometry via the relation between spanning distance and arc radius (equation (2.7)). For each cell type of interest, our model parameters can be fitted to the experimentally observed cell shape on a reference pattern and than used to predict cell shape and forces on other patterns. As more information becomes available for the detailed molecular structure of actin cortex and peripheral fibers, our model can be modified to include such information, e.g. by replacing the TEM-term in the energy functional of equation (2.8) by a more detailed expression.

There are two important aspects of cell adhesion to micropatterns that are not addressed in the current study. First our model does not describe the effect of internal

structures like non-peripheral stress fibers. We expect that this is a good approximation as long as several cells are averaged to obtain a generic result that averages out individual inhomogeneities. Otherwise more detailed models are required that also include internal stress fibers [113]. Such extensions might profit from recent advances in our understanding of the internal structure and dynamics of different kinds of stress fibers [29, 114]. Second our model does not explicitly describe the effect of the mechanical feedback between elastic substrate and cell adhesion that allows the cell to sense the rigidity of its environment [18, 32, 115]. In order to include this important aspect into our model, it had to be extended by models for the mechanosensitive organization of the adhesion structure and the actin cytoskeleton [116]. At the current stage, the effect of stiffness is incorporated by fitting the model parameters to experimental reference data and by calculating displacement fields with the correct rigidity values of the substrate.

Here we have focused on spreading dynamics and steady state properties of sessile cells. In this case, the Metropolis approach is expected to work well because the cell is essentially relaxing to local mechanical equilibrium. The next chapters will extend the model to describe cell division, persistent cell movement on single micropatterns or on networks of micropatterns.

3 Multicellular Systems

3.1. Introduction

The CPM was originally developed to explain spatial sorting of two cell species [82, 83] and provides a natural way to implement cell-cell interactions by interface energies associated with domains of different spin orientations. As a multicellular model, it has been hardly used to describe systems consisting of only a few cells [84, 85]. Our approach started with a single cell and we will extend it by cell-cell interactions in this chapter. But before cells can interact, they need to divide. More than a hundred years ago it was already observed that cell shape has an influence on cell division. Cells divide preferentially along their shortest axis [117]. Micropatterns are the perfect tool to study how shape influences the division plane orientation and data is readily available [38–40, 118]. Of special interest for the design of micropattern networks are geometries where the division plane orientation is stable and daughter cells are always in the right spot to move on to the next pattern.

We first address how the orientation of the cell division plane can be predicted from the pattern geometry by the CPM. The second part of this chapter extends our single cell model to multicellular system by introducing cell-cell adhesion.

3.2. Cell Division

Figure 3.1a shows snapshots of a dividing cell. The initially spread out cell starts to contract, becomes completely spherical, divides and the two daughter cells spread out again. The orientation of the division plane is set by the cell shape before division [41]. Since the cell is completely spherical when the actual division takes places it needs to maintain information about its previous shape. This information is assumed to come from retraction fibers left behind by the cell when it contracts, connecting

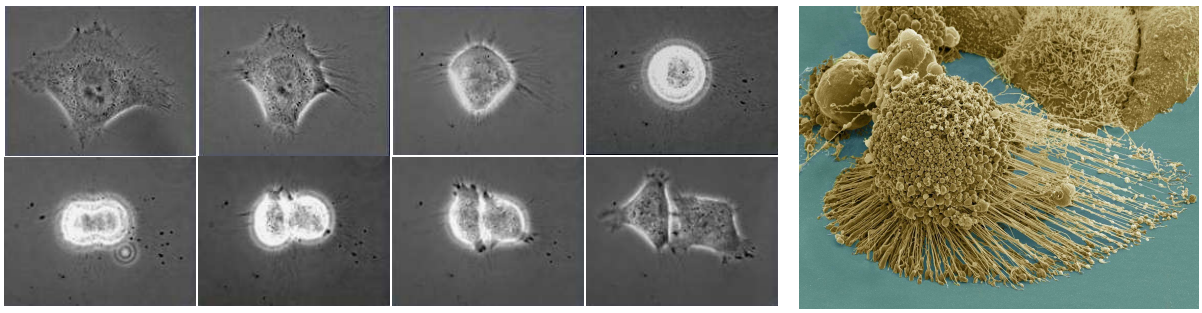

(a) (b)

Figure 3.1. (a) Phase contrast images of a dividing cell. The cell contracts, becomes spherical and divides [119]. (b) Scanning electron micrograph of a HeLa cell [120] . The cell shown is dying but its clearly visible retraction fibers are similar to fibers of a dividing cell.

it to its previously occupied area [14, 38, 39]. Retraction fibers are membrane tubes under tensions [39] filled with actin as shown in Figure 3.1b.

To investigate the mechanisms which sets the division plane micropatterns are perfectly suited. Cells on patterns have defined shapes before division and retraction fibers left behind during contraction can only adhere to the defined patterns [40]. For HeLa cells retraction fibers play an important role as demonstrated by laser cutting of fibers which can trigger an reorientation of the division plane [39]. On the other hand, the division plane of nonadherent cells is also influenced by their shape prior to division although they have no retraction fibers [118]. This raises the question how exactly cues from fibers or the shape set the orientation of the division plane.

During cell division the chromosomes are duplicated and a set of chromosomes needs to be distributed to each daughter cell. This happens via the mitotic spindle. The ellipsoidal shaped spindle is constructed from microtubules (MT) originating from the two spindle poles forming an anti parallel array at the spindle center as shown in Figure 3.2a. The bipolar organization of the MT at the center is used to separate the chromosomes during division. The division axis is perpendicular to the pole-pole axis leaving each daughter cell with a complete set of chromosomes. A second group of MT, the astral MT, is oriented away from the spindle center towards the cell cortex [121]. Those astral MT receive cues through the retraction fibers [38, 40] or the shape [118] resulting in a torque on the spindle inducing rotation into the correct orientation.

On micropatterns, the adhesive geometry is mapped to the cell cortex via the retraction fibers as shown in Figure 3.2b. The interacting of the astral MT with the cortex translate the mapping into a spindle orientation and hence set the orientation of the division plane which depends on the micropattern geometry. Models predicting the division axis on micropatterns usually assume a two dimensional spindle geometry as depicted in Figure 3.2c [38]. MT grow radially outwards from the two spindle poles, intersecting MT form the spindle and all other MT are considered to by astral. Each astral MT is subjected to a force acting with magnitude proportional to the

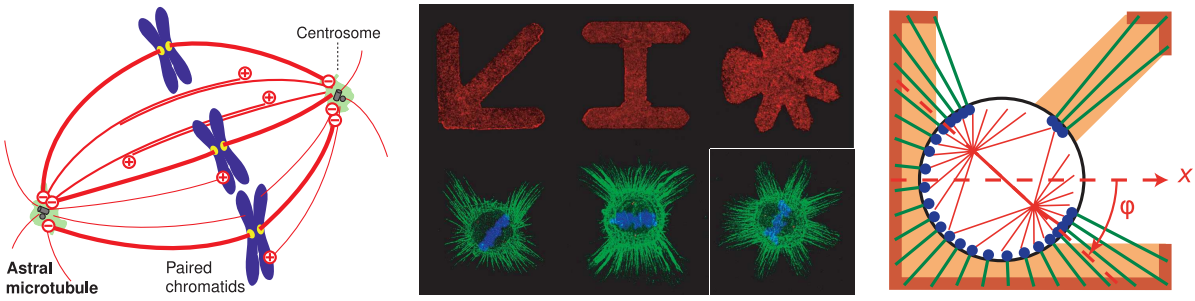

(a) (b) (c)

Figure 3.2. (a) Mitotic spindle with chromosome pairs (blue) microtubules (red) and spindle poles (green). The astral MT grow outwards form the poles and the division plane is perpendicular to the pole-pole axis. Image adapted from [121]. (b) Micropatterns (top row) and retraction fibers (bottom row). The retraction fibers are stained in green and the chromosomes in blue. The division plane will be along the chromosome axis. (c) Model spindle (red) on [arrow] pattern with retraction fibers (green). All MT ending at the cell cortex (black circle) are considered astral MT. The spindle orientation is denoted by φ.

density of retraction fibers at the corresponding cortex position. The actual mapping of the pattern to the cortex happens through the retraction fiber distribution. They emerge radially from the circular cell and end at the pattern boundary as depicted in Figure 3.2c. The density along the pattern boundary is constant giving rise to a higher density of fibers at the cell cortex in regions which are further away from the pattern boundary. The force acting on the astral MT generate a torque on the spindle due to the variable retraction fiber density. The spindle is assumed to perform an overdamped fluctuating random motion in a potential defined by this torque. With the strength of the random torque fluctuations as fit parameter very good agreement with experiments is obtained [38].

A similar model has been used to predict orientations for nonadherent cells in microchambers [118]. Instead of retractions fibers as cues the cell shape before division was used and MT pull on the cortex with a length dependent force.

3.2.1. Division Plane Prediction with the Cellular Potts Model

In a nutshell, the above models predict division plane orientation by mapping the cell shape or adhesive geometry onto a circle. The mapping seems to be more important than the torque generating mechanisms because a random fluctuating torque is added masking the torque generating details. The strength of the fluctuations needs to be adjusted for each pattern layout and varies by a factor of five [38] which makes predictions for arbitrary patterns impossible with this model since the strength of the fluctuations is only known from experiments.

Previous implementations of the CPM have paid little attention to the division

plane, they either selected it randomly [122] or by using the shortest axis [123, 124]. The Dependence of the network topology on the division plane in vertex models has been addressed more systematically [125] and dynamic implementations also choose the plane randomly [73, 87] or by the shortest axis [88].

Our approach puts emphasis of the mapping of the pattern to a circle because there is a natural way to implement it in a CPM. But instead of a circle we take a mapping to an ellipse. Letting the cell contract by increased myosin activity and lowered adhesion turns it into a circle. During this process, the initially patterned shaped cell is transformed continuously, first into an ellipse and then into a circle. Real cells perform a similar transformation as shown in Figure 3.3. During the contraction the spindle poles rotate into position and reach their final orientation when the cell is still elliptical. Likewise, we set the division plane by fitting an ellipse to the contracting cell and taking its its shorter axis as orientation for the division. The time point of ellipse fitting is our only parameter and universal for all patterns. The actual division takes place by splitting the cell into two cells by turning all pixels along the minor axis of the ellipse into boundary pixels.

How does contraction takes place? Before round up stress fibers and focal adhesion disassemble [41] which is mimicked by setting the elastic modulus EA and the adhesive energy density to zero. Increased myosin contractility drives the cell into a spherical shape which cannot be described in our two dimensional model. However, the projection of a sphere can be described. If interpreted as three dimensional model the line tension λ_s takes the role of a surface tension and the surface tension that of a pressure resisting contraction. Thus, we invert the sign of the surface tension to mimic a pressure resisting contraction and adjust the line tension accordingly. The parameter changes for contraction are

$$\sigma \rightarrow \quad \overline{\sigma} = -\sigma \tag{3.1}$$

$$\lambda_s \rightarrow \quad \overline{\lambda}_s = -2\sigma\sqrt{A_{\text{before}}/\pi} \tag{3.2}$$

$$T \rightarrow \quad \overline{T} = T\frac{\overline{\lambda}_s}{\lambda_s} \tag{3.3}$$

$$EA \rightarrow \quad \overline{EA} = 0 \tag{3.4}$$

$$W \rightarrow \quad \overline{W} = 0. \tag{3.5}$$

The choice for the new line tension is explained by the behavior of a circular cell with constant negative surface tension $\overline{\sigma}$ and line tension $\overline{\lambda}_s$. It either contracts to zero or expands to infinity which can be seen when the Hamiltonian is written as function of the area: $H = \overline{\sigma}A + 2\overline{\lambda}_s\sqrt{A\pi}$. This Hamiltonian has a maximum at $\overline{\lambda}_s = -\sigma\sqrt{A/\pi}$. If the area is above the maximum, the cell grows, below the maximum it shrinks. Setting $\overline{\lambda}_s$ to two times this value in equation (3.2) ensures that the cell contracts. The results are insensitive if its two or e.g. four times this value. In equation (3.2) A_{before} is the cell area before contraction starts. The temperature T is rescaled to have similar membrane fluctuations during round up as before.

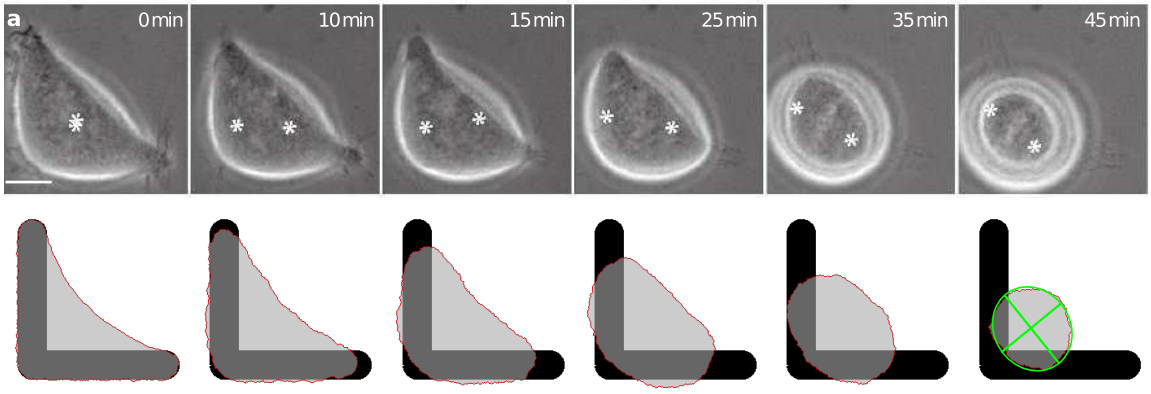

Figure 3.3. The top row shows phase contrast images of a cell on [L] which contracts and spherical for division [40]. The spindle poles are marked by white asterisks and rotate into position during round up. The scale bar represents 10 µm. The bottom row shows the same process for a simulated cell. An ellipse (green) is fitted to the almost round cell to determine the division plane . The spacing of MCS in the simulation matches the real time intervals of the experiment.

The bottom row of Figure 3.3 shows a cell contracting on [L] with parameters changed according to equations (3.1) - (3.5). The ellipse fitted to the cell in the last frame has an aspect ratio close to one and the effect we are using to predict the division plane is small. However, it is sufficient to predict spindle orientations in good agreement with experiments for a wide range of patterns as shown in Figure 3.4. Several key aspects are predicted correctly by our model. Patterns with similar envelopes such as [L dot] and [H] have similar cell shapes before division but differ in the distributions of the spindle axis which is correctly captured by our model. The rotation of the spindle axis by 90° when going from [H] to [H squeezed] is reproduced and the modification of [L] to [L dot] results in a broadening of the distribution. Our model also predicts asymmetric distributions of daughter cells correctly. E.g. on [star] it is most likely that one daughter cell sits on the left areal with the connected arms and the other sits on the right areal. The division does not obey the pattern symmetry (remember that the spindle axis is orthogonal to the division plane). A similar behavior is indicated for [crossbow] while [arrow] and [pacman] have divisions in accordance with their symmetry direction.

Despite the good agreement of our model with most patterns there are a few oddities. The [H] and [2 bar] pattern differ only in the absence of the central bar and the CPM predicts the same distributions for both. The spindle torque model [38] can adjust for the narrower peaks observed on [2 bar] by a smaller amplitude of the random torque fluctuations which would correspond to fitting the ellipse earlier in our approach. However, it is not clear if the central bar changes the spindle orientation or if the observed difference is due to this difference of the patterns. The [H] pattern has a a width of 36 µm while the [2 bar] has just 30 µm [38, Supplement]. For the simulations this makes almost no difference, but the details depend on how good cells

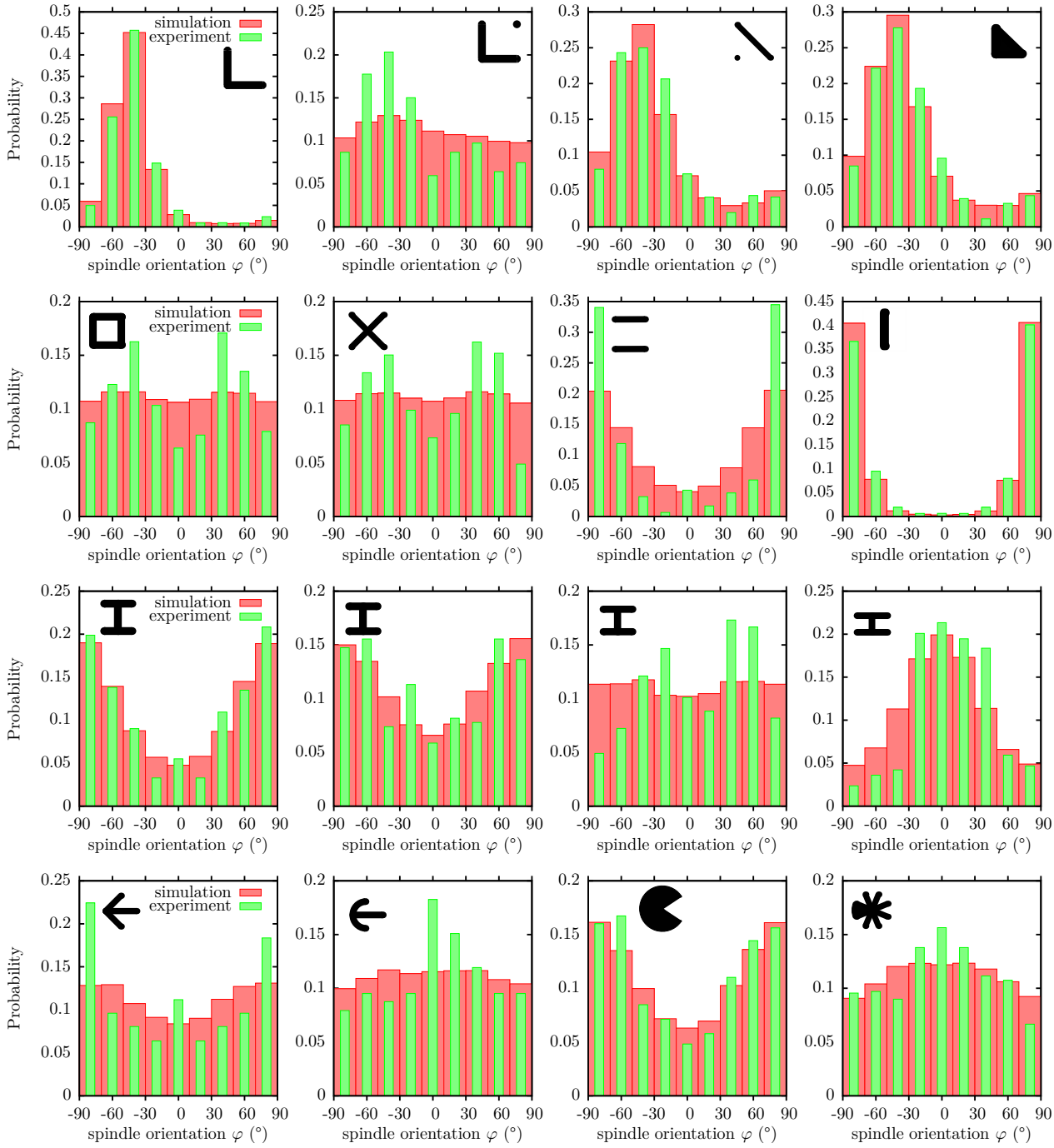

Figure 3.4. Comparison of the experimental (green) taken from [38] and simulated (red) spindle orientations. The spindle orientation is orthogonal to the division plane. All patterns except the bottom and top row have a two fold symmetry. The simulation recorded orientations for 20000 cell divisions and where performed for a generic cell with $\sigma = 1\,\mathrm{nN\,\mu m^{-1}}$, $\lambda_s = 10\,\mathrm{nN}, EA = 50\,\mathrm{nN}$, $A_0 = 1300\,\mathrm{\mu m^2}$, $W = 20\,\mathrm{nN\,\mu m^{-1}}$. The ellipse was fit to the cell at an area ratio of 0.36.

can cover large patterns. For the [arrow] (width 48 µm) and [crossbow] (width 38 µm) size difference is even larger and the observed trend in the simulations to rotate the division axis by 90° is only due to the size difference. The large [arrow] would require cells with an area of more than 2000 µm^2 to be fully covered which seems to large for HeLa cells[1] and retraction fibers do not extend across the full [arrow] (see Box 2 in [126]). The simulations assumes a target area of $A_0 = 1300\,\mu\text{m}^2$ and cells localize to the tip of the large [arrow] which elongates them perpendicular to the symmetry axis giving rise to the observed spindle orientation. [Arrows] with a size matching the cell area have a distribution similar to [crossbow].

For all other patterns the pattern size matches the cell size and simulation and experiment are quite consistent and our predicted distributions can be considered accurate enough to address cell division on networks of micropatterns.

3.2.2. Parameter Dependence

Nothing has been said about when the ellipse is fitted to the contracting cell so far. The cell area A_{before} before contraction and the area A during contraction can be used to define an ratio $r = A/A_{\text{before}}$. The ellipse is fitted at a constant value of the ratio r for all patterns. To determine the best value of r the same norm as in the previous chapter is used

$$L_2 = \sum_{\text{bin } i} \frac{(p_{\text{exp},i} - p_{\text{sim},i})^2}{p_{\text{exp},i}^2} \tag{3.6}$$

to determine the goodness of fit. It is the squared and normalized distance between the experimental $p_{\text{exp},i}$ and simulated $p_{\text{sim},i}$ distributions. Figure 3.5 shows the L_2 norm as function of the ratio r and other parameters averaged over the 16 patterns shown in Figure 3.4. The location of the minimum and its value are indicated by a white square. At ratios r close to one the cells still look very similar to the patterns they are on and the best fitting ellipses have one dominant rotation resulting in narrow peaks for most patterns. Histograms of the distributions with the ellipse fitted at $r = 0.6$ are shown in the Appendix, Figure A.8. The optimal value for the ratio is at $r = 0.36$. Below the optimum almost all information about the previous shape is lost and the cells are almost circular with a uniform spindle orientation.

From Figure 3.5a it can be seen that the line tension has almost no effect on the predicted spindle orientations. For line tension above $\lambda_s = 6\,\text{nN}\,\mu\text{m}^{-1}$ the best fitting ratios r and the minimum L_2 norm are independent of λ_s. For small line tensions below $\lambda_s < 6\,\text{nN}\,\mu\text{m}^{-1}$ the cells nonadhesive edges are strongly invaginated and they cannot stretch out to the isolated dots on [L dot] and [bar dot]. The predicted spindle orientations become those of [L] and [bar] which do not agree with the experiments resulting in a higher L_2 norm. Varying the elastic modulus EA has the same effect. EA also controls how invaginated the free spanning arcs are and the map varying EA looks almost identical to Figure 3.5a. A constant L_2 norm is reached for $EA > 20\,\text{nN}$.

[1] Personal communication with Vytaute Starkuviene-Erfle

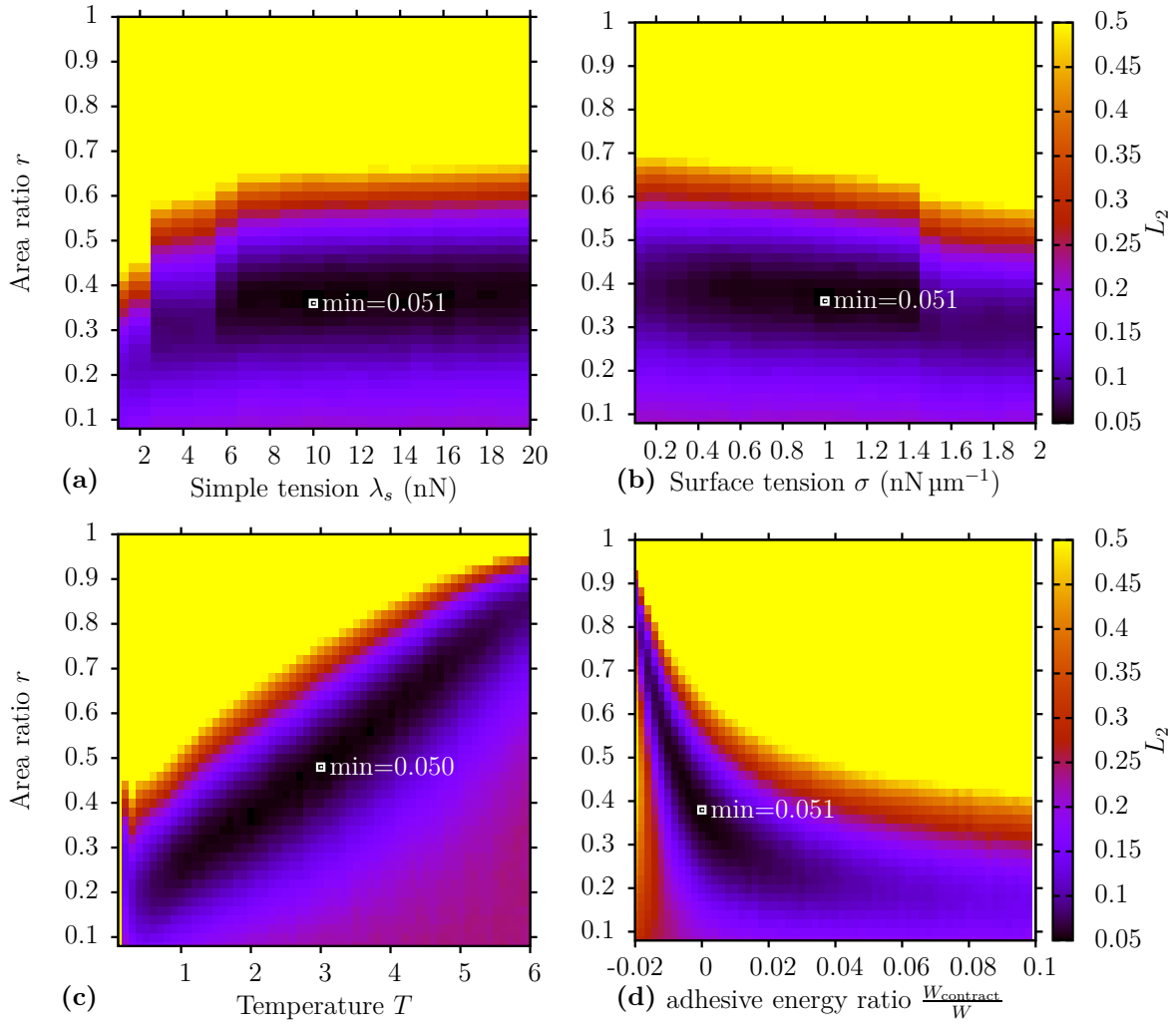

Figure 3.5. Maps of the L_2 norm defined in equation (3.6) estimating the quality of the predicted spindle orientations. The L_2 value is averaged for the 16 patterns of Figure 3.4. If not varied, the used parameters are $\sigma = 1\,\text{nN}\,\mu\text{m}^{-1}$, $\lambda_s = 10\,\text{nN}$, $EA = 50\,\text{nN}$, $A_0 = 1300\,\mu\text{m}^2$, $W = 20\,\text{nN}\,\mu\text{m}^{-1}$, $T = \lambda_s 0.1\,\text{nN}^{-1}$. All maps are capped at 0.5 for better visibility. (a) Map as function of the simple tension λ_s. The simulation temperature is set to $T = \lambda_s 0.1\,\text{nN}^{-1}$ to have the same membrane fluctuations for all values. (b) Map as function of surface tension σ. (c) Map as function of simulation temperature T. (d) Map as function of the fraction of remaining adhesive energy density.

Changing the surface tension also barely effects the distributions. The L_2 norm stays constant at a constant r value. For strongly contractile cells with $\sigma > 1.4\,\text{nN}\,\mu\text{m}^{-1}$ cells are again to invaginated to occupy the dots of [L dot] and [bar dot].

Simple line tension, surface tension and elastic modulus set the cell shape before division. To be more precise, they set the radius of the free spanning arcs. One can therefore conclude, that the shape has no impact on the spindle orientation since the

L_2 norm is independent of the shape controlling parameters over a wide range.

Temperature controls the size of membrane fluctuations and therefore sets the scale how fast information about the pattern geometry is lost during contractions. In accordance, Figure3.5c shows that a higher simulation temperature requires a larger ratio for an optimal fit. The quality of the fit remains the same over a wide temperature range. For very low temperatures the lattice anisotropy prevents a good fit, for high temperatures the pattern is ignored. The temperature during contraction can be seen similar to the strength of the random torque fluctuations in the previously described model [38]. Changing the temperature during contraction can e.g. narrow peaks as shown in Figure A.9 in the Appendix. The predictions for [square] and [X] get better, but for many other patterns the distributions become to narrow giving an overall worse minimal L_2 value.

The importance of retraction fibers for the division plane orientation has been demonstrated by laser cutting. They also exert a force of several nN on the contracting cell [39]. To investigate if this force influences contraction they can by mimicked in our model by leaving an residual amount W_{contract} of the adhesion energy density W behind. If W_{contract} is small enough, contraction is not prevented but slowed down above adhesive areas. Figure 3.5d shows that any remaining adhesion makes the agreement with experiments worse, it also demonstrates that stronger contraction above adhesive areas (negative energy ratio) does not work. This suggests that retraction fibers have no influence on the shape during contraction but does not state anything about how they influence forces on the spindle.

Other approaches to achieve cell contraction or to define a suitable measure when to fit the ellipse are possible. Contraction can be achieved by introducing an elastic area constraint $\lambda(A - A_D)^2$ with A_D being the target area when the cell divides. However, this approach performs rather poorly most likely because of the huge energy downhill gradient at the beginning of contraction due to the mismatch of A and A_D. This breaks the Metropolis dynamics which requires the membrane speed to be less than one lattice site per MCS. The area ratio which decides when the ellipse is fit can be defined with the target area A_0 or with the perimeter of the cell. Both approaches perform poorly.

In summary, our approach can predict spindle orientations in good agreement with experiments. The quality of the predictions does not depend on the used parameters. With the division implemented, we now turn to the interaction between cells.

3.3. Cell Interaction

3.3.1. Line Tension Driven Adhesion

Development of the CPM was driven by the differential adhesion hypothesis [127] which explains cell sorting in tissue. It states that cells of different type adhere to each other with different strength. The tissue being less cohesive should surround the more cohesive one and the analogy of an oil droplet in water is often used for

the two tissues [128]. This might certainly hold on a scale where cells can be seen similar to molecules in a liquid. But what happens in systems composed of only a few cells? Coming back to the oil water analogy a description involving direct interaction seems more appropriate than a surface tension for systems composed of only a few molecules. Nevertheless, the same arguments applied to tissue and liquids are used for interactions between two cells. Namely, that an increase of adhesion molecules in a cell-cell junctions decreases the the surface tension of this junction [98]. But this is not how cell-cell adhesion works. The actin cortex is still contractile at cell-cell junctions, therefore, the surface tension remains essentially the same. Besides, at cell-cell contacts two membranes with a contractile actin cortex beneath each of them come into contact. Hence, one would expect twice the contractility there. Adhesion of cells to each other is mediated through cadherins which form discrete connections between cells [23]. Those transmembrane proteins are interacting with actin, but per se, they do not increase or lower any actin generated tension. One can assume that an energy is associated with breaking and forming them. For a two-dimensional model this energy lead to the idea of implementing it by lowering the line tension between adhering cells resulting in the Hamiltonian

$$H = H_{\text{Area}} + \lambda_s l + \frac{1}{2}\gamma l_j. \tag{3.7}$$

With H_{Area} regulating the cell area, l being the total cell perimeter, l_j the cell-cell interface length, λ_s the line tension in the contour and $\gamma < 0$ the cell-cell interaction energy (calculated e.g from the cadherin density, energy per cadherin bond and height of the cell-cell interface). Only half of the interaction energy is taken because two cells share it. Thus, the line tension in the cell-cell junction becomes $\lambda = \partial H/\partial l_j = \lambda_s + \gamma/2$ because the junction is also part of the total cell perimeter l. This approach is implemented by many CPM either directly by an adhesion energy γ [96, 129] or by assuming different line tension λ_s for different surface types [82–84, 122, 130–132] and is certainly correct on a coarse scale where cells can be treated analogous to fluid molecules. But coming down to systems consisting of a few cells this approach bears some problems. Getting a stronger adhesion between cells, e.g. by having more cadherins would require to lower the line tension at cell junctions which makes them unstable as shown in Figure 3.6a. The limit for the cell-cell adhesion energy is set by the requirement of a positive line tension. For the above Hamiltonian (3.7) this means $-\gamma/\lambda_s < 2$ and knocking down myosin activity responsible for λ_s should either make the junctions as fuzzy as in Figure 3.6a or lower the adhesion strength. Myosin inhibition by blebbistatin reduces the force required to separate cells [129, Figure S2f]. But compared to the almost complete loss of cortex tension [129, Figure 2d] this force reduction is negligible. With barely any cortex tension left after inhibition adhesion between cells cannot be achieved by reducing it even further. This suggest that lowering line tension to drive adhesion is not the correct approach and cadherins mediating the adhesion need to be taken into account explicitly.

Vertex models can use a negative line tension because they have infinite bending

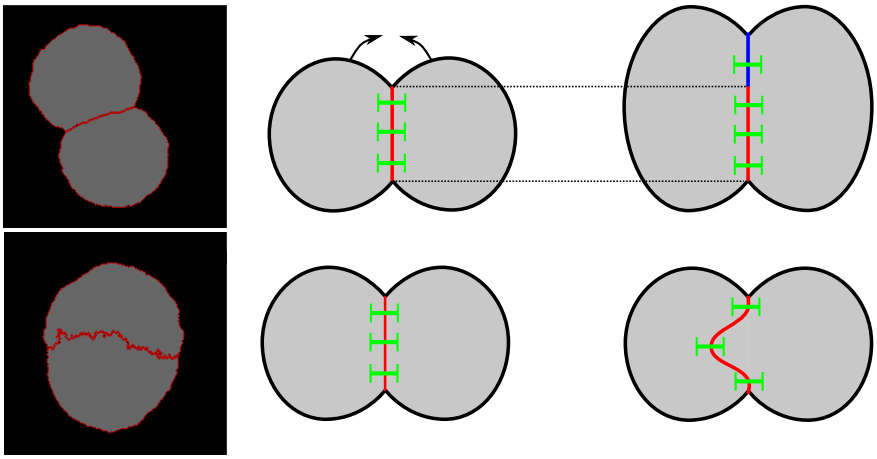

(a) (b)

Figure 3.6. (a)Two cells adhering to each other implemented by an reduced line tension at cell-cell junctions as defined by the Hamiltonian (3.7). At the top for $\gamma = -\lambda_s$ and at the bottom for $\gamma = -1.5\lambda_s$. (b) Cell-cell junctions with cadherin connections (green) between cells. New cadherin connections are only formed when two formerly unconnected membrane areas come in contact (top). The blue part of the cell junction indicates the length l_{cc}. Deformation of existing cell-cell junctions as shown in the bottom picture does not change the number of cadherins and $l_{cc} = 0$.

rigidity except for points where more than two cells meet [73]. But they are not suitable for systems with small cell numbers. To circumvent the limit of positive line tension in the CPM a perimeter constraint of the type $\kappa(l - l_0)^2$ can be introduced resulting in a variable line tension at cell-cell junctions of $\lambda = \partial H/\partial l_j = \lambda_s + \gamma/2 + 2\kappa(l - l_0)$ [84, 96, 129–131]. But this leads to unstable cells if the perimeter l is much smaller than the target perimeter l_0 and is only consistent with experiments if $-\gamma/\lambda_s > 2$ [96, Supplement]. Since the constraint acts globally, changing the perimeter at one side of the cell would instantaneously change the line tension generated by myosin activity throughout the complete cell which makes it difficult to interpret.

3.3.2. Contact Driven Adhesion

An implementation of cell adhesion should leave the line tension at cell junctions similar to the one of cell medium interfaces. Changes in the cell energy should only occur when formerly disconnected parts of cells come in contact or break up as illustrated in Figure 3.6b. So far, this is essentially the same as the previous approaches. The difference is in the deformation of cell-cell junctions which is assumed to happen without the formation of new cadherin bonds and therefore does not change the energy. The corresponding Hamiltonian is

$$H = H_{\text{Area}} + \lambda_s l + \frac{1}{2} e_{cc} n_{cc}, \tag{3.8}$$

where e_{cc} is the energy per cadherin bond and n_{cc} the number of bonds. This is a rather formal way to write down the Hamiltonian since it is not stated yet how to count cadherin bonds. For the Metropolis dynamics only energy differences are of interest. The cell-cell contact part of the energy difference reads

$$\Delta H_{\mathrm{cc}} = c_e l_{cc}, \tag{3.9}$$

where l_{cc} is the length of newly formed or broken membrane contacts during a spin flip as depicted in top of Figure 3.6b and c_e the line energy density for cadherin bonds. l_{cc} is zero for spin flips which just deform the cell junction as in the bottom of Figure 3.6b. The energy e_{cc} and the line energy density c_e are connected through the cadherin density by $c_e = \rho_c e_{cc}$. The total energy of a cell becomes history depend with this approach, but for the dynamics only energy changes are of interest. A related approach would be to treat the cell-cell junction as in a vertex model and taking only the end to end distance of the junction as l_j to set the energy in equation (3.7). But this might lead to large energy barriers e.g. when two previously separated junctions are joined into one.

In general, the line tension at cell-cell junctions and free edges can be different [133]. To have control of the line tension and the adhesion strength simultaneously a combination of the Hamiltonians (3.7) and (3.8) is used. The full Hamiltonian reads

$$H = \sigma A + \lambda_s l + \sum_{\text{arc } i} \frac{EA}{2L_{0,i}}(L_i - L_{0,i})^2 - \frac{E_0}{A_{\mathrm{ref}} + A_{\mathrm{ad}}} A_{\mathrm{ad}} + \frac{1}{2}\gamma l_j + \frac{1}{2} e_{cc} n_{cc}, \tag{3.10}$$

where γ controls the tension along the junction and e_{cc} how strong the cells adhere to each other. For the implementation it is easier to work with newly formed an broken membrane junctions and equation (3.9) is used together with with the cadherin density c_e instead of the energy per cadherin bond e_{cc}.

If a system consists of two cells, each cell is described by the Hamiltonian (3.10) and the line tensions at the cell-cell junction add up. For $-\gamma < \lambda_s$ the tension at the junction is stronger than the cell-medium tension. The value of γ is not known, but from separating adhering cells by force it is known that cells have a reduced cortex tension in the previously adhering areas [133] suggesting $\gamma < 0$. We therefore assume $\gamma = -\lambda_s$ throughout the rest of this work. This choice results in the same line tension at cell-cell and cell-medium interfaces.

The impact variations of γ and e_{cc} have on the shape of cell pairs is shown in Figure A.10 in the Appendix. It demonstrates that our approach indeed can vary line tension in cell-cell junctions and strength of cell-cell adhesion independently.

3.3.3. Shape of Cell Pairs

Figure 3.7a shows two MCF10A cells on an [H] pattern with cadherins stained in green marking the cell-cell junction. Cadherins mainly localize to the ends of the horizontal junction but are also present in lower quantities along it [50]. The localization to the

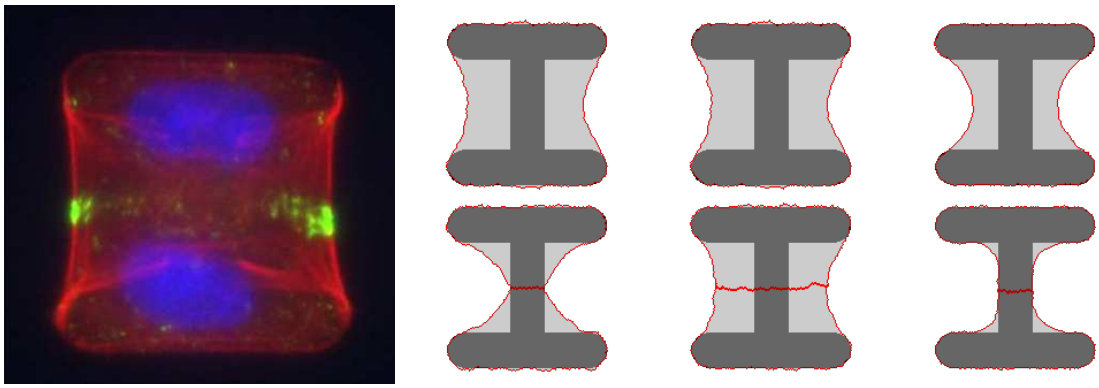

(a) **(b)** $c_e = 0\,\mathrm{nN}$ **(c)** $c_e = -5\,\mathrm{nN}$ **(d)** $c_e = -5\,\mathrm{nN}$

Figure 3.7. Variation of the cell-cell contact mechanisms for cells on [H] pattern. (a) Pair of MCF10A cells on [H], actin is stained in red, the nuclei in blue and e-cadherins in green marking the cell-cell interface [50]. (b) Free spanning arcs on [H] without cell-cell junctions (top) have a similar invagination as the experimental cells. Cell-cell adhesion in the bottom picture is generated by setting $\gamma = -\lambda_s$ which is not sufficient to let cell-cell junction spread above nonadhesive areas. Used parameters: $\sigma = 0.2\,\mathrm{nN\,\mu m^{-1}}$, $\lambda_s = 2.3\,\mathrm{nN}$, $EA = 40\,\mathrm{nN}$. (c) Same as previous figure, but with a cadherin energy line density of $c_e = -5\,\mathrm{nN}$. Junctions can now extend above nonadhesive areas and are similar to experiments. (d) The optimal fit parameters of the previous chapter were used: $\sigma = 0.83\,\mathrm{nN\,\mu m^{-1}}$, $\lambda_s = 2.3\,\mathrm{nN}$, $EA = 40\,\mathrm{nN}$. Which results in strongly invaginated cells.

ends supports our approach to only consider them when junctions break or form but not when they elongate internally.

The free spanning arcs of the single cell shown in the top Figure 3.7b have a similar invagination as observed experimentally for a the cell pair in Figure 3.7a. However, the junction of a simulated cell pair is too contractile to let the cells spread above nonadhesive areas when the cadherin line energy density c_e is set to zero (bottom of Figure 3.7b). Spreading is only possible by reducing the tension in the junction, but to get to the level of the single cell or experiments the tension in the junction would need to be close to zero which dissolved the cell-cell interface. Only with a finite cadherin energy density c_e a shape similar to the experiments can be obtained as shown in Figure 3.7c with $c_e = -5\,\mathrm{nN}$. The shape of the arcs with the junction in between depends on the size of c_e. For low c_e the arcs have a kink at the junction (compare Figure A.10). Increasing c_e flattens the kink until the whole cell medium interface becomes circular. At this point, the cadherin based adhesion mechanism cannot extend the cell any further above the nonadhesive substrate.

The cells shown in Figure 3.7a are the same cell type as in the previous chapter used for the traction force measurements. Using the optimal fit parameters obtained there results in cells which are far more invaginated (see Figure 3.7d) than the experimental cells. The cells are so contractile that even increasing c_e to very high values will not

help to spread the junction above the nonadhesive areas. For the single cell, spreading is possible because of one connected arc spanning the whole gap. For two cells the arc is split into two, each arc adhering to the pattern at one end and at the other end to a cell. This results in spanning distances d which are roughly halved compared to the single cell arc and the arcs have less pulling force to extend the membrane. In principle, transcellular actin cables can be introduced and they allow to spread further above non adhesive areas, but the tension from the junction remains leaving the cell still far more invaginated as observed experimentally. Little is known about transcellular cables and for simplicity we do not use them.

A different set of parameters is needed to obtain agreement between experimentally observed shapes and simulations. E.g. increasing the simple line tension λ_s or the elastic modulus EA would result in less invaginated arcs. The same holds for or a reduction of the surface tension as shown in Figure 3.7c. The required changes can have several reasons: First of all, the two experiments were performed on different substrates. The cells in Figure 3.7a are on glass [50] and the cells used for the traction force experiments on elastic polyacrylamide [36]. Cells on stiffer substrates are assumed to be more contractile [33] but how this increased contractility is distributed among line and surface tension is not known. An increase of both results in the same radius of the free spanning arcs. It is also possible that the combination of two cells alters the contractility. Another aspect to consider is the source of the surface tension. It originates from the actin cortex beneath the membrane and nonperipheral stress fibers spanning across the cell. The nonperipheral stress fibers can have focal adhesions on both ends or they can connect to the cortex with one end [29] but they are usually not attached to peripheral fibers. Instead they run parallel to peripheral fibers [10] and therefore do not contribute in contraction perpendicular to them. This suggests that the surface tension may be anisotropic or lower above nonadhesive areas of the substrate, but so far there is no evidence to support this assumption.

3.3.4. Cell Sheets

Our implementation of the CPM is not restricted to cell pairs. Also large numbers of cells can be simulated as shown in Figure 3.8. A single cell sitting on a comb shape pattern starts to divide and forms a tissue like cell sheet with hexagonal geometry at the bottom of the pattern. As the cells reach the vertical bars they extend further and pull the cell sheet outwards above the nonadhesive areas as observed experimentally [51]. A low surface tension is required to allow the formation and outward pulling of the sheet. The cells at the lower edge of the sheet still have contact to the substrate and want to keep it. Their adhesive energy density is not saturated due to the small contact area and they adhere strongly and resist outward pulling into the nonadhesive region. However, the cells at the top of the vertical bars have more adhesive area left to explore and pull the rest of the cell sheet behind them. As a result, cells above nonadhesive areas of the substrate are considerably larger than cells at the bottom.

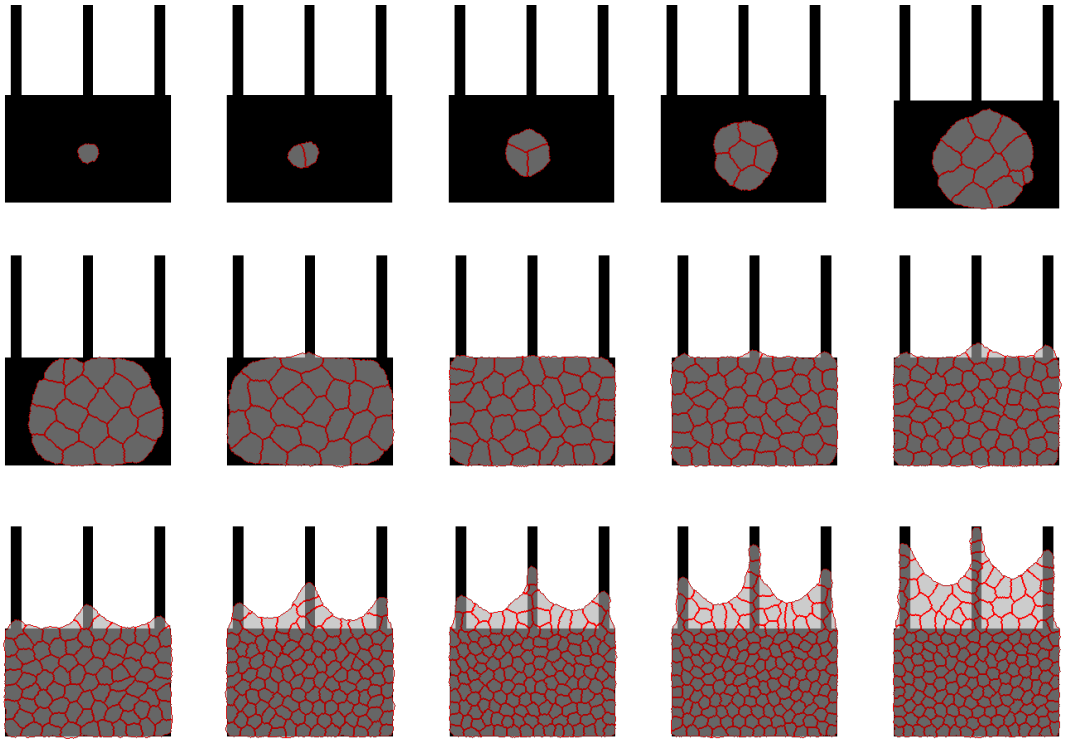

Figure 3.8. Cells growing on a comb shape pattern. The pattern has a width of 400 µm and is represented on a lattice with 200×250 sites. The used parameters are: surface tension $\sigma = 0.01\,\mathrm{nN\,\mu m^{-1}}$, line tension $\lambda_s = 5\,\mathrm{nN}$, elastic tension $EA = 100\,\mathrm{nN}$ and cell-cell adhesion energy line density $c_e = -5\,\mathrm{nN}$. Cell division happens after cells have reached a minimum age with a Poisson distributed probability. If the cell area is below $800\,\mu\mathrm{m}^2$ no division takes place.

3.4. Conclusion

This chapter introduced multicellular systems. The first part established a model for cell division plane orientation which has been investigated in great detail on micropatterns [38–40, 118]. During division cells become spherical which is achieved in our model by detachment from the substrate and an increased line tension contracting the cells. The orientation of the division plane is determined by the minor axis of an ellipse fitted to the cell while it becomes spherical. The time point of the fit is the only parameter and our predictions agree well with experiments. Independence of parameters relevant for the cell shape demonstrate that our approach is universal.

Our model leaves the question about the biological mechanism setting the division plane unanswered. Astral microtubules and their interaction with retraction fibers are thought to be the driving factor [38]. On the other hand, it has been demonstrated that an ellipsoidal shape alone is sufficient to align a spindle by its growing astral microtubules without the help of retraction fibers[134]. Given this, the biological mechanism behind our model could be that astral microtubules grow against the cell

wall and align the spindle by the ellipsoidal shape during round up. The time point during round up when the spindle is assembled sets the degree of memory of the previous shape. If this interpretation is correct, cells with narrow distributions of their division plane should have spindles which assemble early during the round up. Indeed, nonadherent cells in microchambers which barely change shape before division have very narrow distributions of the division plane [118]. Delaying or enhancing the speed of spindle assembly should also alter division plane orientation.

Models have used retraction fibers to map the pattern to a circle [38]. A similar mapping can be used to map the pattern to an ellipse, e.g. by demanding a constant density of fiber attachment points on the contracting cell. Such mapping will predict a single ellipse orientation for each pattern and requires to add noise manually to obtain an actual distribution which is not necessary in our approach.

Another interesting project arises in the combination of traction force and division plane prediction. It is known that cells preferentially divide perpendicular to the plane of sustained tension [41] and it has been shown that the dynamics of traction forces during division can be quite complex [135]. It was also suggested that forces act as a memory for orientation information [135]. The combination of dynamic cell shapes, on the fly traction force predictions and cell division in our model are ideal to study their interplay on micropatterned substrates.

The second part of this chapter introduced cell-cell interactions. Based on the differential adhesion hypothesis [127] classical CPMs use a reduced line tensions at cell-cell junctions opposed to cell-medium interfaces to achieve cell-cell adhesion. Driving cell-cell adhesion through a reduced line tension sets a limit on adhesion strength by the requirement of a positive line tension. Although cadherins, which mediate cell-cell adhesion, alter the tension at junctions [133] we conclude that this is not the driving mechanism for adhesion. Instead, we propose that the energy associated with the formation and breaking of cadherin bonds needs to be added to the Hamiltonian. Our approach allows us to control adhesion strength and junction stability independently.

Early implementations of the CPM circumvented the problem of low line tension and unstable junctions by their low resolution of a cell target area of 40 lattice sites [82] (here: 16000 lattice sites). The lattice anisotropy, area constraint and small resolution limit the size of membrane fluctuations for low interface tensions similar to a bending rigidity. Later models with finer resolution constrained the cell perimeter to achieve a positive line tension [84, 96, 129–131] at interfaces but global constraints are difficult to interpret biologically.

We are confident that our approach still allows cell sorting in the fashion described by the differential adhesion hypothesis. In addition we show that we can predict shapes of cell pairs with junctions above nonadhesive areas which is of special interest in the context of wound healing and has been addressed on comb shaped patterns [51], although not with single cell based models.

At this point, our model contains all constituents of the classical CPM whereupon each term was motivated biologically. The next chapter will add cell migration to complete the model.

4 Cell Migration

4.1. Introduction

So far, mainly cells on isolated islands matching the cell area have been considered. With no adhesive area or neighbouring patterns left to explore, those cells remain stationary which is exactly the purpose of micropatterns [10]. However, in experiments in which cells can divide the micropatterns have to fulfill different requirements. In particular, patterns have to be arranged in such a way that the daughter cells can migrate to neighbouring patterns after division. In turn, this must be described correctly by the model used to optimize the pattern layout.

This chapter first addresses how forces generated by actin polymerization and myosin contraction drive cell migration. Several models with various degrees of detail in the actomyosin description have been proposed and will be discussed. The cellular Potts model (CPM) is among them. Our approach to describe cell motility combines a coarse grained description for actomyosin activity determining the cell shape with a velocity alignment model setting the long term migration behavior. The last part of this chapter focuses on cell migration on micropatterns. Making cells switch between persistent motion and stationary state by means of pattern geometry [50] is of special interest for pattern optimization and is addressed in great detail in the last part. Here, we also show that with our previously developed model excellent agreement with experiments is achieved.

The Migration Machinery

Cell migration is driven by actin polymerization in the lamellipodium, a flat actin rich protrusion at the leading edge of a moving cell. In the lamellipodium actin polymerizes against the cell membrane and drives it forward [20, 27, 28]. In order to work, the polymerizing actin network needs to be anchored to the substrate through focal

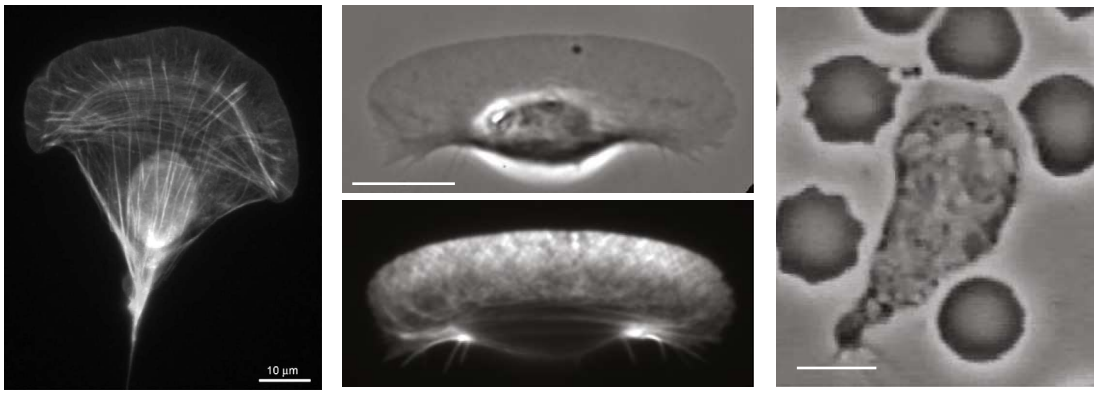

(a) Fibroblast **(b)** Keratocyte **(c)** Neutrophil

Figure 4.1. Various shapes of motile cells with migration directed facing upwards. (a) Fibroblast stained for actin, a broad lamellipodium is visible at the top. (b) Phase contrast image (top) and actin staining (bottom) of Keratocyte. Actin enrichment is visible at the leading edge. (c) Neutrophil surrounded by red blood cells. Scale bars are 10 µm. Images adapted from [136].

adhesions forming in the lamella, a second type of network linked to the lamellipodium [136]. At the rear of the cell myosin contracts the actin network and actin filaments are depolymerized. Anchorage and elongation at the front together with depolymerization at the back lead to a steady state similar to a treadmill when the rates of polymerization, contraction and depolymerization are balanced [34]. In an idealized cell the actin cytoskeleton remains stationary with respect to the substrate and the cell moves by its elongation.

Cell migration can be split into two main aspects. Firstly, the connected action of actin and myosin which lead to force generation resulting in protrusion and retraction of the cell membrane. This aspect is closely coupled to the cell shape which can be quite variable depending on the cell type (compare Figure 4.1). Secondly, cells have to establish and maintain a polarity in order to direct their locomotion. This aspect is relevant for the cell trajectory, e.g. the length and time scale on which a cell moves persistently.

Two mechanism for membrane extension have been proposed [137]. In the graded radial extension model (GRE) the membrane is extended perpendicular to the cell edge with a graded magnitude highest at the midline (see Figure 4.2a). In the parallel extension model (see Figure 4.2b) the membrane is translocated parallel to the movement direction with constant magnitude. By tracking photobleached regions of actin the GRE model was confirmed for keratocytes [137] and the graded magnitude of the extension was supported by a graded actin density along the leading edge [138].

Assuming a gradually decreasing actin density with highest polymerization force at the center of the leading edge and stalling polymerization at the sides, cell aspect ratio, leading edge curvature and speed of keratocyte cells can be related to each other [138]. However, this requires a simplified treatment assuming rectangular cells. Also

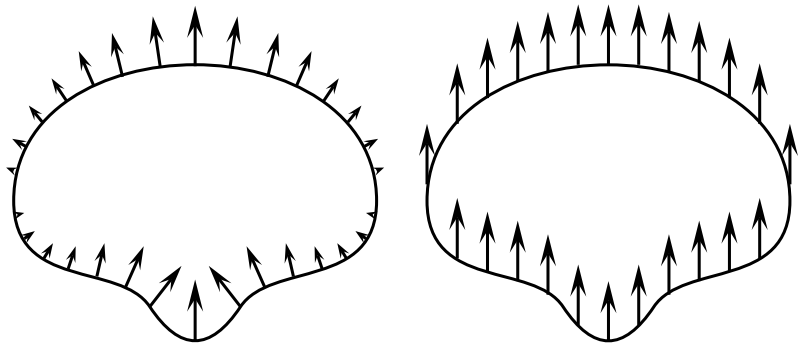

(a) (b)

Figure 4.2. (a) In the graded extension model (GRE) the cell membrane is extended and retracted perpendicular to the cell contour. (b) In the parallel extension model (PE) the membrane is extended parallel to the migration direction. In an alternative view, membrane extensions can be replaced by forces generated by polymerizing actin or myosin contraction.

an active gel theory for actin polymerization and myosin activity which agrees well with measured densities had to use experimental shapes as input [139].

Migration in Models with Dynamic Cell Shapes

At this point the CPM provides an approach to couple the migration machinery and the cell shape. In the CPM framework forces acting on or inside a cell are understood as a bias to the energy change used in the Metropolis algorithm [81, 132, p. 109]. It has been demonstrated that coupling actin dynamics to a CPM Hamiltonian is sufficient to describe a migrating keratocyte [72, 86]. The coupling works by introducing an energy bias in regions with high actin polymerization in favor of membrane extension. Actin dynamic is driven by a reaction diffusion system of the small G-proteins. Namely Cdc42 activating Rac which then activates Rho. Cdc42 and Rho inhibit each other. The mutual inhibition of Cdc42 and Rac can lead to a front back polarity in a cell with actin polymerization being promoted by high Cdc42 concentrations at the front while contraction at the back is promoted by Rac. Cell shape, polarity, speed and reactions to external gradients are correctly predicted by this model. As the reaction diffusion system is solved in the domain predicted by the CPM simulations, the interaction between shape and small G-Protein dynamics can be studied, e.g. how shape changes help cells to react to external stimuli [86]. The long term movement is implicitly included in the reaction diffusion system in such a model. The choice of parameters determines the stability of the Cdc42 and Rho gradient along the cell which sets the cell's polarity direction.

An alternative to having internal reactions setting the polarity direction is velocity alignment. In this model a summation over the past movements sets the current polarity direction. This method usually assumes a global force acting on the whole

cell and, due to its coarser nature, is used for migrating cell sheets [140–142]. Closely related to this approach are phase field models which implement forces acting on a domain boundary in the same way as the CPM [76–78, 80]. In a phase field model a variable $\phi(x, y)$ (the phase field) separates the interior of a cell ($\phi = 1$) from the exterior ($\phi = 0$) with the cell boundary usually at $\phi = 1/2$. The cell shape and mechanics are governed by a free energy $F[\phi]$. To drive the system into two separated phases a double well potential with minimum at $\phi = 0$ and $\phi = 1$ is usually added to the free energy. An equation for the temporal evolution of the phase field can be derived by variation of the free energy. Forces generated by actin and myosin can be added to the free energy, e.g. a force pushing normal to the cell boundary acts in the direction of the gradient $\nabla\phi$ of the phase field [76]. Together with a model for actin and myosin dynamics the predicted cell shapes agree well with keratocytes [76, 78]. Elastic substrates to study mechanotaxis can be introduced [77, 79] and also persistent rotational motion of cells on square patterns has been studied [80].

In most of the above models the polarity direction is either constant or determined by the parameters of a reaction diffusion system. While the correct shape of cells can be predicted in this way, little attention has been paid to the global movement. On short time scales cells move ballistically and transition to a random walk motion on longer scales [143]. To explain this behavior several random walk models have been proposed [144, 145]. While the standard reference is the Ornstein-Uhlenbeck process [146], random walk models with a more complex memory kernel fit data better [146, 147]. One example is velocity alignment model. It calculates the polarity direction from past movements and thus realizes a simple memory kernel. It has been shown to increase persistence on line patterns [148] as reported experimentally [149] and produces persistent rotational movement for cell pairs confined to square patterns [80].

Cell Migration on Micropatterns

Micropatterns can help to understand how environmental cues and cell shape influence directionality in cell migration. It has been demonstrated that fibroblasts preferentially form lamellipodia at corners of micropatterns [43]. Acuter angles at the corners resulted in tighter constrained lamellipodia. This inspired experiments where cells where initially confined to tear-drop shaped patterns and subsequent release of the confinement to study their migration direction [44]. In contrast to the previous study [43] cells displayed larger lamellipodia at the blunt end of the tear-drop patterns and after release of the constrain, they preferentially migrate in this direction although the same cell type was used in both studies. Other cell types move towards the sharp end of tear-drops [47] and arrangement of several tear-drop patterns in a circular geometry allows to study if cells preferentially make transitions from sharp to blunt end. Furthermore, it has been studied how sideward extension of the lamellipodium affects this transition [47]. Linear arrangement of triangles with [45] and without [46] gaps in between them have been shown to trigger migration into the direction of the pointed end. Here, cells are initially polarized towards the broad end of the triangle similar to

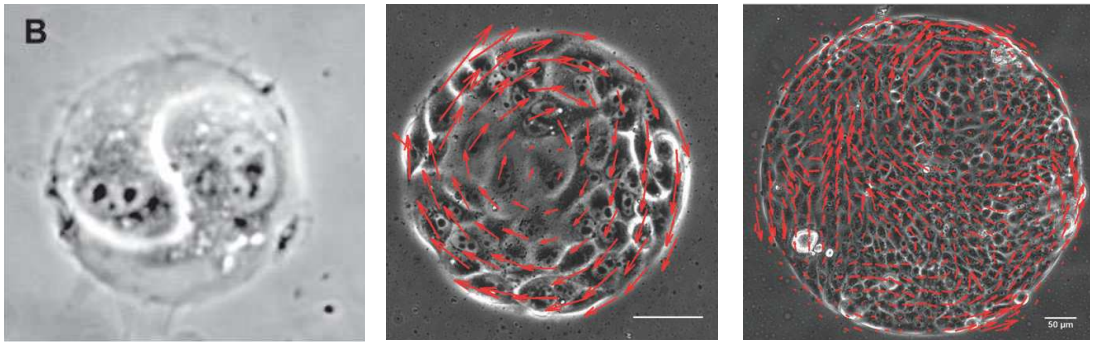

(a) (b) (c)

Figure 4.3. Phase contrast images of migrating cells on micropatterns. (a) Clockwise rotating pair of epithelial cells on [circle] pattern forming a Yin-Yang shape [48]. The bright S-shaped line is the cell-cell junction. (b) The rotational motion persists for larger cell colonies but breaks up (c) into several swirls if the [circle] pattern becomes too large [49].

the case of the tear-drop pattern, but the larger area available when going from the pointed to the broad end on neighbouring triangles dictates the migration direction [45].

Of special interest for the design of micropattern networks is the stability of several cells on a pattern which was first addressed for square and circular shapes [48, 150]. Pairs of endothelial cells undergo a persistent rotational motion with a Yin-Yang shape (see Figure 4.3a) while fibroblast remained stationary on the same pattern. A model predicted that both, coupling and persistence, of the cells must be high enough to enter the Yin-Yang rotation [48]. The persistent rotating Yin-Yang mode requires a continuously adhesive envelope of the pattern, e.g. cells on [C] shaped patterns remain stationary [50]. Rotation is also possible for a larger group of cells on [circles] as shown in Figure 4.3b. If the circle gets too big the motion breaks up into several swirls (Figure 4.3c) [49].

4.2. Graded Force versus Parallel Force Model

In the graded radial extension model (GRE) cells extend and retract their membrane in a graded fashion [137]. As mentioned above, extension and retraction of the membrane is an outcome of actin polymerization and myosin contraction which can be modeled together with reaction diffusion systems [72] giving rise to models with many parameters [86]. We take a simplified approach inspired by the graded radial and parallel extension model. But instead of extensions we assume graded radial forces (GRF) or parallel forces (PF) acting on the membrane as depicted in Figure 4.2. After all, extension are just an outcome of forces applied to the membrane. The graded force distribution is supported by measurements of retrograde actin flow and actin polymerization which are both graded for keratocytes [139].

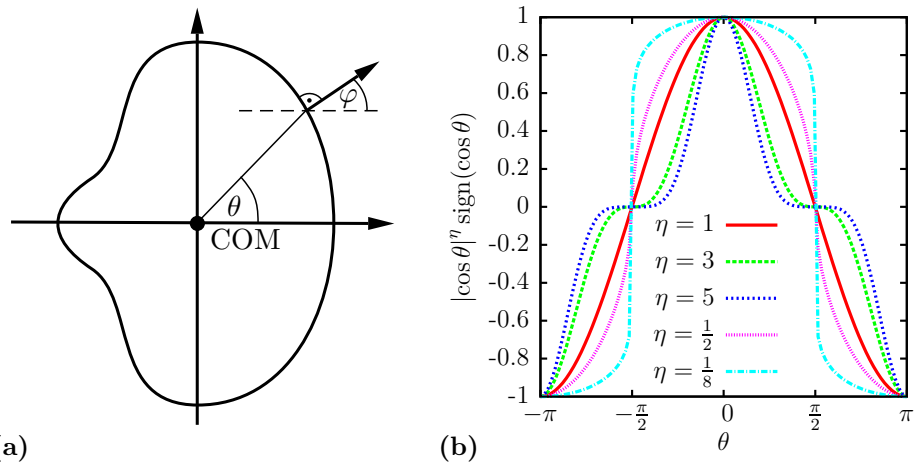

Figure 4.4. (a) Cell with polarity direction along the x-axis and center of mass (COM) in the origin of the coordinate system. The polar angle θ indicates the angle between a point on the cell membrane and the polarity direction. The angle φ sets the angle between the normal of the membrane and polarity direction. If the polarity direction is not along the x-axis its orientation has to be subtracted from θ and φ, respectively. (b) Distributions of the migratory strength (4.1) with different widths controlled by η.

In the GRF model actin pushes normal to the membrane and the force decays with distance from the midline because of a changing actin density. In the PE model actin polymerizes uniformly in one direction with a fixed strength and the resulting force depends on the angle between membrane normal and polymerization direction. At the center of the leading edge the actin polymerization tension (=force per unit length) is denoted by μ . In the simplest version myosin contraction and actin polymerization exert the same force magnitude at the front and back of the cell. The directional tension on the membrane is then $\mu \cos(\alpha)$ which was used before in combination with a CPM [142]. The angle α can either be the polar angle θ in the GRF model or the angle φ between membrane normal and polarization direction in the PF model (compare Figure 4.4a).

The width of the gradation is known to influence cell shape [139] and can be changed by taking powers η of the cosine as shown in Figure 4.4b. Thus, the tension generated by the migration machinery acting on a point of the contour is

$$\sigma_{\text{migration}} = \mu \, |\cos\alpha|^\eta \operatorname{sign}(\cos\alpha), \tag{4.1}$$

which has the dimension of a surface tension. If the cell area is changed by ΔA by a spin flip the cell energy changes by

$$\Delta H_{\text{migration}} = \Delta A \mu \, |\cos\alpha|^\eta \operatorname{sign}(\cos\alpha) \tag{4.2}$$

and the contribution to the total cell energy is

$$H_{\text{migration}} = \mu \iint |\cos\alpha|^{\eta} \operatorname{sign}(\cos\alpha)\, \mathrm{d}A. \tag{4.3}$$

In Figure 4.4a the polarity direction was assumed to be parallel to the x-axis. For a arbitrary direction the angle α needs to be adjusted accordingly.

Care has to be taking setting the strength μ of the migratory machinery in combination with the single spin flip Metropolis dynamics. If chosen too high, all spin flips extending the cell contour in one direction are accepted. The underlying lattice sets the cell shape then resulting in a straight boundary propagating along the lattice directions. Metropolis dynamics is only valid for equilibrium systems and cell migration is not an equilibrium process. Nevertheless, as stated in Chapter 2 Metropolis dynamics can still be used if the membrane equilibrates on a much shorter time scale than the scale relevant for cell migration. This means that the parameters must be chosen to a allow sufficient fluctuations of the cell contour. As described above, a flat contour is a sing of μ being to large. As a rule of thump $\mu < 1.5T$ guarantees sufficient fluctuations. This also means that the COM of a cell propagates by less than one lattice site during a MCS.

4.2.1. The Shape of Motile Cells

Figure 4.5 shows migrating cells simulated with the migration energy (4.3) added to the cell Hamiltonian (2.8). Migration in the Figure takes place on a homogenous substrate and the migratory strength μ and width of the gradation controlled by η are varied. The top panel shows shapes generated with the GRF model which closely resemble shapes of keratocytes for $\eta < 1$ (compare Figure 4.1b) and neutrophils for $\eta > 1$ (compare Figure 4.1c). The PF model shown in the bottom panel predicts shapes which resemble fibroblasts for $\eta < 1$ (compare Figure 4.1a) suggesting that the motility in keratocytes and fibroblasts is driven by radially or uniformly polymerizing actin, respectively. The triangular shapes in the PF model with narrow gradation ($\eta > 1$) lack a biological counterpart.

At first glance it seems unlikely that for $\eta = 1$ the cells are circular. But as stated in the GRE model movement of a circular cell requires membrane extension velocities $v(\theta) \propto \cos(\theta)$ with θ being the polar angle [136, 138, SI, Figure S6]. A circle has constant curvature and the force generated by the line tension is therefore constant along the contour. A constant force is just an offset to the cosine shaped force from the migratory machinery. Since the membrane extension can be assumed proportional to the force and both, surface and line tension, just give a constant offset along the contour the cell can be translocated as a circle.

This changes when the force generated by the migration machinery deviates from a cosine. For a steady state migratory forces and forces generated by line tension must result in a total force which allows translation without shape changes. Thus, the cells must be shaped in a way which allows this force to be generated by the contour curvature giving rise to the various shapes shown in Figure 4.5.

Changes in shape follow changes in the graded force distribution. Making the distribution narrower by increasing η elongates the cell in migration direction while making it wider elongates it perpendicular to it. This effect is enhanced by increasing μ. The simple line tension, which wants to keep the cell circular, becomes less important for larger μ and cells become less circular. As stated before the sides of the lamellipodium are defined by the point where the actin protrusion is stalled [138]. Making the force distribution wider or increasing μ thus shifts this point further outwards making the lamellipodium wider. Changing the surface tension σ has no effect on the shapes since it is balanced by the adhesion energy. Only the line tension λ_s, migratory strength μ and with of the gradation set by η control the cell shape.

In the remaining of this chapter only cells described by the GRF model are considered.

4.3. Velocity Alignment

So far, the polarity direction has been kept fixed, but cells move persistently only over a range of several cell diameters [147, 151], although the movement can become very persistent reaching several hundreds of cell diameters for keratocytes [27, p. 33]. Care has to be taken when talking about persistence length or time. In some cases it is the scale on which directional correlations decay [144, 145, 147, 151], but it can also be the distance it takes to turn by 180° [149] or it is defined by taking the scalar product of initial direction and vector connecting start and endpoint of a cell path [152]. For the latter the persistence length depends on the euclidean distance between start and endpoint but nevertheless allows to quantify the influence of drugs on cell migration. Throughout this work the persistence length is defined as the scale on which directional correlations decay

$$\langle \mathbf{d}(s)\mathbf{d}(0)\rangle = \exp\left(-\frac{s}{l_p}\right), \tag{4.4}$$

where $\mathbf{d}(0)$ and $\mathbf{d}(s)$ are the normalized initial and current direction of a cell trajectory, respectively, with s being the contour length and l_p the persistence length [153, p. 317].

In the velocity alignment model cells tend to align their polarity with their current velocity [154]. It has been used to describe collective cell migration where neighbouring cells can exert forces on each other which leads to a misalignment of polarity and velocity in individual cells but synchronizes the polarity across a cell population [140, 141, 154, 155]. Implementations were performed for circular [154] or point like cells [155] with explicit noise and forces added to the polarity direction or CPM where noise enters implicitly through membrane fluctuations [140, 141]. Velocity alignment can also enhance persistence under stripe shaped confinement [148] as observed experimentally [149] and it can produce persistent Yin-Yang rotational movement on square shaped micropatterns [80].

In the velocity alignment model differences between the velocity and polarity direc-

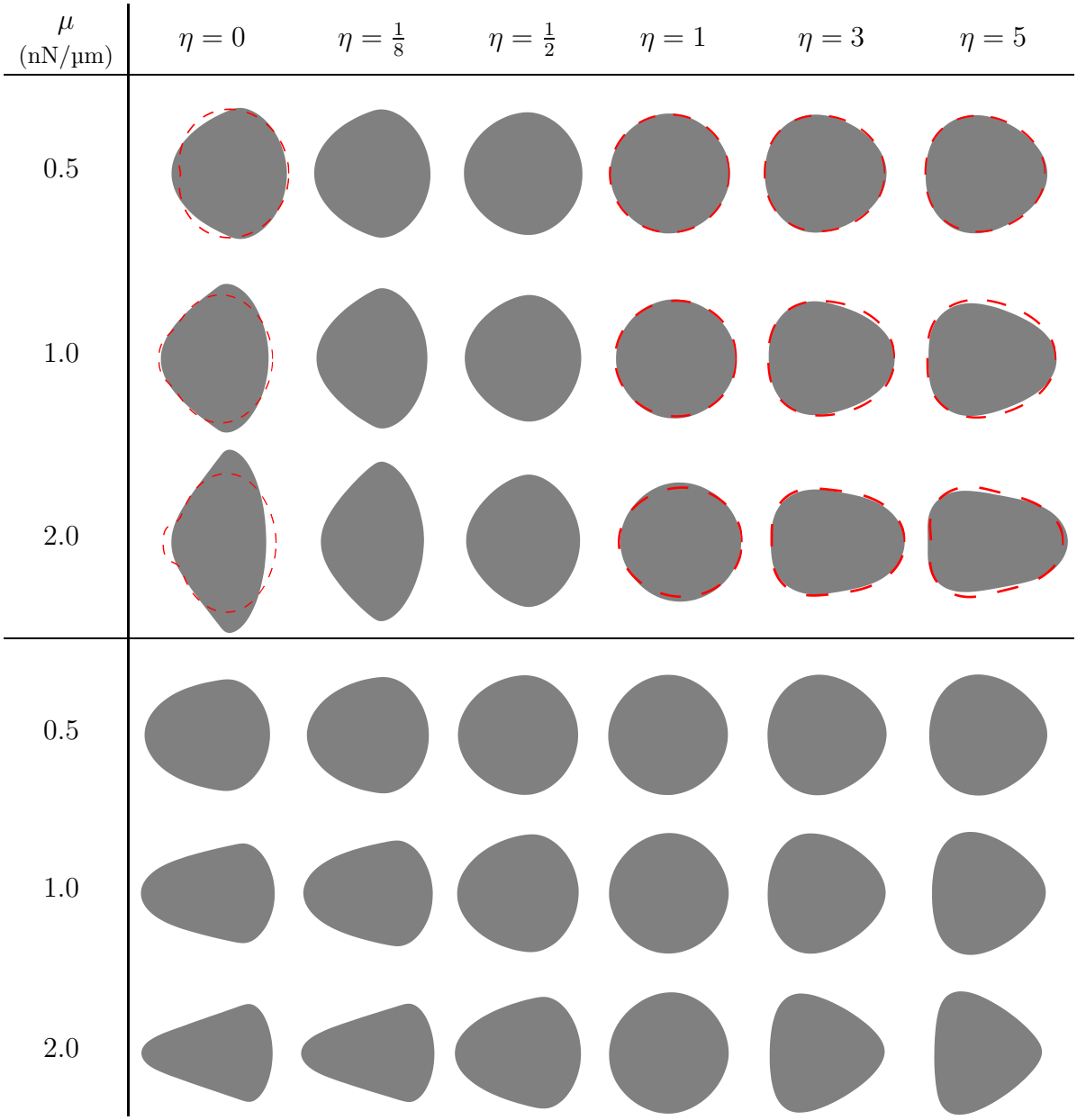

Figure 4.5. Shapes of migrating cells for different exponents η and protrusion tensions μ simulated with the CPM extended by the migratory energy (4.3). The persistence direction is kept fixed along the x-axis and the shapes are averaged over many MCSs. The top panel shows shapes for the GRF model and the bottom panel shapes for the PF model. The simulations are performed with $\sigma = 1\,\mathrm{nN\,\mu m^{-1}}$, $\lambda_s = 10\,\mathrm{nN}$, $W = 20\,\mathrm{nN\,\mu m}$ and $T = 1$. The red dashed shapes are analytical predictions with derivation explained in the appendix, section A.2.4. They are calculated by solving the system of equations (A.32) with constrain (A.33) and $N_{\max} = 5$. For $\eta = 0$ the directional tension in equation (A.32) is replaced by equation (A.28). The regularization parameter is $\alpha = r_0\mu 0.08\,/\mu\mathrm{m}$.

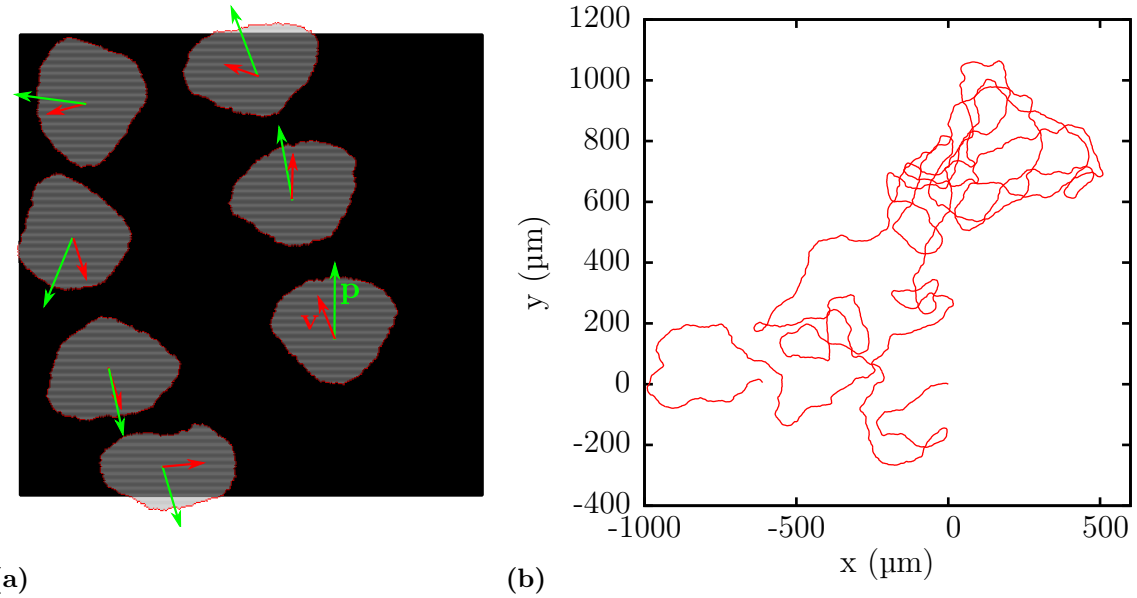

(a) (b)

Figure 4.6. (a) Cell moving on a square shaped micropattern island. The polarity direction (green) and current velocity direction (red) are both indicated by arrows. (b) Trajectory of a cell with $A_0 = 1000\mu m^2$, $\sigma = 1nN\,\mu m^{-1}$, $\lambda_s = 10nN$, $\mu = 1nN\,\mu m^{-1}$, $T = 1, \tau = 50MCS$, $\eta = 3$ resulting in a persistence length $l_p = 130\mu m$.

tion change the polarity direction. In our implementation the change of the polarity direction is defined as

$$\dot{\mathbf{p}} = \mathbf{v} - \frac{\mathbf{p}}{\tau} \tag{4.5}$$

where $\mathbf{v}$ is the current COM velocity and τ sets an alignment strength. The angle between $\mathbf{p}$ and a point on the cell boundary sets the strength of the migratory machinery (4.1) at that point (compare Figure 4.4a). The largest force thus is applied in the direction of $\mathbf{p}$ and the COM displacement during a MCS is assumed to be

$$\mathbf{v} = v_0 \frac{\mathbf{p}}{|\mathbf{p}|} + \xi, \tag{4.6}$$

where v_0 depends, amongst others, on μ, η and the simple line tension λ_s. It can be estimated from the energy changes during displacement in the Aristotelian limit [132]. The noise term ξ is due to the finite simulation temperature which can lead to a COM displacement different from the polarity direction. On planar substrates ξ can be assumed to be white noise since it arises from randomly added and removed membrane sites. For the COM this sums up to white noise because of the central limit theorem. Equation (4.6) is an assumption on how the cell moves during the simulations on a planar substrate and not part of the velocity alignment model.

The whole mechanism is demonstrated in Figure 4.6a where a cell initially moves along its polarity direction with small fluctuations until it reaches the pattern boundary where movement is stalled. The polarity still points outwards and the cell mem-

brane expands across the pattern boundary but the COM barely moves. Eventually fluctuations to one side take over and the cell continues its movement along the boundary. Polarity and velocity align again with the lag controlled by τ. The cell will continue moving along the edge of the island which is also observed experimentally [48] reverting its rotation direction from time to time in one corners of the pattern.

For pattern with discrete boundaries equation 4.6 needs to be modified. A random motion within an energy landscape defined by the pattern can be considered. But the noise ξ is likely to depend on the pattern geometry because cell shape changes at the boundary.

If $\mathbf{v}$ in equation (4.5) is treated as an independent function a formal solution for the differential equation can be written down:

$$\mathbf{p}(t) = \int_0^t \mathbf{v}(t')\, \mathrm{e}^{-\frac{t-t'}{\tau}}\, \mathrm{d}t', \tag{4.7}$$

which allows to interpret the mechanism behind velocity alignment. The cell integrates all its past displacements with an exponential memory kernel to get the current polarity direction. It has been demonstrated before that cells have a memory of their past velocity and the same kernel was used, although for the acceleration of cells [146]. For the implementation a discrete version of (4.7) is used with $\mathbf{p} = \sum \mathbf{v}(i) \exp(-i/\tau)$ where $\mathbf{v}(i)$ denotes the velocity i MCS ago and the sum is truncated when the exponential is small enough. A trajectory of a cell on a planar substrate is shown in Figure 4.6b which can be used to calculate the persistence length defined in equation (4.4). On short times the cell displays directional persistent movement while on long time scales the trajectory looks like a random walk.

4.3.1. Persistent Cell Movement

The directional correlation defined by (4.4) decays exponentially as shown in Figure 4.7a. The persistence length l_p, setting the scale of the decay, depends on both the migratory strength μ and the relaxation time τ. In addition, it also depends on the fluctuations ξ of the COM displacements setting $\mathbf{v}$ in equation (4.6).

The amplitude of the fluctuations ξ depend on the simulation temperature. Membrane fluctuation amplitudes can be calculated in the limit of low temperatures [156–158]. But this limit is well below typical temperatures used here. In addition, cut-off frequencies must be introduced in the calculations which are present in the lattice based simulations naturally, i.e. the smallest fluctuation wavelength is set by the lattice spacing. However, this makes the fluctuation amplitude lattice dependent.

The Langevin equation (4.6) can be solved, but the fluctuation amplitude will appear in the solution which is only known for low temperatures. In addition, the dependence of the parameter v_0 on τ is not known and the solution of the Langevin equation cannot be used to predict persistence lengths.

Nevertheless persistence lengths can be obtained from simulations and their scaling

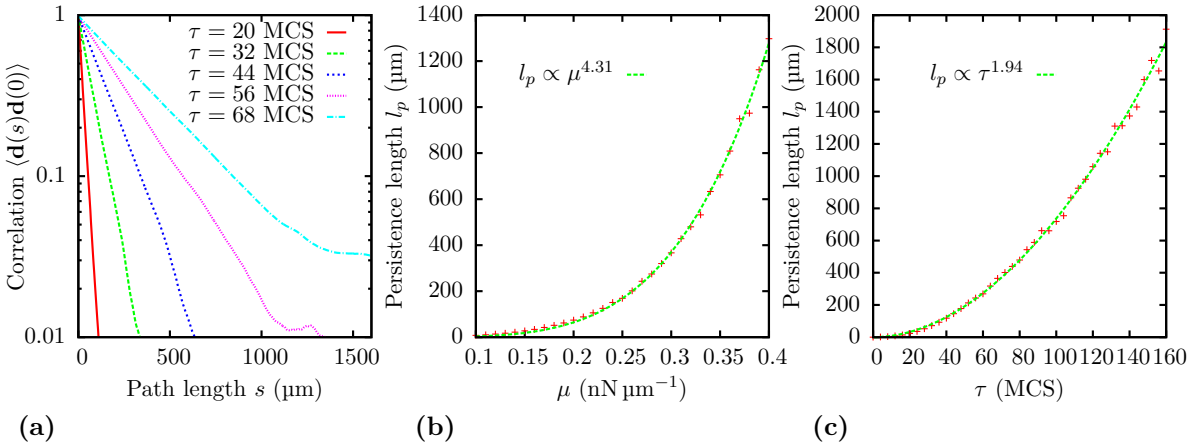

(a) **(b)** **(c)**

Figure 4.7. (a) Decay of the directional correlation as function of the path length s for different values of the relaxation time τ. (b) Scaling of the persistence length l_p defined by equation (4.4) with the migratory strength μ and power law fit. (c) Scaling with the relaxation time τ. Parameters used here are the same as in section 4.5.

dependence on μ and τ are shown in Figure 4.7b and 4.7c, respectively together with a power law fit.

4.4. Migration on Micropatterns

On micropatterns cell migration is influenced by non adhesive areas. If the patterned island are large enough the cell will migrate freely until it reaches the edge, extend an lamellipodia beyond it and will eventually get deflected by the pattern boundary (compare Figure 4.6a). Lamellipodia above nonadhesive areas also appear in cells confined to small islands as shown in Figure 4.8a. They mainly form in regions with low curvature which is in agreement with the idea of a larger resistance by the line tension there. Lamellipodia do not form at free spanning arcs. The actin organization in the arcs is different from the organization at the adhesive edge and arcs are usually above non-adhesive regions where the anchoring support by the substrate for the polymerizing actin is missing. Therefore, we assume that no protrusive activities take place at arcs by setting the energy bias (4.2) to zero for lattice sites belonging to arcs.

4.4.1. Bridging Gaps

Above the adhesive substrate the surface tension is balanced by the adhesive energy which changes when the cell extends over nonadhesive areas. Naively, the cell migratory machinery would push the boundary outwards over the edge while the surface tension driven by myosin contractility resists the expansion. Since the cell wants to generate a protrusion it would make no sense to polymerize against its own contraction. We therefore assume that the surface tension does not resist extension in polarity

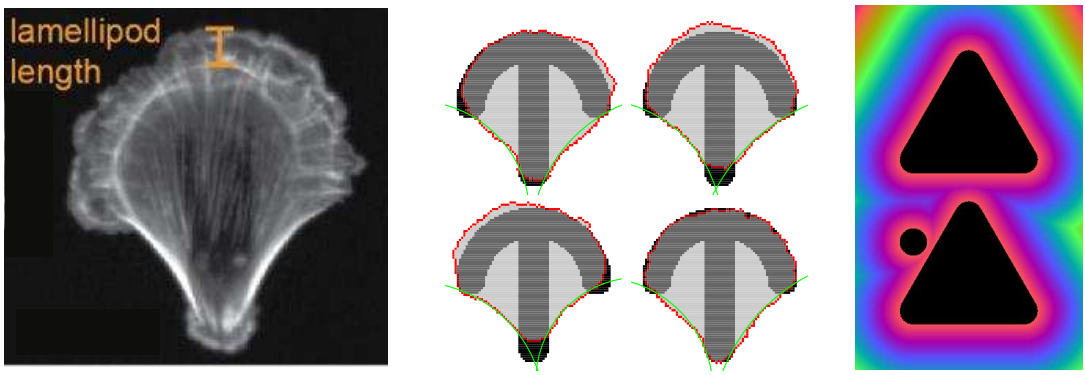

(a) (b) (c)

Figure 4.8. (a) Cell on [crossbow] pattern with large lamellipodium at the top, small at bottom and non at free spanning arcs [152, Supplement]. (b) Simulation snapshots of a cell on a [crossbow]. Due to the confinement no stable polarity direction is established, instead wave like protrusions are observed. A protrusion starts at the top right and travels to the left. Arcs have no protrusions and protrusions at the bottom are small due to the high curvature. (c) Distance map with distance from closest pattern edge encoded by color.

direction above non adhesive areas and modify the migratory energy bias (4.2) to

$$\Delta H_{\text{migration}} = \Delta A \left[\mu \left|\cos\alpha\right|^{\eta} \operatorname{sign}(\cos\alpha) + \sigma\delta_{i,\text{NA}}\Theta(\operatorname{sign}(\cos\alpha))\right], \tag{4.8}$$

where $\delta_{i,\text{NA}}$ is one for nonadhesive lattice sites, zero otherwise and Θ denotes the Heaviside function needed to allow normal contraction at the rear of the cell. Support for this idea comes from the organization of the leading edge. Myosin driven contraction starts in the lamella which is located a few microns behind the leading edge [136]. Therefore, contraction responsible for σ and polymerization are separated spatially. The lamella is also the area where adhesions anchoring the actin network start to form. Above non adhesive areas this support is missing and the polymerizing actin mesh can only reach a certain extension before polymerization just pushes the mesh backwards without extending the boundary. This is put into effect by reducing the protrusion strength μ with distance from adhesive islands

$$\mu_{\text{eff}} = \mu\, \mathrm{e}^{-d/d_0}, \tag{4.9}$$

where d is the distance measured normal to the edge of the nearest adhesive island and d_0 sets the scale of how far the lamellipodium can extend beyond the edge. An image with the distance d encoded by color is shown in Figure 4.8c. An interesting effect arises because d is taken to be the distance to the closest pattern. The protrusion strength decays up to the midpoint between two adhesive island and than rises again. For polymerizing actin there is no mechanism increasing the pushing strength when coming close to another pattern, but the increase can be interpreted as a filopodia like

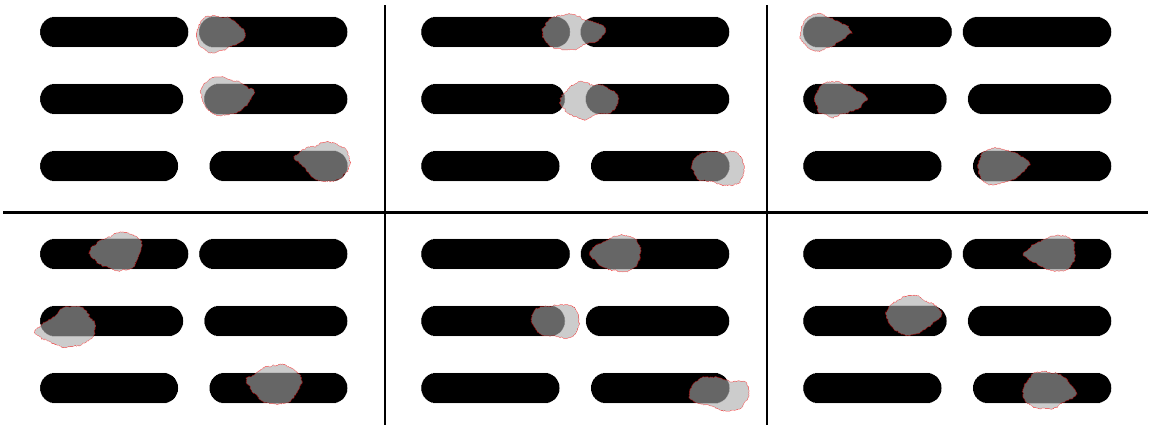

Figure 4.9. Snapshots of identical cells trying to bridge gaps of variable width.

mechanism. Filopodia are spike shaped protrusions with parallel actin bundles inside known to be involved in bridging gaps between patterns [45]. They sense the surrounding and cells are more likely to move to neighbouring island when more adhesive area can be explored by them [45]. With the protrusion strength regulated by equation (4.9) it is more likely to form larger protrusions in the direction with neighbouring patterns mimicking the activity of filopodia. The same mechanism also supports initial attachment to patterns. Since cells are seeded randomly in experiments on the substrate some cells are not in range of a pattern. These cells move in search of a pattern, but without any adhesive surface movement is very limited. Without a pattern in the immediate vicinity they die. Likewise, simulated cells initialized in nonadhesive regions are biased towards patterns by the mechanism described above.

Both, cells migrating on relatively large islands as shown in Figure 4.6a and cells completely occupying an island can now be described. In the latter case no clear polarity directions is established and the cell has protrusions traveling along the contour. At sides with small curvature protrusions are larger (compare Figure 4.8b).

The scaling of the protrusion strength with distance from patterns through the parameter d_0 allows to tune the bridging capabilities of cells as shown in Figure 4.9. Here, all cells are identical but the gap widths between the stripes varies. As the cells move along the stripes only the topmost cell is able to bridge the gap every time, the middle sometimes and the bottom never. Increasing d_0 would also allow the middle cell to bridge more frequently.

4.4.2. Contact Inhibition

Cells have been demonstrated to migrate collectively with and without cell junctions connecting them implying that they communicate to coordinate their movement [159]. Indeed, on contact cells retract their protrusions and change directions [159] which is called contact inhibition. This most likely happens through cadherins which are transmembrane proteins responsible for cell-cell junctions. They influence, through intermediate proteins, the small G-proteins which drive actin protrusion and retraction.

The loss of contact inhibition plays an important role in diseases. Without it, cells can start to invade other tissue [159]. Contact inhibition has also be demonstrated to play a role in persistent rotational Yin-Yang movement on micropattern islands [80]. We implement contact inhibition by setting the migratory energy bias (4.8) to zero if a cell invades another cell. This only happens if the protrusive activity is directed outwards ($\text{sign}[\cos(\alpha)] > 0$), retraction is still possible with bias (4.8) at cell-cell contacts.

4.5. Stability of Cell Pairs

Examples of collective cell migration on micropatterns range from large swirls of a few tens of cells on circular islands [49] down to the Yin-Yang shaped motion of cell pairs on squares and circles [48]. The exact shape of the pattern can either lead to Yin-Yang movement or stabilize the cell pair [50]. This switch is of particular interest in the design of patterns since cell migration should only be allowed after division but otherwise prevented to normalize cells. A two cell system is also the simplest system for coordinate movement and we analyze it in detail by comparing our predictions for the nucleus-nucleus axis orientation to experimental observations [50] for eight different patterns. The experiments were performed on MCF10A cells, which is the same cell type used to measure traction forces in Chapter 2 and the parameters used here should agree with our previous estimates.

The Role of Cell Junctions

Typical snapshots of a cell pair on a [square] are shown in Figure 4.10a. The top frames show the simulation starting with a single cell migrating and dividing on the pattern. The two daughter cells spread out, cover the whole pattern and start to rotate in a Yin-Yang fashion very similar to real cells also shown in the Figure. A lamellipodium extending beyond the pattern forms both in the simulation and experiments (dark parts) at the leading edge and the cells rotate persistently switching directions from time to time (not shown).

Cell pairs do not always rotate on patterns. On on [C],[H] and [hourglass] they are stationary while a slight movement is observed on [X], [X bar] and [C1]. Persistent rotation is only present on [square] and [C2] [50] (pictograms of the patterns are shown in Figure 4.11, [C1] and [C2] are the intermediate patterns between [C] and [square]). This suggests that rotation works best if the convex hull of a pattern is adhesive. In the framework of our model this can be explained by the requirement of an adhesive area to support actin polymerization (equation (4.9) and by the energy associated with the cell-cell junctions. Cell-cell junctions are contractile due to the simple line tension. In a minimal energy state cell pairs are oriented to minimize their junction length as shown in Figure 4.10c. Free spanning arcs have different invagination depending on whether they have junction junctions in between or not. On patterns such as [square] junctions usually extend to the rim of the pattern due to the adhesive tension opposing the contraction. For rotation junctions must be stretched and reach at

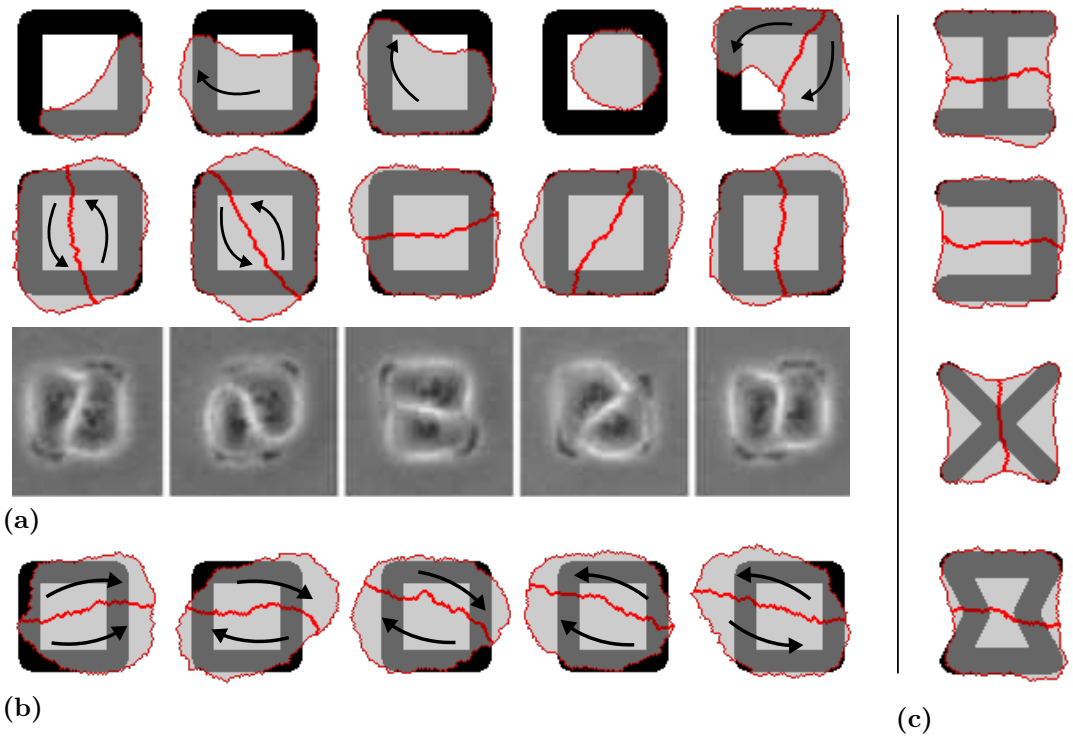

Figure 4.10. (a) Cell pair rotating on [square]. At the top simulations snapshots starting with a single cell which divides are shown and at the bottom phase contrast images from [50]. Bright regions indicate the boundaries of the two cells. The dark protrusions at the leading edge are the lamellipodia. The parameters are from the optimal fit: $\lambda_s = 2.3\,\mathrm{nN}$, $\sigma = 0.083\,\mathrm{nN\,\mu m^{-1}}$, $EA = 40\,\mathrm{nN}$, $A_0 = 670\,\mu\mathrm{m}^2$, $c_e = -5.5\,\mathrm{nN}$, $\mu = 0.3\,\mathrm{nN\,\mu m^{-1}}$, $\tau = 69\,\mathrm{MCS}$, $\eta = 3$, $W = 20\,\mathrm{nN\,\mu m^{-1}}$, $d_0 = 20\,\mu\mathrm{m}$, $T = 0.23$ resulting in a persistence length of $l_p \approx 350\,\mu\mathrm{m}$. (b) Snapshots of cell pair which does not retract the rear when in contracts. (c) Shape of cell pairs on various patterns

least the diagonal extension of the patterns which is energetically unfavorable. The required energy comes from the migration machinery and large energy differences make it unlikely that the cell maintains it polarity long enough to cross the unfavorable state with a cell-cell junction oriented diagonally. Persistent rotation can be promoted by increasing the migratory strength μ or the persistence time τ which makes it easier to overcome the barrier. Alternatively the simple line tension λ_s can be decreased.

Figure 4.11 shows distributions of the nucleus-nucleus axis for various patterns (green). On all patterns orientations with the shortest cell-cell junctions are most likely (the cell-cell junction is usually perpendicular to the nucleus-nucleus axis) but the degree of bias towards the shortest junctions varies. Among the shown patterns [H] and [X] offer the possibilities for the shortest junctions by putting them in the middle of the free spanning arcs. Indeed, the distribution on [H] is sharply peaked which also lacks adhesive area near the junction to anchor polymerizing actin. The peak becomes broader on [hourglass] and [C] where minimal junction length is longer opposed to [H]. This trend continuous for the transition from [C] to [Square]. The

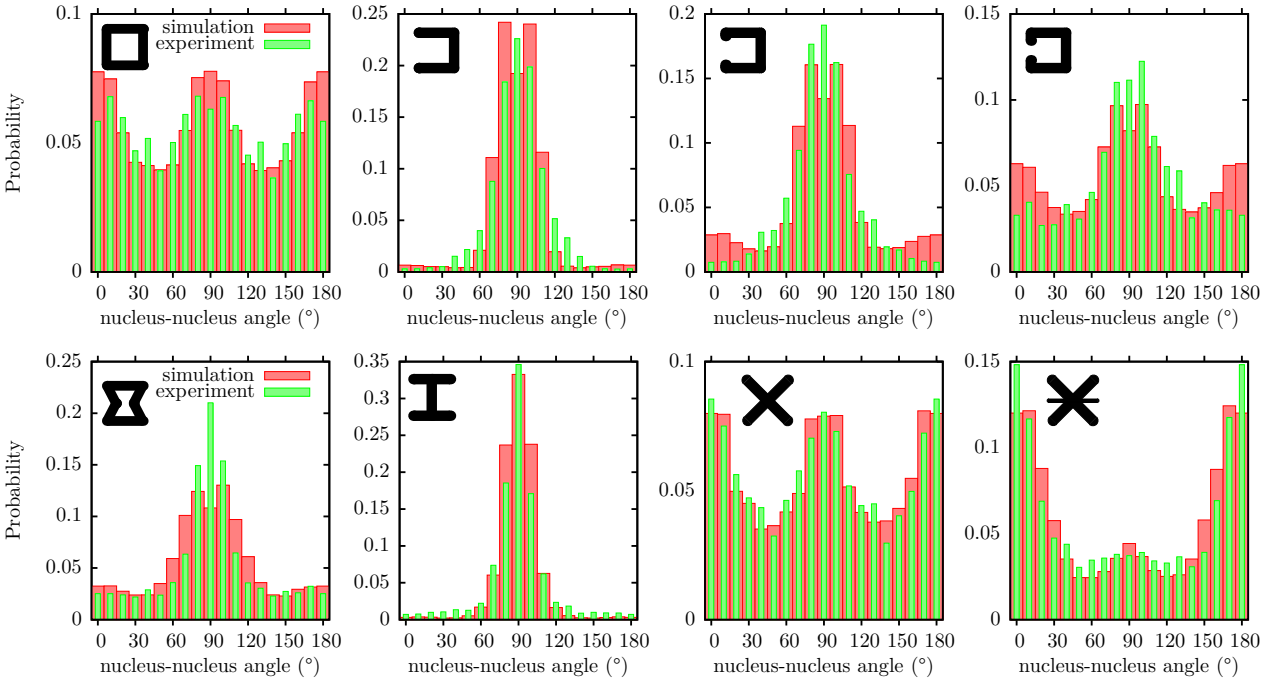

Figure 4.11. Comparison of experimental distributions (green) of the nuclei-nuclei axis and the best fitting simulated distributions of the COM-COM axis for various patterns. The bins at 0° and 180° are identical. The best fitting parameters are the same as in Figure 4.10a

contour becomes less invaginated and the length difference of the horizontal and diagonal oriented cell-cell junctions smaller. Providing support of the free spanning arcs as in the case of [X bar] shifts the preferred orientation in the same way.

Parameter Choice

We fit our model parameters to the experimental distributions of the nucleus-nucleus axis. Our cells lack a nucleus and we take the COM instead. The traction force experiments in chapter 2 were also performed with epithelial MCF10A cells, therefore we set the simple line tension to $\lambda_s = 2.3\,\mathrm{nN}$ and the elastic modulus to $EA = 40\,\mathrm{nN}$. As discussed in the previous chapter the surface tension σ is expected to be lower as in the traction force measurements. We also expect the target area to be lower because the phase field movies reveal that single cells do not fully cover the patterns used here [50][Supplement]. This might be due to a different density of the extracellular matrix proteins. Changes in cell area can be achieved by lowering the adhesive energy W or by directly changing the target area A_0. We choose to leave $W = 20\,\mathrm{nN\,\mu m^{-1}}$ to be constant and fit the target area because it is experimentally easier to access. The gradation width of the migration force is set to $\eta = 3$ (see equation (4.8)). This leads to a relatively narrow lamellipodium as seen experimentally in Figure 4.10a. In summary our fit parameters are the cell-cell contact strength c_e, surface tension

σ, target area A_0 and the newly introduce parameters in this chapter, the migration strength μ, persistence time τ (equation (4.8) and (4.7)) and the decay length of protrusions d_0 (equation (4.9)). For each set of parameter values 400 cells are seeded at random positions and migrate freely for some time and then divide. After division the COM-COM axis is recorded and the simulated and experimental distributions are compared.

The results for the best fitting parameters are shown in Figure 4.11 and agree well with the experimental distributions. The goodness of the fit is mainly limited by the variance in the experimental data. Our model covers the main observations of the experiments. Namely, the broadening of the peak when going from [H] to [C], the transition from one peak into two from [C] to [square] and disappearance of one peak from [X] to [X bar]. Good agreement of the nucleus-nucleus axis distributions does not necessarily mean that the simulated cells rotate persistently on [square] and [C1] but visual inspection (see Figure 4.10a) and the analysis of the mean rotation angle covered before switching the rotational direction conducted below confirm that our cells show the right behavior.

Various model components can be tested for their influence. Contact inhibition has been demonstrated to play an important role [80]. Our implementation of contact inhibition assumes that cells do not invade each other but still contract their rear driven by μ when in contact. If cells are also not allowed to contract when in contact a perfect fit to the experimental data for all patterns can still be obtained, but cell movement becomes a left-right or up-down oscillation. Figure 4.10b shows such cells. Both cells extend quite far across the edge of the pattern with the optimal fit parameters. At some point one of the cells starts to move in the opposite direction while the other lags behind. The lagging cell soon catches up and the movement starts over. It can also be shown that a finite cell-cell contact energy c_e is necessary to obtain a good fit and that broadening the lamellipodium by decreasing η also gives good agreement, although with different parameters.

Parameter Landscape

The fast implementation of our model allows to explore the parameter space more systematically. To quantify the quality of a fit the same L_2 norm (3.6) as in the previous chapters is used.

Maps of the L_2 norm averaged across the eight patterns are shown in Figure 4.12 and 4.13 for different combinations of parameters. Figure 4.12a addresses the effect of the migration machinery through μ and τ. With either μ or τ small the agreement is very poor. Cells lack the energy or directionality to stretch the cell-cell junction above the diagonal as required for rotation and sit still. The fluctuations from the finite simulation temperature barely changes the position and the nucleus-nucleus axis orientations is sharply peaked at orientations with minimal cell-cell interface (see Figure A.11). The curve with $\mu\tau = \text{const}$ defines the optimal values. Increasing μ provides more force to overcome the energy barrier while increasing τ makes movement uphill in the energy landscape more persistent. The question remains if the movement

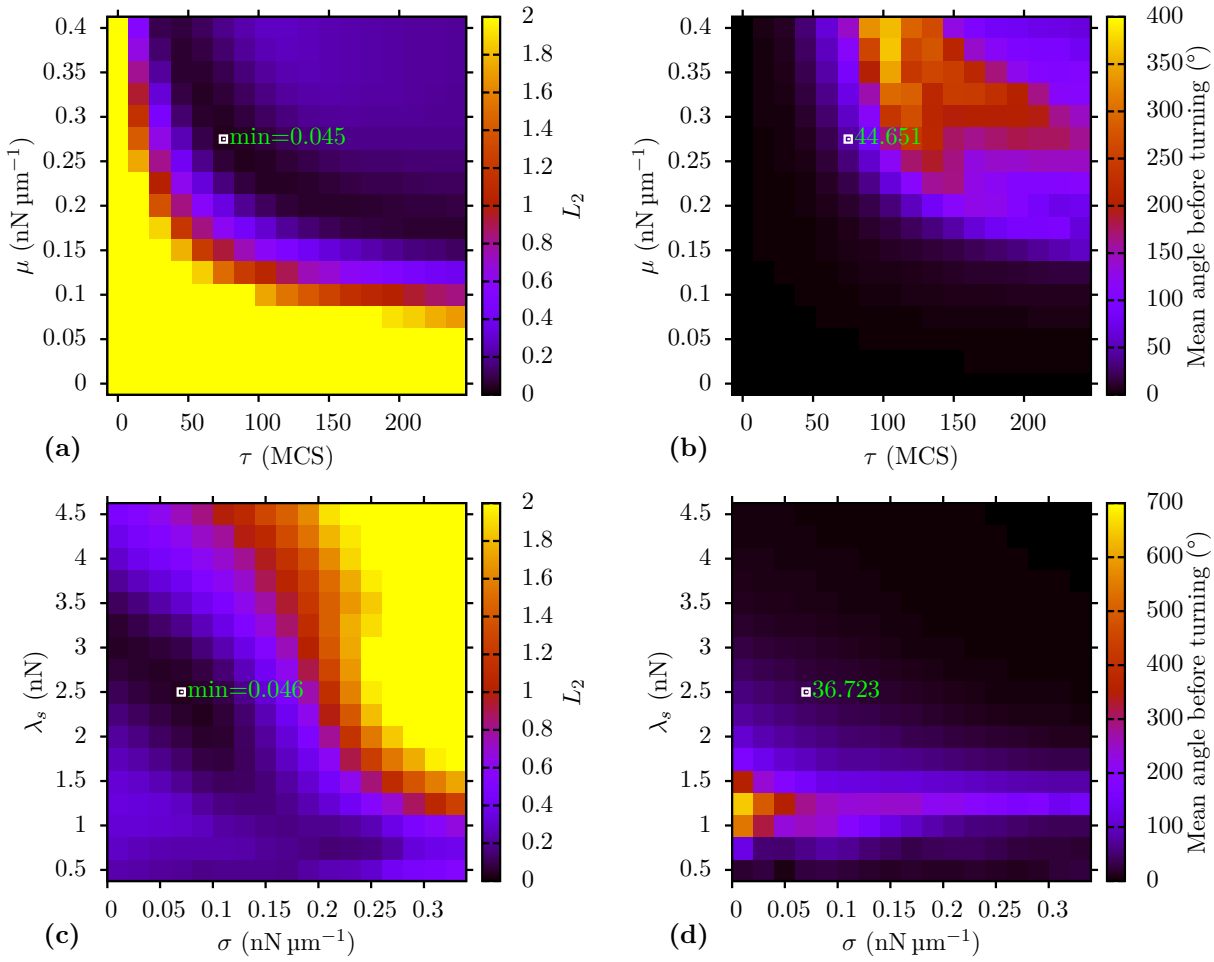

Figure 4.12. Maps of the L_2 norm defined in equation (3.6) (left column) and of the mean angle before rotation inversion (right column). Each map shows the variation of two parameters while the other parameters are held fixed at the best fit value. The maps of the L_2 norm are capped at two for better visibility.

is just oscillations or rotations. Here, the mean angle covered by the cells before the rotation direction is inverted helps. Figure 4.12b shows a map of this angle with the location of the best fit and its value indicated by a white square. An angle of 44.7° covered before turning at first seems very small, but the angle is averaged over all patterns used and cells on [H], [C1] and [hourglass] are not expected to rotate. For the [square] alone this angle is above 120° and this value still contains contributions from very short succeeding turns when the cell pairs direction is undecided. Hence, persistent rotational motion is confirmed by this map. Increasing μ and τ further makes the cells rotate wildly ignoring the pattern geometry first. Increasing the values even further leads to a drop in the mean angle before turning map. Cells become to persistent for rotational motion. They want to keep moving straight slowing down the rotational speed. For very large μ and τ cells are expected to oscillate similar to the

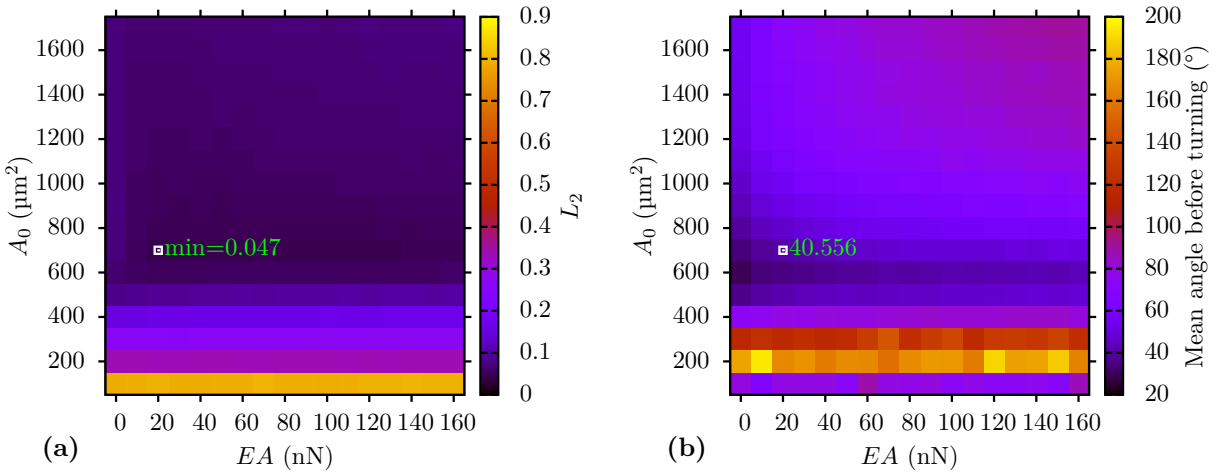

Figure 4.13. Same as Figure 4.12 but with the target area A_0 and elastic modulus EA varied.

cells in Figure 4.10b.

The role of simple line tension λ_s and surface tension σ is conjugated (Figure 4.12c). Decreasing σ makes the cells less invaginated across nonadhesive areas. The cell junctions are still contractile but get longer because the contribution from the surface tension is lowered. It therefore takes less energy to extend the junction up to the diagonal extension of the patterns and rotation becomes easier as confirmed by the mean angle map in Figure 4.12d. A lower σ can be compensated by a higher λ_s since this makes the cell-cell junctions more contractile again also reflected by the reduced rotation. Decreasing λ_s increases the rotation as seen experimentally by the inhibition of Rho kinase (ROCK) which lowers cell contractility and makes cell pairs on [hourglass] unstable [50]. For very low λ_s rotation also decreases because the migratory machinery is then strong enough for cells to completely ignore the patterns and move exploiting the periodic boundaries used in the simulations. The reduced mean angle before turning at the optimal fit location compared to the map of μ and τ is due to the finite resolution of the maps.

The target area A_0 and elastic modulus EA have little effect on the motion (Figure 4.13a) since the patterns are fully covered and the cell contours are relatively straight without transcellular actin cables. Lowering the target area first requires the cells to extend their junctions further to rotate. Lowering the area even further makes rotation easier again because cells are sitting in the center or corners of the patterns and rotate there.

Fit Results

The set of final fit parameters is in a reasonable range. The simple line tension was held fixed at $\lambda_s = 2.3\,\mathrm{nN}$ which is the value obtained from traction force experiments in Chapter 2. Also fitting it resulted in $\lambda_s = 2.6\,\mathrm{nN}$ which can be considered to be the same because the L_2 norm landscape is very shallow in this region (compare Figure

4.12c). The elastic modulus EA has no effect and was left at the value from Chapter 2. The surface tension $\sigma = 0.083\,\mathrm{nN\,\mu m^{-1}}$ is significantly lower as for the traction force measurements $\sigma_{\mathrm{TM}} = 0.83\,\mathrm{nN\,\mu m^{-1}}$. Constraining both λ_s and σ to the values from the traction force measurements results in a very poor fit. As already discussed in the previous chapter this supports the idea of a reduced tension above nonadhesive areas. The best fitting $\mu = 0.3\,\mathrm{nN\,\mu m^{-1}}$ and $\tau = 69\,\mathrm{MCS}$ result in a persistence length of 350 µm which is large but not unreasonable. A value of 290 µm has been used before [80] (estimated from the parameters in the supporting material, note the different definition of the persistence time there). The length scale $d_0 = 20\,\mu\mathrm{m}$ on which the migratory strength decays results on lamellipodia which extend about 5 µm beyond the pattern edge which is consistent with the gap size that can be bridged by MCF10A cells [47]. The cell-cell contact energy of $c_e = -5.5\mathrm{nN}$ is in a similar range as the adhesive energy density $W = 20\,\mathrm{nN\,\mu m^{-1}}$ when the height of the contacting membrane is assumed to be around 0.5 µm. The target area $A_0 = 670\mu\mathrm{m}^2$ is lower as for the traction force measurements ($A_0 = 1700\mu\mathrm{m}^2$) but MCF10A cells have been reported to have smaller areas before [160] and the area plays no role for both migration and traction force if it is not too small.

4.6. Conclusion

In this chapter cell migration was included into the CPM by splitting into two main aspects. The first one being the machinery which generates protrusion and contraction and the second one the mechanism which sets the direction of this machinery. Previous models have treated these aspects as one and used complicated reaction diffusion systems with many parameters [72, 86]. The strength of those models lies in the detailed pathways used which allow to study the role of each component involved. But in our context only shape, gap bridging capabilities and large scale movement matter which can be accurately reproduced with a much simpler model. To address shape we take the graded and radial force models which make a simple assumption on how forces are distributed based on actin densities and flow. This simplified model does not only predict cell shapes of keratocytes, fibroblasts and neutrophils correctly but also suggests a simple explanation for shape differences. Namely, actin in fibroblast polymerizes uniformly in one direction while actin in keratocyte polymerizes radially.

Line tension and its increased resistance to membrane extension in regions with high curvature determines the cell shape in our approach. Models with fixed cell shapes [138] lack this component and are shown to by unstable [161] when the shape constraint is released and only a surface tension resisting the migration machinery is assumed. This raises the question if shapes remain stable in our approach or if the alternating right left turns observed for some cells [143] arises from mechanical instabilities. I.e. that there exists no shape that combines forces from line tension and migratory machinery in a way that allows translation without shape change.

For the determination of the polarity direction we use the established velocity alignment model which typically assumes that the polarity direction is subjected to noise

[148, 154]. We do not explicitly add a noise term to the polarity direction, instead noise enters implicitly through the finite simulation temperature which makes it difficult to predict length scales on which cells move persistently. But this opens possibilities for further projects.

Cells can have multiple lamellipodia exploring the surrounding in several directions. One way to include this is by introducing several polarity directions with different alignment strengths into a cell. The polarity directions will most likely synchronize. But in situations where the main direction is not set, e.g. when cells encounter a dead end, they can form in different directions.

Micropatterns and cell-cell contacts require additional rules for the implementation. Our model assumes a strongly contractile cell, but contraction and extension cannot happen in the same region simultaneously. We therefore reduced contraction at the leading edge above nonadhesive areas. One can investigate if surface tension, migratory tension and adhesive energy can be combined into one anisotropic tension in the future giving a more natural way of implementing it. A first step would be to assume a lower surface tension above non adhesive areas.

With the model set we investigated how shape changes of micropatterns influence cell stability. We find very good agreement with experimental data [50] and the parameters used agree well with the traction force predictions (except for the surface tension) where the same cell type was used. Our interpretation for the stability of cell pairs on certain patterns is mainly based on the contractility of the cell-cell junction. Analytical treatment may be possible with an persistent random walker moving in angular space on an energy landscape set by the length of the cell-cell junction.

5 Network Optimization

5.1. Introduction

The cell model can now be considered complete to address the optimization of micropattern layouts. Cell shape, mechanics, division, interaction and stability on micropatterns are predicted correctly as explained in the previous chapters.

We use a genetic algorithm (GA) to optimize the layout. This chapter first motivates the use of GA and introduces the working principle of the algorithm in detail. The representation of pattern by a genome is an important part of it. This happens by arc like structures as used in almost every micropattern experiment and Fourier descriptors, a two-dimensional shape representation by a Fourier transform. To explore the algorithm we first apply it to a test case: Finding the optimal pattern for a given cell shape. We then move on to design layouts which bias cell migration into one direction and finally turn to the optimization of micropattern networks.

Advantages of a Genetic Algorithm

GA are inspired by natural evolution. A set of individuals, the pattern layouts, need to compete in an selective environment. Only the fittest individuals are allowed to reproduce and live on in the next generation. In the implementation of an GA the selection pressure is generated by a fitness measure, e.g. how well a given pattern layout normalizes cells. Those patterns which perform best are more likely to be selected for reproduction which can happen e.g. by averaging the shapes of the patterns. Reproduction results in a new generation which is again evaluated for its fitness and so forth until a desired fitness value is reached.

Genetic algorithm are are a standard tool [162–165] in the class of natural problem solvers which have two prominent examples: “The human brain, that created the wheel, New York, wars and so on and the evolutionary process that created the human brain” [163]. Reading this, one could think that the potential of a GA is almost unlimited. So, what are the advantages GAs have above traditional optimization methods such as simulated annealing or descent methods? Most optimization techniques explore a fitness landscape. For traditional problems this can be the mean

square deviation of a function an experimental values or an energy landscape. The sign of a fitness landscape is usually opposite, but this is irrelevant for the search strategy and throughout this chapter an optimal solution corresponds to maximum fitness, although this might actually mean minimal energy. Descent methods explore the landscape often be means of gradients, which first of all, require the computation of a gradient and secondly, knowledge about the landscape to ensure absolute convergence. Gradients are costly to evaluate if no analytical expression for the fitness function is known and sensitive to noise. Descent methods can also get stuck easily at local maxima. Simulated annealing strategies can escape from local extrema, but they are also limited by very large barriers or rough landscapes [162].

Genetic algorithm explore the fitness landscape in parallel. One can picture it as the members of the algorithm being distributed across the landscape communicating which each other through reproduction. With the algorithm progressing, individuals should cluster in regions with high fitness giving multiple good solution at once [162]. No prior knowledge about the fitness landscape is required. That is why they can also be applied to combinatorial problems as the Traveling salesman, Eight Queens or Knapsack problem where the landscape is discrete. In the Eight Queens problems eight queens are tried to be placed on a chessboard in a way that not two of them can check each other [163]. Fitness can be defined by the number of queens checking each other, but a meaningful gradient is difficult to define. In the Knapsack [163] problem one tries to put a number of items, each associated with a value c_i and volume v_i into a back of finite volume. The aim is to maximize the value of the bag under the constraint of finite volume. Again, the discrete nature of the problem makes the definition of a gradient difficult.

To summarize, we use a GA to optimize the pattern layout. Our main reason is the lack of knowledge about the fitness landscape. It may be very rough with high barriers and depend on how the patterns are represented but a GA is considered ideal in this case [163]. It is also robust to noise which is inevitable in biological experiments, e.g. the seeding location of cells cannot be controlled easily. In addition, a GA generates a set of solutions instead of just one which allows to test multiple candidates experimentally. It is not guaranteed to find the best solution in finite time, but a good working solution is sufficient in our context. It has also been used before in a similar context to optimize patterns of motors in motility assays to transport microtubules efficiently [166].

5.2. Genetic Algorithm

5.2.1. Principle

This section mainly follow the book by Eiben and Smith [163]. The principle of a GA is shown in Figure 5.1. The optimization by a GA starts out with a population consisting of several randomized individuals. In our case each individual is a pattern consisting of elementary building blocks called genes. E.g. the [Y] shaped patterns

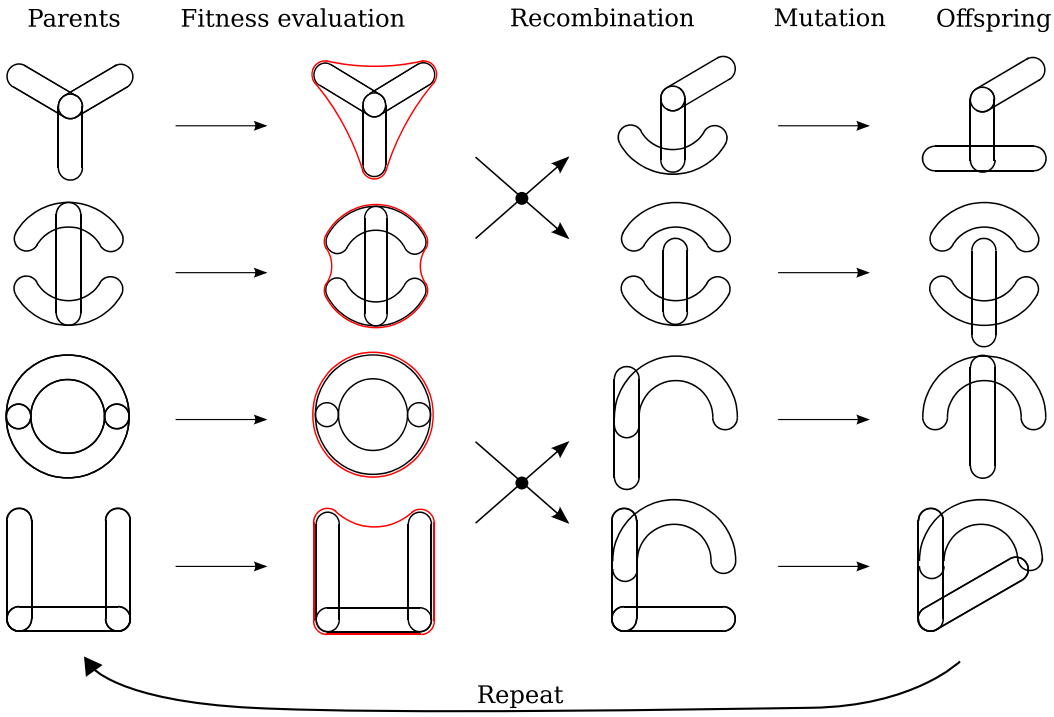

Figure 5.1. Pictorial representation of an iteration step in a genetic algorithm (GA). Members of a parent population are evaluated for their fitness, e.g. how well a cell on a member matches the shape of a target cell (cell shapes on the pattern are indicated by a red outline). According to their fitness they are selected (not shown in this pictorial representation) for recombination in a crossover process. This generates a new generation which is subjected to mutation resulting in the offspring generation. The offspring become the new parents and the iterations starts again.

is made by three genes each encoding a straight line but with different orientations. How patterns are encoded is discussed in detail below. The algorithm usually starts out with a random configuration but for better illustration the pattern in Figure 5.1 are very regular.

To mimic evolution the fitness of each individual (=pattern) is evaluated. In the shown example the fitness is determined by how well a cell shape (red outline) matches the shape of a target cell. In the recombination step individuals are selected to cross their genomes and form offspring. The likelihood of being selected depends on the fitness of each individual. This mimics the selective pressure of the environment. For illustration the fitness based selection is dropped in Figure 5.1. Two patterns generate two offspring, respectively. The crossover of the genomes in the recombination step generates new patterns which have attributes of both parents. In the last step mutation randomly changes the properties of some genes and one arrives at the final offspring generation. The offspring become the new parent and the iterations starts again.

The crossover and mutation operations are the main search operators of the algorithm which explore the fitness landscape while the fitness based parent selection

ensures that good changes persist. The mutation step is important to maintain a diversity in the population.

To explain the algorithm in detail a simple example is most instructive. In many problems a binary representation of individuals is used. A sample genome looks like this:

$$\text{Genome} \qquad G = \boxed{1}\boxed{0}\boxed{0}\boxed{1}\boxed{1}\boxed{0}\boxed{1}\boxed{0}\boxed{1}, \tag{5.1}$$

where each box represents a gene and this individual has a genome consisting of nine genes. The first one being $g_1 = 1$, the second $g_2 = 0$ and so on. A very simple Fitness function would be

$$F(G) = \sum_{\text{Gene}i} g_i \tag{5.2}$$

which has a maximum for all genes g_i being one. The algorithm now works as follows:

1. Start with a random population. E.g. with four individuals

$$\begin{aligned} \text{Member 1}: \quad G_1 &= \boxed{1}\boxed{0}\boxed{0}\boxed{1}\boxed{1}\boxed{0}\boxed{1}\boxed{0}\boxed{1} \\ \text{Member 2}: \quad G_2 &= \boxed{1}\boxed{1}\boxed{0}\boxed{0}\boxed{1}\boxed{0}\boxed{1}\boxed{1}\boxed{1} \\ \text{Member 3}: \quad G_3 &= \boxed{0}\boxed{0}\boxed{1}\boxed{1}\boxed{1}\boxed{1}\boxed{1}\boxed{0}\boxed{0} \\ \text{Member 4}: \quad G_4 &= \boxed{1}\boxed{1}\boxed{1}\boxed{0}\boxed{1}\boxed{1}\boxed{1}\boxed{0}\boxed{1}. \end{aligned} \tag{5.3}$$

2. Fitness evaluation of each individual. With the Fitness function (5.2) this is

$$\begin{aligned} F(G_1) &= F\left(\boxed{1}\boxed{0}\boxed{0}\boxed{1}\boxed{1}\boxed{0}\boxed{1}\boxed{0}\boxed{1}\right) = 5 \\ F(G_2) &= F\left(\boxed{1}\boxed{1}\boxed{0}\boxed{0}\boxed{1}\boxed{0}\boxed{1}\boxed{1}\boxed{1}\right) = 6 \\ F(G_3) &= F\left(\boxed{0}\boxed{0}\boxed{0}\boxed{1}\boxed{1}\boxed{1}\boxed{1}\boxed{0}\boxed{0}\right) = 4 \\ F(G_4) &= F\left(\boxed{1}\boxed{1}\boxed{1}\boxed{0}\boxed{1}\boxed{1}\boxed{1}\boxed{0}\boxed{1}\right) = 7 \end{aligned} \tag{5.4}$$

3. Parent selection according to their Fitness. The simplest method is fitness proportional selection with probability $p_i = F(G_i)/\sum_j F(G_j)$ for the i-th individual. For the population above we assume that G_4 is select twice and G_1 and G_3 once.

4. Recombination: The genomes of parents selected for recombination are crossed e.g. by one point crossover where genomes of couples are split at random location and then mixed.

$$\begin{aligned} P_1: \ G_1 &= \boxed{1}\boxed{0}\boxed{0}\,\|\,\boxed{1}\boxed{1}\boxed{0}\boxed{1}\boxed{0}\boxed{1} & O_1: \ G_1 &= \boxed{1}\boxed{0}\boxed{0}\boxed{0}\boxed{1}\boxed{1}\boxed{1}\boxed{0}\boxed{1} \\ P_2: \ G_4 &= \boxed{1}\boxed{1}\boxed{1}\,\|\,\boxed{0}\boxed{1}\boxed{1}\boxed{1}\boxed{0}\boxed{1} & O_2: \ G_2 &= \boxed{1}\boxed{1}\boxed{1}\boxed{1}\boxed{1}\boxed{0}\boxed{1}\boxed{0}\boxed{1} \\ P_3: \ G_3 &= \boxed{0}\boxed{0}\boxed{1}\boxed{1}\boxed{1}\,\|\,\boxed{1}\boxed{1}\boxed{0}\boxed{0} & O_3: \ G_3 &= \boxed{0}\boxed{0}\boxed{1}\boxed{1}\boxed{1}\boxed{1}\boxed{1}\boxed{0}\boxed{1} \\ P_4: \ G_4 &= \boxed{1}\boxed{1}\boxed{1}\boxed{0}\boxed{1}\,\|\,\boxed{1}\boxed{1}\boxed{0}\boxed{1} & O_4: \ G_4 &= \boxed{1}\boxed{1}\boxed{1}\boxed{0}\boxed{1}\boxed{1}\boxed{1}\boxed{0}\boxed{0} \end{aligned} \tag{5.5}$$

The colors illustrate the crossover of the genomes. Pairing of parents is random

from the ones selected in step three but usually self crossover (G_4 with G_4) is avoided. Parents are labeled with P_i and offspring with O_i. Selection and crossover have increased the average fitness from 5.5 to 6 in this example.

5. Mutation of offspring e.g. by randomly flipping a bit of the offspring population with a certain probability.

6. The offspring become the new parent generation and the iteration starts again at step 2.

The algorithm is terminated when a certain fitness is reached or no significant changes occur over several iteration steps.

There exist a large variety of parent selection, crossover and mutation operators [163] discussed below. GA algorithm are also not restricted to using a binary genome although binary genomes are addressed in the majority of the literature.

5.2.2. Pattern Representation

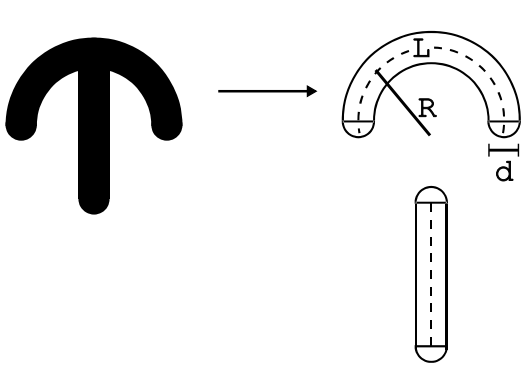


```
Gene 1:
position(x,y) = (13.4,50.3)
length   L    = 110
width    d    = 8
radius   R    = 35
orientation α = 0°

Gene 2:
position(x,y) = (13.4,50.3)
length   L    = 35
width    d    = 8
radius   R    = ∞
orientation α = 90°
```

Figure 5.2. Arc representation of a [crossbow] pattern. The [crossbow] is made from two arcs, each encoded in a gene by six numbers: the position (x, y), length L, width d, radius R and orientation α. Straight arcs have an infinite radius.

To optimize patterns one needs a way to encode them by a genome. The simplest approach would be to use the underlying lattice and a binary representation. The lattice written down in a linear representation with ones denoting adhesive sites and zeros nonadhesive results in a genome as (5.1). But even for a very coarse lattice of 50×50 sites this would give a genome with 2500 genes and a huge search space to explore. Besides, commercially available patterns are limited by a minimum size of 3 µm [167] and the fine resolution individual lattice sites provide would increase the search space unnecessarily.

Almost all patterns used in experiments are constructed from arc like building blocks. The [crossbow] shown in Figure 5.2 is made from two arcs, one curved part at the top and a straight at the bottom. Both arcs can be described by their position (x, y), length L, width d, radius R and orientation α as shown in the figure. The

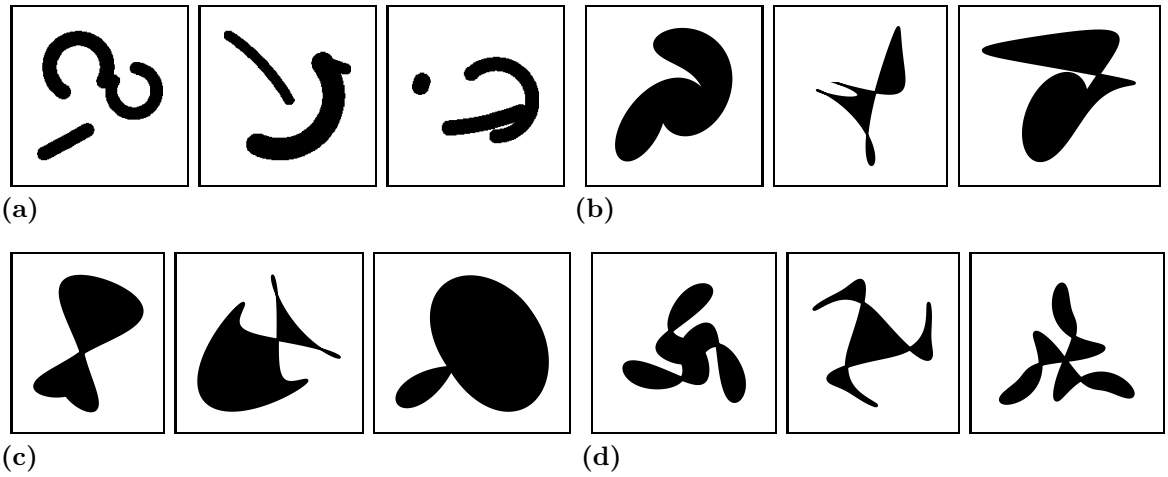

Figure 5.3. (a) Randomly generated patterns from arcs with genomes similar to (5.6). The genome size is restricted to three. (b) Randomly generated patterns from Fourier descriptors (FD) with $N_{\max} = 9$ (see equation 5.7) and genome as defined in (5.8). Subsequent randomly generated coefficients are restricted in size by $z_\nu/z_{\nu+1} = 1.5$. An interactive demonstration of FD can be found at `http://demonstrations.wolfram.com/FourierDescriptors/` [168] (c) Same as previous figure but the shapes fulfill the symmetry condition of equation 5.9. (d) Same as previous figures, but the shapes have a three fold symmetry achieved by only using coefficients with $z_{1\pm3\nu} = z_1, z_4, z_{-2}, z_7, z_{-5} \ldots$. All other coefficients are zero.

straight arc has an radius of infinity. Thus, six numbers are enough to describe one arc and if each number is represented by 16 bits the crossbow is described by a binary genome of 192 genes which is much less than in a lattice based description. Limits for minimum feature size or maximum curvature are also formulated easily in such description.

GA are not limited to binary genomes and the six numbers describing one arc can be taken as one gene. Following the schema in (5.1) a genome would look like

$$G_{\text{Arc}} = \boxed{x_1, y_1, L_1, d_1, R_1, \alpha_1}\boxed{x_2, y_2, L_2, d_2, R_2, \alpha_2}\boxed{x_3, y_3, L_3, d_3, R_3, \alpha_3}, \tag{5.6}$$

with examples shown in Figure 5.3a. Each pattern consists of three genes.

Another approach to describe shapes is by Fourier descriptors (FD) introduced in detail in the Appendix, section A.2. They are a standard tool in image processing [169] and are widely used in biology [170, 171]. For Cartesian FD a shape is represented in the complex plane by

$$z(s) = \sum_{\nu=-N_{\max}}^{N_{\max}} z_\nu \ \mathrm{e}^{2\pi \mathrm{i} \nu s}. \tag{5.7}$$

The curve $z(s)$ with parameter s is an expansion of the actual shape in a Fourier series with complex valued coefficients $z_\nu = x_\nu + \mathrm{i}y_\nu$ truncated at $N_{\max}$. To describe

a pattern one can take the coefficients z_ν as genome, e.g.

$$G_{\mathrm{FD}} = \boxed{z_0}\boxed{z_1}\boxed{z_{-1}}\boxed{z_2}\boxed{z_{-2}}\boxed{z_3}\boxed{z_{-3}}\ldots\boxed{z_{N_{\max}}}\boxed{z_{-N_{\max}}}, \tag{5.8}$$

with examples shown in Figure 5.3b. In contrast to radial FD (also discussed in the Appendix) Cartesian FD are not limited to simple valued boundaries and shapes can have overhangs. Only connected regions can be represented, although the regions can have holes as shown in Figure 5.3b. They have several useful properties discussed in detail in the appendix. To name a few, translation of shape is achieved by changing the coefficient z_0, shapes can be made scale invariant by dividing all coefficients by z_1 [172]. Higher order coefficients represent finer features or, when a cell shape is described, truncating the series early cuts off noise in the shape. As shown in Figure A.5 a crossbow can already by described by $N_{\max} = 5$ coefficients. Mirror symmetry can be achieved if the coefficients fulfill

$$y_\nu = x_\nu \tan(2\pi\nu\Delta s + \psi), \tag{5.9}$$

where ψ denotes the symmetry axis and Δs is the offset of the start point from this axis (see Figure A.6a). Shapes that fulfill equation (5.9) are shown in Figure 5.3c. This condition can also be used to define a measure for how symmetric a shape is. Rotational symmetry is achieved by setting certain coefficients to zero. For a m-fold rotational symmetry only the coefficients with $z_{1\pm\nu m}$ are different from zero. E.g. the three fold symmetrical shapes in Figure 5.3d have only the non-zero coefficients $z_1, z_4, z_{-2}, z_7, z_{-5}$.

With these to methods a wide variety of patterns can be represented. The letter shaped patterns as [C],[H],[Y] with the arcs and spread shapes like triangles or similar with Fourier descriptors.

5.2.3. Parent Selection

We mentioned already the fitness proportional selection method where a parent is selected according to its fitness F_i with probability

$$p_i = \frac{F_i}{\sum_j F_j}, \tag{5.10}$$

where the sum extends over all members of a population. Variants exists [163], e.g. by adding a offset to the sum to make the selection of less fit members more likely. Fitness based parent selection is closely coupled to the definition of the fitness function. A strongly nonlinear fitness measure could make selection of the fittest member much more likely. To avoid this dependence a ranking based selection can be used. Here, members are sorted according to their fitness and selected with a probability proportional to their rank. This avoids problems with large differences in fitness. We will use fitness proportional selection as defined in equation (5.10)

5.2.4. Recombination

As with Parent Selection a wide range of recombination methods exists. We focus on recombination of two parents. Crossover operations between multiple parents exist [163] but are not considered here. Parents can be selected multiple times to generate offspring with different partners, but each pair of parents generates just two offspring keeping the total population size fixed.

One point crossover

One point crossover (5.5) was already mentioned when the algorithm was introduced. It is not restricted to binary genomes. Genes between the parents are exchanged which mimics the chromosome exchange in sexual reproduction

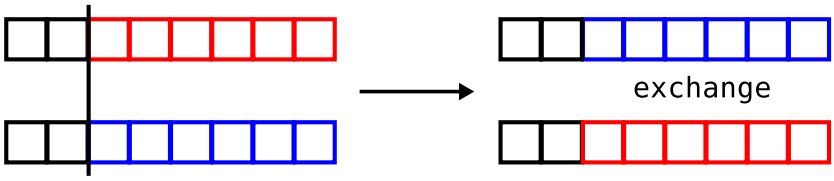

(5.11)

Each square represents a gene. A crossover point is selected indicated by the vertical line and the genes behind the points are exchanged between the two parents. E.g. if patterns are represented by several arcs (=genes), offspring are a combination of the arcs present in the parents as illustrated in Figure 5.1.

This crossover method conserves the order of the genes which is important if patterns are represented by FD where the coefficient scale with their order.

Two point crossover

This method is essentially the same as one point crossover but two crossover points are selected.

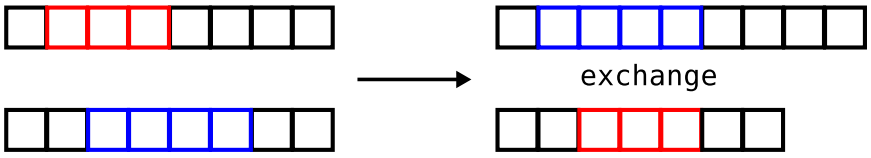

(5.12)

The segments which are exchanged don't need to have the same length which results in variable length genomes. This method does not conserve the order in the genome. There are many more possibilities to exchange genes. We will focus here on one point crossover since it is the simplest method which conserves order.

Single arithmetic

Genomes with a floating point representation allow to average genes. As with the pure crossover operations above different variants exists. They all have the arithmetic

average of a single genes in common. Two offspring genes $o_{1,i}$ and $o_{2,i}$ at genome position i become

$$\begin{aligned} o_{1,i} =& \alpha p_{1,i} + (1-\alpha) p_{2,i} \\ o_{2,i} =& \alpha p_{2,i} + (1-\alpha) p_{1,i}, \end{aligned} \tag{5.13}$$

where $p_{1,i}$ and $p_{2,i}$ denote the parent genes, respectively. The parameter $\alpha \in [0,1]$ controls the strength of the crossover. In a single arithmetic crossover operation one gene i is selected in both parents and crossed

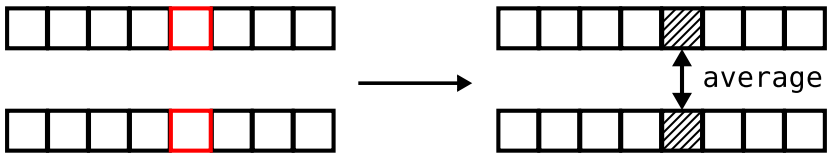

(5.14)

One point arithmetic

Arithmetic crossover can be applied to all genes after a crossover point

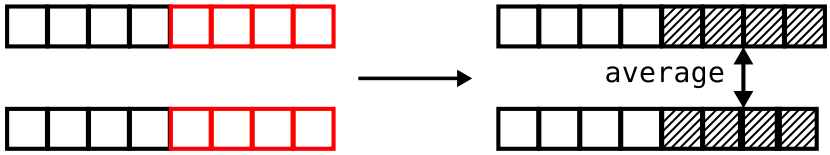

(5.15)

Arithmetic recombination with crossover

A combination of the pure crossover and arithmetic operations is found by this operation. Complementary parts of the parent genes are averaged to generate the offspring

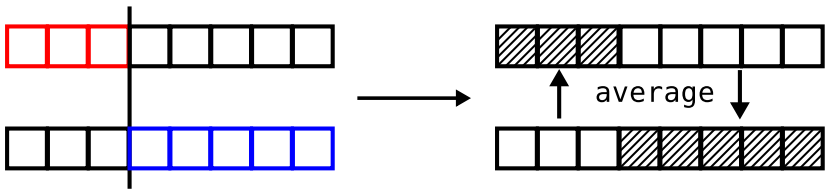

(5.16)

There are further variants. E.g. complete arithmetic crossover where the whole genome is averaged or averaging of genes at different positions.

We focus on one point crossover (5.5) and arithmetic recombination with crossover (5.16) since those because they operate on the whole genome and conserve the order of the genes.

5.2.5. Mutation

For a binary representation of a genome only bit flips are possible which can happen to single genes or to the whole genome. The corresponding operation for a floating point representation of genes is a randomization of the values it encodes

$$g = \mathbf{x} \longrightarrow g = \xi. \tag{5.17}$$

$\mathbf{x}$ stands here for all values a gene encodes. For arc representations this is position, radius, length and so on which all get randomized. The random number ξ is drawn from a uniform distribution. Random mutation of a gene can only by allowed to happen with a small probability p_r, otherwise the whole genome is randomized fast and any progress made by the algorithm is undone.

Opposed to the complete randomization is a gradual change widely used in GA [163]

$$g = \mathbf{x} \longrightarrow g = \mathbf{x} + \mathbf{N}(0, \sigma_m), \tag{5.18}$$

where $\mathbf{N}(0, \sigma_m)$ is a random number drawn from a Gaussian distribution with zero mean and variance σ_m . This mutation is usually applied with probability one and a small variance ensures that most changes are small. Large changes are still possible due to the Gaussian distribution but occur with lower probability.

5.2.6. Elitism

Elitism is a mechanism which avoids loss of the fittest members by mutation or crossover. It keeps track of the fittest members as the algorithm progresses and places them directly into the offspring generation. The members with the smallest fitness are replaced by the best. We apply elitism and carry over for 10% of the fittest members.

5.2.7. Parameter Control

GA are not parameter free. The most important one is the strength of the mutation controlled either by the probability p_r of a random mutation or the variance σ_m of a Gaussian mutation. Other parameters are the population size, crossover ratio α or the crossover method.

In our approach one gene encodes different properties. In an arc representation,a gene encodes position, radius, length and so on as defined in (5.6). Each of these values are constrained by boundaries to avoid situations where arcs are initialized far apart from each other, very thin/thick or too short/long. Written down in a general way a gene with its components labeled by j becomes

$$g = \mathbf{x} = (x_1, x_2, \dots, x_j, \dots) \qquad x_j \in [x_{j,\min}, x_{j,\max}] \tag{5.19}$$

The scale of the boundaries $x_{j,\min}$ and $x_{j,\max}$ is set by the cell scale the patterns are made for. For pattern represented by FD descriptors the size is controlled mainly by the first order coefficient and all subsequent coefficients are expected to be smaller.

The strength of the Gaussian mutation σ_m is scaled with these constraints to adapt mutation to the different types of values encoded. E.g. the length L of an arc as encoded in (5.6) is constrained by $L_{\min} < L < L_{\max}$ and if Gaussian mutation is applied the random number in equation (5.18) is drawn from a Gaussian distribution with variance $\sigma_m(L_{\max} - L_{\min})$. For a general component x_j of a gene this means

$$g_j = x_j \longrightarrow g_j = x_j + (x_{j,\max} - x_{j,\min})\mathbf{N}(0, \sigma_m). \tag{5.20}$$

Mutations beyond the limits $x_{j,\min}$ and $x_{j,\max}$ are allowed.

A population can loose its diversity if the mutation is too weak in a process called premature convergence [163]. Through crossover all members become very similar and no more progress is made. This situation can be avoided by adapting the mutation to the diversity of the population by dividing the Gaussian variance χ by the variance of the population fitness σ_p. Thus mutating with a random number $\mathbf{N}(0, \sigma_m/\sigma_p)$. With the constraints set on the scale of genes the Gaussian mutation (5.18) for a single component x_j of a gene becomes

$$g_j = x_j \longrightarrow g_j = x_j + \frac{x_{j,\max} - x_{j,\min}}{\sigma_p}\mathbf{N}(0, \sigma_m). \tag{5.21}$$

In case of a almost homogeneous population with low σ_p the mutation strength is increased while for very diverse populations it is lowered.

The mutation strength is mainly chosen empirical throughout this chapter. The mutation variance σ_m itself can be made part of the genome [163]. Each member and its genes have their own strength with is also subjected to crossover and mutation. But this approach was found to have little impact on the optimization.

5.3. Shape Matching

To test and investigate the different crossover and mutation operators the GA is applied to a simple test case with known solution. We use the GA to find the optimal pattern for a given cell shape. In Figure 5.4a the [crossbow] pattern and the averaged cell shape on it are shown which we use as target shape. Patterns are generated with the GA and the shape of a cell on a pattern is predicted by the CPM and compared to the target shape. The agreement with the target shape sets the fitness of a given pattern. Hence, a fitness function describing the agreement between the target shape and a simulated shape is needed. The simplest measurement for shape agreement is the number of mismatched pixels

$$D_L = \sum_{x,y} \left|\delta(x,y) - \delta_T(x,y)\right|, \tag{5.22}$$

where the sum extends over all lattice sites and $\delta(x, y)$ is one if a site belongs to a cell and zero otherwise. The same holds for $\delta_T(x, y)$ but with the target cell shape. The fitness is then defined as $F = 1/D_L$. A measure as 5.22 does not take the spatial arrangement of the lattice sites into account. A cell on a [T] pattern could have a similar D_L-value as a cell on a [circle], although the cell on [T] is more similar to the target one on [crossbow]. Image moments [169] are a measurement also taking the shape into account. They are defined as

$$M_{m,n} = \sum_{x,y} x^m y^n \delta(x,y). \tag{5.23}$$

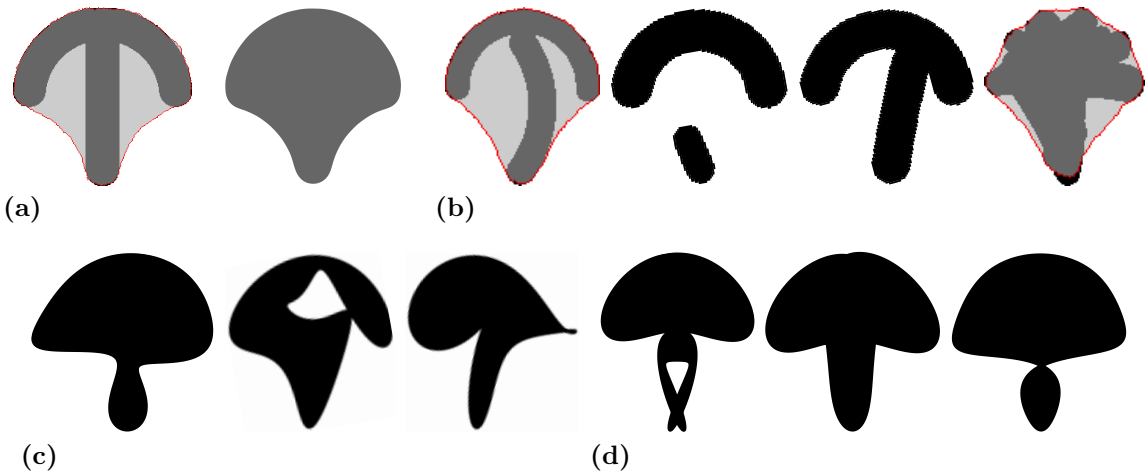

Figure 5.4. (a) [crossbow] pattern with cell (left) used to simulate the target cell shape (right). (b) Pattern encoded by two arcs predicted by the genetic algorithm with cells matching the target shape of the previous figure. The adhesive geometry away from the cell contour has no influence on the cell shape. For the last predicted pattern two point crossover (5.12) was used which does not constrain the genome size. Two patterns are shown with cells for better illustration. (c) Same as previous Figure but with cells encoded by Fourier descriptors with $N_{\max} = 5$. (d) Same as previous Figure but with the symmetry forced by using equation (5.9) to set the imaginary part of the coefficients (first shape) or with the symmetry measure (5.27) added to the shape measure (5.25) (second and third shape).

They can be calculated for simulated cells and the target cell and a distance measure can be defined as

$$D_M = \sum_{m,n} \left| M_{m,n} - M_{m,n}^{(\text{target})} \right| . \tag{5.24}$$

The fitness is again taken as the inverse of this measure. Moments can be combined into invariant measures under certain transformations, e.g. translation and rotation invariant Hu moments [173]. But all of these measures were found to perform poorly in combination with the GA.

Fourier descriptors allow to define another measurement by taking the distance between the absolute values of the coefficients

$$D_{\text{FD}}^2 = \sum_{\substack{\nu=-N_{\max} \\ \nu \neq 0}}^{N_{\max}} \left(|z_\nu| - \left| z_\nu^{(\text{target})} \right| \right)^2 . \tag{5.25}$$

The zeroth order term is excluded to make the measure translation invariant. Taking the absolute value of the coefficients makes it rotation invariant since all rotation

information is contained in the phase [174]. The Fitness is then defined as

$$F = \frac{1}{D_{\mathrm{FD}}}. \tag{5.26}$$

Again, this is a highly nonlinear fitness measure which strongly increases the selection pressure on unfit individuals. This can be prevented by changing the parent selection method to a rank based operator but this is not necessary here and we use fitness proportional selection (5.10).

5.3.1. Results

Figure 5.4b shows optimal patterns encoded by arcs predicted by the GA. The predicted patterns are very similar to the original one in Figure 5.4a used to generate the target shape. However, since the pattern geometry away from the cell contour has little influence on the shape the orientation of the central straight bar is not vertical. When the number of genes is not constrained as in the case for two point crossover (5.12) the algorithm tends to accumulate many arcs to cover almost the whole area under the cell as shown by the right pattern in Figure 5.4b.

Patterns encoded by FD work equally well as shown in Figure 5.4c. Again, only the contour of the patterns matches the pattern defining the cell shape and patterns can be very asymmetric.

The asymmetry can be prevented by using the symmetry constraint (5.9) for the coefficients. Either directly by setting the imaginary part y_ν of the coefficients from the real part x_ν or by introducing a symmetry penalty explained below. The tilt axis ψ and start point offset Δs in equation (5.9) can be calculated from the first coefficient pair. However, changes from mutation or crossover lead to large fluctuations of these values which impacts the imaginary values set by it. In addition, it couples all genes and the GA is found to perform poorly if the mutation strengths are not set carefully. Alternatively a measure for the symmetry of a shape can be defined from equation (5.9) by

$$D^2_{\mathrm{sym}} = \sum_{\nu \neq 0} \left[y_\nu - x_\nu \tan(2\pi\nu\Delta s + \psi) \right]^2, \tag{5.27}$$

where ψ and Δs need to be determined numerically to minimize D_{sym}. The value of D_{sym} can be added to D_{FD} in the fitness measure (5.26) or subtracted from the fitness F. Predicted patterns are shown in Figure 5.4c which are symmetric and closely resemble a [crossbow].

5.3.2. Influence of Crossover, Mutation and Elitism

Figure 5.5 shows how the fitness evolves as the algorithm progresses. The fitness of each member is indicated by a red dot. The mean fitness and its variance by green and blue lines, respectively. The interesting parts of a population are its best members and the mean fitness of the best 10% is shown by a magenta line. The optimization

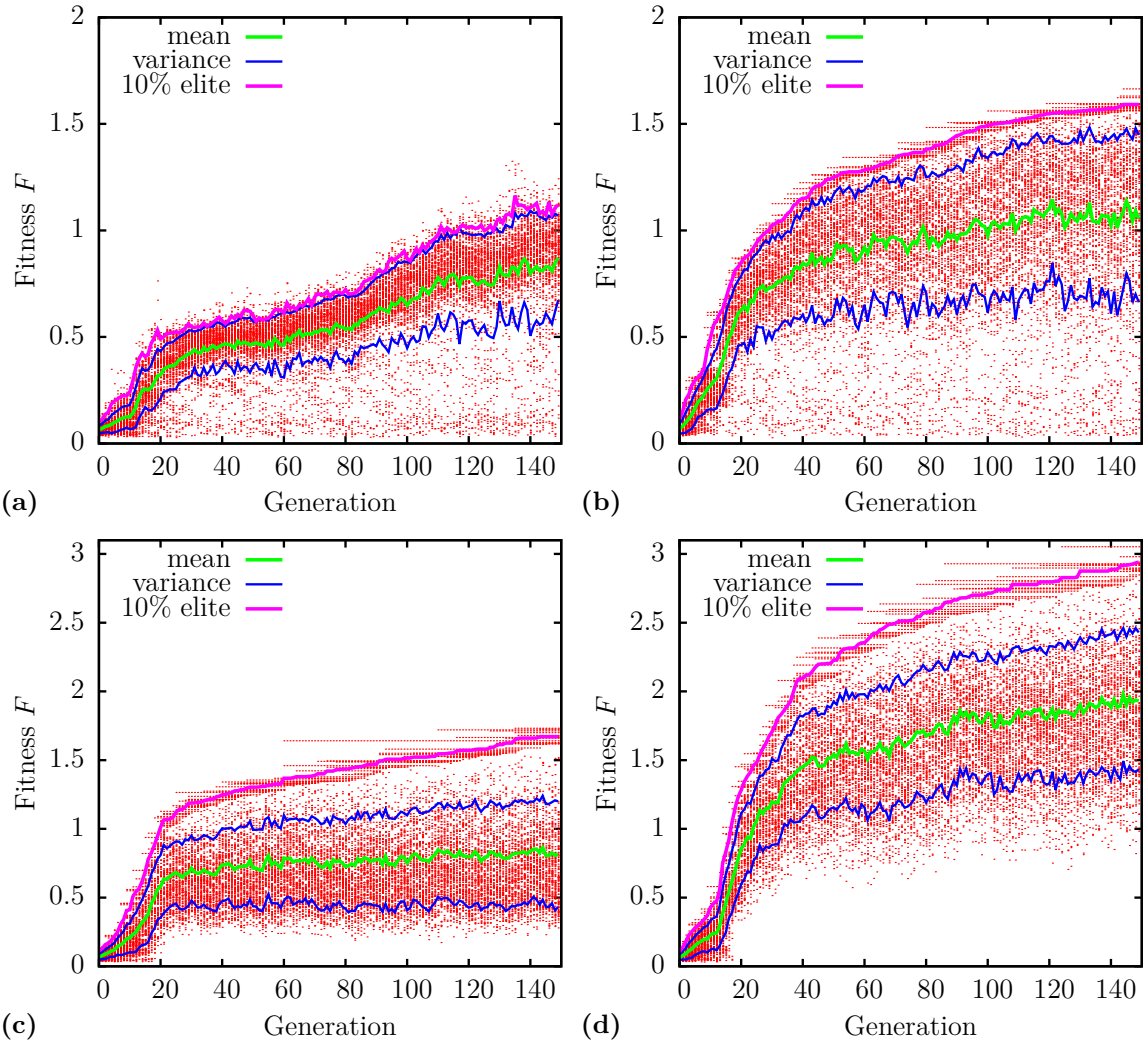

Figure 5.5. Evolution trajectories generated by the genetic algorithm. A population size of 128 was used. The fitness of each individual is indicated by a red dot. Mean fitness (green), its variance (blue) and mean of the fittest 10% are shown as solid curves. One point crossover (5.5) and patterns represented by Fourier descriptors with the constraint $z_\nu \in [-10\,\mu\text{m}/2^\nu, 10\,\mu\text{m}/2^\nu]$ were used. The target pattern has a width of 30 µm (a) Random mutation (5.19) with probability $p_r = 0.01$. (b) Random mutation (5.19) with probability $p_r = 0.01$ and elitism for 10% of the members. (c) Gaussian mutation (5.20) with $\sigma_m = 0.01$ and elitism for 10%. (d) Adaptive Gaussian mutation (5.21) with $\sigma_m = 0.01$ and elitism for 10%.

starts with random patterns similar to the ones in Figure 5.3 which result in a very low fitness that increases with each generation.

Figure 5.5a shows the optimization with one point crossover (5.5) and random mutation (5.19). The fitness is calculated by (5.26). To put it into perspective, the optimal shapes in Figure 5.4 have a fitness value between two and three. A sharp

initial increase is observed where most of the unfit members are eliminated by the selection mechanism. Occasionally members with a much higher fitness occur. They do not persist because their genome is mutated rapidly and cannot propagate to the rest of the population. The fitness slowly increases but the predicted cells do not reach a good agreement with the target shape. A fitness value of one roughly means that the size is estimated correctly. The fitness of the whole population is clustered mainly around the mean but many members with a low fitness are found which is due to the random mutation operator. It can completely reshape a pattern with a single mutation step.

Elitism helps to preserve good changes as shown in Figure 5.5b where 10% of the fittest members are carried over to the next generation without mutation or crossover. The mean fitness strongly increases right from the start. The elite members drag the rest of the population behind leading to an overall increased fitness. Due to the random mutation members with a very low fitness still exist and the diversity seems to increase. But the increased diversity is mainly due to the strongly nonlinear fitness measure.

Gaussian mutation (5.20) performs equally well as random mutation as shown in Figure 5.5c Since it is more likely to have small changes by mutation instead of complete randomization no more individuals with a very low fitness exist. But the low mutation rate comes at the price of not being able to explore the whole parameter space efficiently and the fitness only increases slowly. With adaptive mutation (5.21) the mutation strength is initially strong due to the small diversity in the population and, supported by elitism, a rapid increase is achieved as shown in Figure 5.5d. The increased diversity at a higher fitness decreases the mutation rate and the population is stabilized. The changes introduced by crossover and mutation are still strong enough to further explore the fitness landscape.

It seems that adaptive Gaussian mutation with elitism is the method allowing for the most rapid fitness increase. But only single runs were shown in Figure 5.5 and GA are not deterministic if initialized with a different random seeds. Figure 5.6a shows the fitness of the best 10% of the members averaged over 64 runs and confirms that adaptive Gaussian mutation in combination with one point crossover (OPC) yields the best results. It has the fastest initial increase and is not saturated at the end of the optimization. Only using Gaussian mutation without adaptive strength performs a little bit worse because the initially required large mutation rate hinders progress at a later stage.

Random mutation has a weaker initial increase but also reaches considerable fitness values. This only works when it is combined with elitism.

Patterns can also be optimized to some degree without any crossover. Without crossover the optimization is similar to simulated annealing. The configuration space is explored by random mutations with the mutation strength similar to a temperature. The acceptance probability of a configuration change corresponds to the parent selection method in this case. However, without crossover optimization only works in combination with elitism (data not shown).

Arithmetic recombination with crossover (5.16) performs very poorly. Averaging of

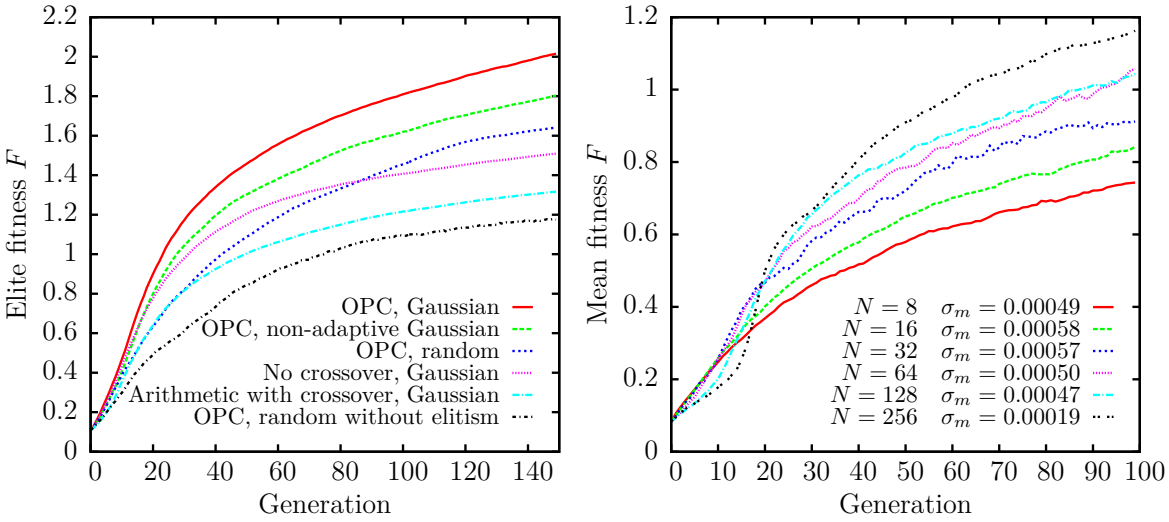

(a) **(b)**

Figure 5.6. (a) Fitness of the best 10% of the population for various mutation and crossover methods averaged over 64 runs. If not stated otherwise all runs were performed with adaptive Gaussian mutation (5.21) and elitism. One point crossover (OPC) performs best. (b) Mean fitness for various population sizes N with optimal mutation strength σ_m. One point crossover with adaptive Gaussian mutation was used. Each population size was averaged over $4096/N$ runs.

genes generates a very homogenous population. The main search operator in this case is mutation but improvements made a are rapidly destroyed by averaging. In contrast, one point crossover (5.5) conserves the values of the genes and just mixes genomes.

The parameters left to explore are the population size and mutation strength. Figure 5.6b shows the mean fitness for runs with different sizes and optimal adaptive Gaussian mutation strength σ_m. The optimal strength was found by taking the area under the fitness curve as measure for performance. It was maximized by using Powell's optimization method [175] with σ_m as optimization parameter . Increasing the population size makes it more likely to find fit members in the initial generation. It takes longer for those fit members to take over in large population, but for the averaged runs shown a higher mean fitness is reached in the end. The optimal mutation strength decreases with population size. This is expected because for adaptive Gaussian mutation (5.21) the strength scales with the diversity σ_p of the population which changes with population size.

Increasing the population size is limited by the computational time needed and benefits quickly saturate above 256 members. Optimizing other parameters is also restricted by the computational time. On a current state desktop processor evaluating the fitness of a population with 128 members takes about 10 seconds. This involves pattern generation, cell spreading which takes about 2000 MCS and averaging the cell shape for another 2000 MCS. Statistics needs to be collected for multiple runs and Powell's method takes about 50 function evaluations to converge. This makes

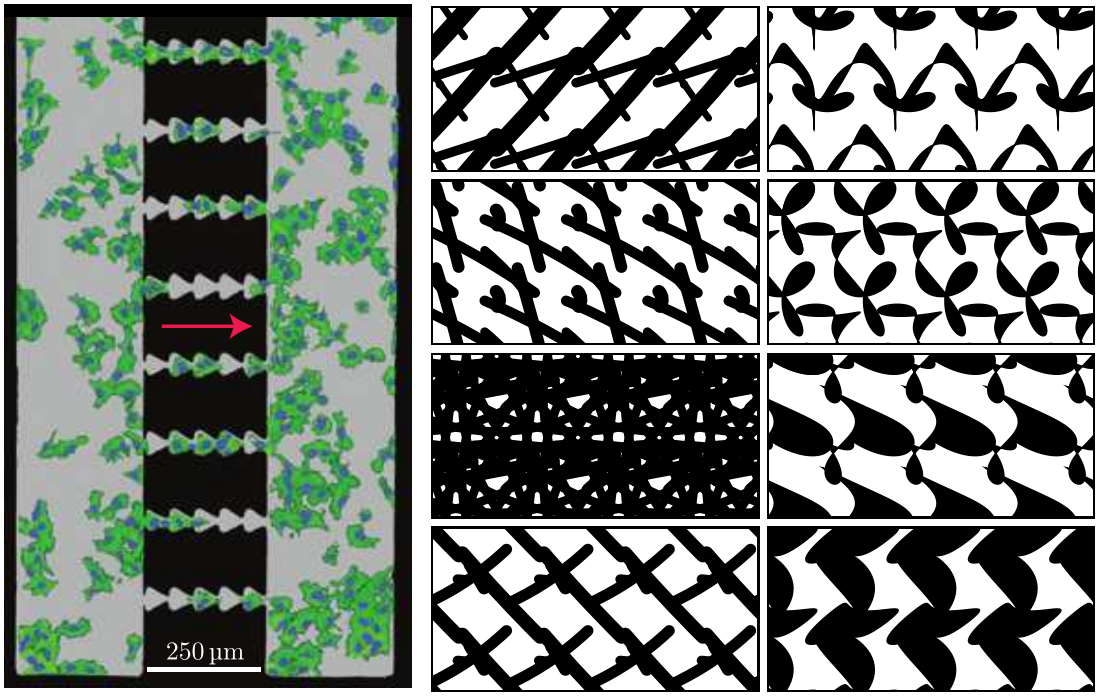

Figure 5.7. (a) Triangular micropatterns arranged into an ratchet with cell reservoirs on both sides. Cells are stained for actin (green) and the nucleus (blue) and migrate preferentially to the right. Adapted from [46]. (b) Randomly generated ratchet patterns with arc representation. Unit cells containing four arcs are arranged in a 4×2 square lattice with periodic boundary conditions. The unit cell width is 50 µm as in experiments [46]. (c) Same as previous Figure but with patterns represented by Fourier descriptors.

parameter optimization unfeasible for more complex optimization. We therefore set the parameters empirically in the remaining part of this chapter.

In summary, one point crossover (5.5) with adaptive Gaussian mutation 5.21 yields the best results. A population size of 128 members is chosen for computational efficiency and close to sizes used previously in similar context [166]. The Gaussian mutation strength is set to $\sigma_m = 0.001$.

5.4. Cell Migration Biased by Micropatterns

It has been demonstrated that ratchet shaped structures as shown in Figure 5.7a can bias cell migration into one direction [45, 46]. Likewise, we use the GA to find geometries which maximize the bias of the migration direction. To generate ratchet geometries we arrange patterns into a square lattice with four repetitions. Examples are shown in Figure 5.7b for arcs and Figure 5.7c for Fourier descriptors.

In experiments it is difficult to control where cells attach to the pattern. Initially,

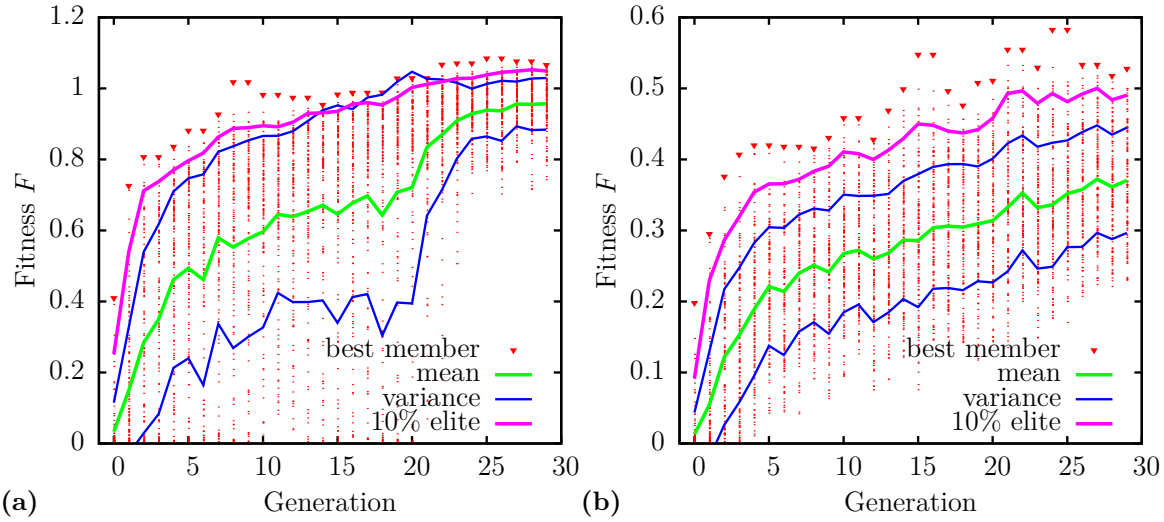

Figure 5.8. Evolution trajectories for optimal migration bias. The fitness (5.28) is shown as function of the GA generation. For each pattern 32 cells were placed and the migration followed for 10000MCS (sufficient to cross the ratchet two times). The green and blue curves are the mean fitness and variance, respectively. The magenta curve is the fitness of the best 10%. Individuals are indicated by red dots with the best individual marked by a triangle. Cells were simulated with the optimal parameters for MCF10A cells from chapter 4. Patterns represented by Fourier descriptors, a population size of 128, one point crossover (5.5) with Gaussian mutation (5.20) (constraint $z_\nu \in [-20\,\mu\text{m}/1.5^\nu, 20\,\mu\text{m}/1.5^\nu]$, strength $\sigma_m = 0.01$) were used. (a) Ratchet without reservoir and cells initialized as circles at random positions. (b) Ratchet with reservoir (50 µm width) and cells initialized at random positions within the reservoir.

cells are suspended in a medium and make contact at random positions. Large reservoirs as shown in Figure 5.7a make sure that most cells attach there and have no biased migration direction from the start. However, this does not prevent initial contact of cells on one of the ratchets. Simulating cells with the CPM allows to control the starting position. Cells can either be placed random on completely periodic lattices as shown in Figure 5.7b and 5.7c or reservoirs can be added at the left and right of the lattices. Cells are than only placed at random within one of the reservoirs.

We investigate both seeding mechanism, random placement without reservoir and random placement only within a reservoir. As fitness measure we take

$$F = \frac{d_r}{d_0}, \tag{5.28}$$

where d_r is the distance migrated by a cell to the right during a fixed number of MCS. It is normalized by the distance d_0 migrated on a homogeneously adhesive substrate when the polarity direction is kept fixed. Many cells are placed at random on the patterns and their fitness is averaged. The fitness measure (5.28) can become larger

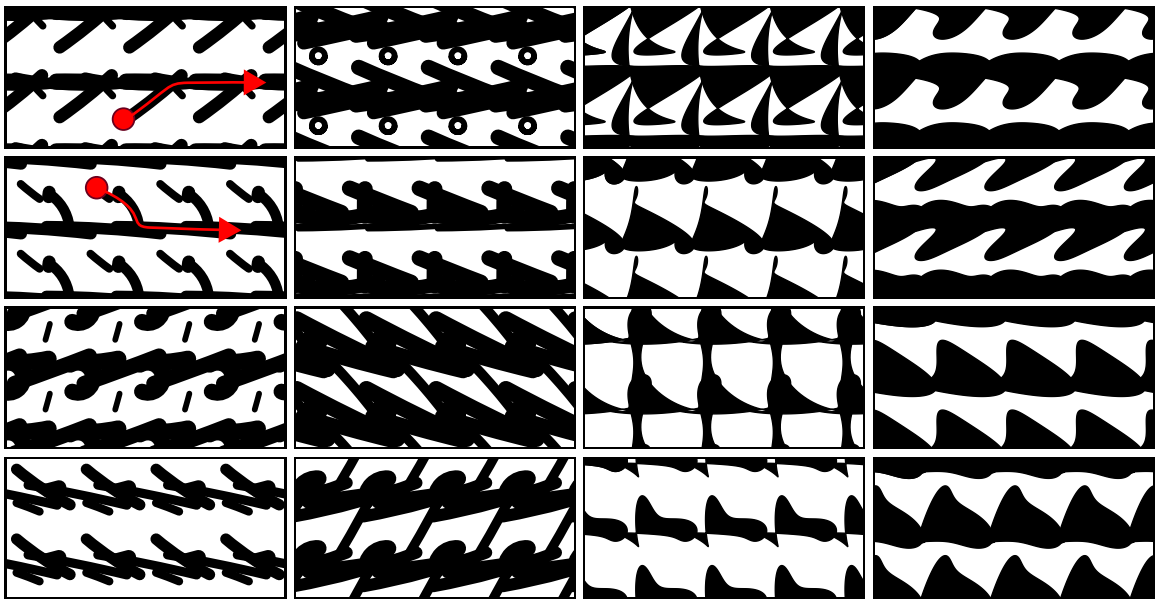

(a) **(b)** Reservoir **(c)** **(d)** Reservoir

Figure 5.9. Optimal patterns formed by arcs ((a),(b)) and Fourier descriptors ((c),(d)) predicted by the genetic algorithm to bias cell migration to the right. In (a) and (c) no reservoir was used and cells are placed at random position. In (b) and (d) cells were initially placed in reservoirs (not shown).

than one. Cells confined to a narrow line move faster than free cells because their shape allows maximum force from the graded force model introduced in the previous chapter on front and rear. The measure can become negative when cells preferentially move to the left and is set to zero in this case to allow parent selection.

5.4.1. Results

Figure 5.8 shows the fitness as the optimization progresses for both ratchets with and without reservoirs. Here, the full potential of the algorithm is illustrated. Within a few optimization steps a significant bias for cells migrating to the right is generated. For patterns without reservoirs (Figure 5.8a) layouts form which allow a faster migration than on homogeneously adhesive substrates as indicated by the fitness which is larger than one. For ratchets with reservoirs (Figure 5.8b) cells spend time migrating on the reservoirs in vertical direction not finding the transition to a ratchet. The optimal Fitness is lower but the bias is still very strong.

Figure 5.9 shows optimal pattern layouts to bias the migration. Most have a triangular shape, but not the equilateral one used in experiments (compare Figure 5.7a). The triangles are rotated and two corners lie on a horizontal line forming an almost straight horizontal edge.

Without reservoirs and arc patterns occasionally triangles facing the opposite way are formed (Figure 5.9a top two patterns). These triangles have been reported to

bias migration before when the tip angle is acute enough [16]. Two mechanism are used here. Firstly, the narrow triangle provides a continuous track without gaps. It is covered by the cell completely along its narrow width leaving no room to migrate vertically. Cells then tend to move in the direction of more available adhesive area. Secondly, the arms protruding from the continuous track catch randomly seeded cells as indicated figure by the red arrows and bias them into the right direction.

Arms protruding from the patterns are not present when cells are only allowed to start from an reservoir (Figure 5.9b and 5.9d). Patterns described by Fourier descriptors perform better here, most likely because it is easier to form triangles from them. Cells migrating to the left on asymmetric triangles encounter a vertical edge when they deviate from the horizontal path. Depending on the exact shape, this either acts as a dead end (e.g. third pattern in Figure 5.9d) which makes cells turn completely or it acts as a vertical barrier. Cell migrate along the vertical barrier until they reach the continuous track again. Here, they encounter a horizontal barrier and movement to the right provides more adhesive area to them. The whole movement is shown in Figure 5.10 where a cell initially moves to the left and is turned by the pattern geometry. This effect can be enhanced by misalignment of the continuous track as for the bottom pattern in Figure 5.9c. The small triangular patch at the bottom of the pattern is right in the migration direction for cells moving to the right and used to bridge the gap between patterns. For cells moving to the left it has an offset of several microns from the cell front and the cells seldom adhere to it. Instead, they turn around.

Equilateral triangles as in Figure 5.7a are not predicted by the optimization. Likely because they offer less vertical edge to turn and when cells migrate in vertical direction they move past the continuous horizontal track on them.

5.5. Network Optimization

The normalization micropatterns provide for single cells ceases when cells start to divide. For single cells, the size of the patterns is chosen to match the cell area and becomes too small for two cells sitting on the same patterns. Cells with insufficient space available start to migrate or crawl above each other which makes normalization and imaging complicated. Many experiments require cells to stay on patterns for several days and they start to divide. Networks of micropatterns are thought to provide normalization in this case when daughter cells after division are able to move on to unoccupied neighbouring patterns.

As demonstrated throughout this work, shape, migration, stability and division are strongly influenced by pattern geometry and are predicted correctly by the developed CPM. We now aim to optimize the network layout to provide maximum cell normalization even after several cell divisions.

For epithelial cells as MCF10A, it is unlikely that cells can be separated once they have adhered to each other. In animals the main purpose of the epithelium is to provide a protective closed layer around organs without holes. Micropatterns do not change

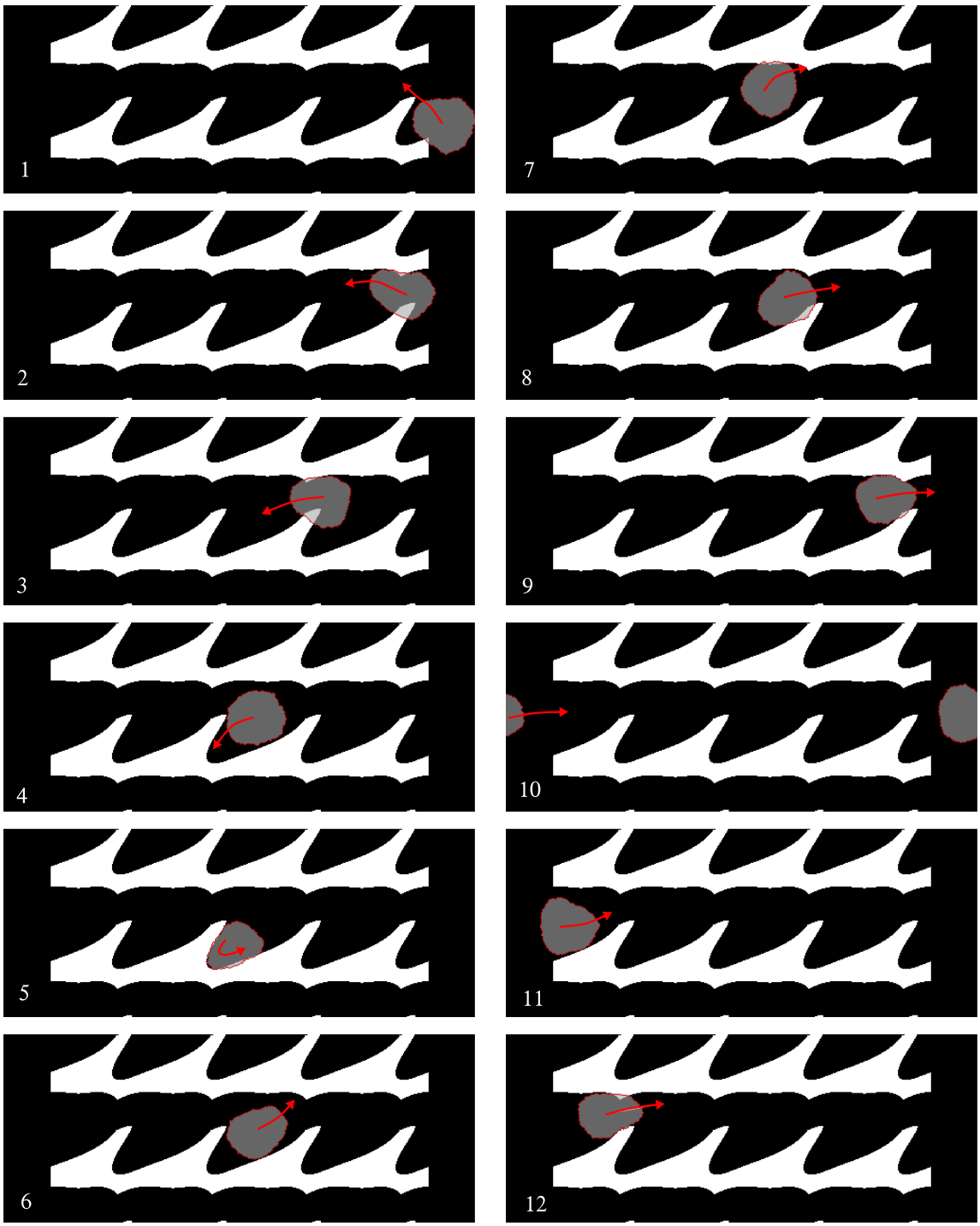

Figure 5.10. Cell migrating on ratchet micropattern. Initially the cell moves to the left but deviates from the horizontal track and turns at a dead end corner of one of the triangular shapes. It moves back to the horizontal track where it continuous moving to the right across the reservoirs at the sides. The triangular shapes bias the movement to the right. The optimal fit parameters for MCF10A cells in chapter 4 are used.The reservoir has a width of 50 µm and the ratchet is 200 µm long.

the cohesiveness as demonstrated for cells forming a closed sheet above nonadhesive regions [51]. We therefore do not require the cells to be without any cell-cell contacts on the networks. It is also not known if cells can be normalized into a specific shape on networks and we choose a fitness function which only demands that all cells have the same shape. To compare shapes the same measure as in equation (5.25) is used

$$\bar{D}^2_{\mathrm{FD}} = \frac{2}{N_c(N_c-1)} \sum_{i=1}^{N_c-1} \sum_{j=i+1}^{N_c-1} \sum_{\nu\neq 0} \left(|z_{i,\nu}| - |z_{j,\nu}|\right)^2 \tag{5.29}$$

which compares the shape of every cell with the shape of every other cell. The number of cells on a network is labeled with N_c, $z_{i,\nu}$ and $z_{j,\nu}$ are the Fourier coefficients of order ν for cell i and j, respectively. The sum over the coefficient is typically truncated at a value $N_{\max} = 10$. The fitness function is then given by

$$F = \frac{1}{\bar{D}_{\mathrm{FD}}}, \tag{5.30}$$

and is again strongly nonlinear as in equation (5.26).

To minimize the computation time required only one cell is initially placed on a network. Cell-cell interaction is established through division. After cells have reached a certain age and have a size above a threshold they divide with a certain probability during each MCS leading to a Poisson distribution for the cell division time. During the typical simulations a total of three cell divisions is possible corresponding to 60 hours for MCF10A cells. The fitness of a network layout is obtained at the end of the simulation from equation (5.30). For each pattern the fitness of multiple runs starting with different initial positions is averaged. Care has to be taken about the cell size. One way to obtain optimal fitness for cells represented on a lattice is by making the patterns very small. Cells also become very small then and all shape features are lost in the finite lattice resolution. To avoid this during the optimization the fitness is strongly penalized when the cell area drops beneath half of the target area.

Figure 5.11 shows some of the network layouts investigated. For all networks units cells are generated containing the patterns and are arranged into square and hexagonal lattices. Patterns described by Fourier descriptors can be made with a rotational symmetry matching the symmetry of the lattice with examples shown in Figure 5.11b and 5.11d.

5.5.1. Results

Snapshots of a simulation of several cells on a hexagonal lattice made of [Y] patterns are shown in the Appendix in Figure A.12. The simulation displays several characteristics of cells observed experimentally on micropatterned networks. Namely, cells forming adhesive contacts above nonadhesive areas between patterns by the adhesion mechanism described in Chapter 3. Clusters of several adherent cells are bridging larger nonadhesive region. Huge cells spreading the entire network are allowed by

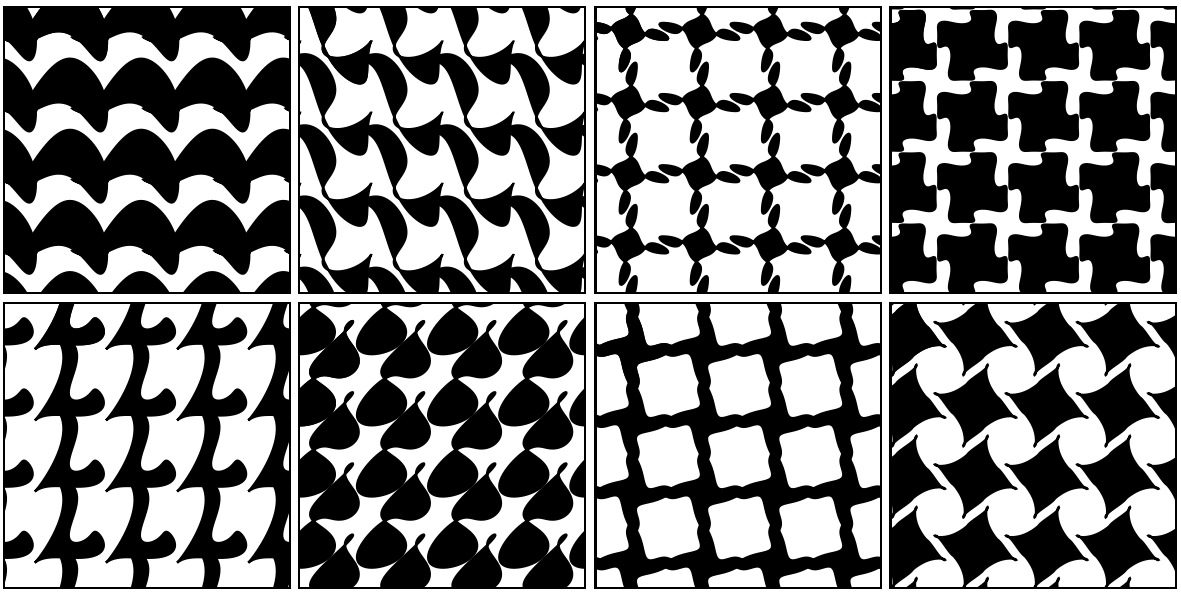

(a) Square lattice without symmetry **(b)** Square lattice with 4-fold symmetry

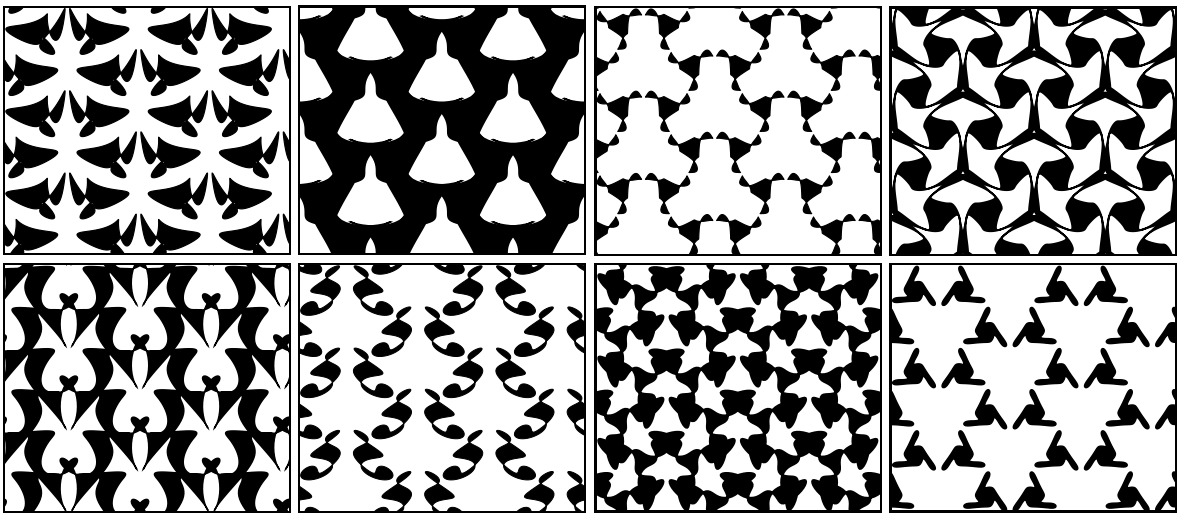

(c) Hexagonal lattice without symmetry **(d)** Hexagonal lattice with 3-fold symmetry

Figure 5.11. Examples of randomly generated networks by the genetic algorithm. Unit cells containing a pattern generated with Fourier descriptors are arranged in square and hexagonal lattices. Rotational symmetry is generated by setting certain coefficients to zero (see section 5.2.2)

the unconstrained cell area introduced in Chapter 2. Cells migration from pattern to pattern is driven by the migration machinery introduced in Chapter 4.

With all those mechanism set the GA is used to optimize the layout and results for square lattice networks without symmetry are shown in Figure 5.12a. The optimization by the GA turns the two dimensional networks into one dimensional lines to achieve cell normalization. The cell-cell junctions are stabilized by the absence of adhesive area

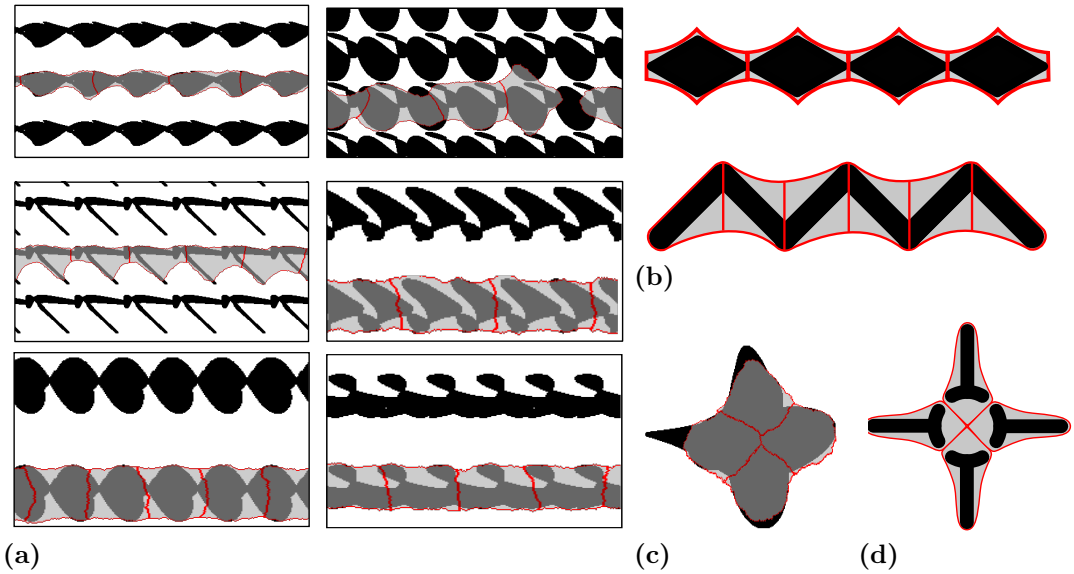

Figure 5.12. (a) Optimal networks for cell normalization predicted by the GA for square lattices. One point crossover (5.5) with adaptive Gaussian mutation (5.21) was used ($\sigma_m = 0.01$). The GA transforms the two dimensional networks into lines with nonadhesive areas stabilizing the cell-cell junctions. (b) Proposed layouts derived from the previous figure with expected cell shapes on them. (c) Predicted layout for isolated island with four cells. (d) Proposed layout derived from the previous figure with expected cell shape. The non continuously adhesive contour is expected to stabilize the cell junctions

between the cells similar to the stabilization of cells on [H] and [hourglass] patterns described previously [50]. This suggests that layouts as shown in Figure 5.12b are ideal to normalize cells. The arrangement of several [diamond] and [L] shapes into lines provide sufficient adhesive area for the cells to spread. The tension acting in the junctions contracts them with minimal junction extension possible only above nonadhesive areas. Extending the junction requires energy if interpreted in the CPM picture and cell continue to stay in their minimal energy configuration. In addition, polymerizing actin partially lacks the support of the substrate to push against the junction on [L] or is inhibited by contact inhibition.

To force a two-dimensional topology square lattice networks made from units cells with four fold symmetry as shown in Figure 5.11b can be used. But the GA is not able to find any layouts with notable normalization. Also, for networks with an hexagonal lattice no normalization is achieved. Cells spread and migrate very irregular on these networks similar to the ones shown in Figure A.12a. It seems that the two dimensional networks give the cells too many possibilities to interact. They also allow cell sheets to be formed which are suppressed in a one dimensional geometry.

Patterns described by arcs and arranged into a lattice also show no appreciable level of cell normalization. However, when the requirement of a network is dropped and isolated island for several cells are optimized star shaped structures as shown in

Figure 5.12c are predicted. These cells can rotate but by disrupting the continuously adhesive contour as shown in Figure 5.12d it may be possible to stop the rotation and stabilize the cells.

In summary, only one dimensional arrangements provide normalization to cells. It is not known if normalization on networks is not possible in principle or if the GA fails to predict good layouts. The same parameter for the GA were used to optimize cell migration and network layout because the parameters performed well for the migration optimization. For the networks the optimal parameter set might be different but the parameters are difficult to explore because of the increased computational complexity here.

5.6. Conclusion

This chapter introduced Genetic algorithms (GA) as a general tool to optimize micropattern layouts. GA where chosen because they do not require knowledge about the optimization landscape and they are considered robust under noise. The principle of the algorithm with different selection, crossover and mutation operators was introduced in the first part. Special emphasis was put on how to generate and encode patterns. Two complementary approaches were chosen. Arc shaped structures are best to represent letter shaped patterns and Fourier descriptors can represent more spread out shapes. Fourier descriptors also easily allow to generate patterns with mirror or rotational symmetry and concave shapes can be forced by adjusting the ratio of the axis of the first and second ellipse.

To study the algorithm, is was used to find the optimal pattern which generates a given cell shape. This task can be easily solved manually with some background about cell shapes. Nevertheless, insights about the different crossover and mutation operator are gained from it and parameters can be varied systematically because the fitness function for this task allows fast evaluation. It also gives insights on how to compare shapes. Direct pixel mismatch measures (5.22) and moment based measures (5.24) were found to perform poorly compared to Fourier descriptor based measures (5.25). Good understanding of the shape matching methods is important because it forms the basis for the shape comparison of cells in network simulations.

Bias of cell migration by micropatterns was chosen as a second system to be optimized by the algorithm. It has been investigated to a large extend experimentally [45–47] and symmetric triangular ratchets where found to bias migration [45, 46]. Optimal patterns predicted by the GA are also triangular for patterns represent by arcs and Fourier descriptors. However, the triangles are asymmetric which is thought to generate less possibilities for deviations from the bias direction as the symmetric case. An improvement of the bias by a change from a symmetric to asymmetric layout would be difficult to predict without the help of an optimization algorithm. For this problem, the GA also converged withing 30 iteration steps (compare Figure 5.8) revealing its true potential. However, the benefit of asymmetric triangles still need experimental verification.

The asymmetric shape of the patterns reminds of transport by a Brownian ratchet [176]. But the cells here are not subjected to a periodically switching or moving potential driving the transport. Instead, the cells move similar to active Brownian particles described by the velocity alignment mechanism (4.5) in a potential set by the pattern geometry. Depending on the movement direction the potential has different slopes. Active Brownian particles have been demonstrated before to move in asymmetric potential [177–179] and the simplicity of the velocity alignment mechanism should allow further analytical or numerical analysis of how the bias benefits from asymmetric triangles.

In the last part of this chapter optimal network designed was addressed. Here, all of the components introduced in the previous chapter come together to describe cell movement on networks. Namely, cell shape prediction, cell division, cell-cell adhesion and cell migration. The GA only partly succeeded by predicting line patterns as optimal solution for cell normalization. It failed when a two-dimensional network was enforced to find layouts which normalize all cells. At this point it is not clear if cell normalization is not possible in two-dimensional geometries or if the algorithm fails to predict it. However, the line patterns predicted might be a good alternative to networks.

The GA turns out to be a powerful tool to design pattern but it needs to be adjusted to the problems. The three optimization tasks described in this chapter were not the only ones investigated. Fitting of a function, shape matching of patterns without cells and complete coverage of a pattern by a path with minimal path self-intersection was also investigated. The optimal crossover, mutation method and strength depend on the specific problem and need to be adjusted which can take a considerable amount of time. The failure of the algorithm with respect to network optimization might by due to badly tuned parameters. A starting point for improvement could be the strongly nonlinear fitness measure (5.30) which induces a strong selective pressure. For the migration bias optimization a linear fitness (5.28) was used which performed well and the same might work for the network design.

6 Summary and Outlook

The objective of this thesis was to develop versatile model for cell dynamics on micropatterned substrates. Apart from improving our physical understanding of cell dynamics on micropatterns, this model also provides a method to design micropattern layouts.

Micropatterns and their normalization effect where introduced in the first chapter along basic principles of cell mechanics. The idea of networks of micropatterns to allow cell normalization during several cell cycles was put forward.

The second chapter introduced the well established cellular Potts model (CPM) to describe cells on micropatterns. It has the advantage of combining cell dynamics with shape predictions and is simple to implement. The classical CPM [82, 83] has a phenomenological Hamiltonian motivated by the differential adhesion hypothesis [127]. As a multicellular model it has received little attention [72, 85, 86] on how well it describes isolated cells. Cells are highly contractile which should be reflected by the model describing them. We revised the formulating of the CPM starting from a single contracting cell on a micropattern [3]. This bottom up approach revealed that the multicellular Hamiltonian of the classical CPM requires several changes to describe single cells correctly. I.e., the unconstrained cell area and edge bundles both motivated by the simple-tension model [15]. Our careful biological motivation allowed us to interpret terms appearing in the CPM Hamiltonian as traction forces and to predict them. The good agreement of predicted forces with experiments on micropatterns [36] not only showed the mechanical correctness of our model, but also allowed to fit its parameters to specific cells. Cell shapes and traction forces on arbitrary patterns can be predicted by it. It offers many possibilities for future studies, e.g. how patterns influence the prominent force direction of cells [56].

Our contour based approach would also allow to predict traction forces from cell shapes alone. Several images of cells need to by averaged to obtain a mean shape for this.

The third chapter extended our model to multicellular systems. The first part introduced a mapping of the cell contour defined by micropatterns to an ellipse to predict the cell division plane. Our approach of implementing the mapping directly with the CPM dynamics is very similar to the actual biological process of cells becoming spherical before division. It allows to predict the division plane of cells on arbitrary geometries. In contrast to a previous approach [38] we only require one parameter for all geometries to obtain good agreements with experiments. In future studies traction force and division plane predictions can be combined which is of special interest as cells have been found to divide preferentially perpendicular to the direction of sustained tension and forces act as memory of cell shape [135].

The second part of the third chapter addressed the mechanism behind cell-cell adhesion. The classical CPM [82, 83] motivated by the differential adhesion hypothesis described cell-cell adhesion in analogy to surface tension in liquids. For systems consisting of only a few cells the analogy of cells and molecules of a liquid breaks down. Cell-cell adhesion had to be revised to work for the reduced cell density encountered on micropatterns. Discrete cadherin bonds were introduced mediating the adhesion. This allows to control adhesion strength and cell-cell junction contractility independently. Our model in combination with the shape of cells pairs on concave patterns can give further insights into how tensions are generated and balanced at cell-cell contacts above nonadhesive areas. E.g. by measuring the angle at which the free boundaries of two cells join to form a common junction.

Cell migration on micropatterns was addressed in the fourth chapter. Cell locomotion is driven by actin and myosin generated forces applied to the cell membrane and is a complicated and highly dynamic process [27]. We simplified it by prescribing a force applied to the cell contour based on actin and myosin densities. Varying the distribution of the force allowed us to predict the shape of various migrating cell types. To set the long time movement direction we used a velocity alignment model which has the simple interpretation of the cell integrating over its past movement to set its current direction. The good agreement of our model for cell pairs performing rotational migration on micropatterns [50] was shown for a wide range of patterns. The same cell type type as for the traction force measurements in the second chapter was used here and parameters agreed well except for the surface tension which had to be reduced for migrating cell pairs. It was also demonstrated that the cell-cell adhesion mechanism introduced in the second chapter is necessary to achieve agreement with experiments.

The simplicity of our migration implementation might allow to predict cell movement to some extend analytically when cells are considered to perform a persistent random walk in an energy landscape defined by the pattern geometry. However, the cell shape influences the locomotion in our approach which might lead to feedback effects. E.g. cells become faster on narrower tracks.

Traction force measurements, cell division and migration of cell pairs has only be investigated on symmetric micropatterns. Our model is not limited by the geometry and can predict all of these quantities on asymmetric patterns. One application would be to study how how asymmetry can bias rotational motion of cell pairs into one

direction.

The last chapter addressed pattern layout optimization. We used a genetic algorithm because it is considered robust under noise and does not require knowledge about the optimization landscape. The model developed in the previous chapters was used in the genetic algorithm to evaluate how well pattern layouts perform for example with respect to cell normalization or how they bias cell migration. Two complementary methods to encode patterns were introduced. Arc shapes are best to encode letter shaped patterns while shapes encoded by Fourier descriptors are more spread out and can be made symmetric or concave easily.

We were able to predict geometries with the genetic algorithm which are thought to bias cell migration stronger into one direction as existing ratchet patterns [46]. To normalize cell shape after multiple divisions the algorithm predicted one dimensional line layouts with undulations. The absence of adhesive surface beneath cell-cell junctions is thought to stabilize cells there.

A total of nine parameters had to be used to model cell behavior on micropatterned substrates. One of them, the cell area is well known. The adhesive energy density is found to have little influence leaving seven relevant parameters. The tension related parameters where set by the traction force measurements [3]. The parameters related to cell-cell adhesion and migration where set by the persistent rotational motion of cells on various pattern [36]. All parameters were motivated rigorously from biological principles and for the complex behavior the model is able to describe the parameter set can be considered small.

In summary, the balancing act of creating a versatile model describing many aspects of cells on micropatterns and keeping the number of parameters low and motivated worked out well.

A Appendix

A.1. The Cellular Potts Model

A.1.1. Radius Spanning Distance Relation with Area Constraint

Many cellular Potts models (CPM) [82, 83, 85] or vertex models [73, 84, 87] for cells in tissue use an elastic (harmonic) constraint for the cell area or volume in combination with a simple line tension mediating cell-cell interaction. In addition, some models also include an elastic line tension [73, 84]. For a single cell the simplest energy functional combines a simple line tension with the elastic area constraint.

$$E = \lambda_s l + k(A - A_0)^2, \tag{A.1}$$

where the first term accounts for the simple line tension λ_s which scales with the cell perimeter l and the second term describes the area elasticity with elastic coefficient k and target area A_0.

As in the tension-elasticity model (TEM), the dependence of the arc radius R on the spanning distance d can be found by a force balance. First we define surface tension $\sigma = \partial E/\partial A$ and line tension $\lambda_s = \partial E/\partial l$. The surface tension pulls inwards perpendicular to the contour and the line tension exerts a force depending on the curvature of the contour. The force balance then reads

$$\sigma \mathbf{n} = \lambda_s \frac{\mathrm{d}\mathbf{t}}{\mathrm{d}l} = \lambda_s \frac{1}{R}\mathbf{n}, \tag{A.2}$$

where the contour is parameterized by its length l, and $\mathbf{n}$ and $\mathbf{t}$ are the normal and the tangent to the contour, respectively. Calculating the derivative of equation (A.1), equation (A.2) becomes

$$2R(A - A_0) - \frac{\lambda_s}{k} = 0. \tag{A.3}$$

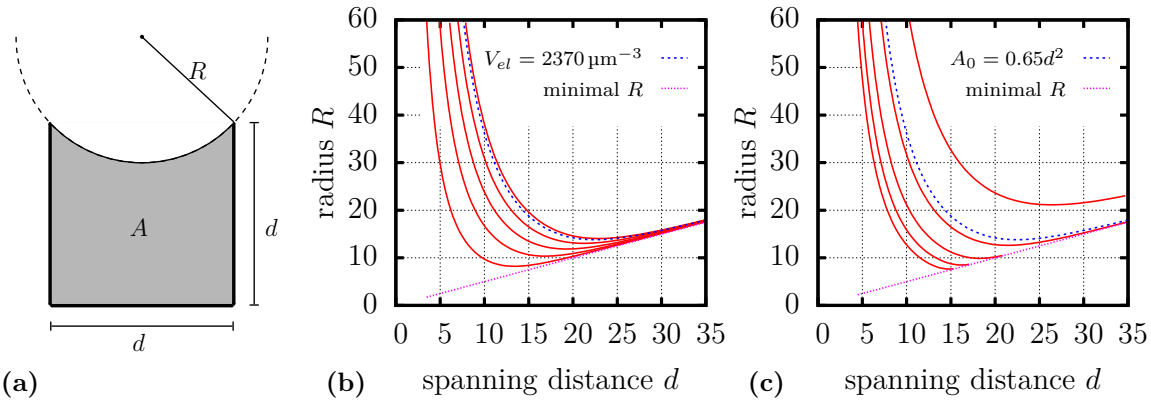

Figure A.1. (a) Cell with area A confined to a U-shaped micropattern with a single circular arc. (b) $R(d)$ dependence calculated from equation (A.4) with $V_{el} = \lambda_s/k$ increasing from $500\,\mu m^{-3}$ (bottom curve) to $2500\,\mu m^{-3}$ (top curve) and a target area of $A_0 = 0.65d^2$. (c) $R(d)$ dependence for a target area increasing from $A_0 = 0$ (bottom curve) to $A_0 = 0.8d^2$ (top curve) and $V_{el} = 2370\,\mu m^{-3}$. The blue dashed curves are the same in both figures with $V_{el} = 2370\,\mu m^{-3}$ and $A_0 = 0.65d^2$ both taken from [85].

This shows that the cell area A and the arc radius R are not independent of each other. In contrast to the TEM or simple-tension model (STM), the arc radius now is not controlled locally, but depends on the overall cell shape. Area changes at one end of the cell can influence the arc radius at the other end. For a cell on a U-shaped micropattern as depicted in Figure A.1a, the implicit equation for the arc radius is found from equation (A.3) as

$$2R\left(\frac{d}{4}\sqrt{4R^2 - d^2} - R^2 \arcsin\left(\frac{1}{2}\frac{d}{R}\right) + dy - A_0\right) - \frac{\lambda_s}{k} = 0. \tag{A.4}$$

As in the TEM the arc radius depends on the spanning distance d, but in addition also the height y of the U-shaped pattern influences the radius. In the following only the case of quadratic shapes with $y = d$ is considered.

There are two modes of controlling the cell shape, either by changing the target area A_0 or by changing the ratio of simple tension and the strength of the area constraint $V_{el} = \lambda_s/k$. Figure A.1b shows $R(d)$ for different values of $V_{el} = \lambda_s/k$. The monotonously increasing relation between arc radius and spanning distance observed in experiments [15] can be achieved by shifting V_{el} to very small values. However, this brings the radius very close to the minimal possible radius of $R = d/2$ and such strongly invaginated cells are usually not observed experimentally. In Figure A.1c the target area A_0 is changed. For small target areas equation (A.4) does not have a solution for all spanning distances and the $R(d)$ curve ends at the minimal radius condition. Cells would collapse in such geometries. Figure A.1b and A.1c also show $R(d)$ (blue curves) for parameters used previously [85]. Neither changing the strength

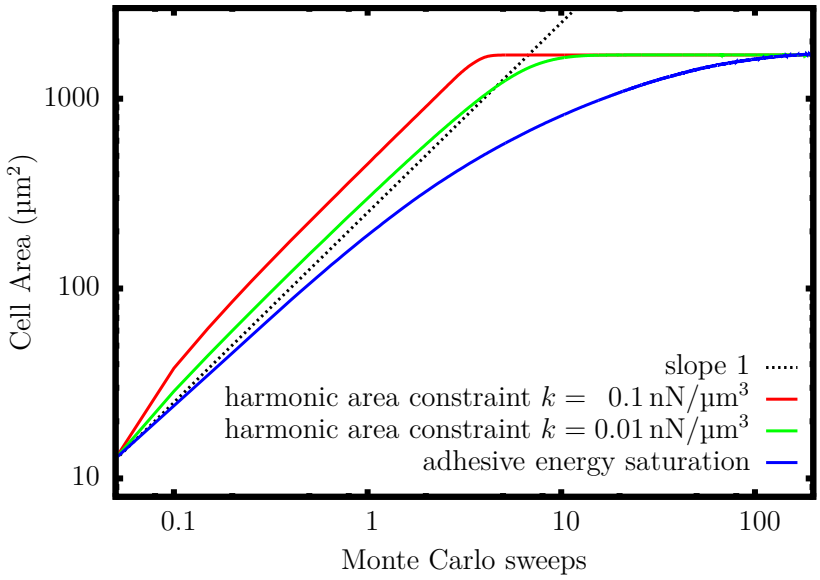

Figure A.2. Cell radius during spreading as function of Monte Carlo sweeps for an elastic area constraint (see equation (A.1)) and an saturation of the number of adhesion molecules (see equation (2) in the main text). The simulations are carried out with a simple line tension of $\lambda_s = 10\,\mathrm{nN}$, elastic rigidity as stated in the legend, target area $A_0 = 1700\,\mu\mathrm{m}^2$. For the model with saturation of adhesive energy the same parameters as for Figure 3 of the main text where used ($\sigma = 0.6\,\mathrm{nN}$, $W = 60\,\mathrm{nN}\,\mu\mathrm{m}^{-1}$, one Monte Carlo sweep consists of 2×10^4 inversion attempts).

$V_{el} = \lambda_s/k$ nor changing the target area A_0 can achieve a monotonously increasing relation between arc radius and spanning distance without yielding strongly invaginated cells. The addition of an elastic line tension as in the TEM to the energy functional (A.1) does not change this outcome.

A.1.2. Spreading Dynamics

The spreading dynamics of a cell with an elastic area constraint as in equation (A.1) and a cell with a saturation of the number of adhesion molecules as in equation 2 of the main text is expected to be different. For the former the quadratic area constraint yields a large contribution throughout the spreading process as long as cell area A and target area A_0 do not match. For the latter the energy gain from forming new adhesion contacts stays within the same order throughout the whole spreading process. This is reflected by the simulated cell area as function of Monte Carlo sweeps shown in Figure A.2. For an elastic area constraint the linear area growth stops only shortly before the target area is reached. Within the Metropolis dynamics all steps increasing the cell size are accepted due to the large contribution of the area term. The growth cannot be faster than linear since only single lattice sites are inverted during each step. In

a model where the cell spreads against a viscous force the area would initially grow stronger than linear. With a saturation of the adhesive energy the growth gradually slows down similar to what is seen in experiments [105, 112]. Reducing the strength k of the elastic area constraint makes the transition to the steady state less abrupt, but it also results in larger fluctuations around the target area.

We also note that the limitation in adhesive area used here is similar to a limitation in membrane tension. For a cell on a homogeneously adhesive substrate the cell area and adhesive area are equal $A = A_{\mathrm{ad}}$ and no actin edge bundles exist. With the adhesive energy density $W = E_0/A_{ref}$ the energy functional equation (2) of the main text becomes

$$\begin{aligned} E &= \lambda_s l + \sigma A - \frac{E_0}{A_{ref} + A} A \\ &= \lambda_s l + \sigma A - \frac{E_0}{A_{ref} + A} A - WA + WA \\ &= \lambda_s l + \underbrace{\left[\sigma + \frac{WA}{A_{ref} + A}\right]}_{\sigma'} A - WA \end{aligned} \tag{A.5}$$

where σ' now takes the role of the surface tension. It increases with the cell area which can be interpreted as an increase due to a finite amount of membrane area. Since the energy functional stays essentially the same, the spreading dynamics and the force measurements are not directly affected by the different interpretations of the energy functional.

A.1.3. Implementation

In the lattice-based CPMs a cell is represented by a set of occupied lattice sites as illustrated in Figure A.3a. Under normal conditions it is very unlikely that cells form spontaneous holes or that new part of the cell nucleate without contact to the bulk. We therefore use a modified Metropolis algorithm [83] which only allows to invert sites at the cell boundary.

The red sites in Figure A.3a are occupied by the cell and form the outermost border layer of the cell. They are surrounded by the outside layer of sites (green) not occupied by the cell but being adjacent to one of the border sites. Updates by the Metropolis algorithm only happen in these two layers. The gray lattice sites belonging to the cell bulk are passive (no holes are formed), as are the white medium sites (no nucleation away from the bulk). Occupied lattice sites can get isolated from the bulk of the cell when the cell retracts.

To define the cell boundary we use the marching square algorithm, a two-dimensional variant of the marching cube algorithm [180]. Given four lattice sites the marching square algorithm defines the orientation and length of the boundary between those four sites. To calculate the contribution of a single lattice site to the cell perimeter the occupation of its eight surrounding sites needs to be known. The marching square

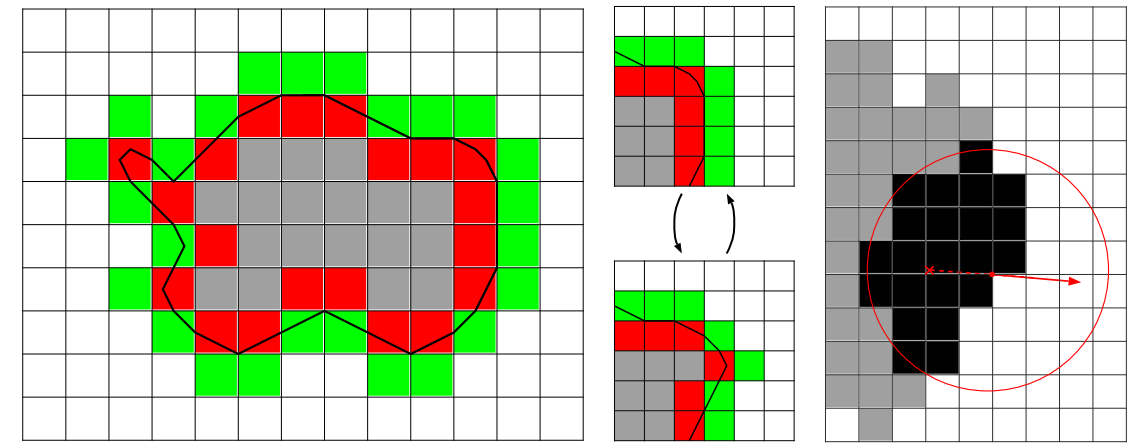

Figure A.3. Cell represented on a lattice. Sites inside the cell are gray, sites in the border layer of the cell are red and sites not being occupied by the cell but in the neighborhood of border sites are green. The cell periphery is indicated by the black line. (a) Representation of a whole cell. (b) Update of a single lattice site. (c) Circular mask applied to the cell boundary to define the normal.

algorithm allows only boundary orientations of $0°, 45°, 90°, \ldots$, which results in a high lattice anisotropy. The anisotropy can be reduced by allowing more possibilities for the boundary orientation and length by taking a larger neighborhood. Each occupied lattice sites gets a value assigned increasing with the number of occupied neighbors. A higher value pushes the boundary further away from this site. Similar methods to refine the marching square algorithm have been used in image processing [181]. We use a square of 4x4 lattice sites to define length and orientation of the boundary between the four central sites. The boundary contribution of a single site is then defined by its 24 neighbors. The resulting cell outline is shown in Figure A.3a as black line. The length of this line is used as the cell perimeter in the energy functional equation (2) of the main text. The cell area is defined by the number of occupied lattice sites.

Figure A.3b illustrates the inversion of a lattice site. A new site is added to the green outside layer in this case. The changes required by the inversion in the red border and green outside layer are stored in a lookup table which requires knowledge about the identity of the four surrounding sites. The change in circumference calculated by the refined marching square method is also stored in a lookup table requiring the occupation values of the 24 surrounding sites.

The orientation of the normal to the cell border is found by applying a circular mask to the lattice as illustrated in Figure A.3c. The vector connecting the geometrical center (cross) of the occupied lattice sites within the circle (black sites) and the circle center defines the normal direction $\mathbf{n}$ at the circle center. With this normal the boundary segments left and right of the original segment and their normal orientations

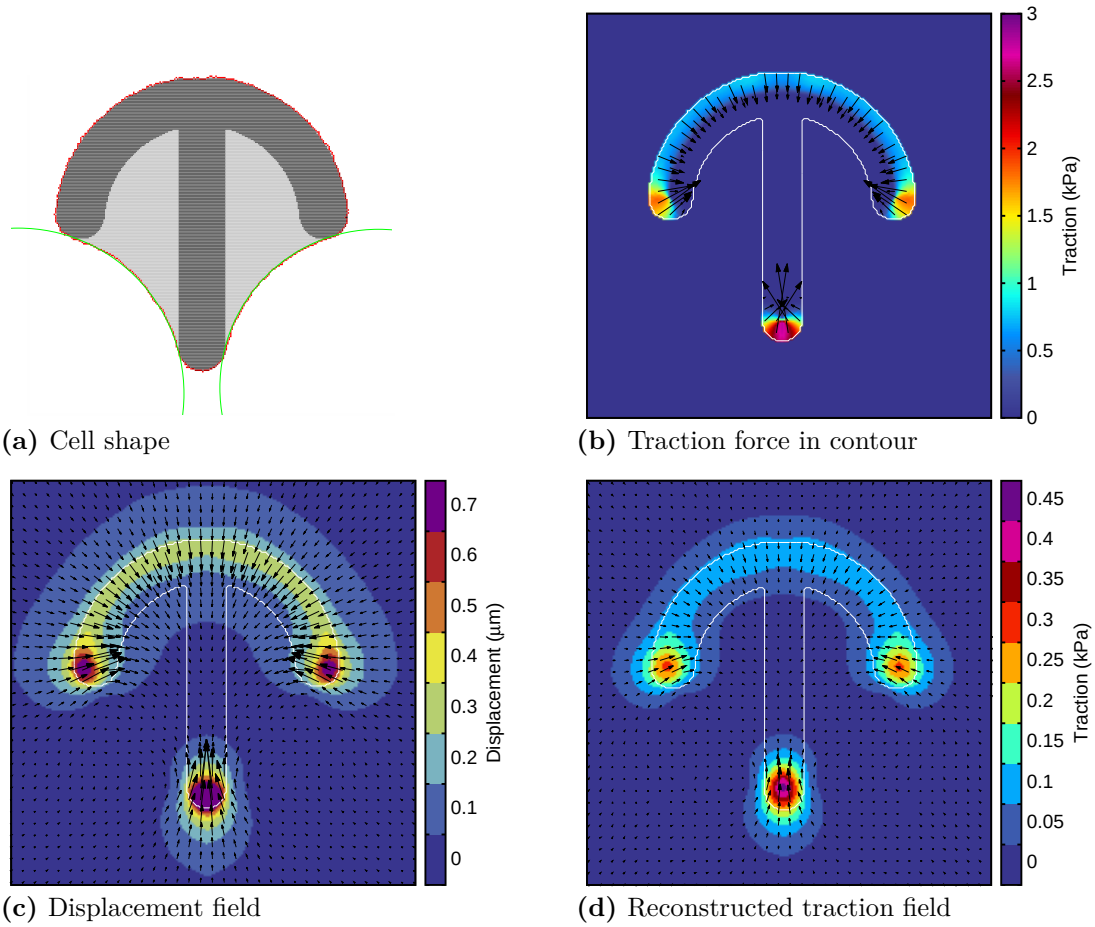

(a) Cell shape

(b) Traction force in contour

(c) Displacement field

(d) Reconstructed traction field

Figure A.4. Different stages of the reconstruction of traction forces from the CPM.

ϕ_l and ϕ_r can be identified. The curvature is then approximated by

$$\kappa = \frac{1}{2}\frac{\phi_l - \phi_r}{l}, \tag{A.6}$$

where l is the length of the boundary segment. The factor $1/2$ arises from two boundary segments sharing one kink in the boundary.

A.1.4. Reconstruction of Traction Force from Simulated Force Fields

As described in the main text, the simulated traction force is used to calculate a displacement field from which the traction can be reconstructed with the Fourier-transform traction cytometry method [54] to make it comparable to experimental results. First, the cell shape is obtained as shown in Figure A.4a. Due to the finite simulation temperature the membrane fluctuates and the traction force in the cell contour is obtained by averaging over 2×10^5 Monte Carlo sweeps. The traction force

is distributed over a 2 µm wide stripe beneath the membrane. To be more precise, we apply a disk shaped kernel with a radius of 2 µm to each lattice site distributing the forces to the surrounding sites. In combinations with a pattern-shaped kernel it is ensured that traction forces are only applied to adhesive parts of the patterns and that forces from membrane fluctuation above non-adhesive parts are propagated to the pattern. Both magnitude and vector field of the traction force are shown in Figure A.4b. Figure A.4c shows the displacement field found by our finite element method for the traction field in Figure A.4b on a substrate with Young modulus of 5 kPa. From the displacement field the traction force is reconstructed with the Fourier-transform traction cytometry method with a regularization parameter of 3×10^{-8} µm^2 /Pa^2 arriving at the final result shown in Figure A.4d. Our choice of the regularization parameter yields the same total traction before and after reconstruction.

A.2. Fourier Descriptors

Fourier descriptors (FD) are one of many feature extraction techniques [182] and a standard tool in image processing [169]. They describe shapes by a superposition of circles or ellipses which makes them ideal for shapes without sharp kinks as it is the case of cells. In addition, the possibility to suppress noise by neglecting higher order coefficients makes them ideal for biological images and they find a wide range of applications in biology [170, 171].

FD allow to construct a translation, rotation and scale invariant measure to compare shapes, therefore they a mainly applied in shape matching and recognition [172]. In combination with genetic algorithm they have been used to detect symmetry of shapes [183] which also works for shapes subjected to a parallel projection [184]. FD descriptors are usually restricted to connected shapes (which can have holes) but extension to broken shapes exist [185].

This section introduces Fourier descriptors and derives some of their properties. The Hamiltonian used to describe cells can be expressed with Fourier descriptors which allows to predict cell shapes analytically with approximations.

A.2.1. Cartesian Fourier Descriptors

Cartesian FD use a region in the complex plane to represented a shape. Given a connected shape with contour $z(s) = x(s) + \mathrm{i}y(s)$ in parameter representation with parameter $s \in [0, 1)$, the periodicity $z(s + n) = z(s),\ n \in \mathbb{Z}$ can be used to expand the contour in a Fourier series

$$z(s) = \sum_{\nu=-\infty}^{\infty} z_\nu \ \mathrm{e}^{2\pi \mathrm{i} \nu s}, \tag{A.7}$$

with coefficients

$$z_\nu = \int_0^1 z(s) \ \mathrm{e}^{-2\pi \mathrm{i} \nu s} \, \mathrm{d}s. \tag{A.8}$$

Usually a set of N sample points of a contour are known as illustrated in Figure A.5a which can be boundary pixels of an image. If the sample points are equidistant the coefficient integrals (A.8) become

$$z_\nu = \frac{1}{N} \sum_{n=0}^{N-1} z\left(\frac{n}{N}\right) \; \mathrm{e}^{-2\pi \mathrm{i} \nu \frac{n}{N}}, \tag{A.9}$$

which is a discrete Fourier transformation and can be calculated with the Fast Fourier transform. The corresponding reverse transform reads

$$z(s) = \sum_{\nu=-\frac{N}{2}}^{\frac{N}{2}-1} z_\nu \; \mathrm{e}^{2\pi \mathrm{i} \nu s}. \tag{A.10}$$

The relation $z_{-\nu} = z_{N-\nu}$ for $0 < \nu < N/2$ can be obtained from equation (A.9). Together with the Riemann Lebesgue lemma which states that $z_\nu \to 0$ for $\nu \to \infty$ it becomes apparent that coefficients with small $|\nu|$ contribute most to the expansion and the series (A.11) can be truncated at a value $N_{\max}$ [185] yielding

$$z(s) = \sum_{\nu=-N_{\max}}^{N_{\max}} z_\nu \; \mathrm{e}^{2\pi \mathrm{i} \nu s}. \tag{A.11}$$

An interpretation of the coefficients is best seen when the series is rewritten as a two dimensional function $z(s) = (x(s), y(s)$ with coefficients $z_\nu = x_\nu + \mathrm{i} y_\nu$

$$\begin{pmatrix} x(s) \\ y(s) \end{pmatrix} = \begin{pmatrix} x_0 \\ y_0 \end{pmatrix} + \sum_{\nu=1}^{N_{\max}} \begin{pmatrix} (x_\nu + x_{-\nu}) \cos(2\pi\nu s) - (y_\nu - y_{-\nu}) \sin(2\pi\nu s) \\ (y_\nu + y_{-\nu}) \cos(2\pi\nu s) + (x_\nu - x_{-\nu}) \sin(2\pi\nu s) \end{pmatrix}. \tag{A.12}$$

Each term in the sum is an ellipse and the shape is constructed from a superposition of them. Each ellipse is centered around the first zeroth-order term (x_0, y_0) and has four degrees of freedom $(x_\nu, x_{-\nu}, y_\nu, y_{-\nu})$, which correspond to the two semi-axis, the tilt and the phase of the start point as illustrated in Figure A.5b. Depending on the coefficients and order the ellipses can be cycled in negative or positive direction several times when the parameter s is increased from zero to one. The different phases for the start point of each ellipse allow to describe shapes with a non single valued contour as the crossbow pattern in Figure A.5c. Figure A.5d shows the ellipses of first (green) and second (red) order with green arrows indicating the starting phase and direction. During one circulation of the green (first order) ellipse the red (second order) is cycled two times. Hence, when $s = 1/4$ the value of the green ellipse at 90° is added to the value of the red ellipse at −90°. The superposition of all points results in the blue shape. Figure A.5e and A.5f show the same for higher orders. The red ellipses are always the new ones added to the green shapes obtained from previous superposition resulting in the blue shapes. Higher order reconstructions are shown in Figure A.5g. The changes from $N_{\max} = 15$ to $N_{\max} = 20$ are barely noticeable, and higher orders will only change the kinks at the intersection of the curved arc and straight line of the

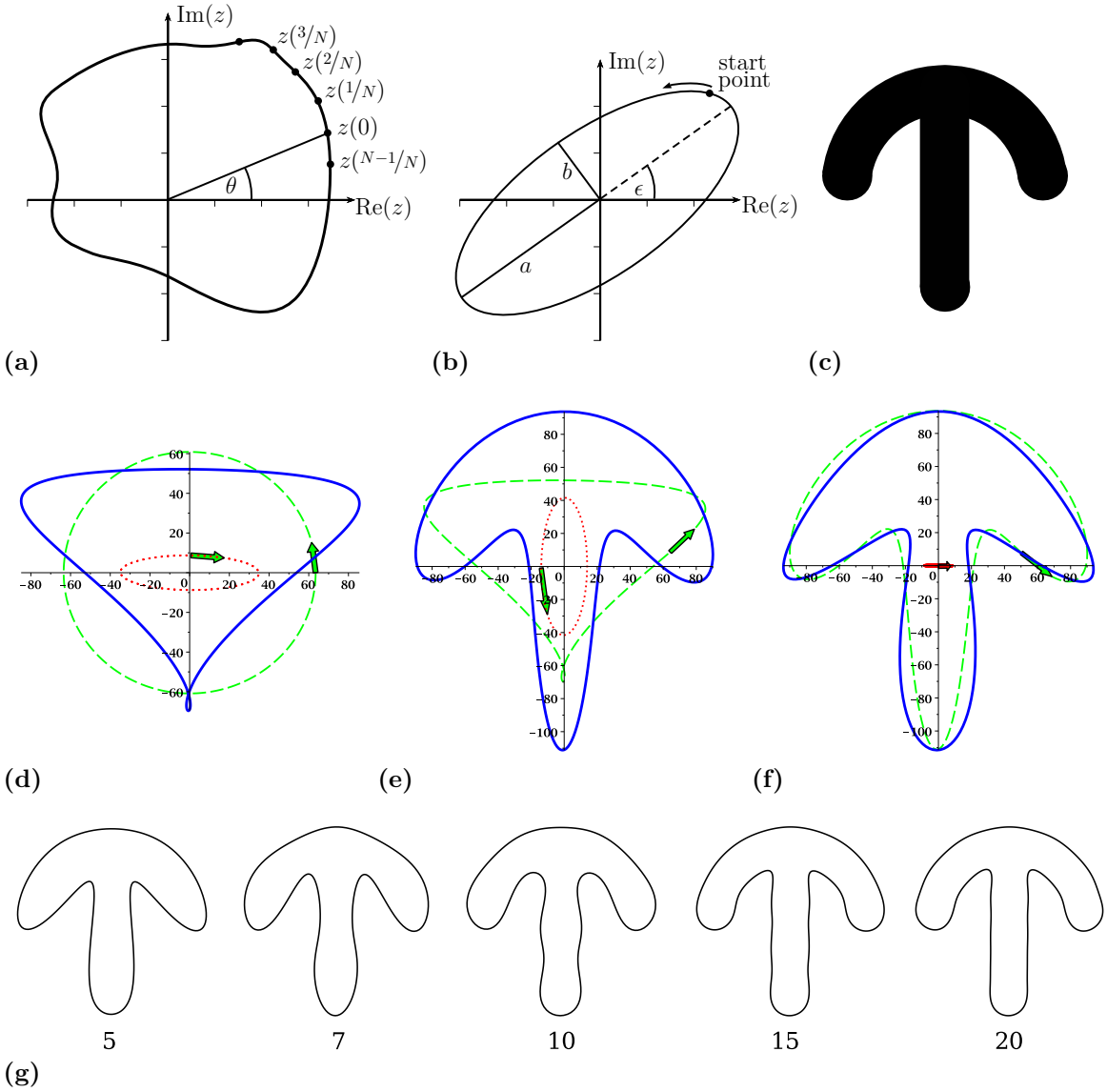

Figure A.5. (a) Two dimensional shape in the complex plane with equidistant sample points. (b) Ellipse with four degrees of freedom, the semi-axis a, b, tilt ϵ and phase of the start point. (c) Crossbow pattern as example for a non single valued contour. (d), (e), (f) Superposition of the first orders of the crossbow pattern. The green dashed line is always the current lowest order shape and the red dotted the next ellipse to be added resulting in the blue solid shape. Arrows indicate the phase and direction of each ellipse. The blue shapes correspond to (d) $N_{\max} = 2$, (e) $N_{\max} = 3$ and (f) $N_{\max} = 4$ in equation (A.11). (g) Higher order reconstructions from equation (A.11). The values of $N_{\max}$ are indicated below the shapes.

crossbow.

From equation (A.12) it also becomes clear that higher order terms are strongly fluctuating which makes FD ideal to study cell shapes since membrane fluctuations or noisy image data can be suppressed be neglecting higher order terms. The inability of Fourier Descriptors to represent shapes with sharp kinks is also not important because kinks do not appear in cells due to the line tension and also pattern shapes have no sharp kinks due to the manufacturing process.

For images, sample points of the contour are usually boundary pixels and not equidistant depending on the neighborhood used. For an 8-neighborhood steps between neighbouring sample points are 1 and $\sqrt{2}$. Equation (A.9) can still be used as illustrated in Figure A.5g where hardly any difference between the reconstructed and original shape can be observed, although the sample points where not generated equidistant in this case.

A generalization of the coefficients (A.9) where s is an arbitrary parameter and not proportional to the contour length can be achieved by writing the integral (A.8) as the corresponding Riemann sum for a discrete transformation. One has to keep in mind that s is not proportional to the arc length in general, e.g. when coefficients are obtained from minimizing an Hamiltonian the resulting function $z(s)$ calculated with equation (A.7) is not parametrized by contour length in general.

Ellipse Properties

The semi-axis of the ellipse shown in Figure A.5b belonging to the coefficient pair $(z_\nu, z_{-\nu})$ are $a_\nu = |z_\nu| + |z_{-\nu}|$ for the major axis and $b_\nu = ||z_\nu| - |z_{-\nu}||$ for the minor. The tilt of the ellipse is $\epsilon_\nu = (\varphi_\nu + \varphi_{-\nu})/2$ where $\varphi_\nu = \mathrm{Arg}(z_\nu)$ [172]. The initial phase is $\mathrm{Arg}(z_\nu + z_{-\nu})$.

Translation, Scaling, Rotation and Phase Shift

From equation (A.12) it can be seen that the ellipses are centered around z_0. Hence, changing this coefficients translates the whole shape. It is important to note that z_0 is not the geometric center of a shape in general. Scaling of a shape is achieved by multiplying each coefficient by the same number. In a similar way a shape is rotated by an angle α when all coefficients are multiplied by $\exp(\mathrm{i}\alpha)$. The initial phase of the shape can be changed by multiplying all coefficients with $\exp(\mathrm{i}\alpha\nu)$, where ν is the order of the corresponding coefficient and α the phase shift [169, 185]. Translation, Scaling and Rotation can be used to define a invariant measure under these transformations when shapes are compared [172]. E.g. since rotation is only a phase shift a measure which compares absolute values of coefficients is already invariant under rotation.

Symmetry

For mirror symmetry with respect to the x-axis and starting point on the x-axis it holds that $z(s) = \overline{z}(-s)$, where the bar denotes the complex conjugate. From equation (A.11) one can see that this requires real valued coefficients z_ν. In the same way

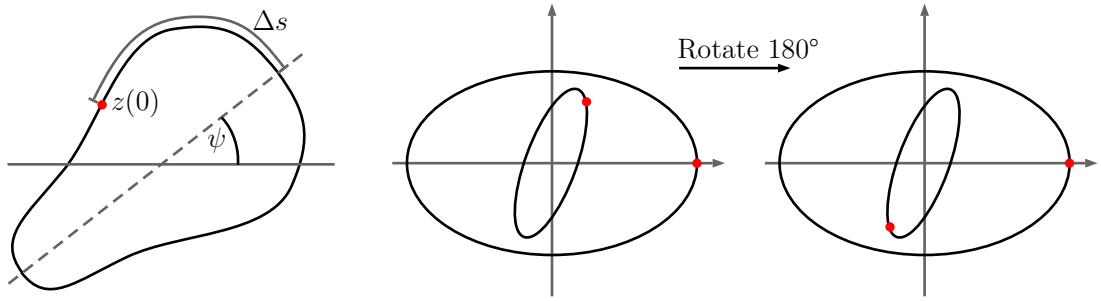

(a) (b)

Figure A.6. (a) Mirror symmetry with respect to the dashed axis. The start point indicated by the red dot is shifted by Δs from the symmetry axis. (b) First and second order ellipse with their corresponding start points (red dots). Rotation by 180° and normalization of the start point of the first ellipse leaves the first start point unchanged. The phase of the second start point in both configurations can be used to remove the ambiguity in the orientation of the first ellipse.

shapes with mirror symmetry to the y-axis and starting point on the y-axis must fulfill $z(s) = -\overline{z}(-s)$ which holds for imaginary z_ν. In the general case with the symmetry axis rotated by ψ and a shift of the starting point by Δs from the symmetry axis (see Figure A.6a) the contour fulfills $z(s - \Delta s)\exp(-\mathrm{i}\psi) = \overline{z(-s - \Delta s)\exp(-\mathrm{i}\psi)}$ and the symmetry condition for the coefficients $z_\nu = x_\nu + \mathrm{i}y_\nu$ reads

$$y_\nu = x_\nu \tan(2\pi\nu\Delta s + \psi). \tag{A.13}$$

For shapes with rotational symmetry certain coefficients need to be zero. If the shape has a m-fold rotational symmetry only the coefficients with $z_{1\pm\nu m}$ do not vanish. E.g. for a square with four-fold symmetry all but $z_1, z_5, z_{-4}, z_9, \ldots$ are zero [169].

Normalization

Shapes taken from experiments or simulation have a fluctuating boundary because of the finite image resolution and noise or the finite simulation temperature, respectively. In order to suppress noise and fluctuations or to get the averaged shape of several cells sitting on the same type of pattern the FD need to be averaged. To do so, first the cycle direction needs to be normalized. The shape is cycled in positive direction if $|z_\nu| > |z_{-\nu}|$. If this is not the case positive and negative coefficients are swapped. In a second step the start point needs to be normalized by shifting the overall phase to the phase φ_1 of z_1 which means multiplying all coefficients by $\exp(-\mathrm{i}\nu\varphi_1)$. This renders all but the first coefficient rotation invariant [169].

Coefficients normalized in this way are sufficient to average shapes of cells which sit on patterns with the same orientation or of migrating cells as long as the persistence direction does not change. In both cases the first coefficient stays the same as the cells do not rotate.

To average shapes with different orientations, e.g. cells migrating in different directions also the first coefficient needs to be normalized. This can be done by rotating the overall shape by the orientation of the first ellipse $\epsilon_1 = (\varphi_1 + \varphi_{-1})/2$ [172]. Because it is an ellipse, the rotation angle ϵ_1 has an ambiguity of π which can be removed by comparing the start point of the first and second order ellipse as demonstrated in Figure A.6b. If the shape is rotated by π and the start point of the first coefficient is normalized the angle between the start points changes and the π ambiguity can be removed by taking the configuration with the smaller angle. This works because normalization of the start point of the first coefficient means shifting it by π which leaves the start point of the second ellipse unchanged since it is shifted by 2π. One has to be very careful applying this method because it is not stable for shapes where the first ellipse is almost circular. Normalizing circle orientation and start point as described in the first part are sufficient for most applications.

A.2.2. Polar Fourier Descriptors

A contour $r(\theta)$ given in polar coordinates can be expanded in polar Fourier Descriptors. Here, the contour is parametrized by the polar angle θ and the series for a contour with N sample points reads

$$r(\theta) = \sum_{\nu=-\frac{N}{2}}^{\frac{N}{2}-1} r_\nu \, \mathrm{e}^{\mathrm{i}\theta}. \tag{A.14}$$

The polar Fourier coefficients r_ν are given by

$$r_\nu = \frac{1}{N} \sum_{n=0}^{N-1} r\left(\frac{n}{N}\right) \, \mathrm{e}^{-2\pi \mathrm{i} \nu \frac{n}{N}}, \tag{A.15}$$

where the sample points $r(n/N)$ are real valued. As with the Cartesian descriptors the coefficients fulfill $r_{-\nu} = r_{N-\nu}$ and the series (A.14) can be truncated at a value $N_{\max}$.

Polar descriptors allow only to represent single valued shapes which is sufficient to describe cell in most cases but e.g. a crossbow shaped pattern cannot be described. Since $r(\theta)$ needs to be a real valued function another constriction for the coefficients arises,

$$\overline{r}_\nu = r_{-\nu}. \tag{A.16}$$

This condition allows to rewrite the series (A.14) to allow interpretation. With $r_\nu = x_\nu + \mathrm{i} y_\nu$ it becomes

$$r(\theta) = r_0 + \sum_{\nu=1}^{N_{\max}} x_\nu \cos(\nu\theta) - y_\nu \sin(\nu\theta). \tag{A.17}$$

r_0 is the mean radius of the shape and each subsequent order adds a polar rose to the previous shape. In contrast to equation (A.12) each rose has only two degrees of

freedom which reflects the restriction to single valued contours again. In addition, the center of a shape is not related to the zero order coefficient any more and translation of the shape is not as simple as in the Cartesian case.

Rotation of a shape by an angle α corresponds to a shift of the polar angle θ which means multiplying each coefficient by $\exp(\mathrm{i}\nu\alpha)$. For symmetry to an axis with orientation ψ it must hold that $r(\theta - \psi) = r(-\theta - \psi)$ resulting in the condition $r_\nu = r_{-\nu}\exp(\mathrm{i}\nu 2\psi)$. Together with equation (A.16) the condition on the coefficients $r_\nu = x_\nu + \mathrm{i}y_\nu$ reads

$$y_\nu = x_\nu \tan(\nu\psi). \tag{A.18}$$

For symmetry with respect to the x-axis it must hold that $r_\nu \in \mathbb{R}$.

A.2.3. Cell Hamiltonian with Fourier Descriptors

Cells on homogeneously adhesive substrates have no edge bundles and the Hamiltonian consists only of area and perimeter term and in case of migrating cells a persistence movement contribution. All of these terms can be expressed with Fourier Descriptors using

$$\int_0^{2\pi} \mathrm{e}^{\mathrm{i}k\theta} = 2\pi\delta_{k,0}. \tag{A.19}$$

Area

For polar Fourier descriptors (A.14) the area is given by

$$\begin{aligned} A &= \int_0^{2\pi}\int_0^{r(\theta)} \tilde{r}\,\mathrm{d}\tilde{r}\,\mathrm{d}\theta \\ &= \frac{1}{2}\int_0^{2\pi} \sum_k \sum_l r_k r_l\,\mathrm{e}^{\mathrm{i}(k+l)\theta}\,\mathrm{d}\theta \\ &= \pi \sum_k r_k r_{-k} = \pi \sum_{k=-N_{\max}}^{N_{\max}} |r_k|^2 \end{aligned} \tag{A.20}$$

where equation (A.16) and (A.19) were used. For the the calculation with Cartesian descriptors the area integral needs to be transformed into an contour integral. This can be done either by Greens Theorem or by using polar coordinates where the polar angle is the argument of $z(s) = x(s) + \mathrm{i}y(s)$. For polar coordinates the substitution of the parameter s by θ is

$$\theta(s) = 2\arctan\frac{y}{\sqrt{x^2+y^2}+x} \qquad \frac{\mathrm{d}\theta}{\mathrm{d}s} = \frac{\dot{y}x - y\dot{x}}{2\,|z|^2}. \tag{A.21}$$

With $\Im$ denoting the imaginary part and a dot the derivative with respect to s the area becomes

$$\begin{aligned} A &= \iint \mathrm{d}A = \Im\frac{1}{2}\int_0^1 \overline{z}\dot{z}\,\mathrm{d}s \\ &= \Im\frac{1}{2}\int_0^1 \sum_k \sum_l \overline{z}_k z_l 2\pi l\mathrm{i}\,\mathrm{e}^{2\pi\mathrm{i}(l-k)s}\,\mathrm{d}s \\ &= \pi \sum_{k=-N_{\max}}^{N_{\max}} |z_k|^2\, k, \end{aligned} \tag{A.22}$$

which is an oriented area. The sign depends on the direction in which the shape is circled.

Perimeter

The perimeter cannot be calculated exactly in general. The approximations used here make use of the small ratio of first (or zeroth) and subsequent coefficients. For shapes where the contour intersects itself (see e.g. Figure A.7b) this ratio is not small anymore, but such shapes are of no interest in our case. With the abbreviation $S = \sum_l r_{-l} r_l (1+l^2)$ the perimeter in polar coordinates becomes

$$\begin{aligned} L &= \int_0^{2\pi} \sqrt{r^2 + \dot{r}^2}\,\mathrm{d}\theta \\ &= \int_0^{2\pi} \left(\sum_{m,l} r_m r_l (1 - ml)\,\mathrm{e}^{\mathrm{i}(m+l)\theta} \right)^{\frac{1}{2}} \mathrm{d}\theta \\ &= \int_0^{2\pi} \sqrt{S} \left(1 + \frac{1}{S} \sum_{m\neq l} r_m r_l (1 - ml)\,\mathrm{e}^{\mathrm{i}(m+l)\theta} \right)^{\frac{1}{2}} \mathrm{d}\theta \\ &\approx \sqrt{S}\left(2\pi + \frac{1}{2S} \underbrace{\int_0^{2\pi} \sum_{m\neq l} r_m r_l (1 - ml)\,\mathrm{e}^{\mathrm{i}(m+l)\theta}\,\mathrm{d}\theta}_{=0,\ \text{see(A.19)}} + \dots \right) \\ &= 2\pi \left(\sum_{l=-N_{\max}}^{N_{\max}} |r_l|^2 (1 + l^2) \right)^{\frac{1}{2}} \qquad \text{(A.23)} \\ &\approx \pi \left(r_0 + \frac{1}{r_0} \sum_{l=-N_{\max}}^{N_{\max}} |r_l|^2 (1 + l^2) \right) \qquad \text{(A.24)} \end{aligned}$$

The calculation for polar Fourier descriptors use the same approximation. The perimeter is

$$L = \int_0^1 |\dot{z}(s)|\,\mathrm{d}s \approx 2\pi \left(\sum_{l=-N_{\max}}^{N_{\max}} |z_l|^2\, l^2 \right)^{\frac{1}{2}}. \tag{A.25}$$

This is also the result if $|\dot{z}(s)| = L$ which is exact when s is proportional to the contour length since $L^2\,\mathrm{d}s^2 = \mathrm{d}z\overline{\mathrm{d}z}$ [186, p. 6] then. For the crossbow (width=30 µm) shown in figure A.5c the Fourier coefficients where calculated with chain code and an eight-neighborhood which means that s is not proportional to the contour length. Nevertheless equation (A.25) yields $L \approx 132.02\,\mu\mathrm{m}$ which is very close to $L = 131.17\,\mu\mathrm{m}$ calculated by evaluating the contour integral numerically.

Persistence Force

The contribution to the cell energy by the migration machinery is given by the integral

$$P = \int_0^{2\pi} \int_0^{r(\theta)} |\cos^\eta(\chi)|\,\mathrm{sign}(\cos(\chi))\tilde{r}\,\mathrm{d}\tilde{r}\,\mathrm{d}\theta, \tag{A.26}$$

where χ can either be the angle between persistence direction and connection between COM and point on membrane (graded radial force model) or the angle between normal and persistence direction (parallel force model) (compare Figure 4.4a). For the former χ can be approximated by the polar angle when origin and COM are close. For shapes described by radial FD this should hold as long as the shapes do not deviate too much from circles and have no kinks (e.g. a cardioid) but requires regularization in the shape calculations below.

To further simplify the calculation η is restricted to odd numbers, even values of η can be treated by splitting the integral (A.26). With odd η and χ equal to the polar angle as in the graded radial force model (A.26) becomes

$$\begin{aligned} P_{\mathrm{GRF},\eta} &= \frac{1}{2}\int_0^{2\pi} \cos^\eta(\theta) r^2(\theta)\,\mathrm{d}\theta \\ &= \frac{1}{2}\int_0^{2\pi} \frac{1}{2^\eta} \sum_{\nu=0}^{\eta} \binom{\eta}{\nu} \mathrm{e}^{\mathrm{i}\theta(\eta-2\nu)} \sum_{k,l} r_k r_l\,\mathrm{e}^{\mathrm{i}\theta(k+l)} \\ &= \frac{\pi}{2^\eta} \sum_{\nu=0}^{\eta} \binom{\eta}{\nu} \sum_{l=-N_{\max}}^{N_{\max}} r_{2\nu-l-\eta} r_l, \end{aligned} \tag{A.27}$$

where (A.19) was used and $r_\nu = 0$ for $|\nu| > N_{\max}$. For $\eta < 1$ the integral cannot be solved and the approximation $\cos^\eta(\theta) \to \mathrm{sign}(\pi/2 - |\theta|)$ for $\eta \to 0$ is used

$$\begin{aligned} P_{\mathrm{GRF},0} &\approx \frac{1}{2}\int_0^{2\pi} \mathrm{sign}(\pi/2 - |\theta|) r^2(\theta)\,\mathrm{d}\theta \\ &= \frac{1}{2} \sum_{k,l=-N_{\max}}^{N_{\max}} r_k r_l \frac{4\sin\left(\frac{1}{2}\pi(k+l)\right)}{k+l}. \end{aligned} \tag{A.28}$$

In the parallel force model χ is equal to the angle φ between normal and persistence direction and it is best to use Cartesian descriptors. If the contour $z(s) = x(s) + \mathrm{i}y(s)$ is parameterized with a positive circularity the outwards pointing normal is $\mathbf{n} = [\dot{y}(s), -\dot{x}(s)]$ with orientation $\varphi = \mathrm{Arg}(-\mathrm{i}\dot{\bar{z}})$ (compare Figure 4.4a). Using the tangent

half-angle formula for the argument the angle component can be rewritten as

$$\cos(\varphi) = \frac{\dot{y}}{\sqrt{\dot{x}^2 + \dot{y}^2}} \approx \frac{\dot{y}}{L}, \tag{A.29}$$

where the approximation is exact if s is proportional to the contour length (compare equation (A.25)). With restriction to odd η the integral (A.26) for the parallel force model becomes

$$P_{\mathrm{PF},\eta} = \frac{1}{2L^\eta} \Im \int_0^1 \Im(\dot{z})^\eta \overline{z} \dot{z} \, \mathrm{d}s. \tag{A.30}$$

The integral can be eliminated in the same way as for the area calculation by using equation (A.19) but each power of η introduces another summation in the result which makes this approach cumbersome.

A.2.4. Cell Shape Prediction

The cell Hamiltonian can now be written as function of Fourier coefficients which allow to minimize it when the coefficients are treated as independent variables. On a continuously adhesive substrate the adhesive energy balances the surface and line tension and the cell area is close to the target area A_0. The addition of a directional persistent tension barely changes the area. The nonlinear adhesive energy term and surface tension can be omitted from the Hamiltonian when the cell area is kept constant by a constraint during minimization. The Hamiltonian for a cell described by the graded radial force model, persistence direction along the x-axis ($r_l \in \mathbb{R}$) and odd η reads

$$\begin{aligned} H &= \lambda_s L - \mu P_{\mathrm{GRF},\eta} + \alpha R \\ &\approx \lambda_s \pi \left(r_0 + \frac{1}{r_0} \sum_l r_l^2 (1 + l^2) \right) - \mu \frac{\pi}{2^\eta} \sum_{\nu=0}^{\eta} \binom{\eta}{\nu} \sum_l r_{2\nu - l - \eta} r_l + \alpha \pi \sum_{l \neq 0} \frac{r_l^2}{|l|}, \end{aligned} \tag{A.31}$$

where equation (A.24) and (A.27) where used. The last term in the above equation is required for regularization. Without it, minimization yields shapes as depicted in Figure A.7. In case of cells described by the graded radial force model the persistence integral (A.27) can be maximized (and the Hamiltonian minimized) if $r^2(\theta) \approx 0$ for $\cos(\theta) < 0$ which is the case if $r_0 \approx r_1 > 0$. Such shapes violate the approximation that the COM is close to the coordinate origin and can be avoided by keeping r_l small for $l \neq 0$ as ensured by the regularization term.

The strength of the regularization penalty is governed by the regularization parameter α and reduces for higher order coefficients since the coefficients are expected to decrease with order. α is expected to scale with the system size given by r_0 and the strength of the directional tension μ.

To find the shape with minimal energy all partial derivatives with respect to r_k of

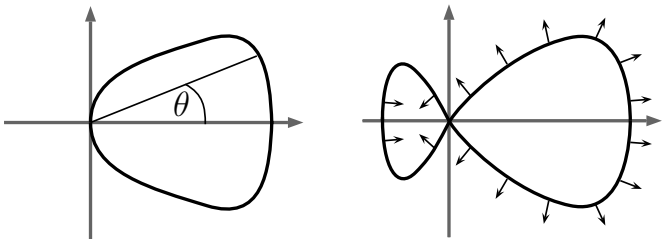

Figure A.7. (a) Cell with COM persistence described by polar Fourier Descriptors. If $r_0 \approx r_1 > 0$ and other coefficients are negligible cell shapes mainly have positive x-values with $r(\theta)^2 \cos(\theta) \gtrsim 0$ and COM displaced from the origin.(b) Cell with normal persistence described by Cartesian descriptors. For certain coefficients shapes can have intersections which changes the circularity and direction of the normals.

the Hamiltonian (A.31) must vanish

$$\frac{\partial H}{\partial r_k} = \pi r_k \left(\frac{\lambda_s}{r_0}(1+k^2) + \frac{\alpha}{|k|} \right) - \mu \frac{\pi}{2^{\eta-1}} \sum_{\nu=0}^{\eta} \binom{\eta}{\nu} r_{2\nu-k-\eta} = 0 \tag{A.32}$$

with $k = -N_{\max}, \ldots, -1, 1, \ldots, N_{\max}$. The coefficient r_0 is determined by the constraint of the area to A_0. With equation (A.21) it becomes

$$r_0 = \left(\frac{A_0}{\pi} - \sum_{l \neq 0} r_l^2 \right)^{\frac{1}{2}} \approx \sqrt{\frac{A_0}{\pi}}. \tag{A.33}$$

The last approximation means that the cell shape is dominated by the zeroth order coefficient. Using it leaves the system of equations (A.32) linear and the regularization term ensures that a minimum is found by solving it. The red dashed shapes in Figure 4.5 in the main text are the solution for $N_{\max} = 5$ and $\alpha = 0.08\,/\mu\mathrm{m} r_0 \mu$. Deviations are mainly due to the approximation of the COM by the origin of the coordinate system.

The minimization of the cell Hamiltonian of the parallel force model faces similar issues. For certain coefficients shapes can intersect themselves as depicted in Figure A.7b which changes the circularity and normal orientation. The change in normal orientation decreases the overall energy compared to a shape without intersection. Intersections also allow the cell to grow in absolute area since the area (A.22) depends on the circularity and the part of the cell located left of the y-axis has negative area in Figure A.7b. To some extend this can be compensated by regularization but in addition the system of equations which needs to be solved is not linear anymore (compare equation (A.30)) and this approach is not continued here.

A.3. Multicellular Systems

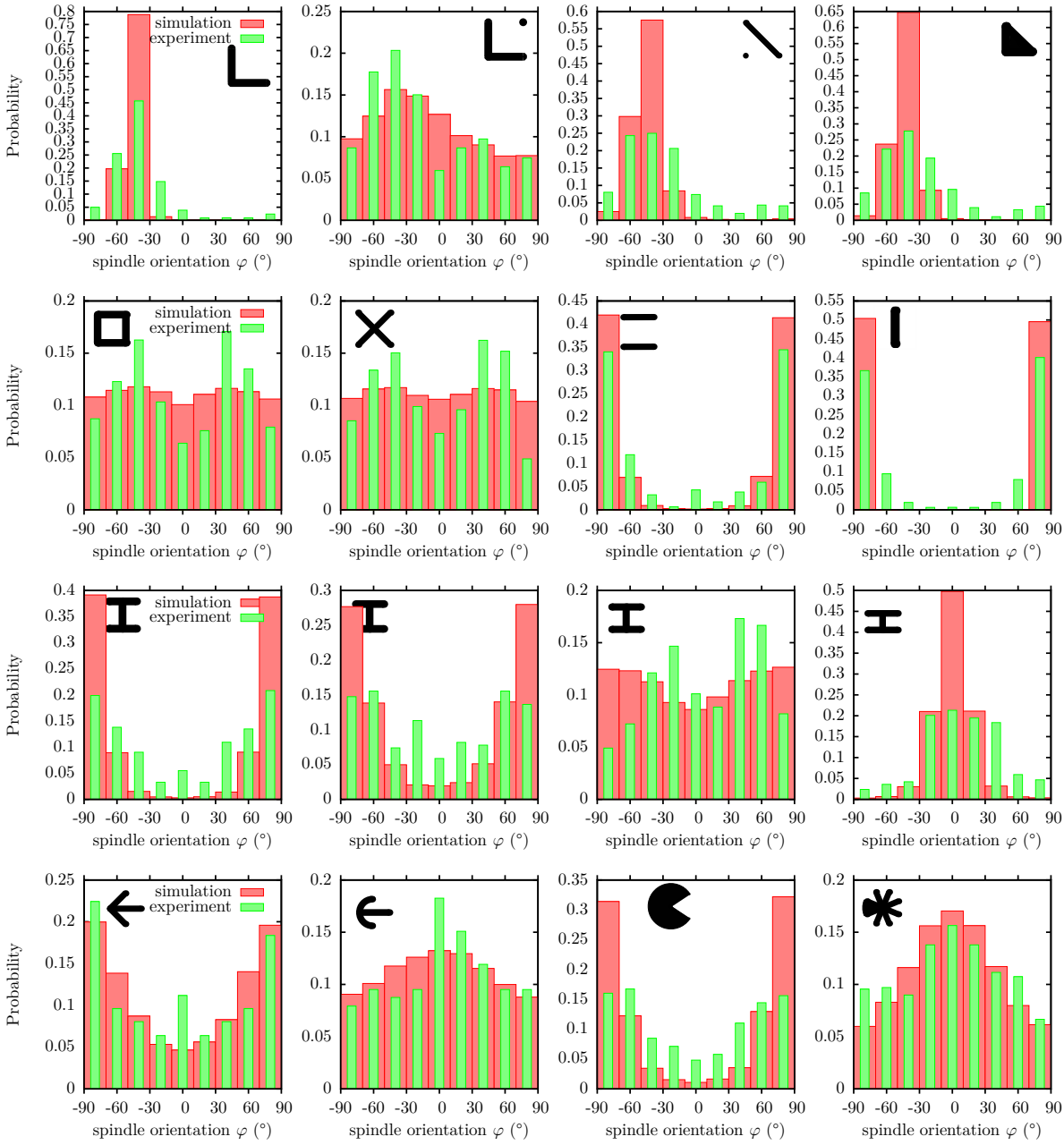

Figure A.8. Comparison of the experimental (green) taken from [38] and simulated (red) spindle orientations. The spindle orientation is orthogonal to the division plane. The simulation recorded orientations for 20000 cell divisions and where performed for a generic cell with $\sigma = 1\,\mathrm{nN\,\mu m^{-1}}$, $\lambda_s = 10\,\mathrm{nN}, EA = 50\,\mathrm{nN}$, $A_0 = 1300\,\mathrm{\mu m^2}$, $W = 20\,\mathrm{nN\,\mu m^{-1}}$. Similar to Figure 3.4 of the main text, but the ellipse is fit to the cells at an area ratio of 0.6 which results in narrower peaks for most patterns.

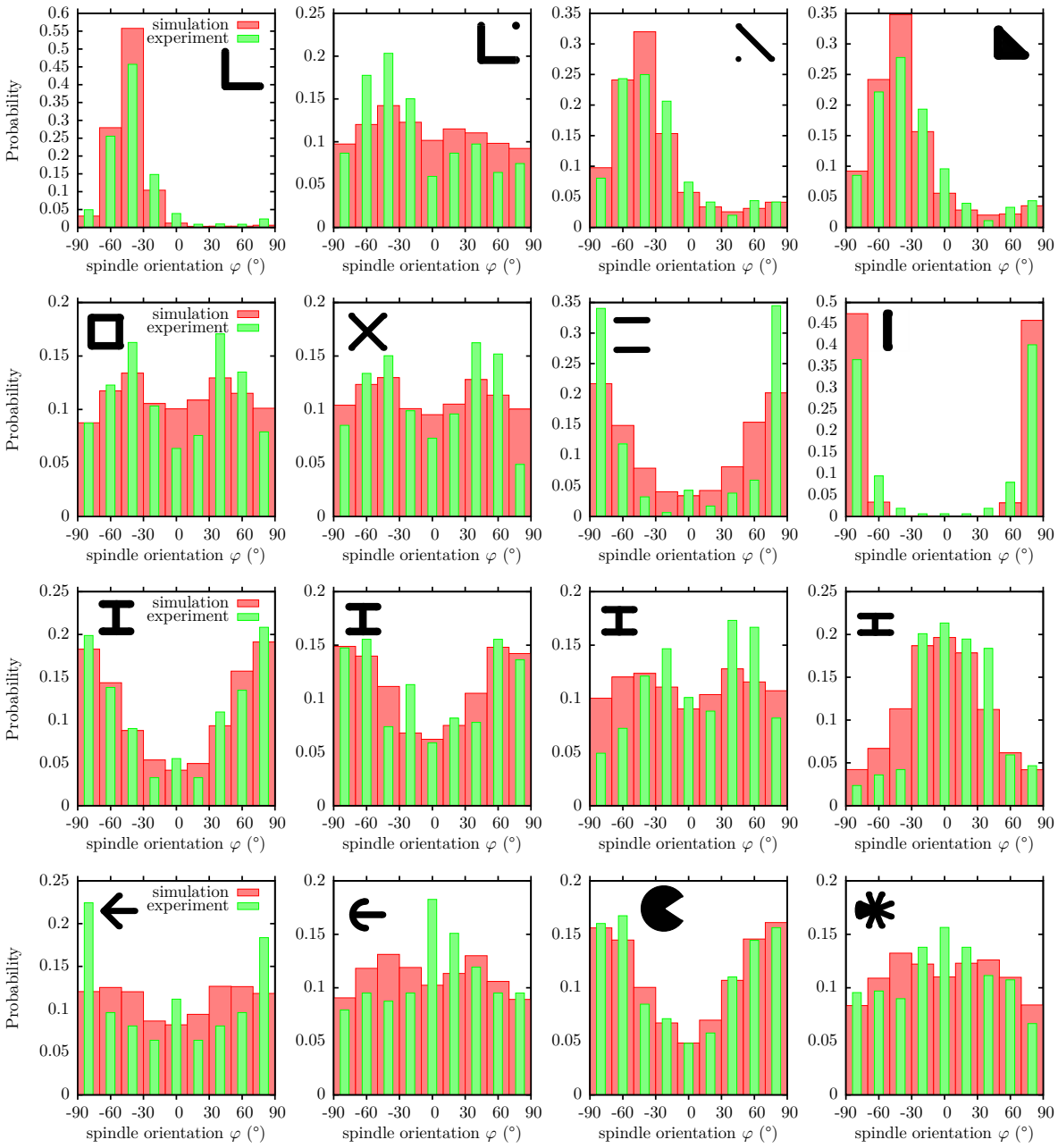

Figure A.9. Comparison of the experimental (green) taken from [38] and simulated (red) spindle orientations. The spindle orientation is orthogonal to the division plane. The simulation recorded orientations for 5000 cell divisions and where performed for a generic cell with $\sigma = 1\,\mathrm{nN\,\mu m^{-1}}$, $\lambda_s = 10\,\mathrm{nN}, EA = 50\,\mathrm{nN}$, $A_0 = 1300\,\mathrm{\mu m^2}$, $W = 20\,\mathrm{nN\,\mu m^{-1}}$. Similar to Figure 3.4 of the main text, but the ellipse is fit to the cells at an area ratio of 0.28 (optimum) and the temperature during contraction is halved.

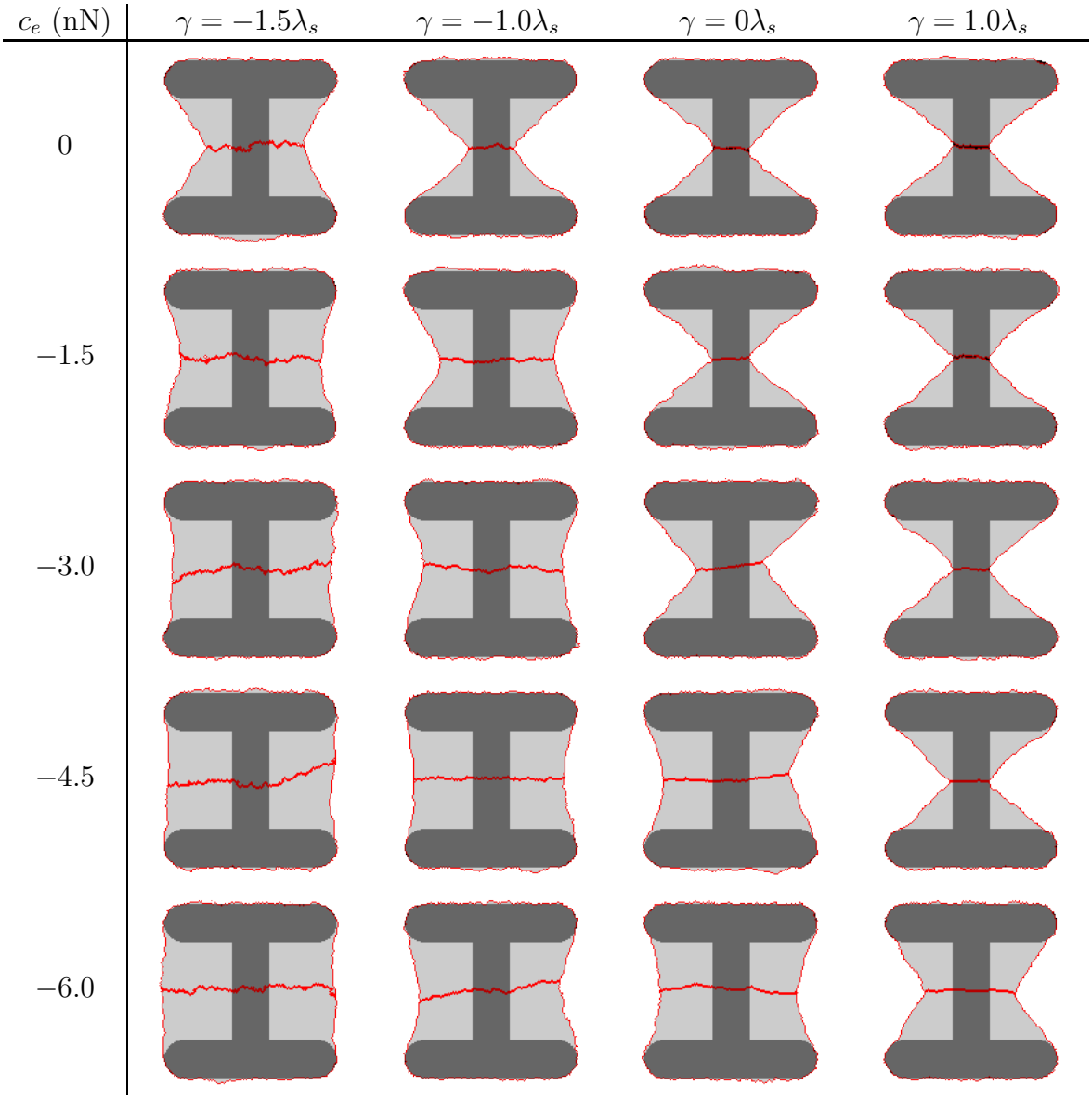

Figure A.10. Cell pairs on [H] pattern with different line tension at the cell-cell interface controlled by γ and cell-cell adhesion energies controlled by c_e. Decreasing γ makes the cells less invaginated and the cell-cell junction more fuzzy. Decreasing c_e also makes the cells less invaginated, but keeps the fluctuations at the junctions the same. Therefore, cell-cell junction tension and cell-cell adhesion can be controlled independently and arbitrary value can be chosen for both of them. For $\gamma > -\lambda_s$ the line tension at the junction is larger than the tension at the cell medium interface and the fluctuations smaller. For $\gamma < -\lambda_s$ the fluctuations at the interface are larger. For γ approaching $-2\lambda_s$ the cell-cell junction dissolves (not shown). The cells are simulated with the Hamiltonian (3.10) and the remaining parameters are $\sigma = 0.1\,\mathrm{nN\,\mu m^{-1}}$, $\lambda_s = 2.3\,\mathrm{nN}$, $EA = 350\,\mathrm{nN}$.

A.4. Cell Migration

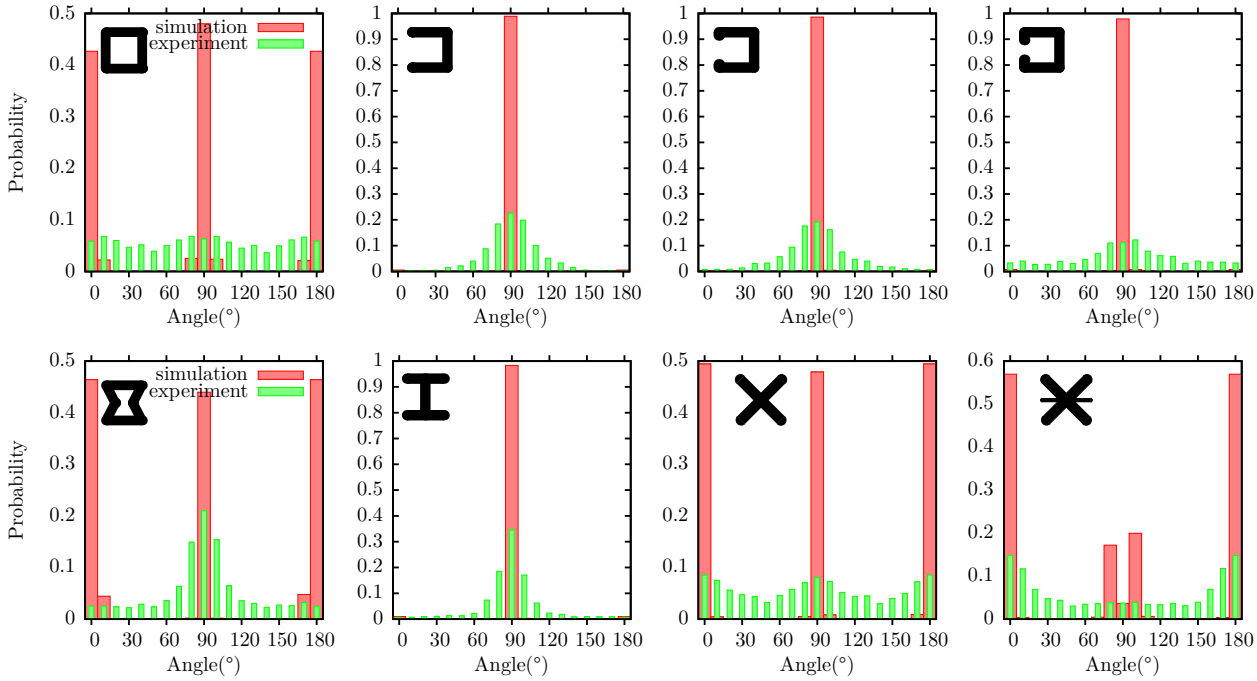

Figure A.11. Comparison of experimental (green) nuclei-nuclei axis distribution with simulated COM-COM distributions without any migratory activity $\mu = 0$

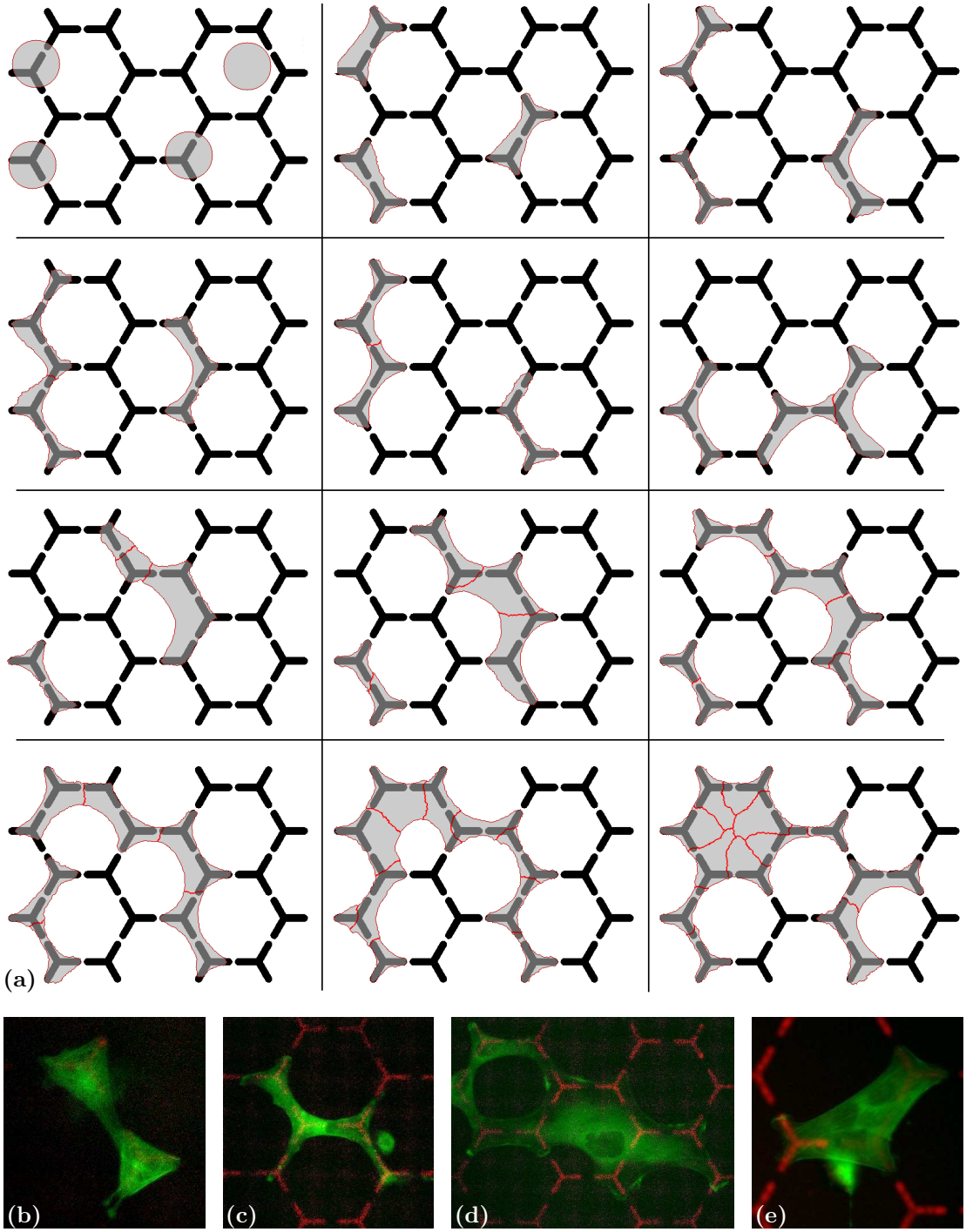

Figure A.12. (a) Cells spreading, migrating and dividing on a hexagonal lattice of [Y] shaped patterns. The cells display several characteristics observed experimentally. Namely, (b) cells forming contacts between patterns, (c) single cells spanning multiple patterns, (d) huge cells spreading almost the entire network and (e) several cells bridging nonadhesive areas. Experimental images of HeLa cells obtained by the collaboration with Sebastien Degot and Yoran Margaron. The network has a width of 300 µm and is represented on a lattice with 600×482 sites.

Bibliography

[1] Thorsten Erdmann, Philipp J Albert, and Ulrich S Schwarz. **Stochastic dynamics of small ensembles of non-processive molecular motors: the parallel cluster model.** *J. Chem. Phys.*, **139**(17):175104, November 2013.
(Referenced on pages 1 and 6.)

[2] Philipp J Albert, Thorsten Erdmann, and Ulrich S Schwarz. **Stochastic dynamics and mechanosensitivity of myosin II minifilaments**. *New J. Phys.*, **16**(9):093019, September 2014.
(Referenced on page 6.)

[3] Philipp J Albert and Ulrich S Schwarz. **Dynamics of cell shape and forces on micropatterned substrates predicted by a cellular Potts model.** *Biophys. J.*, **106**(11):2340–52, June 2014.
(Referenced on pages 1, 13, 97, and 99.)

[4] Christopher S. Chen, Milan Mrksich, Sui Huang, George M. Whitesides, and Donald E Ingber. **Geometric Control of Cell Life and Death**. *Science (80-.).*, **276**(5317):1425–1428, 1997.
(Referenced on pages 1, 2, and 6.)

[5] Christopher S. Chen, Jose L. Alonso, Emanuele Ostuni, George M. Whitesides, and Donald E. Ingber. **Cell shape provides global control of focal adhesion assembly**. *Biochem. Biophys. Res. Commun.*, **307**(2):355–361, July 2003.

[6] Dennis E Discher, David J Mooney, and Peter W Zandstra. **Growth Factors, Matrices, and Forces Combine and Control Stem Cells**. *Science (80-.).*, **324**(5935):1673–1677, 2009.

[7] Adam Engler, Lucie Bacakova, Cynthia Newman, Alina Hategan, Maureen Griffin, and Dennis Discher. **Substrate Compliance versus Ligand Density in Cell on Gel Responses**. *Biophys. J.*, **86**(1):617–628, January 2004.
(Referenced on page 1.)

[8] Manuel Théry. **Micropatterning as a tool to decipher cell morphogenesis and functions.** *J. Cell Sci.*, **123**(Pt 24):4201–13, December 2010.
(Referenced on pages 1 and 3.)

[9] Biomedical Microscopy Core. `https://lh3.googleusercontent.com/-VNrU0F7SJdA/UMtc8WxKIdI/AAAAAAAAA0k/g-a2GOJv8ZI/Humancell20x.jpg?imgmax=912`. [link].
(Referenced on page 2.)

[10] Manuel Théry, Anne Pépin, Emilie Dressaire, Yong Chen, and Michel Bornens. **Cell distribution of stress fibres in response to the geometry of the adhesive environment.** *Cell Motil. Cytoskeleton*, **63**(6):341–355, June 2006.
(Referenced on pages 2, 6, 17, 23, 24, 25, 46, and 49.)

[11] Sami Alom Ruiz and Christopher S Chen. **Microcontact printing: A tool to pattern**. *Soft Matter*, **3**(2):168–177, 2007.
(Referenced on page 2.)

[12] Jenny Fink, Manuel Thery, Ammar Azioune, Raphael Dupont, Francois Chatelain, Michel Bornens, and Matthieu Piel. **Comparative study and improvement of current cell micro-patterning techniques**. *Lab Chip*, **7**(6):672–680, 2007.
(Referenced on page 2.)

[13] Andrew D Doyle, Francis W Wang, Kazue Matsumoto, and Kenneth M Yamada. **One-dimensional topography underlies three-dimensional fibrillar cell migration**. *J. Cell Biol.*, **184**(4):481–490, 2009.
(Referenced on page 2.)

[14] Manuel Théry, Victor Racine, Matthieu Piel, Anne Pépin, Ariane Dimitrov, Yong Chen, Jean-Baptiste Sibarita, and Michel Bornens. **Anisotropy of cell adhesive microenvironment governs cell internal organization and orientation of polarity.** *Proc. Natl. Acad. Sci. U. S. A.*, **103**(52):19771–19776, December 2006.
(Referenced on pages 3, 17, 21, and 34.)

[15] Ilka B IB Bischofs, Franziska Klein, Dirk Lehnert, Martin Bastmeyer, and Ulrich S Schwarz. **Filamentous network mechanics and active contractility determine cell and tissue shape.** *Biophys. J.*,

95(7):3488–3496, October 2008.
(Referenced on pages 3, 6, 7, 8, 9, 17, 18, 20, 24, 97, and 102.)

[16] Timothée Vignaud, Laurent Blanchoin, and Manuel Théry. **Directed cytoskeleton self-organization**. *Trends Cell Biol.*, **22**(12):671–682, December 2012.
(Referenced on pages 3, 7, and 90.)

[17] Ulrich S Schwarz and Samuel A Safran. **Physics of adherent cells**. *Rev. Mod. Phys.*, **85**(3):1327–1381, August 2013.
(Referenced on pages 3 and 8.)

[18] Benjamin Geiger, Joachim P Spatz, and Alexander D Bershadsky. **Environmental sensing through focal adhesions.** *Nat. Rev. Mol. Cell Biol.*, **10**(1):21–33, January 2009.
(Referenced on pages 3, 5, 8, and 32.)

[19] Jonathon Howard. *Mechanics of motor proteins and the cytoskeleton*. Sinauer Associates ; Macmillan, Sunderland, Mass. ; Basingstoke, 2006.
(Referenced on pages 3 and 4.)

[20] Laurent Blanchoin, Rajaa Boujemaa-Paterski, Cécile Sykes, and Julie Plastino. **Actin Dynamics, Architecture, and Mechanics in Cell Motility**. *Physiol. Rev.*, **94**(1):235–263, January 2014.
(Referenced on pages 3, 4, 5, 6, and 49.)

[21] Philip Nelson and Marko Radosavljević. *Biological physics*. Freeman, New York [u.a.], 2004.
(Referenced on page 3.)

[22] Thomas D Pollard, Laurent Blanchoin, and R Dyche Mullins. **MOLECULAR MECHANISMS CONTROLLING ACTIN FILAMENT DYNAMICS IN NONMUSCLE CELLS**. *Annu. Rev. Biophys. Biomol. Struct.*, **29**(1):545–576, June 2000.
(Referenced on page 4.)

[23] Bruce Alberts, Alexander Johnson, Julian Lewis, David Morgan, Martin Raff, Keith Roberts, and Peter Walter. *Molecular Biology of the Cell*. Garland Science, 6 edition, 2014.
(Referenced on pages 4 and 42.)

[24] Guillaume Salbreux, Guillaume Charras, and Ewa Paluch. **Actin cortex mechanics and cellular morphogenesis**. *Trends Cell Biol.*, **22**(10):536–545, October 2012.
(Referenced on page 4.)

[25] Stéphanie Pellegrin and Harry Mellor. **Actin stress fibres.** *J. Cell Sci.*, **120**(Pt 20):3491–9, October 2007.
(Referenced on page 4.)

[26] Romain Levayer and Thomas Lecuit. **Biomechanical regulation of contractility: spatial control and dynamics**. *Trends Cell Biol.*, **22**(2):61–81, February 2012.
(Referenced on page 5.)

[27] Peter Lenz, editor. *Cell Motility (Biological and Medical Physics, Biomedical Engineering)*. Springer, 1 edition, 2007.
(Referenced on pages 4, 5, 49, 56, and 98.)

[28] Mark S Bretscher. **On the shape of migrating cells — a 'front–to-back' model**. *J. Cell Sci.*, **121**(16):2625–2628, August 2008.
(Referenced on pages 4 and 49.)

[29] Pirta Hotulainen and Pekka Lappalainen. **Stress fibers are generated by two distinct actin assembly mechanisms in motile cells**. *J. Cell Biol.*, **173**(3):383–394, 2006.
(Referenced on pages 4, 5, 32, and 46.)

[30] Miguel Vicente-Manzanares, Xuefei Ma, Robert S Adelstein, and Alan Rick Horwitz. **Non-muscle myosin II takes centre stage in cell adhesion and migration.** *Nat. Rev. Mol. Cell Biol.*, **10**(11):778–90, November 2009.
(Referenced on page 4.)

[31] Pakorn Kanchanawong, Gleb Shtengel, Ana M Pasapera, Ericka B Ramko, Michael W Davidson, Harald F Hess, and Clare M Waterman. **Nanoscale architecture of integrin-based cell adhesions**. *Nature*, **468**(7323):580–584, November 2010.
(Referenced on page 5.)

[32] Ulrich S Schwarz and Margaret L Gardel. **United we stand: integrating the actin cytoskeleton and cell-matrix adhesions in cellular mechanotransduction.** *J. Cell Sci.*, **125**(Pt 13):3051–3060, July 2012.
(Referenced on pages 6 and 32.)

[33] Dennis E Discher, Paul Janmey, and Yu-Li Wang. **Tissue cells feel and respond to the stiffness of their substrate.** *Science (80-.).*, **310**(5751):1139–1143, 2005.
(Referenced on pages 6 and 46.)

[34] J a Theriot. **The polymerization motor.** *Traffic*, **1**(1):19–28, January 2000.
(Referenced on pages 6 and 50.)

[35] Sebastian Rausch, Tamal Das, Jérôme RD Soiné, Tobias W Hofmann, Christian HJ Boehm, Ulrich S Schwarz, Heike Boehm, and Joachim P Spatz. **Polarizing cytoskeletal tension to induce leader cell formation during collective cell migration**. *Biointerphases*, **8**(1):1–11, 2013.
(Referenced on page 7.)

[36] Qingzong Tseng, Irene Wang, Eve Duchemin-Pelletier, Ammar Azioune, Nicolas Carpi, Jie Gao, Odile Filhol, Matthieu Piel, Manuel Théry, and Martial Balland. **A new micropatterning method of soft substrates reveals that different tumorigenic signals can promote or reduce cell contraction levels.** *Lab Chip*, **11**(13):2231–40, July 2011.
(Referenced on pages 7, 8, 26, 27, 28, 46, 97, and 99.)

[37] Jane James, Edgar D Goluch, Huan Hu, Chang Liu, and Milan Mrksich. **Subcellular curvature at the perimeter of micropatterned cells influences lamellipodial distribution and cell polarity**. *Cell Motil. Cytoskeleton*, **65**(11):841–852, 2008.
(Referenced on page 6.)

[38] Manuel Théry, Andrea Jiménez-Dalmaroni, Victor Racine, Michel Bornens, and Frank Jülicher. **Experimental and theoretical study of mitotic spindle orientation.** *Nature*, **447**(7143):493–496, May 2007.
(Referenced on pages 6, 33, 34, 35, 37, 38, 41, 47, 48, 98, 118, and 119.)

[39] Jenny Fink, Nicolas Carpi, Timo Betz, Angelique Betard, Meriem Chebah, Ammar Azioune, Michel Bornens, Cecile Sykes, Luc Fetler, Damien Cuvelier, and Matthieu Piel. **External forces control mitotic spindle positioning**. *Nat Cell Biol*, **13**(7):771–778, July 2011.
(Referenced on pages 34 and 41.)

[40] Manuel Thery, Victor Racine, Anne Pepin, Matthieu Piel, Yong Chen, Jean-Baptiste Sibarita, and Michel Bornens. **The extracellular matrix guides the orientation of the cell division axis**. *Nat Cell Biol*, **7**(10):947–953, October 2005.
(Referenced on pages 33, 34, 37, and 47.)

[41] Manuel Théry and Michel Bornens. **Cell shape and cell division**. *Curr. Opin. Cell Biol.*, **18**(6):648–657, December 2006.
(Referenced on pages 6, 33, 36, and 48.)

[42] Kristine Schauer, Tarn Duong, Kevin Bleakley, Sabine Bardin, Michel Bornens, and Bruno Goud. **Probabilistic density maps to study global endomembrane organization.** *Nat. Methods*, **7**(7):560–566,

July 2010.
(Referenced on pages 6 and 10.)

[43] Amy Brock, Eric Chang, Chia-Chi Ho, Philip LeDuc, Xingyu Jiang, George M Whitesides, and Donald E Ingber. **Geometric Determinants of Directional Cell Motility Revealed Using Microcontact Printing†**. *Langmuir*, **19**(5):1611–1617, 2003.
(Referenced on pages 6 and 52.)

[44] Xingyu Jiang, DA Derek A Bruzewicz, Amy P Wong, Matthieu Piel, and George M Whitesides. **Directing cell migration with asymmetric micropatterns**. *Proc. Natl. Acad. Sci. U. S. A.*, **102**(4):975–978, 2005.
(Referenced on pages 6 and 52.)

[45] David Caballero, Raphaël Voituriez, and Daniel Riveline. **Protrusion Fluctuations Direct Cell Motion**. *Biophys. J.*, **107**(1):34–42, January 2015.
(Referenced on pages 7, 52, 53, 62, 87, and 95.)

[46] Goher Mahmud, Christopher J Campbell, Kyle J M Bishop, Yulia A Komarova, Oleg Chaga, Siowling Soh, Sabil Huda, Kristiana Kandere-Grzybowska, and Bartosz A Grzybowski. **Directing cell motions on micropatterned ratchets**. *Nat Phys*, **5**(8):606–612, August 2009.
(Referenced on pages 7, 52, 87, 95, and 99.)

[47] Keiichiro Kushiro, Stephanie Chang, and Anand R Asthagiri. **Reprogramming directional cell motility by tuning micropattern features and cellular signals.** *Adv. Mater.*, **22**(40):4516–9, October 2010.
(Referenced on pages 7, 52, 69, and 95.)

[48] S Huang, C P Brangwynne, K K Parker, and D E Ingber. **Symmetry-breaking in mammalian cell cohort migration during tissue pattern formation: Role of random-walk persistence**. *Cell Motil. Cytoskeleton*, **61**(4):201–213, 2005.
(Referenced on pages 7, 53, 59, and 63.)

[49] Kevin Doxzen, Sri Ram Krishna Vedula, Man Chun Leong, Hiroaki Hirata, Nir S Gov, Alexandre J Kabla, Benoit Ladoux, and Chwee Teck Lim. **Guidance of collective cell migration by substrate geometry**. *Integr. Biol.*, **5**(8):1026–1035, 2013.
(Referenced on pages 7, 53, and 63.)

[50] Qingzong Tseng, Eve Duchemin-Pelletier, Alexandre Deshiere, Martial Balland, Hervé Guillou, Odile Filhol, and Manuel Théry. **Spatial organization of the extracellular matrix regulates cell-cell junction positioning.** *Proc. Natl. Acad. Sci. U. S. A.*, **109**(5):1506–11, January

2012.
(Referenced on pages 7, 44, 45, 46, 49, 53, 63, 64, 65, 68, 70, 94, and 98.)

[51] Sri Ram Krishna Vedula, Hiroaki Hirata, Mui Hoon Nai, Agusti Brugués, Yusuke Toyama, Xavier Trepat, Chwee Teck Lim, and Benoit Ladoux. **Epithelial bridges maintain tissue integrity during collective cell migration**. *Nat Mater*, **13**(1):87–96, January 2014.
(Referenced on pages 7, 46, 48, and 92.)

[52] Micah Dembo and Yu-Li Wang. **Stresses at the Cell-to-Substrate Interface during Locomotion of Fibroblasts**. *Biophys. J.*, **76**(4):2307–2316, April 1999.
(Referenced on page 8.)

[53] James P Butler, Iva Marija Tolić-Nø rrelykke, Ben Fabry, and Jeffrey J Fredberg. **Traction fields, moments, and strain energy that cells exert on their surroundings**. *Am. J. Physiol. - Cell Physiol.*, **282**(3):C595 —-C605, 2002.
(Referenced on pages 21 and 28.)

[54] Benedikt Sabass, Margaret L Gardel, Clare M Waterman, and Ulrich S Schwarz. **High resolution traction force microscopy based on experimental and computational advances.** *Biophys. J.*, **94**(1):207–20, January 2008.
(Referenced on pages 8, 21, 28, and 106.)

[55] Andrew D Rape, Wei-Hui Guo, and Yu-Li Wang. **The regulation of traction force in relation to cell shape and focal adhesions.** *Biomaterials*, **32**(8):2043–2051, March 2011.
(Referenced on pages 8 and 22.)

[56] Kalpana Mandal, Irène Wang, Elisa Vitiello, Laura Andreina Chacòn Orellana, and Martial Balland. **Cell dipole behaviour revealed by ECM sub-cellular geometry.** *Nat. Commun.*, **5**:5749, January 2014.
(Referenced on pages 8 and 97.)

[57] Nico Hampe, Thorsten Jonas, Benjamin Wolters, Nils Hersch, Bernd Hoffmann, and Rudolf Merkel. **Defined 2-D microtissues on soft elastomeric silicone rubber using lift-off epoxy-membranes for biomechanical analyses**. *Soft Matter*, February 2014.
(Referenced on page 8.)

[58] P Kollmannsberger, C M Bidan, J W C Dunlop, and P Fratzl. **The physics of tissue patterning and extracellular matrix organisation: how cells join forces**. *Soft Matter*, **7**(20):9549–9560, 2011.
(Referenced on page 8.)

[59] M S Zand and G Albrecht-Buehler. **What structures, besides adhesions, prevent spread cells from rounding up?** *Cell Motil. Cytoskeleton*, **13**(3):195–211, January 1989.
(Referenced on pages 8 and 17.)

[60] R Bar-Ziv, T Tlusty, E Moses, S a Safran, and Alexander D Bershadsky. **Pearling in cells: a clue to understanding cell shape.** *Proc. Natl. Acad. Sci. U. S. A.*, **96**(18):10140–10145, August 1999.
(Referenced on pages 8 and 17.)

[61] Ilka B Bischofs, Sebastian S Schmidt, and Ulrich S Schwarz. **Effect of Adhesion Geometry and Rigidity on Cellular Force Distributions**. *Phys. Rev. Lett.*, **103**(4):1–4, July 2009.
(Referenced on pages 8, 19, and 20.)

[62] Mehdi Farsad and Franck J Vernerey. **An {XFEM-based} numerical strategy to model mechanical interactions between biological cells and a deformable substrate**. *Int. J. Numer. Methods Eng.*, **92**(3):238–267, 2012.
(Referenced on pages 8 and 9.)

[63] P. Guthardt Torres, I. Bischofs, and U. Schwarz. **Contractile network models for adherent cells**. *Phys. Rev. E*, **85**(1):1–13, January 2012.
(Referenced on pages 8 and 9.)

[64] Celeste M Nelson, Ronald P Jean, John L Tan, Wendy F Liu, Nathan J Sniadecki, Alexander A Spector, and Christopher S Chen. **Emergent patterns of growth controlled by multicellular form and mechanics.** *Proc. Natl. Acad. Sci. U. S. A.*, **102**(33):11594–11599, 2005.
(Referenced on page 8.)

[65] Carina M. Edwards and Ulrich S. Schwarz. **Force Localization in Contracting Cell Layers**. *Phys. Rev. Lett.*, **107**(12):128101, September 2011.

[66] Aaron F. Mertz, Shiladitya Banerjee, Yonglu Che, Guy K. German, Ye Xu, Callen Hyland, M. Cristina Marchetti, Valerie Horsley, and Eric R. Dufresne. **Scaling of Traction Forces with the Size of Cohesive Cell Colonies**. *Phys. Rev. Lett.*, **108**(19):198101, May 2012.
(Referenced on pages 8, 19, and 22.)

[67] Shiladitya Banerjee and M Cristina Marchetti. **Controlling cell–matrix traction forces by extracellular geometry**. *New J. Phys.*, **15**(3):35015, March 2013.
(Referenced on page 8.)

[68] Vikram S Deshpande, Robert M McMeeking, and Anthony G Evans. **A bio-chemo-mechanical model for cell contractility**. *Proc. Natl. Acad.*

Sci., **103**(38):14015–14020, 2006.
(Referenced on page 8.)

[69] Vikram S Deshpande, Robert M McMeeking, and Anthony G Evans. **A Model for the Contractility of the Cytoskeleton Including the Effects of Stress-Fibre Formation and Dissociation**. *Proc. R. Soc. A Math. Phys. Eng. Sci.*, **463**(2079):787–815, March 2007.
(Referenced on page 8.)

[70] Amit Pathak, Vikram S Deshpande, Robert M McMeeking, and Anthony G Evans. **The simulation of stress fibre and focal adhesion development in cells on patterned substrates.** *J. R. Soc. Interface*, **5**(22):507–24, May 2008.
(Referenced on page 8.)

[71] J P McGarry, J Fu, M T Yang, C S Chen, R M McMeeking, A G Evans, and V S Deshpande. **Simulation of the Contractile Response of Cells on an Array of Micro-Posts**. *Philos. Trans. R. Soc. A Math. Phys. Eng. Sci.*, **367**(1902):3477–3497, September 2009.
(Referenced on page 8.)

[72] Athanasius F M Marée, Alexandra Jilkine, Adriana Dawes, Verônica a Grieneisen, and Leah Edelstein-Keshet. **Polarization and movement of keratocytes: a multiscale modelling approach.** *Bull. Math. Biol.*, **68**(5):1169–1211, July 2006.
(Referenced on pages 9, 10, 13, 51, 53, 69, and 97.)

[73] Reza Farhadifar, Jens-Christian Röper, Benoit Aigouy, Suzanne Eaton, and Frank Jülicher. **The influence of cell mechanics, cell–cell interactions, and proliferation on epithelial packing.** *Curr. Biol.*, **17**(24):2095–2104, December 2007.
(Referenced on pages 9, 10, 19, 36, 43, and 101.)

[74] Mark F Coughlin and Dimitrije Stamenovic. **A Prestressed Cable Network Model of the Adherent Cell Cytoskeleton**. *Biophys. J.*, **84**(2):1328–1336, February 2003.
(Referenced on page 9.)

[75] Raja Paul, Patrick Heil, Joachim P Spatz, and Ulrich S Schwarz. **Propagation of mechanical stress through the actin cytoskeleton toward focal adhesions: model and experiment.** *Biophys. J.*, **94**(4):1470–82, February 2008.
(Referenced on page 9.)

[76] Danying Shao, Wouter-Jan Rappel, and Herbert Levine. **Computational Model for Cell Morphodynamics**. *Phys. Rev. Lett.*, **105**(10):108104,

September 2010.
(Referenced on pages 10 and 52.)

[77] Jakob Lober, Falko Ziebert, and Igor S Aranson. **Modeling crawling cell movement on soft engineered substrates**. *Soft Matter*, **10**(9):1365–1373, 2014.
(Referenced on page 52.)

[78] Falko Ziebert, Sumanth Swaminathan, and Igor S Aranson. **Model for self-polarization and motility of keratocyte fragments.** *J. R. Soc. Interface*, **9**(70):1084–1092, May 2012.
(Referenced on page 52.)

[79] Falko Ziebert and Igor S Aranson. **Effects of adhesion dynamics and substrate compliance on the shape and motility of crawling cells.** *PLoS One*, **8**(5):e64511, January 2013.
(Referenced on page 52.)

[80] Brian a Camley, Yunsong Zhang, Yanxiang Zhao, Bo Li, Eshel Ben-Jacob, Herbert Levine, and Wouter-Jan Rappel. **Polarity mechanisms such as contact inhibition of locomotion regulate persistent rotational motion of mammalian cells on micropatterns**. *Proc. Natl. Acad. Sci.*, **111**(41):14770–14775, September 2014.
(Referenced on pages 10, 52, 56, 63, 66, and 69.)

[81] Alexander Anderson and Katarzyna Rejniak, editors. *Single-Cell-Based Models in Biology and Medicine (Mathematics and Biosciences in Interaction)*. Birkhäuser Basel, 1 edition, 2007.
(Referenced on pages 10, 15, 16, 17, 31, and 51.)

[82] François Graner and J.A. A Glazier. **Simulation of biological cell sorting using a two-dimensional extended Potts model**. *Phys. Rev. Lett.*, **69**(13):2013–2016, 1992.
(Referenced on pages 10, 13, 15, 16, 19, 33, 42, 48, 97, 98, and 101.)

[83] J.A. A Glazier and François Graner. **Simulation of the differential adhesion driven rearrangement of biological cells**. *Phys. Rev. E*, **47**(3):2128, 1993.
(Referenced on pages 10, 13, 15, 16, 33, 97, 98, 101, and 104.)

[84] Jos Käfer, Takashi Hayashi, Athanasius F M Marée, Richard W Carthew, and François Graner. **Cell adhesion and cortex contractility determine cell patterning in the Drosophila retina.** *Proc. Natl. Acad. Sci. U. S. A.*, **104**(47):18549–18554, November 2007.
(Referenced on pages 10, 33, 42, 43, 48, and 101.)

[85] Benoit Vianay, Jos Käfer, Emmanuelle Planus, Marc Block, François Graner, and Hervé Guillou. **Single Cells Spreading on a Protein Lattice Adopt an Energy Minimizing Shape**. *Phys. Rev. Lett.*, **105**(12):3–6, September 2010.
(Referenced on pages 10, 13, 19, 31, 33, 97, 101, and 102.)

[86] Athanasius F M Marée, Verônica a Grieneisen, and Leah Edelstein-Keshet. **How cells integrate complex stimuli: the effect of feedback from phosphoinositides and cell shape on cell polarization and motility.** *PLoS Comput. Biol.*, **8**(3):e1002402, January 2012.
(Referenced on pages 10, 13, 31, 51, 53, 69, and 97.)

[87] Lars Hufnagel, Aurelio a Teleman, Hervé Rouault, Stephen M Cohen, and Boris I Shraiman. **On the mechanism of wing size determination in fly development.** *Proc. Natl. Acad. Sci. U. S. A.*, **104**(10):3835–40, March 2007.
(Referenced on pages 10, 19, 36, and 101.)

[88] Maryam Aliee, Jens-Christian Röper, Katharina P Landsberg, Constanze Pentzold, Thomas J Widmann, Frank Julicher, and Christian Dahmann. **Physical Mechanisms Shaping the Drosophila Dorsoventral Compartment Boundary**. *Curr. Biol.*, **22**(11):967–976, 2012.
(Referenced on pages 10 and 36.)

[89] Christophe J Echeverri and Norbert Perrimon. **High-throughput RNAi screening in cultured cells: a user's guide.** *Nat. Rev. Genet.*, **7**(5):373–84, May 2006.
(Referenced on page 10.)

[90] Angela Reynolds, Devin Leake, Queta Boese, Stephen Scaringe, William S Marshall, and Anastasia Khvorova. **Rational siRNA design for RNA interference.** *Nat. Biotechnol.*, **22**(3):326–30, March 2004.

[91] Tariq M Rana. **Illuminating the silence: understanding the structure and function of small RNAs.** *Nat. Rev. Mol. Cell Biol.*, **8**(1):23–36, January 2007.
(Referenced on page 10.)

[92] F Y Wu. **The Potts model**. *Rev. Mod. Phys.*, **54**(1):235–268, January 1982.
(Referenced on pages 13 and 14.)

[93] J Olejarz, P L Krapivsky, and S Redner. **Zero-temperature coarsening in the 2d Potts model**. *J. Stat. Mech. Theory Exp.*, **2013**(06):P06018, 2013.
(Referenced on page 14.)

[94] Klaus-Dieter Keller. `http://commons.wikimedia.org/wiki/File:2-dimensional_foam.jpg`. [link].
(Referenced on page 14.)

[95] Edward Pleshakov. `http://en.wikipedia.org/wiki/File:CrystalGrain.jpg`. [link].
(Referenced on page 14.)

[96] M Lisa Manning, Ramsey A Foty, Malcolm S Steinberg, and Eva-Maria Schoetz. **Coaction of intercellular adhesion and cortical tension specifies tissue surface tension**. *Proc. Natl. Acad. Sci.*, **107**(28):12517–12522, 2010.
(Referenced on pages 14, 42, 43, and 48.)

[97] D. Weaire and J.a. Glazier. **Modelling Grain Growth and Soap Froth Coarsening: Past, Present and Future**. *Mater. Sci. Forum*, **94-96**:27–38, 1992.
(Referenced on page 15.)

[98] Thomas Lecuit and Pierre-François Lenne. **Cell surface mechanics and the control of cell shape, tissue patterns and morphogenesis.** *Nat. Rev. Mol. Cell Biol.*, **8**(8):633–44, August 2007.
(Referenced on pages 15, 17, and 42.)

[99] Udo Seifert. *Configurations of fluid membranes and vesicles*, **46**. February 1997.
(Referenced on page 16.)

[100] Jc Mombach and Ja Glazier. **Single cell motion in aggregates of embryonic cells.** *Phys. Rev. Lett.*, **76**(16):3032–3035, April 1996.
(Referenced on page 16.)

[101] José C M Mombach, James A Glazier, Richard C Raphael, and Mark Zajac. **Quantitative Comparison between Differential Adhesion Models and Cell Sorting in the Presence and Absence of Fluctuations**. *Phys. Rev. Lett.*, **75**(11):2244–2247, September 1995.
(Referenced on page 16.)

[102] Athanasius F M Marée and P Hogeweg. **How amoeboids self-organize into a fruiting body: multicellular coordination in Dictyostelium discoideum.** *Proc. Natl. Acad. Sci. U. S. A.*, **98**(7):3879–83, March 2001.
(Referenced on page 16.)

[103] D. Umbach and K.N. N Jones. **A few methods for fitting circles to data**. *IEEE Trans. Instrum. Meas.*, **52**(6):1881–1885, December 2003.
(Referenced on page 18.)

[104] Benjamin J Dubin-Thaler, Gregory Giannone, Hans-Günther Döbereiner, and Michael P Sheetz. **Nanometer Analysis of Cell Spreading on Matrix-Coated Surfaces Reveals Two Distinct Cell States and {STEPs}**. *Biophys. J.*, **86**(3):1794–1806, 2004.
(Referenced on page 18.)

[105] Damien Cuvelier, Manuel Théry, Yeh-Shiu Chu, Sylvie Dufour, Jean-Paul Thiéry, Michel Bornens, Pierre Nassoy, and L Mahadevan. **The universal dynamics of cell spreading.** *Curr. Biol.*, **17**(8):694–9, April 2007.
(Referenced on pages 18 and 104.)

[106] N Q Balaban, U S Schwarz, D Riveline, P Goichberg, G Tzur, I Sabanay, D Mahalu, S Safran, a Bershadsky, L Addadi, and B Geiger. **Force and focal adhesion assembly: a close relationship studied using elastic micropatterned substrates.** *Nat. Cell Biol.*, **3**(5):466–72, May 2001.
(Referenced on pages 19 and 27.)

[107] Shinji Deguchi, Toshiro Ohashi, and Masaaki Sato. **Tensile properties of single stress fibers isolated from cultured vascular smooth muscle cells**. *J. Biomech.*, **39**(14):2603–2610, 2006.
(Referenced on page 20.)

[108] Miriam Cohen, Derk Joester, Benjamin Geiger, and Lia Addadi. **Spatial and temporal sequence of events in cell adhesion: from molecular recognition to focal adhesion assembly.** *Chembiochem*, **5**(10):1393–1399, October 2004.
(Referenced on pages 20 and 24.)

[109] Ana Kostic, Christopher D Lynch, and Michael P Sheetz. **Differential matrix rigidity response in breast cancer cell lines correlates with the tissue tropism.** *PLoS One*, **4**(7):e6361, January 2009.
(Referenced on page 20.)

[110] Léa Trichet, Jimmy Le Digabel, Rhoda J Hawkins, Sri Ram Krishna Vedula, Mukund Gupta, Claire Ribrault, Pascal Hersen, Raphaël Voituriez, and Benoît Ladoux. **Evidence of a large-scale mechanosensing mechanism for cellular adaptation to substrate stiffness.** *Proc. Natl. Acad. Sci. U. S. A.*, **109**(18):6933–8, May 2012.
(Referenced on page 27.)

[111] Timothée Vignaud. *Production de forces par le cytosquelette d'actine: mécanismes et régulation par le micro-environnement*. Thesis, Université de Grenoble, 2013.
(Referenced on page 29.)

[112] Nils C Gauthier, Marc Antoine Fardin, Pere Roca-Cusachs, and Michael P Sheetz. **Temporary increase in plasma membrane tension coordinates the activation of exocytosis and contraction during cell spreading**. *Proc. Natl. Acad. Sci.*, **108**(35):14467–14472, 2011.
(Referenced on pages 31 and 104.)

[113] Y Loosli, R Luginbuehl, and J G Snedeker. **Cytoskeleton Reorganization of Spreading Cells on Micro-Patterned Islands: A Functional Model**. *Philos. Trans. R. Soc. A Math. Phys. Eng. Sci.*, **368**(1920):2629–2652, 2010.
(Referenced on page 32.)

[114] Kandice Tanner, Aaron Boudreau, Mina J Bissell, and Sanjay Kumar. **Dissecting Regional Variations in Stress Fiber Mechanics in Living Cells with Laser Nanosurgery**. *Biophys. J.*, **99**(9):2775–2783, November 2010.
(Referenced on page 32.)

[115] Murat Guvendiren and Jason A Burdick. **Stiffening hydrogels to probe short- and long-term cellular responses to dynamic mechanics.** *Nat. Commun.*, **3**:792, January 2012.
(Referenced on page 32.)

[116] Tom Shemesh, Alexander D Bershadsky, and Michael M Kozlov. **Physical Model for Self-Organization of Actin Cytoskeleton and Adhesion Complexes at the Cell Front**. *Biophys. J.*, **102**(8):1746–1756, April 2012.
(Referenced on page 32.)

[117] Oscar Hertwig. *Das Problem der Befruchtung und der Isotropie des Eies, eine Theorie der Vererbung.* Jena, 1884.
(Referenced on page 33.)

[118] Nicolas Minc, David Burgess, and Fred Chang. **Influence of Cell Geometry on Division-Plane Positioning**. *Cell*, **144**(3):414–426, February 2011.
(Referenced on pages 33, 34, 35, 47, and 48.)

[119] Manuel Théry. `https://sites.google.com/site/manuelthery/Home/cell-division`. [link].
(Referenced on page 34.)

[120] National Institutes of Health. `https://imagebank.nih.gov/details.cfm?imageid=1463`. [link].
(Referenced on page 34.)

[121] Sharat Gadde and Rebecca Heald. **Mechanisms and Molecules of the Mitotic Spindle**. *Curr. Biol.*, **14**(18):R797–R805, September 2004.
(Referenced on pages 34 and 35.)

[122] Jc Mombach, de Almeida RM, and Jr Iglesias. **Mitosis and growth in biological tissues.** *Phys. Rev. E. Stat. Phys. Plasmas. Fluids. Relat. Interdiscip. Topics*, **48**(1):598–602, July 1993.
(Referenced on pages 36 and 42.)

[123] P HOGEWEG. **Evolving Mechanisms of Morphogenesis: on the Interplay between Differential Adhesion and Cell Differentiation**. *J. Theor. Biol.*, **203**(4):317–333, April 2000.
(Referenced on page 36.)

[124] Paulien Hogeweg. **Computing an organism: on the interface between informatic and dynamic processes**. *Biosystems*, **64**(1–3):97–109, January 2002.
(Referenced on page 36.)

[125] Matthew C Gibson, Ankit B Patel, Radhika Nagpal, and Norbert Perrimon. **The emergence of geometric order in proliferating metazoan epithelia**. *Nature*, **442**(7106):1038–1041, August 2006.
(Referenced on page 36.)

[126] Michel Bornens. **Organelle positioning and cell polarity**. *Nat Rev Mol Cell Biol*, **9**(11):874–886, November 2008.
(Referenced on page 39.)

[127] Malcolm S Steinberg. **Differential adhesion in morphogenesis: a modern view**. *Curr. Opin. Genet. Dev.*, **17**(4):281–286, August 2007.
(Referenced on pages 41, 48, and 97.)

[128] RA Foty and MS Steinberg. **Cadherin-mediated cell-cell adhesion and tissue segregation in relation to malignancy**. *Int. J. Dev. Biol.*, **48**(5-6):397–409, 2004.
(Referenced on page 42.)

[129] M Krieg, Y Arboleda-Estudillo, P.-H. Puech, J Kafer, F Graner, D J Muller, and C.-P. Heisenberg. **Tensile forces govern germ-layer organization in zebrafish**. *Nat Cell Biol*, **10**(4):429–436, April 2008.
(Referenced on pages 42, 43, and 48.)

[130] Brenda M Rubenstein and Laura J Kaufman. **The role of extracellular matrix in glioma invasion: a cellular Potts model approach.** *Biophys. J.*, **95**(12):5661–80, December 2008.
(Referenced on page 42.)

[131] N Ouchi, J.A. A Glazier, J Rieu, A Upadhyaya, and Y Sawada. **Improving the realism of the cellular Potts model in simulations of biological cells**. *Phys. A Stat. Mech. its Appl.*, **329**(3-4):451–458, November 2003.
(Referenced on pages 43 and 48.)

[132] M Scianna and L Preiosi. **Multiscale Developments of the Cellular Potts Model**. *Multiscale Model. Simul.*, **10**(2):342–382, 2012.
(Referenced on pages 42, 51, and 58.)

[133] Jean-Léon Maître, Hélène Berthoumieux, Simon Frederik Gabriel Krens, Guillaume Salbreux, Frank Jülicher, Ewa Paluch, and Carl-Philipp Heisenberg. **Adhesion Functions in Cell Sorting by Mechanically Coupling the Cortices of Adhering Cells**. *Science (80-.).*, **338**(6104):253–256, 2012.
(Referenced on pages 44 and 48.)

[134] Rui Ma, Liedewij Laan, Marileen Dogterom, Nenad Pavin, and Frank Jülicher. **General theory for the mechanics of confined microtubule asters**. *New J. Phys.*, **16**(1):13018, 2014.
(Referenced on page 47.)

[135] Hirokazu Tanimoto and Masaki Sano. **Dynamics of Traction Stress Field during Cell Division**. *Phys. Rev. Lett.*, **109**(24):248110, December 2012.
(Referenced on pages 48 and 98.)

[136] Alex Mogilner and Kinneret Keren. **The Shape of Motile Cells**. *Curr. Biol.*, **19**(17):R762–R771, January 2015.
(Referenced on pages 50, 55, and 61.)

[137] Juliet Lee, Akira Ishihara, JA Julie A Theriot, and Ken Jacobson. **Principles of locomotion for simple-shaped cells**. *Nature*, **362**(6416):167–171, March 1993.
(Referenced on pages 50 and 53.)

[138] Kinneret Keren, Zachary Pincus, Greg M Allen, Erin L Barnhart, Gerard Marriott, Alex Mogilner, and Julie a Theriot. **Mechanism of shape determination in motile cells.** *Nature*, **453**(7194):475–80, May 2008.
(Referenced on pages 50, 55, 56, and 69.)

[139] Erin L Barnhart, Kun-Chun Lee, Kinneret Keren, Alex Mogilner, and Julie A Theriot. **An Adhesion-Dependent Switch between Mechanisms That Determine Motile Cell Shape**. *PLoS Biol*, **9**(5):e1001059, 2011.
(Referenced on pages 51, 53, and 54.)

[140] András Czirók, Katalin Varga, Előd Méhes, and András Szabó. **Collective cell streams in epithelial monolayers depend on cell adhesion**. *New J. Phys.*, **15**(7):75006, 2013.
(Referenced on pages 52 and 56.)

[141] Alexandre J Kabla. **Collective cell migration: leadership, invasion and segregation**. *J. R. Soc. Interface*, **9**(77):3268–3278, October 2012.
(Referenced on page 56.)

[142] Joost B Beltman, Athanasius F M Marée, Jennifer N Lynch, Mark J Miller, and Rob J de Boer. **Lymph node topology dictates T cell migration behavior**. *J. Exp. Med.*, **204**(4):771–780, 2007.
(Referenced on pages 52 and 54.)

[143] Liang Li, Simon F Nø rrelykke, and Edward C Cox. **Persistent cell motion in the absence of external signals: a search strategy for eukaryotic cells.** *PLoS One*, **3**(5):e2093, January 2008.
(Referenced on pages 52 and 69.)

[144] HG Othmer, SR Dunbar, and W Alt. **Models of dispersal in biological systems**. *J. Math. Biol.*, **26**(3):263–298, 1988.
(Referenced on pages 52 and 56.)

[145] GA Dunn and AF Brown. **A unified approach to analysing cell motility**. *J. Cell Sci.*, **Supplement**:81–102, 1987.
(Referenced on pages 52 and 56.)

[146] David Selmeczi, Stephan Mosler, Peter H Hagedorn, Niels B Larsen, and Henrik Flyvbjerg. **Cell motility as persistent random motion: theories from experiments.** *Biophys. J.*, **89**(2):912–31, August 2005.
(Referenced on pages 52 and 59.)

[147] Brian D Harms, Gina M Bassi, Alan Rick Horwitz, and Douglas a Lauffenburger. **Directional persistence of EGF-induced cell migration is associated with stabilization of lamellipodial protrusions.** *Biophys. J.*, **88**(2):1479–1488, February 2005.
(Referenced on pages 52 and 56.)

[148] Brian A Camley and Wouter-Jan Rappel. **Velocity alignment leads to high persistence in confined cells**. *Phys. Rev. E*, **89**(6):62705, June 2014.
(Referenced on pages 52, 56, and 70.)

[149] Keiichiro Kushiro and Anand R AR Asthagiri. **Modular Design of Micropattern Geometry Achieves Combinatorial Enhancements in Cell Motility**. *Langmuir*, **28**(9):4357–4362, 2012.
(Referenced on pages 52 and 56.)

[150] Clifford Brangwynne, Sui Huang, KevinKit Parker, and DonaldE. Ingber. **Symmetry breaking in cultured mammalian cells**. *Vitr. Cell. Dev. Biol. - Anim.*, **36**(9):563–565, 2000.
(Referenced on page 53.)

[151] MF F Ware, Alan Wells, and DA A Lauffenburger. **Epidermal growth factor alters fibroblast migration speed and directional persistence reciprocally and in a matrix-dependent manner**. *J. Cell Sci.*, **111**(16):2423–2432, 1998.
(Referenced on page 56.)

[152] Ulrike Theisen, Ekkehard Straube, and Anne Straube. **Directional Persistence of Migrating Cells Requires Kif1C-Mediated Stabilization of Trailing Adhesions**. *Dev. Cell*, **23**(6):1153–1166, 2012.
(Referenced on pages 56 and 61.)

[153] Masao Doi and Samuel F Edwards. *The theory of polymer dynamics*. Number 73 in International series of monographs on physics ; 73 ; Oxford science publications ; International series of monographs on physics. Clarendon, Oxford, repr. edition, 1992.
(Referenced on page 56.)

[154] B Szabó, G J Szöllösi, B Gönci, Zs. Jurányi, D Selmeczi, and Tamás Vicsek. **Phase transition in the collective migration of tissue cells: Experiment and model**. *Phys. Rev. E*, **74**(6):61908, December 2006.
(Referenced on pages 56 and 70.)

[155] Koichiro Uriu and Luis G. Morelli. **Collective Cell Movement Promotes Synchronization of Coupled Genetic Oscillators**. *Biophys. J.*, **107**(2):514–526, July 2014.
(Referenced on page 56.)

[156] Samuel A Safran. *Statistical thermodynamics of surfaces, interfaces, and membranes*. Number 90 in Frontiers in physics ; 90 ; Frontiers in physics. Westview, Boulder, Colo. [u.a.], 2003.
(Referenced on page 59.)

[157] Cinzia Esposito, Aiwei Tian, Svetlana Melamed, Corinne Johnson, Shang-You Tee, and Tobias Baumgart. **Flicker Spectroscopy of Thermal Lipid Bilayer Domain Boundary Fluctuations**. *Biophys. J.*, **93**(9):3169–3181, November 2007.

[158] Michael A Lomholt, Bastien Loubet, and John H Ipsen. **Elastic moderation of intrinsically applied tension in lipid membranes**. *Phys. Rev. E*, **83**(1):11913, January 2011.
(Referenced on page 59.)

[159] Eric Theveneau and Roberto Mayor. **Collective cell migration of epithelial and mesenchymal cells**. *Cell. Mol. Life Sci.*, **70**(19):3481–3492, 2013.
(Referenced on pages 62 and 63.)

[160] Maria Teresa Herrera Abreu, William E Hughes, Katarina Mele, Ruth J Lyons, Danny Rickwood, Brigid C Browne, Haley L Bennett, Pascal Vallotton, Tilman Brummer, and Roger J Daly. **Gab2 regulates cytoskeletal organization and migration of mammary epithelial cells by modulating RhoA activation.** *Mol. Biol. Cell*, **22**(1):105–16, January 2011.
(Referenced on page 69.)

[161] Yair Adler and Sefi Givli. **Closing the loop: Lamellipodia dynamics from the perspective of front propagation**. *Phys. Rev. E*, **88**(4):42708, October 2013.
(Referenced on page 69.)

[162] William B Langdon and Riccardo Poli. *Foundations of genetic programming*. Springer, Berlin ; Heidelberg [u.a.], 2002.
(Referenced on pages 71 and 72.)

[163] Agoston E Eiben and James E Smith. *Introduction to evolutionary computing*. Natural computing series. Springer, Berlin ; Heidelberg [u.a.], corr. 2. p edition, 2007.
(Referenced on pages 71, 72, 75, 77, 78, 80, and 81.)

[164] Michael Affenzeller, Stephan Winkler, Stefan Wagner, and Andreas Beham. *Genetic algorithms and genetic programming*. Number 6 in Numerical insights ; 6 ; A Chapman & Hall book ; Numerical insights. CRC Press, Boca Raton [u.a.], 2009.

[165] D.B. B Fogel. **An introduction to simulated evolutionary optimization**. *Neural Networks, IEEE Trans.*, **5**(1):3–14, 1994.
(Referenced on page 71.)

[166] Beat Rupp and Francois Nedelec. **Patterns of molecular motors that guide and sort filaments**. *Lab Chip*, **12**(22):4903–4910, 2012.
(Referenced on pages 72 and 87.)

[167] CYTOO custom chips. `https://cytoo.com/micropattern-products/chips/cytoochips%E2%84%A2-custom-fn-x18`. [link].
(Referenced on page 75.)

[168] Wolfram Demonstrations Project. `http://demonstrations.wolfram.com/FourierDescriptors/`. [link].
(Referenced on page 76.)

[169] Bernd Jähne. *Digital image processing*. Engineering online library. Springer, Berlin ; Heidelberg [u.a.], 5., rev. a edition, 2002.
(Referenced on pages 76, 81, 107, 110, and 111.)

[170] Z PINCUS and J A THERIOT. **Comparison of quantitative methods for cell-shape analysis**. *J. Microsc.*, **227**(2):140–156, August 2007.
(Referenced on pages 76 and 107.)

[171] Pete E [Hrsg.] Lestrel, editor. *Fourier descriptors and their applications in biology*. Cambridge University Press, Cambridge [u.a.], 1997.
(Referenced on pages 76 and 107.)

[172] Andre Folkers and Hanan Samet. **Content-based image retrieval using Fourier descriptors on a logo database**. *Pattern Recognition, 2002. Proceedings. ...*, pages 521–524, 2002.
(Referenced on pages 77, 107, 110, and 112.)

[173] MK Hu. **Visual pattern recognition by moment invariants**. *Inf. Theory, IRE Trans.*, **8**(2):179 – 187, 1962.
(Referenced on page 82.)

[174] Dengsheng Zhang and Guojun Lu. **A comparative Study of Fourier Descriptors for Shape Representation and Retrieval**. In *Proc. 5th Asian Conf. Comput. Vis. (ACCV*, pages 646–651. Springer, 2002.
(Referenced on page 83.)

[175] M J D Powell. **An efficient method for finding the minimum of a function of several variables without calculating derivatives**. *Comput. J.*, **7**(2):155–162, 1964.
(Referenced on page 86.)

[176] R Dean Astumian. **Thermodynamics and Kinetics of a Brownian Motor**. *Science (80-.).*, **276**(5314):917–922, 1997.
(Referenced on page 96.)

[177] Marcelo O Magnasco. **Forced thermal ratchets**. *Phys. Rev. Lett.*, **71**(10):1477–1481, September 1993.
(Referenced on page 96.)

[178] Bao-Quan Ai and Jian-Chun Wu. **Transport of active ellipsoidal particles in ratchet potentials**. *J. Chem. Phys.*, **140**(9):–, 2014.

[179] F Schweitzer, B Tilch, and W Ebeling. **Uphill motion of active brownian particles in piecewise linear potentials**. *Eur. Phys. J. B - Condens. Matter Complex Syst.*, **14**(1):157–168, 2000.
(Referenced on page 96.)

[180] W.E. Lorensen and H.E. Cline. **Marching cubes: A high resolution 3D surface construction algorithm**. In *ACM Siggraph Comput. Graph.*, **21**, pages 163–169. ACM, 1987.
(Referenced on page 104.)

[181] Hubert Mantz, Karin Jacobs, and Klaus Mecke. **Utilizing Minkowski functionals for image analysis: a marching square algorithm**. *J. Stat. Mech. Theory Exp.*, **2008**(12):P12015, December 2008.
(Referenced on page 105.)

[182] Yang Mingqiang, Kpalma Kidiyo, and Ronsin Joseph. **A Survey of Shape Feature Extraction Techniques**. In Peng-Yeng Yin, editor, *Pattern Recognit. Tech. Technol. Appl.*, chapter 3, pages 43–90. InTech, 2008.
(Referenced on page 107.)

[183] Raymond K.K. Yip. **Genetic Fourier descriptor for the detection of rotational symmetry**. *Image Vis. Comput.*, **25**(2):148–154, February 2007.
(Referenced on page 107.)

[184] R K K Yip, P K S Tam, and D N K Leung. **Application of elliptic Fourier descriptors to symmetry detection under parallel projection**. *Pattern Anal. Mach. Intell. IEEE Trans.*, **16**(3):277–286, March 1994.
(Referenced on page 107.)

[185] Christoph Dalitz, Christian Brandt, Steffen Goebbels, and David Kolanus. **Fourier descriptors for broken shapes**. *EURASIP J. ...*, pages 1–11, 2013.
(Referenced on pages 107, 108, and 110.)

[186] Dirk J Struik. *Lectures on Classical Differential Geometry: Second Edition (Dover Books on Mathematics)*. Dover Publications, second edi edition, 1988.
(Referenced on page 115.)

List of Symbols and Abbreviations

A_{ad}	Adhesive area	18
A_{ref}	Controls saturation of adhesive energy	18
c_e	Line energy density for cadherin bond formation	44
EA	One-dimensional elastic modulus	17
e_{cc}	Energy per cadherin bond	44
η	Gradation of the migratory force	54
λ_e	Elastic line tension	17
γ	Reduction of line tension at cell-cell interface	42
σ_m	Variance of Gaussian mutation	80
λ	Line tension	17
l_{cc}	Length of newly formed or broken interfaces	44
l_f	$l_f = EA/\sigma$	18
l_j	Length of cell-cell interface	42
N_{max}	Number of Fourier coefficients	76
l_p	Persistence length	56
p_r	Probability for random mutation	80
σ_p	Variance of the population fitness	81

μ	Migratory strength	54
R_s	Radius predicted by simple Laplace law	17
σ	Surface tension	17
λ_s	Simple line tension	17
τ	Velocity alignment strength	58
z_ν	Fourier descriptor coefficient	76
A	Cell area	18
d_0	Migratory strength decay length above nonadhesive areas	61
E_0	Strength of the adhesive energy	18
F	Fitness	74
L	Arc contour length	17
l	Cell perimeter	18
L_0	Arc contour resting length	17
n_{cc}	Number of cadherin bonds	44
R	Arc radius	17
W	Adhesive energy density	20
$N(\mu, \sigma_m)$	Random Gaussian number with mean μ and variance σ_m	80
ACS	Actin cytoskeleton	4
ATP	Adenosine triphosphate	3
CPM	Cellular Potts model	10
ECM	Extracellular matrix	2
FD	Fourier descriptor	76
FEM	Finite Element Method	8
GA	Genetic algorithm	71
MCS	Monte Carlo sweep	18
STM	Simple tension model	8
TEM	Tension-elasticity model	8

List of Manuscripts

Several manuscripts have been designed, drafted or finalized during the curse of this thesis as listed below. Reference [1] and [2] originated from my diploma thesis and have not been incorporated in this PhD-thesis. Reference [6] will be included in the PhD-thesis of Marco Linke.

	Manuscript	Chapter
[1]	Thorsten Erdmann, Philipp J. Albert and Ulrich S. Schwarz. *Stochastic dynamics of small ensembles of non-processive molecular motors: the parallel cluster model.* J. Chem. Phys. 139: 175104, 2013.	
[2]	Philipp J. Albert, Thorsten Erdmann and Ulrich S. Schwarz. *Stochastic dynamics and mechanosensitivity of myosin II minifilaments.* New J. Phys. 16: 093019, 2014.	
[3]	Philipp J. Albert and Ulrich S. Schwarz. *Dynamics of cell shape and forces on micropatterned substrates predicted by a cellular Potts model.* Biophys. J. 106: 2340–52, 2014.	1,2
[4]	Philipp J. Albert and Ulrich S. Schwarz. *Modeling cell division and migration on micropatterns.* In preparation.	3,4
[5]	Philipp J. Albert, Marco Linke and Ulrich S. Schwarz. *Micropattern network design and optimization by a genetic algorithm.* In preparation.	5
[6]	Marco Linke, Philipp J. Albert, Ulrich S. Schwarz, Holger Erfle, Vytaute Starkuviene-Erfle and coworkers. *Image processing for integrin trafficking on micropatterns.* In preparation.	

Table 1. List of manuscripts

Danksagung

An erster Stelle bedanke ich mich bei meinem Betreuer Prof. Dr. Ulrich Schwarz für seine Unterstützung und die Betreuung während der Doktorarbeit. Er hat mir mit seiner Arbeitsgruppe und der Teilname an vielen Konferenzen ein tiefes Verständnis der Biophysik vermittelt. Neben den fachlich relevanten Themen hat er mir auch einen Einblick in die Uni- und Wissenschaftspolitik ermöglicht. Ohne seine zahlreichen Ideen wäre dies Arbeit so nicht entstanden.

Ich möchte mich auch bei Prof. Dr. Heinz Horner für das Interesse an meiner Arbeit und die Zweitkorrektur bedanken.

Dank geht auch an das MEHTRICS Projekt über das ich finanziert wurde. Innerhalb der MEHTRICS Kollaboration geht der Dank vor allem an Sebastien Degot und Yoran Margaron von Cytoo für die Aufnahme und Bereitstellung vieler Videos von Zellen auf Micropattern. Innerhalb der Kollaboration geht der Dank auch an Dr. Vytaute Starkuviene-Erfle, Holger Erfle, Anastasia Eskova und Gintarė Garbenčiūtė. Sie haben mir mit ihrem Wissen speziell bei Fragen über die Biologie weiter geholfen und mir die Daten von vielen Experimenten zu Verfügung gestellt.

Besonderer Dank geht an meine Arbeitsgruppe. Sie hat zu viel Unterhaltung insbesondere bei Konferenzen beigetragen. Im besonderen möchte ich mich bei Thorsten Erdmann für seine Mitarbeit an der Publikation meiner Diplomarbeit bedanken. Christoph Brand und Jérôme Soiné möchte ich für die Bereitstellung des Finite Elemente Codes und Optimierer danken. Viele Diskussionen über Zellmodelle und Traction Force haben auch zu meiner Arbeit beigetragen. Dank geht auch an Marco Linke für seine Hilfe bei Python, Bildverarbeitung und den Diskussionen über das MEHTRICS Projekt. Heinrich Klein danke ich dafür, dass er vier Jahre neben mir saß. Die vielen Diskussionen mit ihm haben viele Probleme gelöst und zu einem tieferen Verständnis vieler Themen beigetragen. Christoph Koke danke ich für die Unterstützung bei Programmierfragen.

Meinen Freunden möchte ich für die schöne gemeinsame Zeit danken. Besonderer dank geht an Bastian Höltkemeier für das Kochen während des Zusammenschreibens. Dieser dank geht auch an Valerie Wentzky. Ihr möchte ich auch für die Unterstützung in allen Lebenslagen und für ihre Motivation während des schreiben danken.

Meiner Familie danke ich für die Finanzierung meines Studiums und die Unterstützung über viele Jahre.